

# BULLETIN OF THE MINERAL RESEARCH AND EXPLORATION

2022

169

ISSN : 0026-4563  
E-ISSN : 2651-3048

## CONTENTS

### Research Articles

- Some thoughts on the morphotectonic development of the Denizli region.....1  
Yücel YILMAZ
- Recovery of Cu-Ce from copper slag by using flotation and chemical methods.....17  
Bekir BAŞKURT, M. Tayhan SERDENGEÇTİ, Kaan ÖZCELİK and Hüseyin BAŞTÜRKÇÜ
- Investigation of thermal transformation of composite material obtained from granite and recrystallized limestone natural stone wastes .....27  
Gökhan EROL and Devrim PEKDEMİR
- Estimation of blast vibrations by numerical modelling and signal analysis .....39  
Güzin Gülsev UYAR AKSOY, Cemalettin Okay AKSOY and Hasan Eray YAMAN
- Uludağ extensional metamorphic core complex: preliminary field observations.....49  
Gürol SEYİTOĞLU and Korhan ESAT
- Geology, fluid inclusion characteristics and mineral resource estimation of the Güzelyayla porphyry Cu-Mo mineralization (NE Türkiye)...63  
Mustafa Kemal REVAN, Deniz GÖÇ, Mustafa ÖZKAN, Cüneyt ŞEN, Rasim Taylan KARA, Mustafa TOKOĞLU, Semi HAMZAÇEBİ, Rıfat Cihan SEVİM, Fatih SEZEN, Celaleddin BAYRAKTAR and Ömer AKGÜL
- Evaluation of potential rock falls with three-dimensional analysis: example of Oltanbey and Hasanbey districts (Gümüşhane city center)...87  
Selçuk ALEMDAĞ, Rasim Taylan KARA and Hasan Tahsin BOSTANCI
- Assessment of crustal thinning and tectonic stress distribution of Gülbahçe fault zone and its surroundings (İzmir, West Türkiye) using gravity and magnetic anomalies.....105  
Oya ANKAYA PAMUKÇU, Ayça ÇIRMIK, Fikret DOĞRU, Ece ÜNLÜ and Barış Can MALALİÇİ
- Analysis of the stress distribution of North Anatolian Fault Zone for the part between Amasya - Tokat cities.....121  
Ayça ÇIRMIK, Ufuk AYDIN, Oya ANKAYA PAMUKÇU and Fikret DOĞRU
- Formation and tectonic evolution of structural slices in eastern Kargı Massif (Çorum, Türkiye) .....135  
Cihan YALÇIN, Nurullah HANİLÇİ, Mustafa KUMRAL and Mustafa KAYA
- Acknowledgements.....155
- Bulletin of the Mineral Research and Exploration Notes to the Authors .....157

**OWNER ON BEHALF OF MTA GENERAL DIRECTORATE  
GENERAL DIRECTOR**

Vedat YANIK

**EXECUTIVE PUBLICATION EDITORIAL BOARD**

Şule GÜRBOĞA (Chairman)

Serap ARICIOĞLU

Oğuz ALTUN

Buğra ÇAVDAR

Recep GÜNEY

Neşe OYAL

Selim ÖZALP

**EDITOR-IN-CHIEF**

Halim MUTLU (Ankara-Türkiye)

**EDITORIAL BOARD**

Orhan R. ABBASOV (Azerbaijan)

Sinan AKISKA (Ankara-Türkiye)

Oğuz ALTUN (Ankara-Türkiye)

Mustafa Can CANOĞLU (Sinop-Türkiye)

Xi-Jie CHEN (Beijing-China)

Buğra ÇAVDAR (Ankara-Türkiye)

Aydın ÇIÇEK (Ankara-Türkiye)

Fuat ERKÜL (Antalya-Türkiye)

Mustafa Batuhan ERTEKİN (Ankara-Türkiye)

Ranjith Pathegama GAMAGE (Monash-Australia)

Sevda DEMİR (Ankara-Türkiye)

Recep GÜNEY (Ankara-Türkiye)

Alper GÜRBÜZ (Niğde-Türkiye)

Olca İNANÇ (Ankara-Türkiye)

Doğan KALAFAT (İstanbul-Türkiye)

Sándor KELE (Budapest-Hungary)

Cumhur Özcan KILIÇ (Ankara-Türkiye)

Onur Eser KÖK (Hatay-Türkiye)

David LENTZ (New Brunswick –Canada)

Robert MORITZ (Genève-Switzerland)

Eren PAMUK (Ankara-Türkiye)

Neşe OYAL (Ankara-Türkiye)

Semiha ÖNCÜ (Ankara-Türkiye)

Selim ÖZALP (Ankara-Türkiye)

Ayşe ÖZDEMİR (Van-Türkiye)

Ökmen SÜMER (İzmir-Türkiye)

Pınar ŞEN (Ankara-Türkiye)

Deniz TİRİNGA (Ankara-Türkiye)

Ergül YAŞAR (Hatay-Türkiye)

**ADVISORY BOARD**

Erdin BOZKURT (Ankara-Türkiye)

Osman CANDAN (İzmir-Türkiye)

Ahmet GÖKÇE (Sivas-Türkiye)

M. Cemal GÖNCÜOĞLU (Ankara-Türkiye)

Nilgün GÜLEÇ (Ankara-Türkiye)

Cahit HELVACI (İzmir-Türkiye)

Kamil KAYABALI (Ankara-Türkiye)

Nuretdin KAYMAKÇI (Ankara-Türkiye)

Aral İ. OKAY (İstanbul-Türkiye)

Cengiz OKUYUCU (Konya-Türkiye)

Osman PARLAK (Adana-Türkiye)

Okan TÜYSÜZ (İstanbul-Türkiye)

İbrahim UYSAL (Trabzon-Türkiye)

Taner ÜNLÜ (Ankara-Türkiye)

Yücel YILMAZ (İstanbul-Türkiye)

**MANAGING EDITOR**

Banu Ebru BİNAL (Head of the Department of Scientific Documentation and Presentation), e-posta: banu.binal@mta.gov.tr

**LOCATION OF MANAGEMENT**

Bilimsel Dokümantasyon ve Tanıtma Dairesi Başkanlığı

Maden Tetkik ve Arama Genel Müdürlüğü

Çukurambar Mahallesi

Dumlupınar Bulvarı No: 11 06530

Çankaya/ANKARA

e-mail: bilimsel\_dairesi@mta.gov.tr

**TRANSLATIONS**

The translation of Yılmaz and Seyitoğlu et al. were made by the authors. The translations of Alemdağ et al., Aksoy et al., Başkurt et al., Çırmık et al., Devrim et al., Pamukçu et al. and Yalçın et al. were made by Department of International Relations in MTA. The translation of Revan et al. was made by Mustafa Kerem AVCI.

Bull. Min. Res. Exp. is indexed and abstracted in TR Dizin, Emerging Source Citation Index (ESCI), Scopus, The ICI Journals Master List (Copernicus), Directory of Open Access Journals (DOAJ), Open Academic Journals Index (OAJI), Georef, MIAR, EBSCO and Zoological Record.

The Bulletin of the Mineral Research and Exploration is published in three issues in a year. Each volume is published in Turkish and English in pdf format on the website of Bulletin of the Mineral Research and Exploration and English issue published in print. The English volume of the "Bulletin of the Mineral Research and Exploration" can be obtained from "BDT Department" free of charge, either directly or ordered by adding postage fee from the correspondence address. Typesetting and printing operations are carried out and followed by the Publication Service of the Scientific Documentation and Publicity Department.

The section of "notes to the authors", format, copyright and other information can be obtained from [www.mta.gov.tr](http://www.mta.gov.tr) as PDF files.

**Printed Date:** 05.12.2022

**Printing House:** Kuban Matbaacılık - İvedik Organize Sanayi Matbaacılar Sitesi 1514. Sokak No: 20

Phone: 0312 395 2070 • Fax: 0312 395 3723 • [www.kubanmatbaa.com](http://www.kubanmatbaa.com)

**Periodical**

**ISSN:** 0026-4563

**E-ISSN:** 2651-3048

© All rights reserved. This journal and the individual contributions including in the issue are under copyright by the General Directorate of Mineral Research and Exploration (MTA), and may not be reproduced, resold, and used without permission and addressing the bulletin.



# Bulletin of the Mineral Research and Exploration

<http://bulletin.mta.gov.tr>



## Some thoughts on the morphotectonic development of the Denizli region

Yücel YILMAZ<sup>a</sup>

<sup>a</sup>*Istanbul Technical University, Mining Faculty, Maslak, İstanbul, Türkiye*

*Research Article*

Keywords:

Morphotectonics, Horst-Graben, Denizli Basin.

### ABSTRACT

The Denizli region is located to the east of the Buldan Horst. Although they follow the same trends as the Büyük Menderes and Gediz Grabens, the Denizli region has undergone semi-independent evolution during the Quaternary. The essential morphotectonic elements of the area are the Denizli Basin and the surrounding Babadağ and the Güzelpınar Horsts. The Babadağ Horst is the most distinct morphotectonic element of the region. It is bounded in the north by the Denizli fault, a listric normal fault, and possibly a major detachment fault. The Laodicea and Güzelpınar Horsts located within the downthrown block of the fault may be regarded as antithetic structures.

Received Date: 27.04.2022

Accepted Date: 20.07.2022

### 1. Introduction

A recent research project on the ancient rock quarries of western Anatolia has allowed a closer look at the major structures and morphotectonic features of the Denizli region. This paper is based on the data derived from the study. We hope that the views presented initiate future research to test the model proposed.

Essential morphotectonic elements of the Denizli region are the Denizli basin and the surrounding Babadağ (2308 m) Horst and the Güzelpınar (Çökelez Mt 1840 m) Horst (Figure 1a). The region is delimited in the west by the Buldan Horst representing the eastern end of the Bozdağ Mountains (the Bozdağ Horst), which define a plunging anticline (Figures 1a and 1b). The surrounding two large and actively enlarging grabens of western Anatolia, the Büyük Menderes graben and the Gediz graben (Erinç, 1954; McKenzie, 1978; Şengör, 1979; Şengör and Yılmaz 1981; Yılmaz et al., 2000) converge to the east (Figure

1a) (for detailed descriptions of the grabens, a reader is referred to Şengör, 1979; Şengör and Yılmaz, 1981; Seyitoğlu and Scott, 1991, 1996; Yılmaz et al., 2000; Bozkurt ve Sözbilir, 2004; Seyitoğlu et al., 2004; Yılmaz 2017a, b; Sümer et al., 2020). The grabens fragmented the Menderes Massif, which is considered to have been elevated as a core complex along a major detachment-breakaway- fault (Şengör and Yılmaz, 1981; Bozkurt and Park, 1994; Hetzel et al., 1995; Emre and Sözbilir, 1997; Gesner et al., 2001; Lips et al., 2001; Van Hinsbergen, 2010).

Two ridges dissect the eastward continuation of the grabens. These are Kadıköy ridge in the north and Gencelli ridge in the South (KR and GR; Figure 1a). Further east, a 50 km long and 20 km wide Denizli basin (Figures 1b and 2) (Westaway, 1993; Çakır, 1999) lies along with the grabens. There is a thin NW-SE trending horst in the southeastern part of the Denizli basin. The horst is located in the ancient city of Laodicea. Therefore, I call it here the Laodicea Horst (the Karakova horst of Hançer, 2013). The

Citation Info: Yılmaz, Y. 2022. Some thoughts on the morphotectonic development of the Denizli region. Bulletin of the Mineral Research and Exploration 169, 1-15. <https://doi.org/10.19111/bulletinofmre.1146674>

\*Corresponding author: Yücel YILMAZ, [yyilmaz@khas.edu.tr](mailto:yyilmaz@khas.edu.tr)

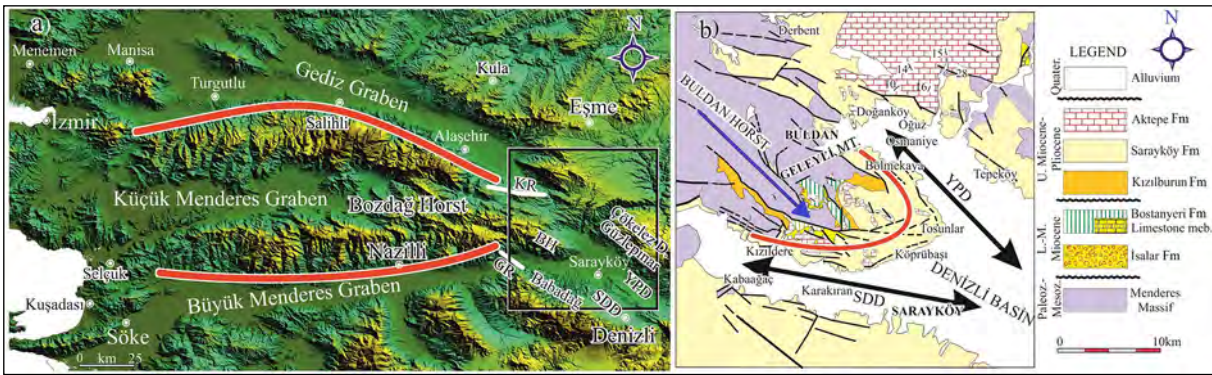


Figure 1- a) Morphotectonic map of the Bozdağ Horst and the surroundings, the central-western Anatolia. The black square shows the location of the map displayed in Figure 1b. Abbreviations for Figures 1a and 1b. GR: The Gencelli Ridge, YPD: The Yenicekent-Pamukkale depression or the Çürüksu graben, SDD; The Sarayköy-Denizli depression, b) simplified geology map of the eastern part of the Bozdağ horst (modified after Bozcu, 2010). Blue arrow; easterly plunging anticline (horst), Black arrows; axes of the graben depressions, red line with black hue; axis of the Neogene fold curving around eastern plunge of the Buldan anticline.

horst divides the Denizli basin into two unequal depressions; the Yenicekent-Pamukkale depression (the Çürüksu graben of Şimşek, 1984) in the north and

the Sarayköy-Denizli depression in the south (YDP and SDD; Figures 1a and 2).

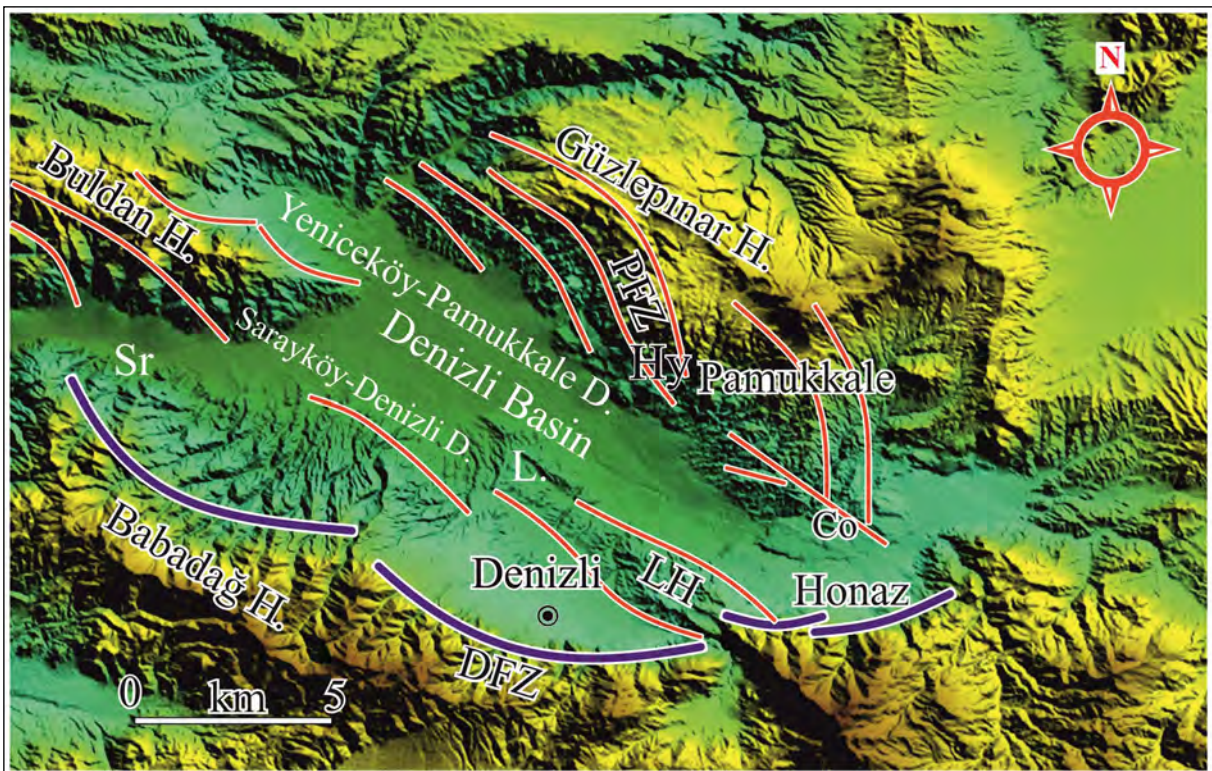


Figure 2- Morphotectonic map of the study area showing the Güzelpınar (Çökelez Mountain), Babadağ (Babadağ Mountain) Horsts, and the Denizli basin. The narrow Laodicea Horst (LH) divides the basin into unequal size depressions; the Yeniceköy-Pamukkale depression (YPD) and the Sarayköy-Denizli depression (SDD). Abbreviations; settlements: Sr: Sarayköy, L: Laodicea antique city, Co: Colossae antique city, Hy: Hierapolis antique city, D: depression, H: horsts, LH: Laodicea Horst, F: faults, DF: the Denizli fault zone, PF: Pamukkale fault zone. The arcuate red lines are gravity faults. Straight red lines extending along boundaries of the grabens and the Laodicea horst are oblique-slip faults with significant strike-slip displacement. Black lines with white hues are listric normal faults, possibly a detachment fault that elevated the metamorphic rocks against the Neogene and Quaternary successions.

## 2. Stratigraphy

In the Denizli region, four tectonostratigraphic units separated by unconformities may be distinguished (Batu et al., 1998; Yılmaz et al., 2000; Şenel, 1997, 2010; MTA, 2002 (Figures 1b and 3)). These are; 1) basement associations consisting of two rock groups, a) metamorphic rocks (M, ML; Figure 3), and b) overlying weakly metamorphosed Mesozoic limestone succession t2K, J2K; Figure 3). Some limestones belong to the Lycian nappes (Yılmaz, 2017a). The metamorphic rocks represent parts of the Menderes Massif that cover large areas in western Anatolia, extending from the Taurus Mountains in the south to the İzmir-Ankara suture zone in the north (Yılmaz, 2017a, b). The basement rocks are mostly exposed in the Babadağ and the Buldan areas (Figures 2 and 3). 2) A Lower-Middle Miocene terrestrial coarse to a fine clastic sedimentary sequence. Rock units of the sequence are defined and described in the Buldan area by Bozcu (2010). The sequence begins with thick (<500 m) red conglomerates (Figure 1b), which transit to fine-grained detrital rocks (Figure 3). 3) Lacustrine marl, claystone, and limestone alternation of the Upper Miocene (Şimşek, 1984; Göktaş, 1990; Taner, 2001; Alçiçek, 2007; Alçiçek et al., 2013, 2019) - Lower

Pliocene (Taner, 2001; Alçiçek, 2010; Alçiçek et al., 2019) age range. They overlie the underlying rocks with a distinct angular unconformity in the Buldan area (Figure 1a). The lacustrine sequence represents western Anatolia's most extensive rock group (Yılmaz, 2017a) (Figure 3). 4) The Quaternary coarse clastic rocks. They were developed as fan conglomerates along horst fronts and fluvial conglomerates deposited in valleys (Hakyemez et al., 1999; Figure 3).

## 3. Structural Geology

The study area is situated around the eastern plunge of the Bozdağ Dome-Horst (Figure 1b; Bozcu, 2010) (black square; Figure 1a) (for a detailed description of the structural elements of the region, a reader is referred to Hançer, 2013).

The Upper Miocene medium to coarse-grained red clastic sediments wrapping around the plunge of the dome (curvilinear red line in Figure 1b) rest on the approximately N-S trending Early- Middle Miocene graben fill with a distinct angular unconformity (Figure 1b; Bozcu, 2010). The rise of the dome began during the Late Miocene because it supplied clastic materials to the surrounding lateral fans (Bozcu, 2010).

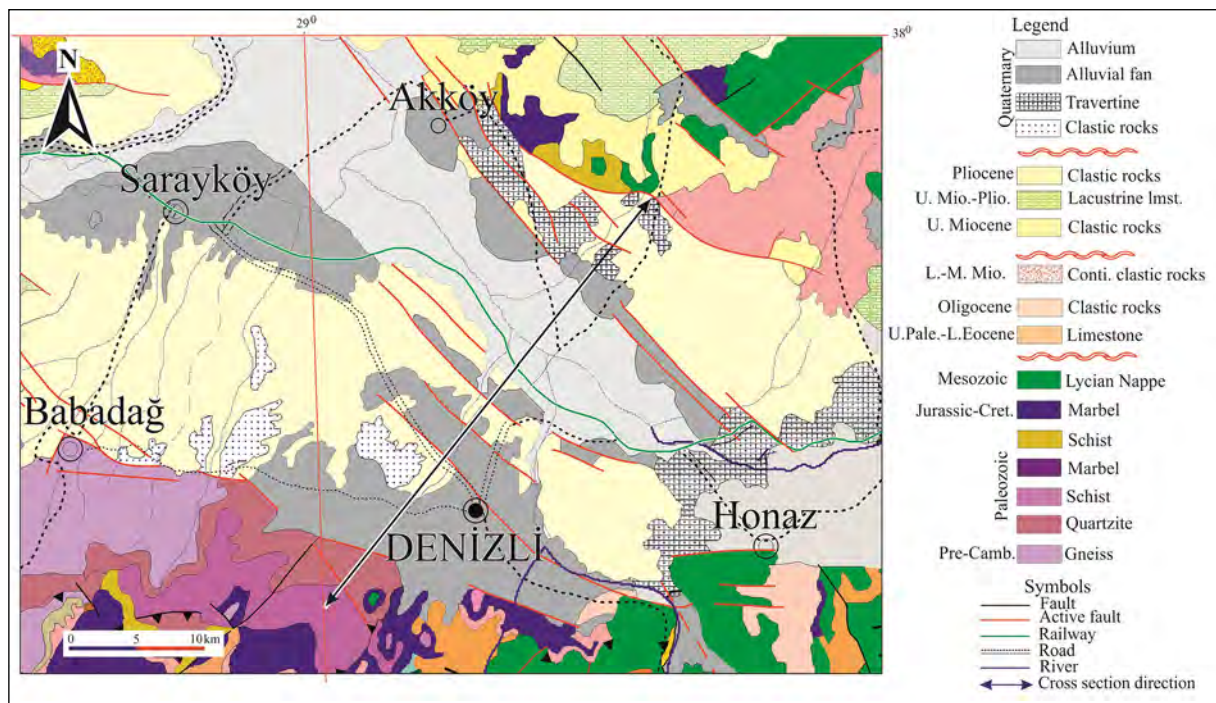


Figure 3- Geology map of the Denizli region (modified after Denizli sheet of the MTA geology map of Türkiye on the scale of 1/500.000).

Two ridges separate the Gediz and Büyük Menderes grabens from the depressions along with their eastward extension (Figure 1a). Hançer (2013) identified the northern ridge. However, the time and mechanism of development of the ridges have long remained unknown. They are morphologically distinct and control the present drainage system (Figures 1a, 4a, 4b, and 4c). The geological and morphological data also reveal that the ridges are bounded by strike-slip faults, which displaced the basement rocks and the overlying Neogene-Quaternary sedimentary sequences, sinistrally in the North (Figures 4a and 4b, and dextrally in the South (Figures 4a and 4c).

Between the two strike-slip fault zones of opposite shear sense, the eastern region of the Bozdağ dome (BH; Figure 4a) appears to have been forced to rotate in the anti-clockwise sense (Figure 4a). The motion is in harmony with the southwesterly advance of the

Anatolia Plate (McKenzie, 1978; Şengör and Yılmaz, 1981; McKenzie and Yılmaz, 1991; Mc Clasky et al., 2000; Reilinger et al., 2006, 2010).

The morphotectonic panorama of the Denizli region may be summarized as an NW-SE trending depression, the Denizli basin (graben) surrounded by the Babadağ Horst in the south (Figure 2) and the Güzelpınar Horst in the north (Figures 1a and 2; Hancer, 2019). The present landform of the Denizli region is young (Erinç, 1954), formed during the Quaternary (Yılmaz et al., 2000; Sarıca, 2000; Sümer et al., 2013; Hançer, 2013; Yılmaz, 2017b, Alçiçek et al., 2019; Özpolat et al., 2020).

The Babadağ Horst is the major morphotectonic element of the region (Figure 2). The Denizli fault (the Babadağ-Honaz fault of Hançer, 2013) defines its northern boundary (DF; Figure 2). It is a normal fault having many branches, which may be traced

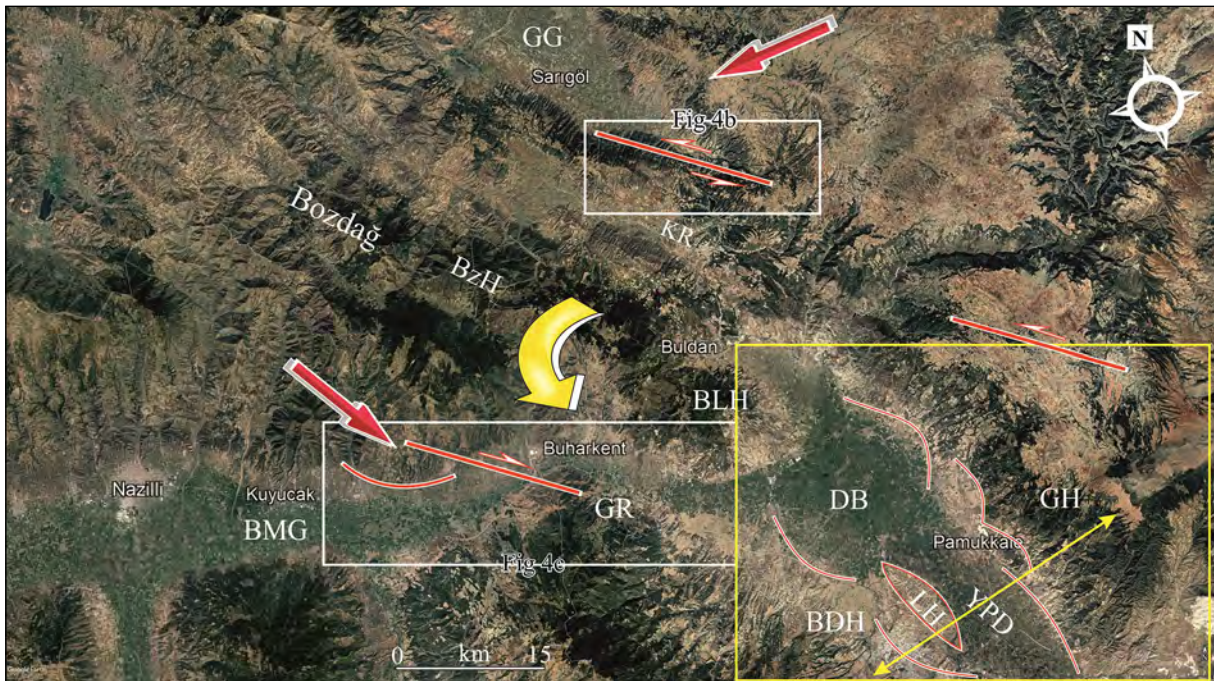


Figure 4- a) Google satellite image showing the Bozdağ Mountains and the surrounding regions. Rectangles show the locations of Figures 4b and 4c. White arrows indicate the motion directions due to the southwesterly advance of the Anatolian Plate. The circular arrow indicates the rotation of the block bounded by the strike-slip faults of opposite shear sense. The strike-slip faults (red lines); are left lateral in the north and right lateral in the south. Abbreviations, GG: Gediz Graben, BMG: Büyük Menderes Graben., BzH; Bozdağ Horst, Blh; Buldan Horst., KR: Kadıköy Ridge, GR: Gencelli Ridge, BDH: Babadağ Horst, GH: Güzelpınar Horst, LH: Laodicea Horst, DB: Denizli Basin, YPD: Yenicekent-Pamukkale Depression, SDD: Sarayköy-Denizli Depression, red line with white hue; major normal fault (detachment fault), b) Google satellite image of area 4b in Figure 4a, showing the strike-slip faults defining the boundary of the Kadıköy ridge (the northern ridge) along which significant imprints of the left-lateral displacements are observed in the morphology, c) the Google satellite image of the Gencelli ridge (the southern ridge; 4c in Figure 4a). The right-lateral offset along the boundary faults is visible in the morphology.

interruptedly more than 50 km from Babadağ in the west to Honaz in the east (Figures 2, 3, and 4a) (the eastern part of the fault was previously described by Bozkuş, 2001 and Özkaymak, 2015).

The fault plane of the Denizli fault is well exposed around Denizli city (Figure 5). It displays a concave map pattern, and the dip angle changes from about  $75^\circ$  to  $40^\circ$  (Figure 2), indicating that it is steeper near the surface and flattens with depth (Figure 5). The flattening manifests its listric normal fault character. The rotational motion of the hanging wall along the concave fault plane causes back tilting, which generated side valleys trending sub-parallel to the central depression (Figure 6).

The Denizli fault is active (Westaway, 1993; Bozkuş et al., 2001; Emre et al., 2018). One of the western branches was reactivated around Denizli city in 1965 ( $M=5.7$ ), and in 2008 earthquakes (the Denizli earthquake 4.8) (Atabey et al., 1982; Tan et al., 2008; Hançer, 2013).

The Denizli basin is subdivided into two semi-independent depressions by the Laodicea Horst (LH;

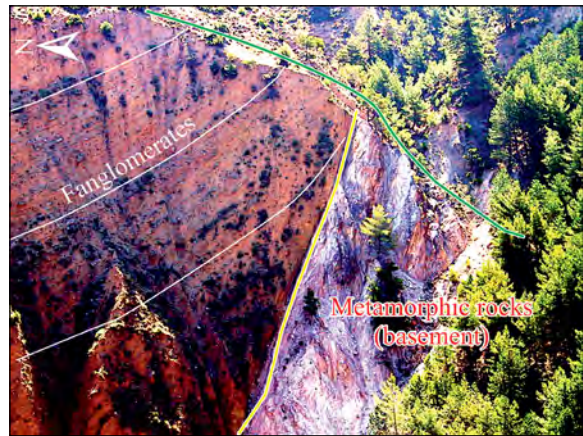


Figure 6- Photo showing the listric normal fault in the south of the Babadağ town, which separates the basement metamorphic rocks from the Neogene continental red beds. Note the stream valley (green line) on the back-tilted slope.

Figures 2, 7, 8, 9, and 10). The sequence elevated above the Laodicea Horst is terrace deposits and fluvial clastic sediments of the Quaternary age (Figure 9). The data reveals that the Laodicea Horst is younger than the Babadağ Horst, which began to rise during the late Miocene (Alçiçek et al., 2013; Hançer, 2019).

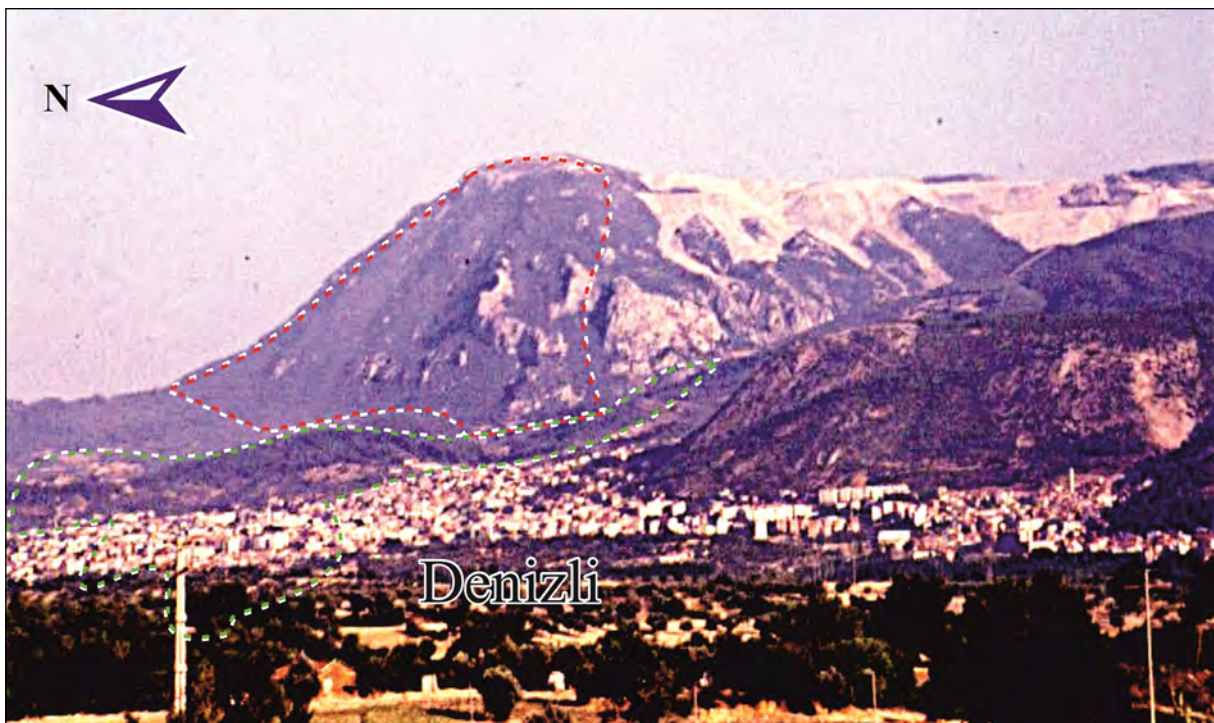


Figure 5- A view of Denizli city and the surroundings from the north. The fault plane of the steeply dipping major normal fault along which the Denizli horst was elevated is clearly observed. The flat-lying erosional surface (the broken lines) may be noted above the horst. A deeply carved lateral alluvial fan (defined by the broken green line) indicates that the rise of the horst is continuing.

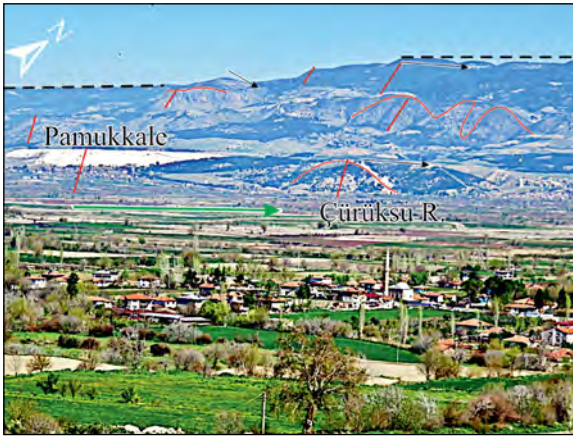


Figure 7- A panoramic view of the southern slope of the Güzelpınar Horst and the Çürüksu river valley (the Yenicekent-Pamukkale depression-graben). Steep slopes-escarpments (thick red lines) correspond to fault planes (thin red lines) of a series of sub-parallel gravity faults formed in response to the rise of the horst. Backward tilting of the downthrown blocks (black arrows) and a progressive increase in the tilting angle toward the valley reveal the listric character of the Pamukkale fault. The green arrow indicates the north-tilted valley floor of the Çürüksu river (Çürüksu R.) toward the Güzelpınar Horst. The white unit on the horst block is the Pamukkale travertine deposit near the Pamukkale town, the ancient city of Hierapolis. The black broken lines are traces of the fragmented erosional surface that remained on the horst blocks. The erosional plains are on the Upper Miocene-Lower Pliocene lacustrine units in the low land along the horizon.

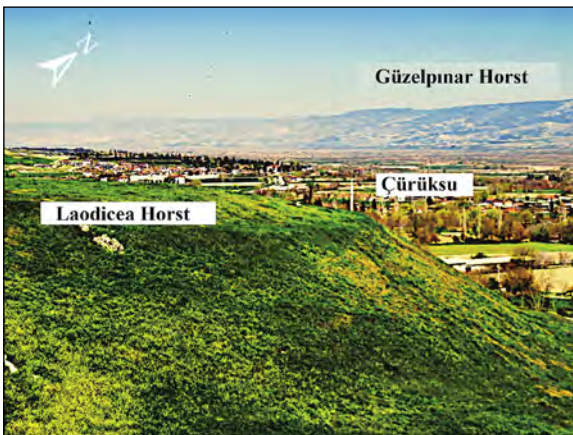


Figure 8- A northerly view from the Laodicea horst to Güzelpınar horsts. On the horizon, the gradual elevation of the flat-lying erosional plains may be noted from low land to the hills.

The Laodicea Horst is bounded by many oblique-slip faults with significant strike-slip coupled with dip-slip components (Figure 2). The discoidal map pattern of the faults (Figure 2) reveals that the horst may also be defined as a tectonic wedge that wedged into the depression (Figure 2).

The rise of the Laodicea Horst caused the northward tilting of the Çürüksu river valley (Figure 7). Consequently, the riverbed migrated toward the Güzelpınar horst (Figures 7 and 8). The historical and instrumentally recorded earthquakes reveal the dynamic character of the faults associated with the Laodicea Horst (Hançer, 2013).

The Güzelpınar Horst surrounding the Denizli graben in the south is also represented by a set of normal faults collectively known as the Pamukkale fault (Figure 7) (Altunel and Hancock, 1993; Altunel and Barka, 1996; Koçyiğit, 2005; Kaymakçı, 2006; Dilsiz, 2006; Van Noten et al., 2013; Hançer, 2013; Emre et al., 2018). Morphotectonic features in and around the fault zone reveal its listric fault character (Figure 7). Among the normal fault branches, oblique-slip displacement with strike-slip and dip-slip offsets are also common (Çakır, 1999; Van Noten et al., 2013).

Hot springs sipping along the faults of the Pamukkale fault zone generated many travertine deposits (Figure 7) (Şimşek, 1984; Altunel and Hancock, 1993; Altunel, 1996, 2000; Dilsiz, 2006; De Filippis et al., 2012; Alçiçek et al., 2013). The antique Roman city of Hierapolis was built on a back-tilted hanging wall of one of these normal faults (Figure 7) (Altunel and Hancock, 1993; Şimşek et al., 2000; Özkul et al., 2013; Alçiçek, 2007; Kele et al., 2011; Kaypak and Gökkaya, 2012; Alçiçek et al., 2013; Van Noten et al., 2013).

Many other travertine deposits associated with the young faults may also be observed in the Denizli region (Özkul et al., 2013; Van Noten et al., 2019; Aratman et al., 2020 and the references therein) (for the various geological features of the travertine deposits, a reader is referred to Altunel and Hancock (1993), Altunel (2000), Özkul et al. (2013), Kele et al. (2011), Van Noten et al. (2013), Hançer (2013), Toker et al. (2015).

According to historical records, Hierapolis was destroyed several times by earthquakes (Altunel and Hancock, 1993; Altunel and Barka, 1996; Piccardi,



Figure 9- Southerly view from the Laodicea horst to the Babadağ Horst. The terrace deposits at the base of the ancient monument of the antique city of Laodicea and the perfectly planar, flat-lying erosional surfaces on the Laodicea Horst (about 270 m) may also be noted above the Babadağ Mountains (< 2000 m). The graben boundary faults cut and dissect the continuity of the erosional surface during the Quaternary.

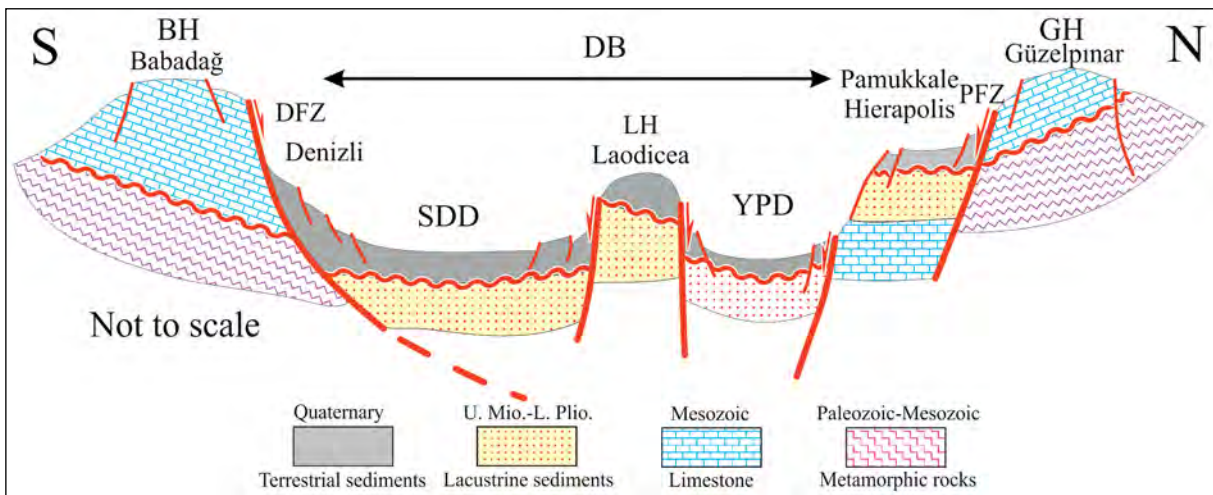


Figure 10- A sketch geological cross-section across the Denizli region showing the Babadağ Horst as a major listric normal fault (detachment fault) and the Laodicea and the Güzelpınar Horsts as antithetic structures developed on the downthrown block. The horizontal distance across the Denizli basin (DB) is about 7 km. Abbreviations. BH: Babadağ Horst, SDD: Sarayköy-Denizli graben (depression), DF: Denizli fault, LH: Laodicea Horst, YDP: Yenicekent-Pamukkale graben (depression), PF: Pamukkale fault, GH: Güzelpınar Horst.

2007; Tan et al., 2008; Utku, 2009). A magnitude six earthquake in BC 60 damaged the ancient city severely (Atabey et al., 1982; Hançer, 2013 and the references therein). The Denizli region's earthquakes have relatively shallow focal depths ranging from 5 to 10 km (Aydan et al., 2005; Kaypak and Gökkaya, 2012).

#### 4. Discussion

Back-arc extension of the Hellenic Trench (McKenzie, 1978; Le Pichon and Angelier, 1979; Meulenkamp et al., 1988) due to its southward retreat and the consequent delamination are considered the mechanisms responsible for the rapid extension of western Anatolia (Wortel and Spakman, 2000; Faccenna et al., 2004; Dilek and Altunkaynak, 2007; Agostini et al., 2008; Jolivet et al., 2013; Philippon et al., 2014; Ring et al., 2017; Yılmaz, 2017*b* and the references therein). The N-S extension generated detachment fault(s) and the associated metamorphic core complexes. The Menderes Massif, one of the good representatives of the core complexes, was partly exposed before the Late Miocene. Evidence for this is metamorphic rock clasts incorporated into the Upper Miocene terrestrial sediments (Yılmaz et al., 2000). The metamorphic rocks cropping out in the Babadağ horst may be regarded as the southeastern part of the Menderes Massif (Yılmaz, 2017*b*, Figure 2).

For the last five-six decades, geological research in western Anatolia has enlightened various geological aspects of the Neogene grabens and the surroundings (Yılmaz, 2017*a, b*; Alçiçek et al., 2019 and the references therein). However, comprehensive studies correlating the basins along and across western Anatolia are few (Yılmaz, 2000; Alçiçek, 2010; Ersoy et al., 2011, 2014). The views on the time and mechanism of the grabens having trends deviating from E-W are also quite diverse (Şengör, 1987; Genç and Yılmaz, 2000; Yılmaz et al., 2000; Genç et al., 2001; Gürer et al., 2001, 2009; Gürer and Yılmaz, 2002; Bozkurt, 2003, 2009; Seyitoğlu et al., 2004; Kaymakçı, 2006; Koçyiğit and Devenci, 2007; Ten Veen et al., 2009; Gürer et al., 2009; Ersoy et al., 2011; Özburan and Gürer, 2012; Şaroğlu and Gürer, 2020; Seyitoğlu et al., 2022; Gürer, 2023).

On the enlargement of the west Anatolian grabens, the views gradually changed through time. The earlier

views favored uninterrupted growth since they began in the late Oligocene-early Miocene (Seyitoğlu and Scott, 1996; Bozkurt, 2000; Sözbilir, 2005). Later studies support the development in pulses (Lips et al., 2001; Purvis and Robertson, 2004; Bozkurt and Rojay, 2005; Beccaletto and Steiner, 2005; Lacassine et al., 2007; Emre and Sözbilir, 2007; Chatzaras et al., 2011; Yılmaz, 2017*a, b*; Alçiçek et al., 2019). The regional angular unconformities separating the three rock groups of the Neogene-Quaternary age (Yılmaz, 1997; Koçyiğit et al., 1999; Yılmaz et al., 2000; Yılmaz, 2017*b*) favor interrupted extension.

The low energy lacustrine sequence reveals that interconnected lakes cover the entire western Anatolia during the late Miocene-Early Pliocene (Becker-Platen, 1970; Benda, 1971; Benda et al., 1974, 1977; Luttig and Stevens, 1976; Yılmaz, 2017*a, b*; Alçiçek et al., 2019). Alçiçek et al. (2019), based on the detailed paleoenvironment analyses, show that the lakes were dried out, and marsh-swamp deposits at the top of the lacustrine succession remained till the Pleistocene. The region suffered a severe erosional stage during the same period, which generated a flat-lying erosional plain above the lake deposits and the underlying rocks. Both events reveal that the region was relatively quiet during the late Miocene-late Pliocene. The development of the present E-W grabens followed the quiet period in the Pleistocene (Angelier et al., 1981, 1982; Yılmaz, 1997; Yılmaz et al., 1999; Sarıca, 2000; Rojay et al., 2005; Westaway et al., 2005; Bozkurt et al., 2011; Yılmaz, 2017*a, b*; Alçiçek et al., 2019; Maddy et al., 2020). Fragments of the flat-lying erosional plains were then elevated to different heights, which is also observed on the horsts surrounding the Denizli Graben (Figures 5, 7, 8, and 9). This key stratigraphic horizon may be used to differentiate the pre and post-erosional geological events and give them a relative age.

In the Denizli region, however, the development of the Babadağ horst possibly began during the Late Miocene (Alçiçek et al., 2019) or Early Pliocene (Taner, 2001) when the interconnected lakes were still covering the surrounding regions (MTA, 2002). Evidence for this is the coarse terrestrial conglomerates of the elevating Babadağ horst interfingering with the lacustrine sediments (Alçiçek, 2007). During this

stage the Denizli basin may thus be regarded as a half-graben (Alçiçek et al., 2019).

The Gediz and the Büyük Menderes grabens were possibly extended to the Denizli region during the initial stage of development because the infill of the grabens in both areas shares a similar coeval stratigraphy (Koçyiğit, 2005; Ergin et al., 2007; Alçiçek, 2007; Çiftçi and Bozkurt, 2009, 2010; Alçiçek et al., 2019). When the KR and GR ridges formed, the grabens collapsed (Ocakoglu, 2020) and were separated. From this period onward, the eastern and the western grabens have experienced independent evolutions.

The dominant morphotectonic element of the Denizli region is the Babadağ Horst (Özpolat et al., 2020). The Denizli fault delimits the horst in the North, which may be regarded as a detachment-breakaway fault along which the deeply buried metamorphic rocks were elevated to the levels of the Neogene and Quaternary successions. The fault may thus be considered as a part of the major detachment fault of western Anatolia (Bozkurt and Park, 1994; Hetzel et al., 1995; Emre and Sözbilir, 1997; Gessner et al., 2001, 2013; Sözbilir, 2005; Çemen et al., 2006; Öner and Dilek, 2011, 2012; Buscher et al., 2013; Wölfler et al., 2017; Heineke et al., 2019; Asti et al., 2019). In the adjacent Büyük Menderes graben, the transition from low to high-angle normal faulting was estimated to have taken place during the latest Pliocene-early Quaternary (Öner and Dilek, 2011; Sümer et al., 2020). Future seismic studies will unravel tectonic nature of the Denizli fault at deeper levels.

The Güzelpınar and Laodicea Horsts are young structures that were formed during the Quaternary (Alçiçek, 2007; Hançer, 2013, 2019; Van Noten et al., 2013, 2019, and the references therein). The development of the Denizli fault appears to have exerted substantial tectonic control in their formation because they are located within the downtown block, similar to many antithetic faults of varying sizes that also formed during this period.

## 5. Results

The low-energy lacustrine sequence reveals that interconnected lakes covered western Anatolia throughout the late Miocene and Early Pliocene. A

regionwide erosional stage that formed a flat-lying erosional plane accompanied this phase. The smooth topography was fragmented when the E-W trending major grabens began to open during the Pleistocene. The eastern and western grabens of the Denizli region were possibly united until this period. The Kadıköy and Gencelli ridges, when formed, separated the grabens during the Quaternary. Development of the ridges may be the consequence of the southwesterly motion of the Anatolian Plate, and the shear stress originated from this rotation. From this time onward, the Denizli Region has undergone a semi-independent evolution.

Major morphotectonic elements of the Denizli region are the NW-SE trending Babadağ and the Güzelpınar horsts. They define the Denizli basin. There is also a thin and narrow Laodicea horst in the basin's southeastern part, dividing it into two depressions of unequal size.

The most distinct morphotectonic entity of the Denizli Region is the Babadağ Horst. The Denizli fault delimits the horst in the north and may be regarded as an eastern extension of the detachment fault along which the Menderes massif was exhumed.

The development of the Denizli fault has possibly controlled the formation of the Laodicea and Güzelpınar Horsts located within the downthrown block. Partly coevally, many other antithetic faults of varying sizes, genetically associated with the young horsts, were also formed.

## Acknowledgements

Some of the data I used in this paper was collected during the course of field study on the ancient rock quarries of the Anatolia Project led by Prof. Dr. Erdoğan YÜZER to whom I extend my sincere thanks.

I wholeheartedly thank Profs Dr. F. GÜRER and Dr. E. YİĞİTBAŞ, who reviewed the manuscript and made many valuable corrections and suggestions, which helped me improve the paper. I extend my thanks to Assoc. Prof. Dr. Ş. GÜRBOĞA encouraged me to write the paper. I also thank MSc S. DEMİR for her technical support in increasing the quality of the manuscript. I am also thankful to Prof. Dr. F. GÜRER and Mr. Serdar AYDOĞAN, who kindly helped me prepare the illustrations.

## References

- Alçıçek, M. C. 2007. Tectonic development of an orogen-top rift recorded by its terrestrial sedimentation pattern: the Neogene Eşen Basin of southwestern Anatolia, Turkey. *Sedimentary Geology* 200, 117–140.
- Alçıçek, H. 2010. Stratigraphic correlation of the Neogene basins in southwestern Anatolia: regional palaeogeographical, palaeoclimatic, and tectonic implications. *Paleogeography, Palaeoclimatology, Palaeoecology* 291, 297–318.
- Alçıçek, M. C., Brogi, A., Capezzuoli, E., Liotta, D., Meccheri, M. 2013. Superimposed basin formation during Neogene–Quaternary extension in SW-Anatolia (Turkey): insights from the kinematics of the Dinar fault zone. *Tectonophysics* 608, 713–727.
- Alçıçek, M. C., Mayda, S., Ten Veen, J. Y., Boulton, S. J., Neubauer, T. A., Alçıçek, H., Tesakov, A. S., Saraç, G., Hakyemez, Y. H., Gökaş, F., Murray, M. A., Titov, V. V., Jiménez-Moreno, G., Büyükmeriç, Y., Wesselingh, F. P., Bouchal, J. M., Demirel, A., Kaya, T. T., Halaçlar, K., Bilgin, M., Van den Hoek Ostende, L. 2019. Reconciling the stratigraphy and depositional history of the Lycian orogen-top basins, SW Anatolia. *Paleobiodiversity and Palaeoenvironments* 99, 551-570.
- Altunel, E. 1996. Pamukkale travertenlerinin morfolojik özellikleri, yaşları ve Neotektonik önemleri. *Bulletin of the Mineral Research and Exploration* 118, 47-64.
- Altunel, E. 2000. Hierapolis ve yakın çevresinde tarihsel deprem aktivitesi (Lattivita Sismica a Hierapolise Nelle Zone Limitrofe). *Ricerche Archeologiche Turche Nella Valle Del Lykos, Lykos Vadisi Türk Arkeoloji Araştırmaları*, 229-325.
- Altunel, E., Hancock, P. L. 1993 Active fissuring and faulting in Quaternary travertines at Pamukkale, Western Turkey. Stewart, I. S., Vita-Finzi, I. C., Owen, L. A. (Ed.). *Neotectonics and Active Faulting. Zeitschrift Geomorphologie Supplementary* 94, 285-302.
- Altunel, E., Barka, A. 1996. Evaluation of archaeoseismic damages at Hierapolis. *Geological Bulletin of Turkey* 39, 65-74.
- Angelier, J., Dumont, J. F., Karamandereci, İ. H., Poisson, A., Şimşek, Ş., Uysal, Ş. 1981. Analyses of fault mechanism and expansion of southwestern Anatolia since Late Miocene. *Tectonophysics* 75, T1–T9.
- Angelier, J. N., Le Pichon, L. X., Barrier, E., Huchon, P. 1982. The tectonic development of the Hellenic Arc and the Sea of Crete: a synthesis. *Tectonophysics* 86, 159–196.
- Aratman, C., Özkul, M., Swennen, R., Hollis, C., Erthal, M. M., Zahra Mohammadi, H. C. E. 2020. The giant quaternary Ballık travertine system in the Denizli basin (SW Turkey): a paleoenvironmental analysis (Le système de travertin quaternaire géant de Ballık dans le bassin de Denizli (sud-ouest de la Turquie): une analyse paléoenvironnementale. *Quaternaire* 31(2).
- Asti, R., Faccenna, C., Rossetti, F., Malusà, M. G., Gliozzi, E., Faranda, C., Lirer, F., Cosentino, D. 2019. The Gediz supradetachment system (SW Turkey): magmatism, tectonics, and sedimentation during crustal extension. *Tectonics* 38(4), 1414-1440.
- Atabey, E., Ateş, R. C., Bayülken, N. 1982. The 19 August 1976 Denizli, Turkey, earthquake: evaluation of the strong motion accelerograph record. *Bulletin of the Seismological Society of America* 72(1982), 1635-1649.
- Agostini, S., Ryan, J. G., Tonarini, S., Innocenti, F. 2008. Drying and dying of a subducted slab: coupled Li and B isotope variations in Western Anatolia Cenozoic volcanism. *Earth Planetary Science Letters* 272, 139-147.
- Aydan, Ö., Kumsar, H., Tano, H. 2005. Multiparameter changes in the earth's crust and their relation to earthquakes in Denizli region of Turkey. *Proceedings World Geothermal Congress*, 24-29 April 2005, 1-10.
- Batı, Z., Yazman, M., Özdemir, İ. 1998. Alkaşehir grabeni ve Alaşehir-1 prospektinin değerlendirme raporu. TPAO, Rapor No: 3864, 147.
- Beccalotto, L., Steiner, C. 2005. Evidence of two-stage extensional tectonics from the northern edge of the Edremit Graben, NW Turkey. *Geodinamica Acta* 18, 283-297.
- Becker-Platen, J. D. 1970. Lithostratigraphische Untersuchungen im Känozoikum Südwest-Anatoliens (Türkei). *Beihefte zum geologischen Jahrbuch*, 97, 1–244.
- Benda, L. 1971. Principles of the palynologic subdivision of the Turkish Neogene. *Newsletters on Stratigraphy* 1-3, 23–26.
- Benda, L., Innocenti, F., Mazzuoli, R., Radicati, F., Steffens, P. 1974. Stratigraphic and radiometric data of the Neogene in northwest Turkey. *Journal of Applied and Regional Geology* 125(2), 183-193.

- Benda, L., Meulenkamp, J. E., Schmidt, R. R., Steffens, P. 1977. Biostratigraphic correlations in the eastern Mediterranean Neogene. Correlation between sporomorph associations and marine microfossils from the Upper Oligocene-Lower Miocene of Turkey Newsletters on Stratigraphy 6, 1–22.
- Bozcu, M. 2010. Geology of Neogene basins of Buldan-Sarıcaova region and their implications in western Anatolian neotectonics. *International Journal of Earth Science* 99(4), 851-861.
- Bozkurt, E. 2000. Timing of extension on the Büyük Menderes graben, Western Turkey, and its tectonic implications. *Geological Society London of Special Publications* 173, 385–403.
- Bozkurt, E. 2003. Origin of NE-trending basins in western Turkey. *Geodinamica Acta* 16, 61–81.
- Bozkurt, E. 2009. Extensional contractional origin for the southern Menderes shear zone, SW Turkey: tectonics and metamorphic implications. *Geological Magazine* 144(1), 1-20.
- Bozkurt, E., Park, R. G. 1994. Southern Menderes Massif: an incipient metamorphic core complex in Western Anatolia, Turkey. *Journal of Geological Society of London* 151, 213-216.
- Bozkurt, E., Sözbilir, H. 2004. Tectonic evolution of the Gediz Graben: field evidence for an episodic, two-stage extension in Western Turkey. *Geological Magazine* 141(1), 63-79.
- Bozkurt, E., Rojay, B. 2005. Episodic, two-stage Neogene extension and short-term intervening compression in western Turkey: field evidence from the Kiraz basin abd Bozdağ Horst. *Geodinamica Acta* 18(3), 299-316.
- Bozkurt, E., Satır, M., Buğdaycıoğlu, C. 2011. Surprisingly young Rb/Sr ages from the Simav extensional detachment fault zone, northern Menderes Massif, Turkey. *Journal of Geodynamics* 52, 406–431.
- Bozkuş, C., Kumsar, H., Özkul, M., Hançel, M. 2001. Seismicity of active Honaz Fault under an extensional tectonic regime. *International Earth Sciences Colloquium on the Aegean Region, İzmir, Turkey*, 7-16.
- Buscher, J. T., Hampel, A., Hetzel, R., Dunkl, I., Glotzbach, C., Struffert, A., Akal, C., Rätz, M. 2013. Quantifying rates of detachment faulting and erosion in the central Menderes Massif. by thermochronology and cosmogenic. *Journal of the Geological Society* 170(4), 669-683.
- Chatzaras, V., Xypolias, P., Kokkalas, S., Koukouvelas, I. 2011. Oligocene-Miocene thrusting in central Aegean: insights from the Cycladic island of Amorgos. *Geological Journal* 46(6), 619-636.
- Çakır, Z. 1999. Along-strike discontinuity of active normal faults and its influence on Quaternary travertine deposition, examples from Western Turkey. *Journal of Earth Sciences* 8, 67–80.
- Çemen, I., Catlos, E. J., Göğüş, O. 2006. Post collisional extensional tectonics and exhumation of the Menderes Massif in the Western Anatolia Extended Terrane, Turkey. *Geological Society of America, Special Paper* 409, 353-379.
- Çiftçi, N. B., Bozkurt, E. 2009. Evolution of the Miocene sedimentary II of the Gediz Graben, SW Turkey. *Sedimentary Geology* 216(3-4), 49-79.
- Çiftçi, N. B., Bozkurt, E. 2010. Structural evolution of the Gediz Graben, SW Turkey: temporal and spatial variation of the graben basin. *Basin Research*, 22(6), 846-873.
- De Filippis, L., Faccenna, C., Billi, A., Anzalone, E., Brillì, M., Özkul, M., Soligo, M., Tuccimei, P., Villa, M. 2012. Growth of fissure ridge travertines from geothermal springs of Denizli Basin, western Turkey. *Bulletin of the Geological Society of America* 124(2012), 1629-1645.
- Dilek, Y., Altunkaynak, Ş. 2007. Cenozoic crustal evolution and mantle dynamics of post-collisional magmatism in western Anatolia. *International Geology Review* 49(5), 431-453.
- Dilsiz, C. 2006. Conceptual hydrodynamic model of Pamukkale hydrothermal field, southwestern Turkey, based on hydrochemical and isotope data. *Hydrology Journal* 14, 562-572.
- Emre, T., Sözbilir, H. 1997. Field evidence for metamorphic core complex, detachment faulting and accommodation faults in the Gediz and Büyük Menderes grabens Western Anatolia. *Proceedings of International Earth Sciences Colloquium on the Aegean Region, I*, 73-93.
- Emre, T., Sözbilir, H. 2007. Tectonic evolution of the Kiraz Basin, Küçük Menderes Graben: evidence for compression/uplift-related basin formation overprinted by extensional tectonics in West Anatolia. *Turkish Journal of Earth Sciences* 16(4), 441-470.
- Emre, Ö., Duman, T. Y., Özalp, S., Şaroğlu, F., Olgun, Ş., Elmacı, H., Can, T. 2018. Active fault database of Turkey. *Bulletin of Earthquake Engineering* 16(8), 3229-3275.

- Ergin, M., Kadir, S., Keskin, Ş., Turhan-Akyüz, N., Yaşar, D. 2007. Late quaternary climate and sea-level changes recorded in sediment composition of the Büyük Menderes Delta (eastern Aegean Sea, Turkey). *Quaternary International* 167-168, 162-176.
- Eriñç, S. 1954. Orta Ege Bölgesi'nin jeomorfolojisi. Maden Tetkik ve Arama Genel Müdürlüğü, Rapor No: 2217, Ankara (unpublished).
- Ersoy, Y. E., Helvacı, C., Palmer, M. R. 2011. Stratigraphic, structural, and geochemical features of the NE-SW trending Neogene volcanosedimentary basins in western Anatolia: implications for associations of supra-detachment and transtensional strike-slip basin formation in extensional tectonic setting. *Journal of Asian Earth Science* 41, 159-183.
- Ersoy, E. Y., Çemen, İ., Helvacı, C., Billor, Z. 2014. Tectono-stratigraphy of the Neogene basins in Western Turkey: implications for tectonic evolution of the Aegean extended region. *Tectonophysics* 635, 33-58.
- Faccenna, C., Piromallo, C., Crespo-Blanc, A., Jolivet, L., Rossetti, F. 2004. Lateral slab deformation and the origin of the western Mediterranean arcs. *Tectonics* 23, TC1012.
- Genç, Ş. C., Yılmaz, Y. 2000. Aliğa dolayının jeolojisi ve genç tektoniği (Geology and young tectonics of the Aliğa region). *Batı Anadolu Depremselliği Sempozyumu (BAD-SEM) Bildiriler Kitabı*, İzmir, 152-159.
- Genç, C. Ş., Altunkaynak, Ş., Karacık, Z., Yazman, M., Yılmaz, Y. 2001. The Çubukludağ graben, south of İzmir: its tectonic significance in the Neogene geological evolution of the western Anatolia. *Geodinamica Acta* 14, 45-55.
- Gessner, K., Ring, U., Johnson, C., Hetzel, R., Passchier, C. W., Güngör T. 2001. An active bivergent rolling-hinge detachment system: central Menderes metamorphic core complex in western Turkey. *Geology* 29(7), 611-614.
- Gessner, K., Gallardo, L. A., Markowitz, V., Ring, U., Thomson, S. N. 2013. What caused the denudation of the Menderes massif: review of crustal evolution, litho-sphere structure, and dynamic topography in southwest Turkey. *Gondwana Research* 24(1), 243-274.
- Göktaş, F. 1990. 1/25.000 ölçekli Denizli M22b1, b2 ve b3 paftalarının jeoloji haritası. Maden Tetkik ve Arama Genel Müdürlüğü, Ankara.
- Gürer, F. Ö. 2023. A new look at the origin of N-S trending young basins of western Anatolia. *Bulletin of the Mineral Research and Exploration* (in press).
- Gürer, Ö. F., Yılmaz, Y. 2002. Geology of the Oren and surrounding areas SW Anatolia. *Turkish Journal of Earth Sciences* 11, 1-13.
- Gürer, Ö. F., Bozcu, M., Yılmaz, K., Yılmaz, Y. 2001. Neogene basin development around Soke-Kuşadası (western Anatolia) and its bearing on tectonic development of the Aegean region. *Geodinamica Acta* 14, 57-69.
- Gürer, Ö. F., Sarıca-Filoreau, N., Özbüran, M., Sangu, E., Doğan, B. 2009. Progressive development of the Büyük Menderes Graben based on new data, western Turkey. *Geological Magazine* 146(5), 652-673.
- Hakyemez, H. Y., Erkal, T., Göktaş, F. 1999. Late Quaternary evolution of the Gediz and Büyük Menderes grabens, western Anatolia, Turkey. *Quaternary Science Reviews* 18(4-5), 549-554.
- Hançer, M. 2013. Study of the structural evolution of the Babadağ-Honaz and Pamukkale fault zones and the related earthquake risk potential of the Buldan Region in SW Anatolia, east of the Mediterranean. *Journal of Earth Science* 24(3), 397-409.
- Hançer, M. 2019. Structural evolution of the northeast-southwest trending tectonic lineament and a model for graben formation in the Denizli region of Western Anatolian (west of the Zagros Fold-and-Thrust Belt). *Tectonics* 3, 83-100.
- Heineke, C., Hetzel, R., Nilius, N. P., Zwingmann, H., Todd, A., Mulch, A., Wölfler, A., Glotzbach, C., Akal, C., Dunkl, I., Raven, M., Hampel, A. 2019. Detachment faulting in a bivergent core complex constrained by fault gouge dating and low temperature thermochronology. *Journal of Structural Geology* 127, 103865.
- Hetzel, R., Ring, U., Akal, C. 1995. Miocene NNE-directed extensional unroofing in the Menderes Massif southwestern Turkey. *Journal of the Geological Society of London* 152, 639-654.
- Jolivet, L., Faccenna, C., Huet, B., Labrousse, L., Le Pourhiet, L., Lacombe, O., Lecomte, E., Burov, E., Denèle, Y., Brun, J.-P., Philippon, M., Paul, A., Salaün, G., Karabulut, H., Piromallo, C., Monié, P., Gueydan, F., Okay, A., Oberhänsli, R., Pourteau, A., Augier, R., Gadenne, L., Driussi, O. 2013. Aegean tectonics: strain localization, slab tearing and trench retreat. *Tectonophysics* 597-598, 1-33.

- Kaymakçı, N. 2006. Kinematic development and paleo stress analysis of the Denizli Basin (western Turkey): implications of spatial variation of relative paleo stress magnitudes and orientations. *Journal of Asian Earth Sciences* 27, 207–222.
- Kaypak, B., Gökkaya, G. 2012. 3-D imaging of the upper crust beneath the Denizli geothermal region by local earthquake tomography, western Turkey. *Journal of Volcanology and Geothermal Research* 211–212, 47-60.
- Kele, S., Özkul, M., Gökğöz, A., Föziz, I., Baykara, M. O., Alçiçek, M. C., Németh, T. 2011. Stable isotope geochemical and facies study of Pamukkale travertines: new evidence of low-temperature non-equilibrium calcite-water fractionation. *Sedimentary Geology* 238, 191-212.
- Koçyiğit, A. 2005. The Denizli graben-horst system and the eastern limit of western anatolian continental extension: basin fill, structure, deformational mode, throw amount and episodic evolutionary history, SW Turkey. *Geodinamica Acta* 18(3–4), 167-208.
- Koçyiğit, A., Deveci, Ş. 2007. An N-S-trending active extensional structure, the Şuhut (Afyon) graben: commencement age of the extensional neotectonic period in the Isparta angle, SW Turkey. *Turkish Journal of Earth Sciences* 16, 391–416.
- Koçyiğit, A., Yusufoglu, H., Bozkurt, E. 1999. Evidence from the gediz graben for episodic two-stage extension in western Turkey. *Journal of Geological Society of London* 156, 605–616.
- Lacassin, R., Arnaud, N., Leloup, P. H., Armijo, R., Meijer, B. 2007. Exhumation of metamorphic rocks in N Aegean: the path from shortening to extension and extrusion. *Earth* 2, 51–63.
- Le Pichon, X., Angelier, J. 1979. The Hellenic Arc and trench system: a key to the Neotectonic evolution of the eastern Mediterranean area. *Tectonophysics* 60, 1-42.
- Lips, A. L. W., Cassard, D., Sözbilir, H., Yılmaz, H. 2001. Multistage exhumation of the Menderes Massif, western Anatolia (Turkey). *International Journal of Earth Sciences* 89, 781-792.
- Luttig, G., Steffens, D. 1976. Explanatory notes for the paleogeographic atlas of Turkey from Oligocene to Pleistocene. *Bundesanstalt für Geowissenschaften und Rohstoffe*, 64.
- Maddy, D., Veldkamp, A., Demir, T., Aytaç, A. S., Schoorl, J. M., Scaife, R., Boomer, I., Stemerding, C., Van DerSchriek, T., Aksay, S., Lievens, C. 2020. Early Pleistocene river terraces of the Gediz River, Turkey: the role of faulting, fracturing, volcanism and travertines in their genesis. *Geomorphology* 358, 107102.
- McClusky, S., Balassanian, S., Barka, A. A., Demir, C., Ergintav, S., Georgiev, I., Gürkan, O., Hamburger, M., Hurst, K., Kahle, H., Kastens, K., Kekelidze, G., King, R., Kotzev, V., Lenk, O., Mahmoud, S., Mishin, A., Nadariya, M., Ouzounis, A., Paradissis, D., Peter, Y., Prilepin, M., Reilinger, R., Sanli, I., Seeger, H., Tealeb, A., Toksöz, M., Veis, G. 2000. Global positioning system constraints on plate kinematics and dynamics in the eastern Mediterranean and Caucasus: *Journal of Geophysical Research* 105(B3), 5695–5720.
- McKenzie, D. P. 1978. Active tectonic of the Mediterranean belt, Aegean sea and surrounding regions. *Geophysical Journal International* 30(2), 109-185.
- McKenzie, D., Yılmaz, Y. 1991. Deformation and volcanism in western Turkey and the Aegean. *Bulletin Technical University of Istanbul Special Issues on Tectonics* 44, 345-373.
- Meulenkamp, J. E., Wortel, M. J. R., Van Wamel, W. A., Spakman, W., Strating, E. H. 1988. On the Hellenic subduction zone and the geodynamical evolution of Crete since the Late Middle Miocene. *Tectonophysics* 146, 203-215.
- MTA. 2002. 1/500000 scale geology map of Turkey, Denizli Sheet. Maden Tetkik ve Arama Genel Müdürlüğü, Ankara, Turkey.
- Ocakoglu, F. 2020. Rapid Late Quaternary denudation of the Karacasu Graben in response to subsidence in the Büyük Menderes Corridor: Insights from morphotectonics and archaeogeology. *Geomorphology*, 107107.
- Öner, Z., Dilek, Y. 2011. Supradetachment basin evolution during continental extension: the Aegean province of western Anatolia. Turkey. *The Geological Society of America* 123(11-12), 2115–2141.
- Öner, Z., Dilek, Y. 2012. Fault kinematics in supradetachment basin formation, Menderes core complex of western Turkey. *Tectonophysics* 608, 1394-1412.
- Özburan, M., Gürer, Ö. F. 2012. Late Cenozoic polyphase deformation and basin development, Kütahya region, western Turkey. *International Geology Review* 54(12), 1401-1418.
- Özkul, M., Kele, S., Gökğöz, A., ChouShen, C., Jones, B., Baykara, O. M., Föziz, I., Németh, T., Chang, Y., Alçiçek, M. Ç. 2013. Comparison of the Quaternary travertine sites in the Denizli extensional basin based on their depositional and

- geochemical data. *Sedimentary Geology* 294, 179-204.
- Özkaymak, Ç. 2015. Tectonic analysis of the Honaz Fault (western Anatolia) using geomorphic indices and the regional implications. *Geodinamica Acta* 27(2-3).
- Özpolat, E., Yıldırım, C., Görüm, T. 2020. The Quaternary landforms of the Büyük Menderes graben system: the southern Menderes Massif, western Anatolia, Turkey. *Journal of Maps* 16(2), 405-419.
- Piccardi, L. 2007. The AD 60 Denizli Basin earthquake and the apparition of Archangel Michael at Colossae (Aegean Turkey). Masse, W. B. (Ed.). *Geological Society of Special Publications* 273, 95-105.
- Philippon, M., Brun, J. P., Gueydan, F., Sokoutis, D. 2014. The interaction between Aegean back-arc extension and Anatolia escape since Middle Miocene. *Tectonophysics* 631, 176-188.
- Purvis, M., Robertson, A. H. F. 2004. A pulsed extension model for the Neogene–Recent E-W-trending Alasehir Graben and the NE-SW-trending Selendi and Gordes Basins, western Turkey. *Tectonophysics* 391, 171–201.
- Reilinger, R., McClusky, S., Vernant, P., Lawrence, S., Ergintav, S., Çakmak, R., Özener, H., Kadirov, F., Guliyev, I., Stepanyan, R., Nadariya, M. 2006. GPS constraints on continental deformation in the Africa-Arabia-Eurasia continental collision zone and implications for the dynamics of plate interactions. *Journal of Geophysical Research: Solid Earth* 111(B5).
- Reilinger, R., McClusky, S., Paradises, D., Ergintav, S., Vernant, P. 2010. Geodetic constraints on the tectonic evolution of the Aegean region and strain accumulation along the Hellenic subduction zone. *Tectonophysics* 488, 22-30.
- Ring, U., Gessner, K., Thomson S. 2017. Variations in fault-slip data and cooling history reveal corridor of heterogeneous back arc extension in the eastern Aegean Sea region. *Tectonophysics* 700, 108-130.
- Rojay, B., Toprak, V., Demirci, C., Suzen, L. 2005. Plio-Quaternary evolution of the Küçük Menderes Graben southwestern Anatolia, Turkey. *Geodinamica Acta* 18, 317–331.
- Sarıca, N. 2000. The Plio-Pleistocene age of Büyük Menderes and Gediz grabens and their tectonic significance on N-S extensional tectonics in West Anatolia: Mammalian evidence from the continental deposits. *Geological Journal* 35(1), 1–24.
- Seyitoğlu, G., Scott, B. 1991. Late Cenozoic crustal extension and basin formation in west Turkey. *Geological Magazine* 128, 155-166.
- Seyitoğlu, G., Scott, B. C. 1996. Age of the Alaşehir Graben (West Turkey) and its tectonic implications. *Geological Journal* 31(1), 1-11.
- Seyitoğlu, G., Işık, V., Çemen, İ. 2004. Complete Tertiary exhumation history of the Menderes Massif, western Turkey: an alternative working hypothesis. *Terra Nova* 16, 358-363.
- Seyitoğlu, G., Tunçel, E., Kaypak, B., Esat, K., Gökkaya, E. 2022. The Anatolian diagonal: a broad left-lateral shear zone between the North Anatolian Fault Zone and the Aegean/Cyprus. *ArcTürkiye Jeoloji Bülteni* 65(2), 93-116 .
- Sözbilir, H. 2005. Oligo-Miocene extension in the Lycian Orogen: evidence from the Lycian molasse basin, SW Turkey. *Geodinamica Acta* 18, 255–282.
- Sümer, Ö., İnci, U., Sözbilir, H. 2013. Tectonic evolution of the Söke Basin: Extension-dominated transtensional basin formation in western part of the Büyük Menderes Graben, Western Anatolia, Turkey. *Journal of Geodynamics* 65, 148–175.
- Sümer, Ö., Sözbilir, H., Uzel, B. 2020. Büyük Menderes Grabeni'nin rolling hinge (yuvarlanan reze) modelinde supra-detachment (sıyrılmaya üstü) havzadan rift havzasına evrimi. *Türkiye Jeoloji Bülteni* 63, 241-276.
- Şaroğlu, F., Güler, B. 2020. Batı Anadolu tektonik kaması'nın güncel deformasyonu: batıya doğru kaçıştan kaynaklanan blok hareketleri. *Türkiye Jeoloji Bülteni* 63(2), 161-194.
- Şenel, M. 1997. 1/100000 scale geological map of Turkey, Denizli-J9 Quadrangle, and accompanying 18 page explanatory booklet. General Directorate of Mineral Research and Exploration, Ankara.
- Şenel, M. 2010. 1:100.000 scale geological maps of Turkey Denizli N23 sheet. Mineral Research and Exploration Directorate of Turkey (MTA), Ankara.
- Şengör, A. M. C. 1979. Türkiye'nin Neotektoniği'nin esasları. *Jeoloji Kurumu Yayını*, 30.
- Şengör, A. M. C. 1987. Cross-fault and differential stretching of hanging walls in regions of low-angle normal faulting: examples from western Turkey. Coward, M. P., Dewey, J. F., Hancock, P. L. (Ed.). *Continental Extensional Tectonics*. Geological Society of London Special Publication 28, 575-589.

- Şengör, A. M. C., Yılmaz, Y. 1981. Türkiye’de Tetis’in evrimi, levha içi tektoniği açısından bir Yaklaşım. Türkiye Jeoloji Kurultayı Özel Dizi.
- Şimşek, Ş. 1984. Denizli-Sarayköy-Buldan alanının jeolojisi ve jeotermal enerji kaynakları. İstanbul Üniversitesi Yer Bilimleri Dergisi 3(1-2), 145-162.
- Şimşek, Ş., Günay, G., Elhatip, H., Ekmekçi, M. 2000. Environmental protection of geothermal waters and travertines at Pamukkale, Turkey. *Geothermics* 29 (4-5), 557-572.
- Tan, O., Cengiz, M., Tapırdamaz, A. Y. 2008. The earthquake catalogues for Turkey. *Turkish Journal of Earth Science* 17(2), 405-418.
- Taner, G. 2001. Denizli Bölgesi Neojeni’ne ait katların stratigrafik konumlarında yeni düzenleme. Türkiye Jeoloji Kurultayı Bildirisi, 54-79.
- Ten Veen, J. H., Boulton, S. J., Alçiçek, M. C. 2009. From palaeotectonics to neotectonics in the NeoTethys realm: the importance of kinematic decoupling and inherited structural grain in SW Anatolia (Turkey). *Tectonophysics* 473, 261-281.
- Toker, E., Kayseri-Özer, M. S., Özkul, M., Kele, S. 2015. Depositional system and palaeoclimatic interpretations of Middle to Late Pleistocene travertines: Kocabaş, Denizli, SW Turkey. *Sedimentology* 62(5), 1360-1383.
- Utku, M. 2009. Etkinlik ve yığınsal etkinlik dönemlerine göre Denizli depremlerinin analizi, *Bulletin of the Mineral Research and Exploration* 138, 9-34.
- Van Hinsbergen, D. J. J. 2010. A key extensional metamorphic complex reviewed and restored: the Menderes Massif of western Turkey. *Earth-Sciences Reviews* 102(1-2), 60-76.
- Van Noten, K., Claes, H., Soete, J., Foubert, A., Özkul, M., Swennen, R. 2013. Fracture networks and strike-slip deformation along reactivated normal faults in Quaternary travertine deposits, Denizli Basin, western Turkey. *Tectonophysics* 588, 154-170.
- Van Noten, K., Topal, S., Baykara, M. O., Özkul, M., Claes, H., Aratman, C., Swennen, R. 2019. Pleistocene-Holocene tectonic reconstruction of the Ballık travertine (Denizli Graben, SW Turkey): deformation of large travertine geobodies at intersecting grabens. *Journal of Structural Geology* 118, 114-134.
- Westaway, R. 1993. Neogene evolution of the Denizli region of Western Turkey. *Journal of Structural Geology* 15(1), 37-53.
- Westaway, R., Guillou, H., Yurtmen, S., Demir, T., Scaillet, S., Rowbotham, G. 2005. Constraints on the timing and regional conditions at the start of the present phase of crustal extension in western Turkey, from observations in and around the Denizli region. *Geodinamica Acta* 18, 209-238.
- Wölfler, A., Glotzbach, C., Heineke, C., Nilius, N. P., Hetzel, R., Hampel, A., Akal, C., Dunkl, I., Christl, M. 2017. Late Cenozoic cooling history of the central Menderes Massif: timing of the Büyük Menderes detachment and the relative contribution of normal faulting and erosion to rock exhumation. *Tectonophysics* 717, 585-598.
- Wortel, M. J. R., Spakman, W. 2000. Subduction and slab detachment in the Mediterranean-Carpathian region. *Science* 290, 1910-1917.
- Yılmaz, Y. 1997. Geology of Western Anatolia. Theme 3: General Geology. Active Tectonics of Northwestern Anatolia-The Marmara Polyproject. A Multidisciplinary approach by Space-Geodesy, Hydrology, Geothermics and Seismology. vdf Hochschulverlag AG an der ETH, Zurich.
- Yılmaz, Y., Genç, S. C., Gürer, Ö. F., Karacık, Z., Altunkaynak, S., Bozcu, M., Yılmaz, K., Elmas, A. 1999. Ege Denizi ve Ege Bölgesi’nin jeolojisi ve evrimi. Görür, N. (Ed.). Türkiye Denizleri, Devlet Planlama Teşkilatı. Türkiye Bilimsel ve Teknolojik Araştırma Kurumu, 211-337.
- Yılmaz, Y., Genç, Ş. C., Gürer, Ö. F., Bozcu, M., Yılmaz, K., Karacık, Z., Altunkaynak, Ş., Elmas, A. 2000. When did the Western Anatolian Grabens begin to develop? Bozkurt, E., Winchester, J. A., Piper, J. D. A. (Ed.). *Tectonics and Magmatism in Turkey and the Surrounding Area*. Geological Society of London Special Publications 173, 353-384.
- Yılmaz, Y. 2017a. Morphotectonic development of Anatolia and the surrounding regions. Çemen, İ., Yılmaz, Y. (Ed.). *Active Global Seismology; Neotectonics and Earthquake Potential of the Eastern Mediterranean Region*. Geophysical Monograph 225, American Geophysical Union, Wiley, New York, 11-91.
- Yılmaz, Y. 2017b. Major problems of Western Anatolian geology. Çemen, İ., Yılmaz, Y. (Ed.). *Active Global Seismology: Neotectonics and Earthquake Potential of the Eastern Mediterranean Region*, Geophysical Monograph Book Series 225, 141-187.





# Bulletin of the Mineral Research and Exploration

<http://bulletin.mta.gov.tr>



## Recovery of Cu-Ce from copper slag by using flotation and chemical methods

Bekir BAŞKURT<sup>a\*</sup>, M. Tayhan SERDENGEÇTİ<sup>a</sup>, Kaan ÖZÇELİK<sup>a</sup> and Hüseyin BAŞTÜRKÇÜ<sup>a</sup>

<sup>a</sup>Mustafa Asım Köksal District, Bozkurt Street, Öksüt Guesthouse, Develi, Kayseri, Türkiye

Research Article

Keywords:

Copper Slag, Cu-Ce Recovery, Flotation, Leaching.

### ABSTRACT

In our days, slags are considered secondary resources due to the metals they contain. Copper slags having economical operating grades in terms of Zn, Cu, Ce, Ni, Co, Mo, and V, have complex mineralogy due to their thermal processing based formations. Methods of recovery for copper and other precious metals from slags, have been studied, and for which, flotation plants in industrial scale are operated. In cases where physical or physico-chemical mineral processing methods are not sufficient, hydrometallurgical methods are applied. In this study, the flotation method was applied to a copper slag with 0.9% Cu grade. Copper recovery and the concentration grade were determined to be approximately 40 and 22.7% Cu, respectively. Metal extractions were examined through direct leaching tests. Using H<sub>2</sub>SO<sub>4</sub> in the leaching, resulted in gel formation, leading to an investigation of the leach parameters using HCl. Cu and Ce extractions of around 70-80% were attained as a result of a test performed for 2 hours with the addition of 25 g/L H<sub>2</sub>O<sub>2</sub> at a rate of 20-25% solids and 300 g/L HCl concentration. An examination of the metal relations, indicated that the dissolution behavior of Cu and Ce was quite similar to the Al dissolution (R<sup>2</sup>=0.9).

Received Date: 05.11.2020

Accepted Date: 12.09.2022

## 1. Introduction

Production of copper in the present day is performed based on methods such as oxidation in high temperatures, namely the pyrometallurgical method and dissolution through acidic or alkaline solutions, known as the hydrometallurgical method. 80% of the copper produced today are obtained through the pyrometallurgical method with the remaining 20% being obtained through the hydrometallurgical processes (Schlesinger et al., 2011).

Copper minerals, 80% of which contain sulphide, are most prominently found as chalcopyrite (CuFeS<sub>2</sub>), bornite (Cu<sub>5</sub>FeS<sub>4</sub>) and chalcocite (Cu<sub>2</sub>S). The pyrometallurgical method is preferred in production of pure copper from sulphide minerals,

as copper demonstrates a low level of dissolution in aqueous mediums. In order; ore preparation, processing, smelting/converting and purification are the steps followed in the pyrometallurgical method. Hydrometallurgical methods on the other hand are applied in cases of oxidized copper ores, low grade sulphide containing copper ores, scrap metal or metal recovery from waste. In order; leaching, purification and electrolytic recovery are the steps to be followed in hydrometallurgical methods (Beşe, 2017).

In pyrometallurgical methods, a large quantity of slag is produced as a byproduct of copper production. For each ton of copper produced, approximately 2.5 tons of copper slag is obtained. Copper production on a country basis amounts to 4 mt/y for the USA, 2 mt/y for Japan and 360.000, 244.000 and 60.000 t/p

Citation Info: Başkurt, B., Serdegeçti, M. T., Özçelik, K., Baştürkçü, H. 2022. Recovery Cu ad Ce from copper slag by using flotation and chemical methods. Bulletin of the Mineral Research and Exploration 169, 17-26. <https://doi.org/10.19111/bulletinofmre.1139294>

\*Corresponding author: Bekir BAŞKURT, [bekir.baskurt@gmail.com](mailto:bekir.baskurt@gmail.com)

for Iran, Brazil and Oman, respectively (Najimi et al., 2011).

Copper slags similar to run-of-mine copper ores in terms of their chemical composition, can be used as secondary copper resources. Slags are usually stored in bulks near the smelter. They generally contain 30-40% iron, 35-40% silicate, less than 10% alumina and oxidized calcite and approximately 1% copper; which makes them suitable in delivering the needs in their usage areas (Sanchez and Sudbury, 2013). According to the studies conducted on utilization of these slags, new areas of use such as road metaling material, casting raw material, cement additive and roofing materials were discovered (Chen et al., 2011).

Due to economic reasons, slag waste is now a necessity to be recovered with additional methods as it produces 3% grade Cu when obtained with pyrometallurgical methods and approximately %50 Cu in its flash matte (Uzkut and Tunçer, 1981).

In addition to flotation, hydrometallurgical methods are also preferred in utilization of copper slags. For the process of flotation, cooled and solidified copper slag is prepared after the size reduction processes. A faster cooling process leads to larger copper crystals whereas a slower cooling process results in finer sizes, in which even when fine grinding is process applied, sometimes liberation may never be observed. Copper can be found in oxidized, sulfide containing and metallic forms inside the slag. Thus, as the collector material, various combinations may be used.

Collector reagents can be exemplified as xanthates, thiocarbamates and dithiophosphates. Information on certain plants performing copper slag flotation are given in Table 1 (Yılmaz, 2018).

The core principle in hydrometallurgical methods is the dissolution of valuable parts of the rock using acidic or alkaline solution environments. Sulfuric acid, nitric acid, hydrochloric and hydrofluoric acids can be named as the most commonly used acidic solubilizers. High consumptions of acidic solubilizers are not sought after, therefore in cases where the usage is high, alkaline solubilizers are preferred. Alkaline solubilizers, although perform a more selective dissolution, have relatively lower rates of efficiency in metal dissolution. Most commonly used solubilizers can be exemplified as sodium hydroxide, calcium hydroxide, ammonium hydroxide, sodium carbonate, ammonium carbonate, and sodium sulfide (Çakır et al., 2016). Additionally, following sulfidation roasting, water leaching helps move metallic valuables to the solution. Parameters that can be considered advantageous for the hydrometallurgical methods of metal recovery from slags can be counted as follows: 1) prompt and basic process; 2) small amount of initial investment and low operational costs; 3) obtaining products with high added value; 4) flexible capacity scaling (Yao et al., 2018)

Simultaneous dissolution of iron and silica can occur in leaching copper slags with sulphuric acid. Moreover, the dissolution of silica causes gelling in the pulp. Iron-silicate bearing mineral phase inside the

Table 1- Information about the copper slag flotation plants.

Plant	Saganoseki, Japan	Toyo, Japan	Pasar, The Philippines
Capacity, tpd	450	450	370
Feed Grade, % Cu	8.33	6.5	12.5
Concentrate Grade % Cu	21.80	28.00	29.0-33.0
Tailing Grade % Cu	0.65	0.4	0.5-0.6
Recovery, %	95.0	95.0	97.0-98.0
Crushing Circuit	Jaw and 2 Cone Crusher	Roll And 2 Cone Crusher	Jaw and Cone Crusher
Grinding Circuit	Ball Mill x2	Ball Mill	Ball Mill x2
Flotation Particle Size, $\mu\text{m}$	%50 - 44 $\mu\text{m}$	%90 - 44 $\mu\text{m}$	%75 - 45 $\mu\text{m}$
Flotation Time, min	30	30	30
Collector	SIPX, Thiocarbamate	KAX, Thiocarbamate	KAX, Dithiocarbamate
Frother	Pine Oil, MF560	Pine Oil	Pine Oil, NF183

slag, reacts to sulphuric acid resulting in silicic acid. The gel structure formed in this process not only affects the metal dissolution efficiency but complicates the solid-liquid separation following the leaching process (Banza et al., 2002).

In studies conducted by Basir and Rabah (1999), the dissolubility of metals Cu, Zn, and Pb using copper slags in various acidic and alkaline environments were investigated. In experiments performed using  $\text{NH}_4\text{OH}$ , 81% Cu and 73% Cu dissolubility efficiencies were obtained albeit a very high  $\text{NH}_4\text{OH}$  concentration such as 13 M was used to achieve such rates of efficiency. This projects a very high level of consumption. Although using ammonium hydroxide results in high metal dissolubility efficiencies, reactive consumption levels are also incremental.

Different size fraction flotation attributes of slag wastes belonging to ETİ Copper Smelting Plant were examined by Yılmaz (2018). In accordance with the working specifications of the plant, 45 and 150 micrometers were selected as fine and large particle sizes for the flotation process, respectively. In the mentioned study, a mixture obtained using slag waste from two different furnace types, flash and converter were used in the ratio of 4:1, in order. For the selection of primary collector, kinetic tests with xanthate type KAX and SIPX reagents in two sizes were performed. For the larger particle size, using SIPX, a concentration of 10.98% Cu was obtained with 89.3% recovery efficiency whereas, with KAX, 8.33% Cu concentration with 97.5% recovery efficiency was observed. In support, flotation tests using Mercaptobenzothioazole, R-Isobutyl Dithiophosphate, and Modified Thiocarbamate reagents. In flotation tests, for the larger particle size, with a reagent combination of SIPX+DTP, 11.46% Cu-containing concentrate was produced with 92.87% Cu recovery efficiency. For the finer particle size, on the other hand, 8.19% Cu-containing concentrate was produced with 97.30% Cu recovery efficiency, marking the best results.

The study conducted by Çakır et al. (2016) on copper recovery from copper reffination slag flotation wastes, was performed in two stages namely the leaching process post-calcination of copper slag and direct leaching. The copper slag was put through a

mechanical activation process in different duration and rpm values. With direct leaching post-mechanical activation process, low dissolution efficiencies of 10-12% were obtained. Subsequently in the study, with the leaching process following the calcination pre-treatment, relatively higher copper dissolution values were obtained. Calcination processes were performed at 600°C with a duration of 2 hours. During the process, it was aimed to form sulfide-containing structures by adding  $\text{Na}_2\text{SO}_4$  in different amounts. The copper slag which was calcinated with 80%  $\text{Na}_2\text{SO}_4$  by weight, was leached at 100 °C with a duration of 1 hour, resulting in %60 Cu dissolution efficiency.

In this study, the aim was to selectively dissolve metals of Cu, Ce and Fe contained inside the selected copper slag waste, targeting to obtain a leach solution rich in Cu and Ce metals. At the outset, flotation was considered and possibilities of obtaining a concentration with sellable quality and efficiency were researched. Subsequently, a dissolution attempt was made with  $\text{H}_2\text{SO}_4$  leach resulting in gelling which consequently led to HCl being used for the rest of the study. In the dissolution process, the effects of parameters such as reaction times, pulp temperature, acid concentration,  $\text{H}_2\text{O}_2$  concentration, and solid ratio on metal dissolution were examined, the relation of dissolution behaviors of the metals was researched.

## 2. Material and Method

In this chapter, information regarding the results of chemical analyses of the sample, mineral composition, methods such as leaching and flotation that are used in the experiments are given.

### 2.1. Material

Within the scope of experimental studies on the copper slag from the Balıkesir region; following the characterization examination, flotation and leaching experiments were conducted. Mineralogical analyses were performed with XRD (X-ray Diffractometer) and chemical analyses were with ICP (Inductively Coupled Plasma).

The XRD analysis was performed to determine the mineral phases of the slag, peak values of delafossite, a copper-iron oxide mineral, and olivine, known as a slag regulator were observed (Figure 1).

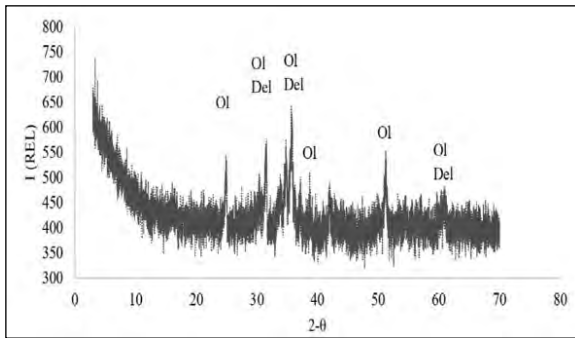


Figure 1- XRD results for the copper slag (Ol: Olivine, Del: Delafossite).

According to the chemical analysis results (ICP), the copper slag contains approximately 40% Fe, 2.2% Al, 5% Ca, 0.90% Cu and up to 78 ppm Ce. The results of the analysis are presented in Table 2. An integrative evaluation of both XRD and ICP results in points to the dominance of metal-containing phases and the remaining content being silicate minerals.

Sieving tests results and metal distributions of various particle size are given in Table 3. According to the cooling conditions of the slags, minerals can collect on different size groups. Nevertheless, according to the fractional analysis results no such event is observed for Cu and SiO<sub>2</sub>. Irregular crystal structure formed in rapid cooling can may be the reason.

### 2.2. Flotation Experiments

In the flotation experiments within the context of processing tests, standard type bond mill was used for grinding. All flotation tests were performed in -38 μm size fraction group using a Denver D-12 flotation machine. Each experiment was conducted with 30%

Table 2- Chemical analysis results.

Element	%	Element	ppm
Al <sub>2</sub> O <sub>3</sub>	4.29	Ce	78.64
CaO	7.00	Co	100.64
Fe <sub>2</sub> O <sub>3</sub>	57.29	Ga	45.22
CuO	1.13	Se	11.90
K <sub>2</sub> O	0.55	V	120.68
MgO	0.60	Mo	108.56
MnO	0.25	Au	0.10
Na <sub>2</sub> O	0.19		
PbO	0.35		
SiO <sub>2</sub>	27.86		
Fire Ignition	0.10		

solid ratio, using 2 kg of sample. In the flotation experiments, KAX (potassium amyl xanthate) and SIPX (sodium isopropyl xanthate), which are commonly used amyl xanthate type collectors and combinations of reagents A208, A238, A407 and A412 were used as supplementary materials. KAX and SIPX being >96% pure, is of Chinese origin. Other reagents, considered as supplementary materials, were procured from Solvay.

### 2.3. Leaching Experiments

In the leaching experiments within the context of chemical processing, tungsten disc mills from the brand Retch were used for grinding. The material was mixed in 500 ml glass beakers using magnetic mixers with temperature control from the brand IKA. In the leaching experiments, chemicals H<sub>2</sub>SO<sub>4</sub> (Merck, 97%) and HCl (Merck, 37%) were used as solvent medium. Dissolution efficiencies were followed up with analysis performed on the solids as well.

Table 3- Sieving test and chemical analysis of run of mine copper slag.

Particle Size, mm	Amount %	Cu, %		Fe, %		Ce, ppm		SiO <sub>2</sub> , %	
		Grade	Distribution	Grade	Distribution	Grade	Distribution	Grade	Distribution
+4	3.9	0.75	3.3	39.16	4.0	78.92	3.9	26.70	3.7
-4+3	14.9	0.79	13.1	39.72	15.6	68.92	13.0	26.30	14.0
-3+2	17.0	0.93	17.6	39.09	17.6	80.86	17.5	26.60	16.2
-2+1	22.3	0.86	21.5	38.67	22.8	84.93	24.1	27.10	21.7
-1+0.5	13.9	0.81	12.7	38.11	14.0	56.99	10.1	27.90	14.0
-0.5	28.0	1.02	31.9	35.32	26.1	88.54	31.5	30.20	30.3
Total	100.0	0.90	100.0	37.90	100.0	78.74	100.0	27.86	100.0

### 3. Mineral Processing

Detailed results of flotation and leaching experiments are presented below.

#### 3.1. Flotation Experiment Results

In flotation experiments, obtaining a concentrate with high copper content was aimed. Xanthate type collectors and supplementary materials were used tandem in the process. The reason for choosing Aerofloat 208 and Aerofloat 238 reagents based on dithiophosphate, A407 and A412 based on mercaptobenzothiazole and dithiophosphate as supplementary materials can be explained as these reagents having common usage in flotation of oxidized ores.

Grade and recovery values of the concentrate are given in Table 4. According to the flotation test results, the highest copper grade of 22.71% was obtained with SIPX, A208 and A238 reagent combination whereas the highest copper recovery of 43.7% was achieved with KAX, SIPX and A407 reagents. Although in concentrations Cu grades of 17-22% were reached, lower than acceptable copper recovery efficiencies were observed. Upon these results, due to the flotation method being not suitable for metal recovery from slag, rest of the study was continued with chemical processing experiments.

#### 3.2. Leaching Experiments

##### 3.2.1. Effects of Duration and Temperature

In order to determine the dissolution behavior of the metals such as Cu, Ce and Fe, a series of experiments with variable temperature and duration values were conducted. In the experiment the solid ratio of 10% and pH value of 2.5 were kept as constants to examine the effects of temperature and duration. (Figure 2)

In the experiments examining the correlation of duration and temperature on the dissolution, temperature was observed to have no effect on copper dissolution, whereas the highest Ce dissolution was achieved at 25 °C. In terms of the duration, a decrease in the pace of dissolution was observed by the end of a 2-hour period for Cu and Ce elements, which indicated 2 hours was the optimal reaction duration. (Figure 2)

##### 3.2.2. Effects of Particle Size

Solvent-mineral contact is one of the most important parameters. Thus, upon achieving adequate particle liberation by applying various size reduction processes, solvent-mineral contact was aimed to be kept at maximum. The cooling conditions of the slag is an important parameter in determining the liberation particle size of the valuable metals contained within. A slow cooling of the slag results in larger crystals whereas with rapid cooling, mineral crystals are not able to grow to sufficient proportions, occasionally being trapped in other mineral matrixes, as inclusions. Even with micronized grinding applied, particle liberation is not achieved sufficiently.

In experiments examining the effects of particle size on dissolution, the solid ratio, pH, duration and temperature values were kept constant. In all experiments, the effect of particle size on metal dissolution efficiency was examined by keeping 25 °C, pH: 2.5, 10% solids ratio and 120 minutes leaching time as constants (Figure 3).

These results clearly indicate the direct correlation of decreasing particle size with increasing dissolution efficiency. Decreasing the particle size to 38 micrometers does not lead to a considerable Cu dissolution efficiency whereas to an increase from 35.8% to 46.4% for Ce, and from 17.5% to 33% for Al. Following the fine grinding, due to its effects on the

Table 4- Copper slag flotation test results.

Collector Type	Concentrate Amount, %	Cu		Fe		SiO <sub>2</sub>			Ce	
		Grade %	Efficiency %	Grade %	Efficiency %	Grade %	Efficiency %	Grade %	Efficiency %	Verim, %
A407, SIPX, KAX	2.5	15.95	43.7	30.15	2.1	18.80	1.7	0.02	2.3	2.3
A208, A238, SIPX	1.6	22.71	40.4	20.99	0.9	18.30	1.0	0.03	1.8	1.8
SIPX, A412, A238	1.9	16.90	36.5	33.59	1.8	18.80	1.3	56.40	1.6	1.6
Feed	100.0	0.90		40.01		25.90		78.00		

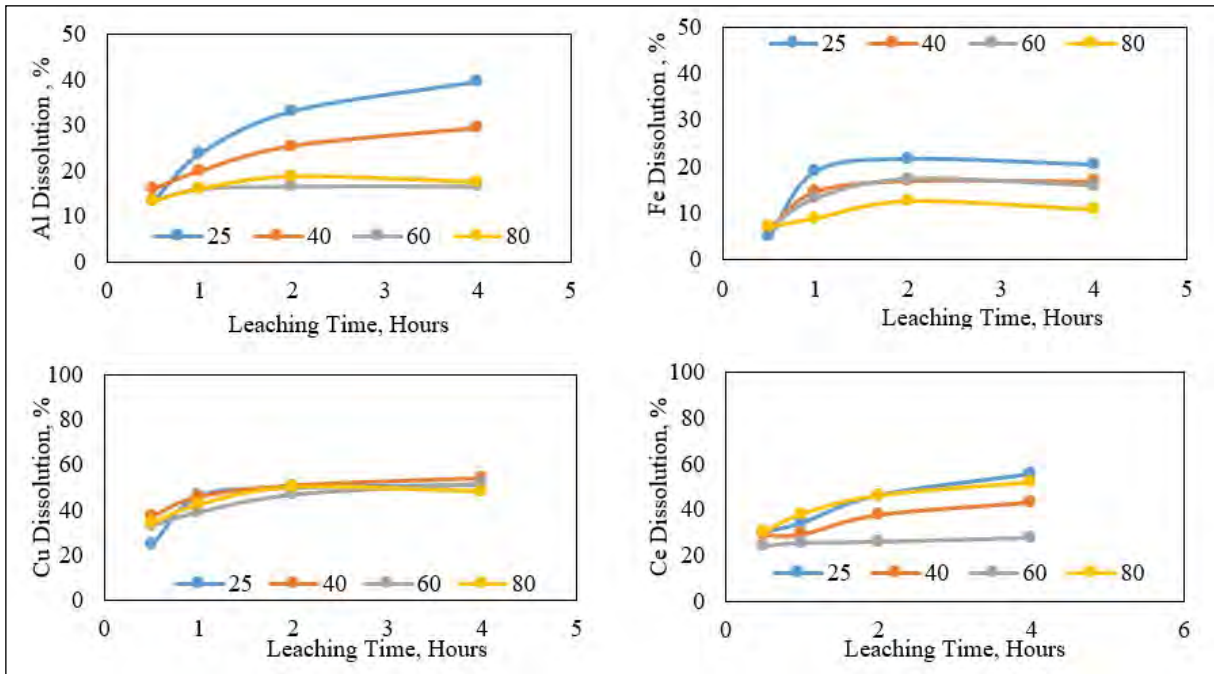


Figure 2- Correlation of duration and temperature on the dissolution efficiencies of Cu-Ce-Fe-Al, with constant solid ratio of 10% and pH value of 2.5.

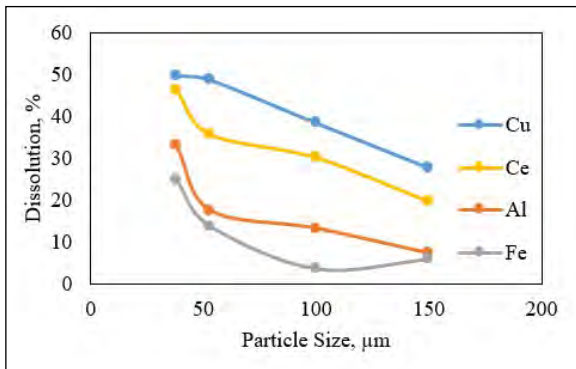


Figure 3- Effects of the particle size on dissolution rate.

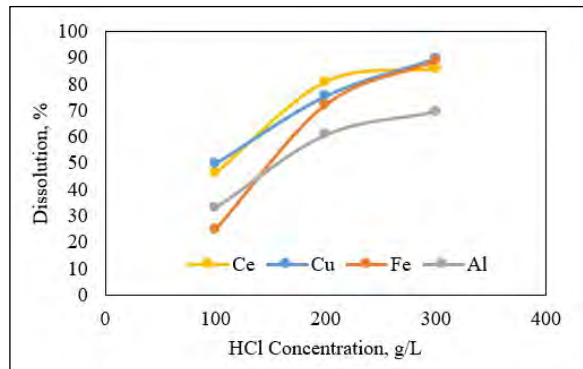


Figure 4- Effects of acid concentration on dissolution rate.

Ce dissolution efficiency, the subsequent experiments were conducted at 38 micrometers particle size as constant.

### 3.2.3. Effects of Acid Concentration

In order to examine the effects of the acid concentration, a series of experiments were conducted using various acid concentrations with a duration of 2 hours at 25 °C. Results of these experiments are given in Table 4.

Increasing the acid concentration from 100 g/L to 200 g/L, an overall increase in metal dissolution

efficiencies was observed. Moreover, an increase to 300 g/L resulted in a considerable increase in Cu and Fe dissolution efficiencies while only causing a mild increase for Al and Ce. Although the dissolution efficiency for Al reached 69.8%, it was observed to stay relatively lower in comparison to the other metals. Dissolution efficiencies of Cu, Fe and Ce metals for 300 g/L were determined to be 89.5%, 88.7% and 85.6%, respectively (Figure 4).

Additionally, effects of high acid concentrations such as 400 g/L and 500 g/L on metal dissolution were examined. Gelling of the pulp post-leaching was

observed and solid-liquid separation was not possible. Therefore, although the curves were not straightened, the most suitable acid concentration was selected as 300 g/L HCl.

### 3.2.4. Effects of $H_2O_2$ Concentration

In experiments conducted to recover valuable metals from copper slag, sufficient dissolution efficiencies for Cu and Ce metals at high acid concentrations were obtained. In addition, it was aimed to reach even higher efficiencies using a highly oxidizing agent  $H_2O_2$ . Therefore, experiments were performed using various  $H_2O_2$  concentrations. With the results given in Figure 5, observations were made that showed an additional 25 g/L, increased Cu dissolution efficiency from 50% to 75%, Ce dissolution efficiency from 46% to 70%, Fe dissolution efficiency from 25% to 67% and Al dissolution efficiency from 33% to 60%. However, it must be noted that increasing  $H_2O_2$  concentration to 50, 75 and 100 g/L results in no considerable increase in the metal dissolution efficiency as per Figure 2.

Dimitrijevic et al. (2017) demonstrated three separate experimental setup strategies in recovery of valuable metals from copper slags using hydrochloric acid. By only adding hydrochloric acid, the first experimental setup had only achieved 36% Cu dissolution efficiency by the end of 2 hours. As per their report, the second setup, a powerful oxidizer 3M  $H_2O_2$  was added inside the pulp in the beginning of the experiment and 40% Cu dissolution rate was achieved. In the third and the last experiment,  $H_2O_2$

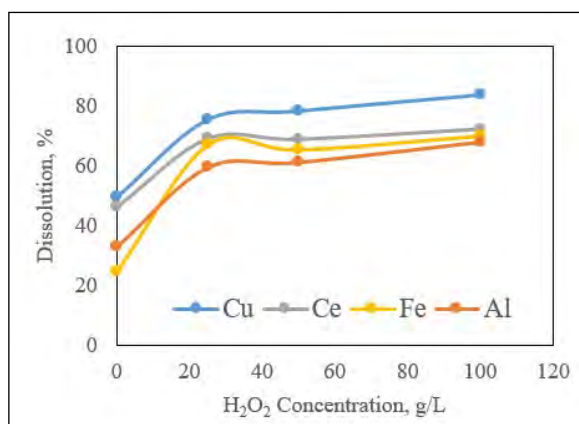


Figure 5- Effects of  $H_2O_2$  concentration on dissolution rate.

was continuously added throughout the duration of the experiment and determined a dissolution rate of 73% was achieved by the end of the 2-hour period. In the meantime, they reported that continuous addition of  $H_2O_2$  prevented the dissolution of iron, dissolution efficiency of which stood around 11%.

### 3.2.5. Effect of Solid Ratio

Experiments were conducted in order to examine the effect of solid ratio on metal dissolution. For which, solid ratios of 10, 20, 30, 40% were used along with 300 g/L HCl and constant 25 g/L  $H_2O_2$  concentration, at room temperature. Results obtained are given in Figure 6.

As it is seen in the Figure 7, increasing the solid concentrations has negatively impacted the dissolution of metals Fe, Cu and Ce. Fe was observed to be the most affected. Although 80-90% Cu and Ce dissolution efficiencies were reached, taking into consideration the industrial conditions, achieving 70-80% rate of dissolution seems feasible with 20-25% solid ratios. The increase in the solid ratio resulted in an observable decrease in Fe dissolution efficiency. Additionally, an observation was made that a more selective dissolution process occurred at 40% solid ratio than 10%.

Another topic that distinguishes this research from the rest of the works in literature is the amount and type of solids used. In previous studies, following sulfidation and chlorination leaching; dissolution with water (Altundoğan et al., 1997; Arslan and Arslan, 2002; Altundoğan ve Turan, 2012) or direct  $H_2SO_4$  leaching with low solid ratios were used. (Herrerros et al., 1998; Altundoğan et al., 2004;

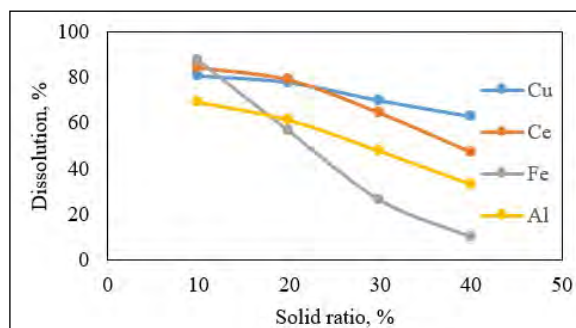


Figure 6- Effects of solid ratio on dissolution rate.

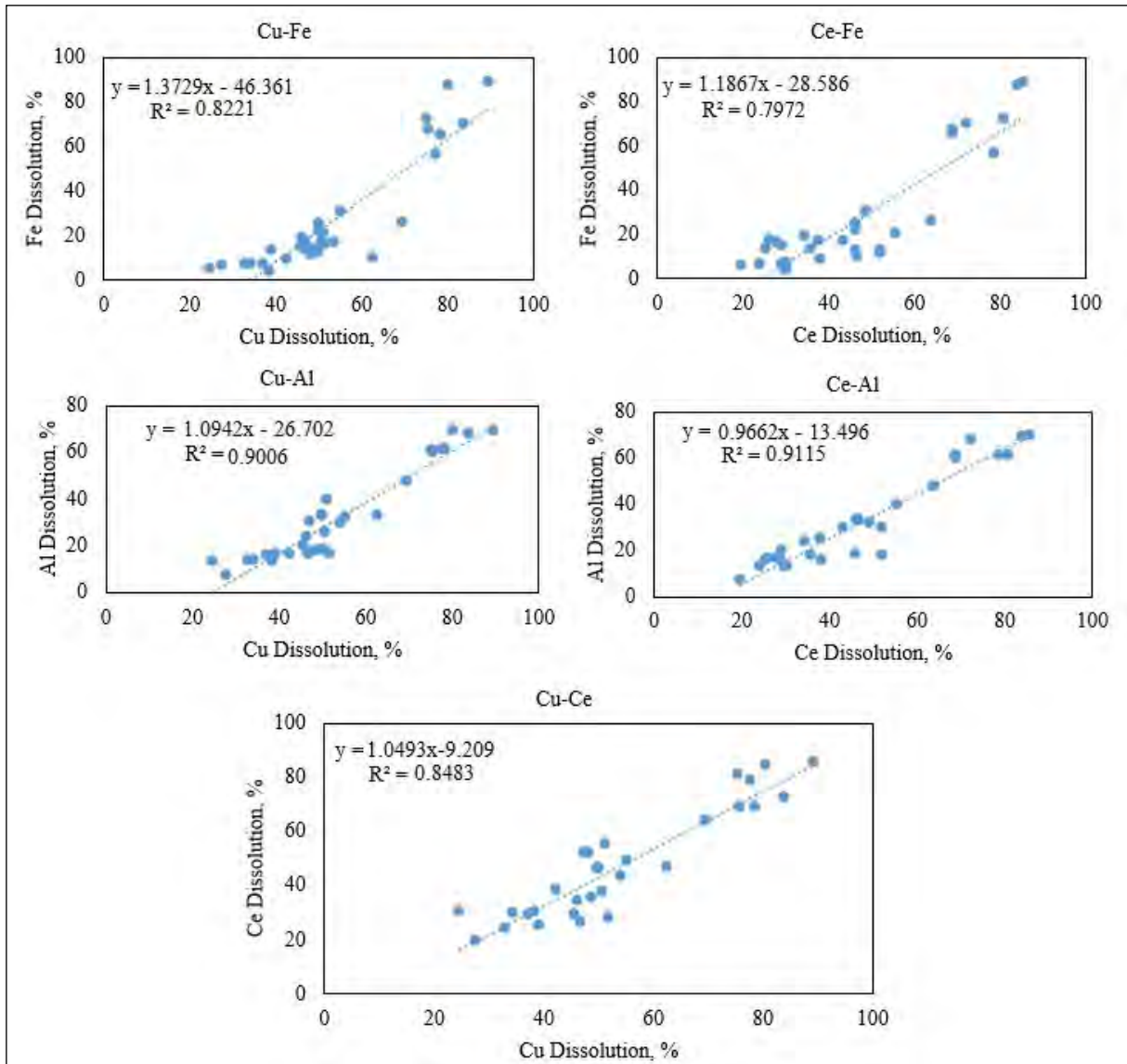


Figure 7- Correlation of Cu-Ce-Fe-Al dissolution rates.

Beşe, 2007) However in this study, due to  $H_2SO_4$  dissolution process being physically impossible, HCl is alternatively used. Although Cu and Ce dissolution rates reach their highest values with low solid ratios, this method allows for acceptable rates of dissolution (70-80%) of metals with 20-25% solid ratios.

#### 4. Results

In this study, mineral processing possibilities of a 0.90% Cu and 78.74 ppm Ce containing copper slag was examined with flotation and hydrometallurgical methods. Based on the results obtained, the following observations were made;

- Although a concentration at a threshold Cu value can be obtained using different origin flotation reagents as a combination, flotation rates were determined to stay below acceptable levels,
- Temperature had no effect on the dissolution efficiency and the value for Cu dissolution dropped following the increase in temperature, 2 hours being sufficient amount of time for the reaction,
- A considerable amount of increase is seen for the Ce dissolution rate upon fine grinding process albeit no considerable change in the Cu dissolution rate,

- Increasing acid concentrations led to a substantial increase in dissolution rates with 300 g/L acid addition being determined as sufficient for Ce and Al metals dissolution,

- Above 300 g/L HCl acid concentration led to gelling and obstructs solid-liquid separation.

- H<sub>2</sub>O<sub>2</sub> amounts more than 25 g/L had no positive effects on metal dissolution,

- Increasing solid ratios generally led to a decrease in metal dissolution efficiencies, Fe being affected the most,

- Examination among metal dissolution rates led to the observation that Cu and Ce dissolution rates had a strong correlation ( $R^2= 0.91$ ) with Al, therefore these metals were co-operating.

In conclusion, the highest Cu and Ce dissolution rates (80.5% Cu and 84.1% Ce) were achieved with leaching under the conditions of -38  $\mu$ m particle size group, 300 g/L HCl concentration, 25 °C temperature, 10% solid ratio, 25 g/L H<sub>2</sub>O<sub>2</sub> addition and 2 hour duration. However, it seems possible to achieve 70-80 percent dissolution rates with 20-25% solid ratios.

Additionally, although no detection was made in the XRD analysis, an assumption can be made as to Cu-Ce and Al being inside a similar mineral phase. To support this assumption, detailed mineralogical analyses must be made on run-of-mine and leach cake.

Moreover, with the flotation method, a concentrate of 23% Cu can be obtained with approximately 40% efficiency. Although the concentrate obtained is of sellable quality, low efficiency is the biggest disadvantage. Alternatively, leaching on flotation waste can be considered, which requires a detailed investigation of leaching conditions on run-of-mine samples.

Selective dissolution of metals, in comparison to other methods, is one of the most important advantages of chemical processing. At the same time, with the dissolution method the relation of metals with each other can be examined, which gives insight into their mineralogical context. This is beneficial for following the characterization on an elemental basis since mineral detection in materials such as slag waste

is not possible due to the complex structures formed by the thermal processing.

All results obtained from the leaching experiments were shown as a figure. Upon examining the dissolution rates of select metals, a strong correlation is understood between the dissolution rates of Cu, Ce and Al metals. The correlation value of Cu-Al is determined to be 0.90 whereas Ce-Al is 0.91. Cu-Fe and Ce-Fe correlation values are 0.82 and 0.79 respectively which brings an assumption that Cu and Ce elements are probably with a Al containing structure rather than Fe.

In addition, high iron concentration leads to the suppression of peaks belonging to other structures in the XRD analysis. Although no Al mineral was detected during the XRD analysis, a statement about copper and cerium elements being related to an Al-containing mineral phase can be made due to the high degrees of metal dissolution correlations.

## References

- Altundoğan, H. S., Tümen, F. 1997. Metal recovery from copper converter slag by roasting with ferric sulphate. *Hydrometallurgy* 44, 261-267.
- Altundoğan, H. S., Boyrazlı, M., Tümen, F. 2004. A study on the sulphuric acid leaching of copper converter slag in the presence of dichromate. *Minerals Engineering* 17, 465-467.
- Altundoğan, H. S., Turan, D. 2012. Bakır converter çürufundan değerli metallerin kükürt kavurması - su liçi yöntemiyle geri kazanılması. *Fırat Üniversitesi Mühendislik Bilimleri Dergisi* 24(1), 37-44.
- Arslan, C., Arslan, F. 2002. Recovery of copper, cobalt, and zinc from copper smelter and converter slag. *Hydrometallurgy* 67, 1-7.
- Banza, A. N., Gock, E., Kongolo, K. 2002. Base metals recovery from copper smelter slag by oxidising leaching and solvent extraction. *Hydrometallurgy* 63(1-3).
- Basir, Abdel, Rabah, S. M., Mahmoud, A. 1999. Hydrometallurgical recovery of metal values from brass melting slag. *Hydrometallurgy* 53, 31-44.
- Beşe, A. V. 2007. Effect of ultrasound on the dissolution of copper from copper converter slag by acid leaching, *Ultrasonics Sonochemistry* 14, 290-296.
- Beşe, A. 2017. Bakır çürufurundan metallerin kazanılması. *Sinop Üniversitesi* 2, 140-149.

- Chen, M. S., Han, Z. R., Wang, L. Z. 2011. Recovery of valuable metals from copper slag by hydrometallurgy. *Advanced Materials Research* 402, 35-40.
- Çakır, M., Kartal, M., Gül, H., Taşkın, E., Uysal, M., Aydın, A. O., Alp, A. 2016. Bakır rafinasyon curufu flotasyon atıklarındaki bakırın geri kazanımı. *Akademik Platform* 200-207.
- Dimitrijevic, M., Urosevic, D., Milic, S., Sokic, M., Markovic, R. 2017. Dissolution of copper from smelting slag by leaching in chloride media. *Journal of Mining and Metallurgy* 53(3), 407-412.
- Herreros, O., Quiroz, R., Manzano, E., Bou, C., Viñals, J. 1998. Copper extraction from reverberatory and flash furnace slags by chlorine leaching. *Hydrometallurgy* 49, 87-101.
- Najimi, M., Sobhani, J., Pourkhorshidi, A. R. 2011. Durability of copper slag contained concrete exposed to sulfate attack. *Construction and Building Materials* 25(4), 1895-1905.
- Sanchez, M., Sudbury, M. 2013. Physicochemical characterization of copper slag and alternatives of friendly environmental management. *Journal of Mining and Metallurgy, Section B: Metallurgy* 49(2), 161-168.
- Schlesinger, M. E., King, M. J., Sole, K. C., Davenport, W. G. 2011. *Extractive Metallurgy of Copper*. Elsevier, UK, 13.
- Uzkut, İ., Tunçer, F. 1981. KBİ Samsun izebe cüruf ve flotasyon artıklarının metal içeriği ve değerlendirilmesi. *Türkiye Bilimsel Madencilik ve Teknik* 7, 295-318.
- Yao, Y., Zhu, M., Zhao, Z., Tong, B., Fan, Y., Hua, Z. 2018. Hydrometallurgical processes for recycling spent lithium-ion batteries: a critical review. *ACS Sustainable Chemistry and Engineering* 6(11), 13611-13627.
- Yılmaz, K. C. 2018. Bakır cürufu flotasyonunda iki farklı toplayıcı kullanımının üç tane boyları verimlerine etkisinin incelenmesi. Yüksek Lisans Tezi, Hacettepe Üniversitesi, Maden Mühendisliği Bölümü, Ankara.



# Bulletin of the Mineral Research and Exploration

<http://bulletin.mta.gov.tr>



## Investigation of thermal transformation of composite material obtained from granite and recrystallized limestone natural stone wastes

Gökhan EROL<sup>a\*</sup> and Devrim PEKDEMİR<sup>a</sup>

<sup>a</sup>General Directorate of Mineral Research and Exploration, Industrial Raw Materials Studies, Ankara, Türkiye

Research Article

### Keywords:

Waste, Limestone, Thermal-Mechanical Behavior, Granite, Natural Stone.

### ABSTRACT

In this study, the usability of granite (magmatic) and recrystallized limestone (metamorphic) natural stone wastes as alternative raw materials in ceramic tile production was investigated. Based on the CaO, SiO<sub>2</sub>, and Al<sub>2</sub>O<sub>3</sub> compounds found in waste powders, mixtures containing 65% granite and 35% recrystallized limestone (by mass) were prepared to obtain the ceramic phases of gehlenite, wollastonite and anorthite as a result of thermal transformation. The grain size of both raw materials is -149 µm (d<sub>90</sub> = 110.957 µm). The powder mixtures were moistened with 7% (by mass) water and shaped in a steel mold with dimensions of 75x20x50 mm with a uniaxial press with a setting of 127 MPa. The first series samples were called as natural building stone (DYT), and the second series samples, in which wood chips of 2% (by mass) -1 mm grain size are added to obtain porous material, were called as natural building stone - porous (DYT-G). The samples belonging to both series was applied heat treatment at 1.160°C. Phase analysis of samples obtained after heat treatment was measured by X-Ray Diffraction (XRD) and Scanning Electron Microscope (SEM-EDS) methods, and sintering properties were measured using water absorption coefficient, flexural strength, modulus of elasticity, density-porosity and color measurement tests. Gehlenite and wollastonite phases were detected in the heat treated samples, but no anorthite phase was observed. According to the test results, it was determined that the flexural strength (22.64 MPa) of the DYT marked sample was in accordance with the ceramic tile standards. In the DYT-G example, despite the decreasing unit volume mass value, it was determined that the bending strength (16.50 MPa) was in the range of ceramic tile strength values.

Received Date: 17.01.2021

Accepted Date: 01.12.2021

## 1. Introduction

Increasing pace of urban development and housing parallel to industrialization in our country has led to an increased usage of natural stones. To meet the increasing demand, production capacities of factories were improved and new natural stone deposits were found. Türkiye holds approximately 40% of the planet's natural stone reserves with 5.1 billion m<sup>3</sup> of minable marble, 2.8 billion m<sup>3</sup> of minable travertine

and 1 billion m<sup>3</sup> of granite reserves. Annual natural stone production of Türkiye is around 11.5 billion tons with a total production capacity of plate manufacturing factories being approximately 6.5 billion m<sup>2</sup>. Almost all of the production is handled by the private sector (Ministry of Trade, the Republic of Türkiye, 2014).

Block and plate productions reaching massive volumes has led to large amounts of natural stone waste which in return became an environmental issue.

Citation Info: Erol, G., Pekdemir, D. 2022. Investigation of thermal transformation of composite material obtained from granite and recrystallized limestone natural stone wastes. Bulletin of the Mineral Research and Exploration 169, 27-38. <https://doi.org/10.19111/bulletinofmre.1081187>

\*Corresponding author: Gökhan EROL, [gokhan.erol@mta.gov.tr](mailto:gokhan.erol@mta.gov.tr)

Due to the inability to reuse the waste in its entirety, it has also caused economic losses. Erol and Pekdemir (2018) has prepared mixtures consisting raw materials of 5% pure aluminum oxide ( $\text{Al}_2\text{O}_3$ ) powder, 35% recrystallized limestone (metamorphic) and 60% granite (magmatic). In the mentioned study, an increase in the intensity of wollastonite and gehlenite phases were observed for the samples with firing temperature of 1.150 °C in contrast to samples that were treated with 1.140 °C. An even further amount of increase in these two phases were observed for 1.160 as well as an observation of an additional anorthite phase. They stated that the occurrence of anorthite phase greatly contributes to the resistance of the sample. It was detected in the study that when the firing temperature was increased from 1.150 °C to 1.160 °C, the elasticity modulus and flexural strength values of the samples increased by 2.4% and 28%, respectively. In red ceramic ware production process, natural stone wastes can be used as potential additive material. (Gustavo, 2019). Genç et al. (2019) researched the possibilities of usage of zeolitic tuffites in wall tiles and consequentially discovered them to be a usable raw material in wall tiles ingredients. Pastor et al. (2019) states that the natural stone industry produces large amounts of industrial waste annually and that these wastes could be used as binding ingredient to decrease the negative environmental effects arising from waste storage processes. In their study, they respectively added 5, 10, 15, 20 and 25 percent limestone by dry mass to the clay raw material and as a result determined an increase in the endurance and a decrease in deformation properties of the samples.

Stoichiometrically, wollastonite phase is calcium meta-silicate ( $\text{CaSiO}_3$ ), a mineral visually white in color and needle shaped. Properties related to its alkali form and crystal structure ensures it to become a commercially valuable product (Ciullo, 1996). Wollastonite dissolves in strong inorganic acids (such as HCl) and has a low level of dissolution in organic acids (such as  $\text{CH}_3\text{COOH}$ ) (Kogel et al., 2006). It could be used as a substitute material for raw materials such as feldspar, calcite, quartz and dolomite in ceramic industry in which it is used widely. It is also used as a preventative material for deformation due to its property of preventing thermal expansion. Moreover, it increases the strength of the raw and fired ceramic products as well as reducing drying times

and energy costs while reducing ceramic firing times (DPT, 2001).

On the other hand, stoichiometric gehlenite phase is calcium aluminosilicate ( $\text{Ca}_2\text{Al}_2\text{SiO}_7$ ). It is considered to be a product of CaO and alumina silicate reaction. (Sousa and Holanda, 2005). In the production of wall tiles, marble powders, talc and dolomite are used as calcium sources. Gehlenite and anorthite phases are formed as a result of the reaction of metakaolin, which is the transition phase of kaolinite in the tile, and CaO, which is formed as a result of thermal decomposition of calcium carbonate (Kara et al., 2006). The Gehlenite phase ( $\text{Ca}_2\text{Al}_2\text{SiO}_7$ ) is formed by hydrated lime and cement components that have been heat-treated at low temperatures ( $<1.200$  °C). Since the stable temperature range of the Gehlenite phase is 900-1.150 °C, it can form at low temperatures. The reason for the absence of gehlenite in the cement is that the clinker is heat treated above this temperature range. Calcium alumina silicate compounds, which are more stable at high temperatures, are formed in cement (Callebaut et al., 2001).

In this study, it is aimed to bring an alternative solution to the environmental pollution that occurs with the economic revaluation of the large amount of waste generated as a result of natural stone mining activities.

## 2. Materials and Methods

### 2.1. Materials

The samples determined as granite and limestone according to the XRD results in accordance with the TS EN 12407 standards. Chemical composition of the aforementioned samples determined as crystallized limestone and granite by XRF (X-ray Fluorescence) results in accordance with the TS EN 15309 are given in Table 1. Granitoids are rocks of magmatic origin rich in silica ( $\text{SiO}_2 \geq 66\%$ ) and alkalies (feldspars) and poor in calcium, magnesium and iron (amphibole, biotite etc.) contents. Granitoids are rich in range of color starting with gray-white, gray, gray-green and even brown-reddish tones. As a rock type they are also quite durable against acids due to their formation and chemical content. (Gündüz, 1995). The origin of the granitoid rock used in the study is the Eskişehir district and is granular in texture. Mineralogical composition

Table 1- Chemical properties of the raw materials used in the study.

Raw Material	SiO <sub>2</sub> (%)	Al <sub>2</sub> O <sub>3</sub> (%)	MgO (%)	CaO (%)	Na <sub>2</sub> O (%)	Fe <sub>2</sub> O <sub>3</sub> (%)	LoI (%)	Other (%)
Granite (Magmatic)	65.9	17.0	0.9	3.8	4.6	3.0	0.5	4.3
Recrystallized Limestone (Metamorphic)	0.3	0.1	0.3	55.2	<0.1	0.1	43.70	0.2

LoI: Loss on Ignition.

of the rock is of plagioclase, quartz, biotite, alkali feldspar and amphibole. Recrystallized limestones are formed due to neomorphism under the effect of heat and pressure. Essentially, they are made up of calcite minerals and contain a minimum of 90% carbonate (CaCO<sub>3</sub>). Color range can differ due to the minerals in their composition and are not durable against acids (HCl, C<sub>6</sub>H<sub>8</sub>O<sub>7</sub>, HNO<sub>3</sub>, H<sub>2</sub>SO<sub>4</sub> etc.). The origin of the limestones used in the study is the Bilecik district and are massive fine grained in texture. Mineralogical composition of this rock belonging to carbonate group minerals (calcite) are intraclast, pellet and ooid and houses fossilized shells.

2.2. Method

Appropriate mixtures were prepared in consideration of the wastes being used as replacement

material in production of floor and wall tiles in accordance with the SiO<sub>2</sub>-Al<sub>2</sub>O<sub>3</sub>-CaO system (Figure 1). In preparing the mixtures, 35% recrystallized limestone (metamorphic) and 65% granite (magmatic) raw materials were used, respectively.

In the beginning of the study, mixtures prepared with natural building stone samples ground to -149 μm (-100 mesh) are ball milled into homogeneity for 30 minutes with a speed of 180 rpm and subsequently dried at a temperature of 100 °C. 7% (6% carboxymethyl cellulose) forming water was added to the mixture and small pellets were pressed under 127 MPa pressure, in continuation of the study. (Figure 2). Pellets were then fired at 1.140, 1.150 and 1.160 °C with an electric oven (Protherm Model PLF 160/15) at a temperature of 5°C/minute and kept in

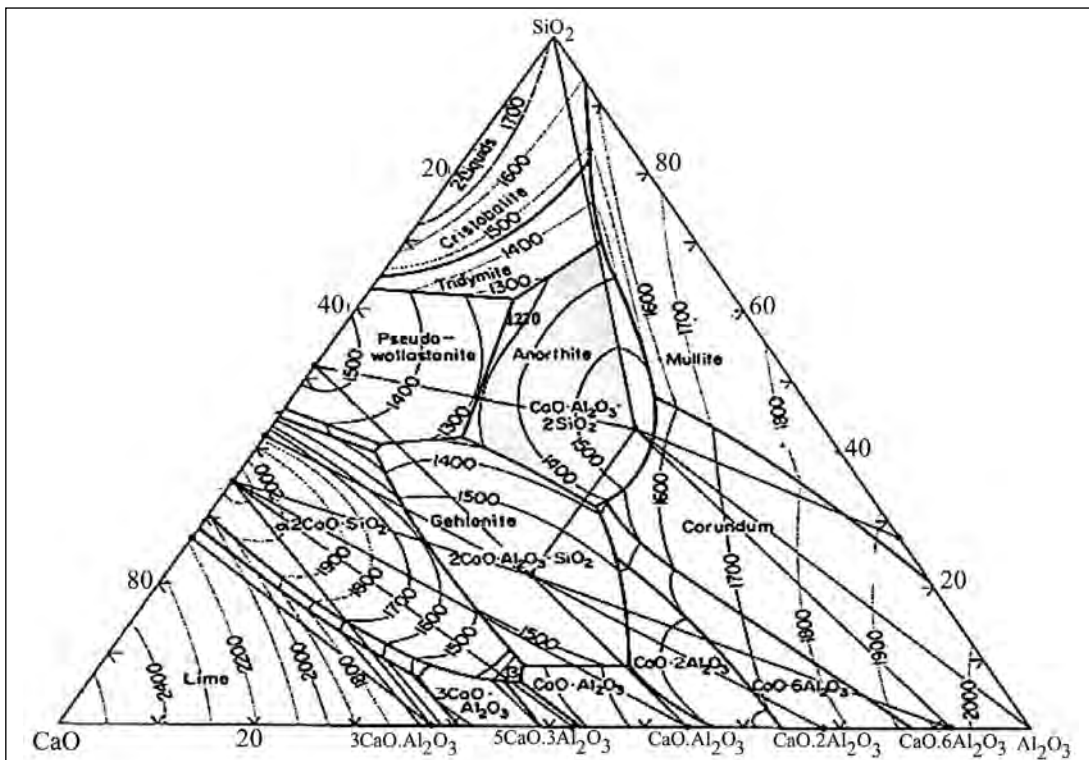


Figure 1- CaO-SiO<sub>2</sub>-Al<sub>2</sub>O<sub>3</sub> phases and isotherms (Sletson and Reed, 1988).

the last temperature for 1 minute. In the second study conducted, (Figure 3), the first procedure was repeated for samples ground to  $-74 \mu\text{m}$  ( $-200$  mesh).

In the continuation of the study, samples that were fired in the oven were sent to XRD analysis. According to the analysis results (Table 2), target phases of wollastonite and gehlenite were determined for all three separate temperature points. Considering the endurance point to be higher due to results, firing temperature and the mixture size of the samples were determined to be  $1.160^\circ\text{C}$  and  $149 \mu\text{m}$ , respectively.

Table 2- XRD analysis results of fired samples.

Heat, °C	More	Medium	Less
1.140	Wollastonite	Gehlenite	Quartz, Akermanite
1.150	Wollastonite	Gehlenite	Quartz, Akermanite
1.160	Wollastonite	Gehlenite	Quartz, Akermanite

Upon determining the process temperature and grain size, raw material samples were ground to a size

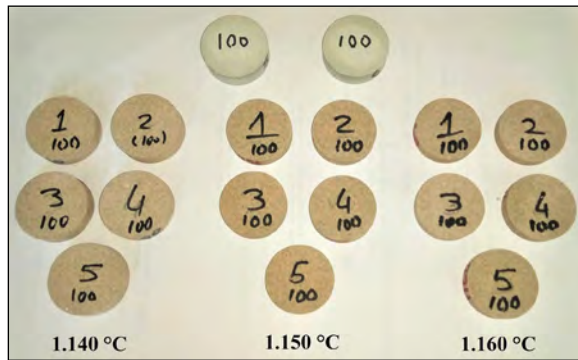


Figure 2- -100 Mesh product samples.

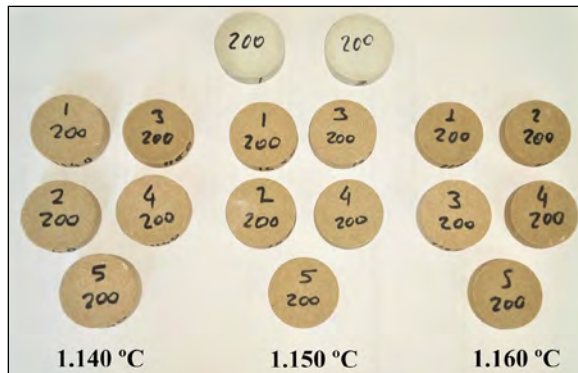


Figure 3- -200 Mesh product samples.

below  $-149 \mu\text{m}$  and then dry sieved. Using laser grain size analyzer (Malvern Mastersizer 2000), operating according to the TS ISO 13320 (Laser Radiation Diffraction Method) standards, a suspension was prepared for the mixture grain size distribution analyses, and were analyzed using the device (Table 3). According to these results, 10% of the grain size of the mixture is below  $6.961 \mu\text{m}$ , 50% is below  $41.546 \mu\text{m}$ , and 90% is below  $110.957 \mu\text{m}$ .

Table 3- Particle size distribution of the mixing materials (% distribution).

Mixture	$d_{10}$ ( $\mu\text{m}$ )	$d_{50}$ ( $\mu\text{m}$ )	$d_{90}$ ( $\mu\text{m}$ )
Particle size	6.961	41.546	110.957

To obtain the DYT (Natural Building Block, working code) product, samples of  $-149 \mu\text{m}$  were mixed, the mixture was molded in a  $75 \times 20 \times 50$  mm steel mold using 7% molding water (6% carboxymethyl cellulose) and under 127 MPa pressure (Figure 4), subsequently fired at  $1.160^\circ\text{C}$ . Following the process, 1 mm wood chip additive material with a content of 2.1% was added to mixture for the DYT-G (Natural Stone - Porous, working code) process to obtain a more porous product and the process was repeated.

### 3. Research and Findings

#### 3.1. Physical Tests

In the tests performed on the samples, results of the Modulus of Elasticity experiment, performed in accordance with the ASTM C1259-15 (2015) standards and a three-point flexural strength test device (Toni Technik Baustoffprüfssysteme GmbH, Germany), as well as the apparent density analyses



Figure 4- Product image of DYT product sample.

performed in accordance with the ASTM D5550-14 (2014) standards were given in Table 4. To determine the water absorption rates of the fired samples, first the samples were dried at 70 °C in the drying oven and weighted 24 hours apart until there was no more mass change. Dried samples were kept under water for 48 hours in room temperature and then weighted 24 hours apart until they reached stable saturation while still being kept underwater besides the weighing process. Physical test results of the samples from the 1.Ç (first study) (Erol and Pekdemir, 2018) were given in Table 4. While the flexural strength of the DYT sample, its modulus of elasticity and apparent density values in comparison to the values of DYT-G sample were respectively, 37.2%, 15% and 4.8% higher, total-open porosity and water absorption coefficient were respectively, approximately 43.7% - 11.3% and 65.9% lower. Flexural strength, the modulus of elasticity and apparent density values of the DYT-G sample in comparison to 1.Ç sample are respectively and approximately 123%, 98.5% ve 21.2% higher, total-open porosity and water absorption coefficient on the other hand are respectively and approximately 56.7% - 25.2% ve 67.6% lower.

### 3.2. Color Measurement Tests

L (white), a (green) and b (blue) color values (Figure 4) of fired samples were made using a color measurement device (Minolta CR300 Chromameter), results of which from the DYT and DYT-G samples are given in Table 5. For the L value representing the whiteness degree, it was determined that the DYT sample (58.37) had a lower value then the DYT-G sample (61.40). For the remaining colors, it was determined that DYT sample had lower amounts of green a (1.50) and blue b (8.847) values in comparison to DYT-G which respectively had values of a (0.98) and b (7.830).

Table 5- Color measurement results of fired samples.

Firing Temperature	Parameters		
	L	a	b
1160 °C			
<b>DYT</b>	58.37	1.50	8.847
<b>DYT-G</b>	61.40	0.98	7.830

### 3.3. SEM-EDS Analyses

SEM and EDS analyses (Figure 5 and Table 6) are performed for the samples of DYT product. According to the results, point of the image marked as 1, unreacted calcium oxide (CaO) can be seen. On point marked as 2, wollastonite (CaSiO<sub>3</sub>) and gehlenite [Ca<sub>2</sub>Al(AlSiO<sub>7</sub>)] phases, on points marked as 3, 4 and 5 silicon dioxide (SiO<sub>2</sub>) and on points 6 and 7, alkali-rich wollastonite (CaSiO<sub>3</sub>) and gehlenite [Ca<sub>2</sub>Al(AlSiO<sub>7</sub>)] phases were detected. On point 8, porosity of approximately 150 μm can be seen, and many micro, meso and macro porosities are found in the structure. According to SEM imaging (Figure 6) and the EDS analysis results (Table 7) of the DYT sample, it is determined that wollastonite (CaSiO<sub>3</sub>) and gehlenite [Ca<sub>2</sub>Al(AlSiO<sub>7</sub>)] phases started to crystallize at points marked as 1-7.

According to the SEM imaging sample (Figure 7) and EDS analyses of the DYT (Table 8), formation of inert calcium oxide (CaO) phases can be seen on point 1. At points 2, alkaline-rich wollastonite (CaSiO<sub>3</sub>) and gehlenite [Ca<sub>2</sub>Al(AlSiO<sub>7</sub>)] phases were formed and the contact point was determined. Strength decreases due to these contact points. SEM imaging belonging to the DYT sample (Figure 8) porosity distribution is determined to be quite homogeneous.

According to the SEM image (Figure 9) and EDS analyses (Table 9) of the DYT-G sample, inert calcium oxide (CaO) is seen in points marked as 9.2 and 7; wollastonite (CaSiO<sub>3</sub>) and gehlenite [Ca<sub>2</sub>Al(AlSiO<sub>7</sub>)]

Table 4- Physical test results of fired samples.

Sample	Flexural Strength (MPa)	Modulus of Elasticity	Visible Density (g/cm <sup>3</sup> )	Real Density (g/cm <sup>3</sup> )	Open Porosity (%)	Total Porosity (%)	Water Absorption Coefficient (%)
<b>DYT</b>	22.64	37.25	1.98	2.78	8.0	28.9	4.1
<b>DYT-G</b>	16.5	32.39	1.89	2.78	14.2	32.17	6.8
<b>1.Ç*</b>	7.40	16.32	1.56	2.75	32.8	43.0	21.0

1.Ç\* (Erol and Pekdemir, 2018).

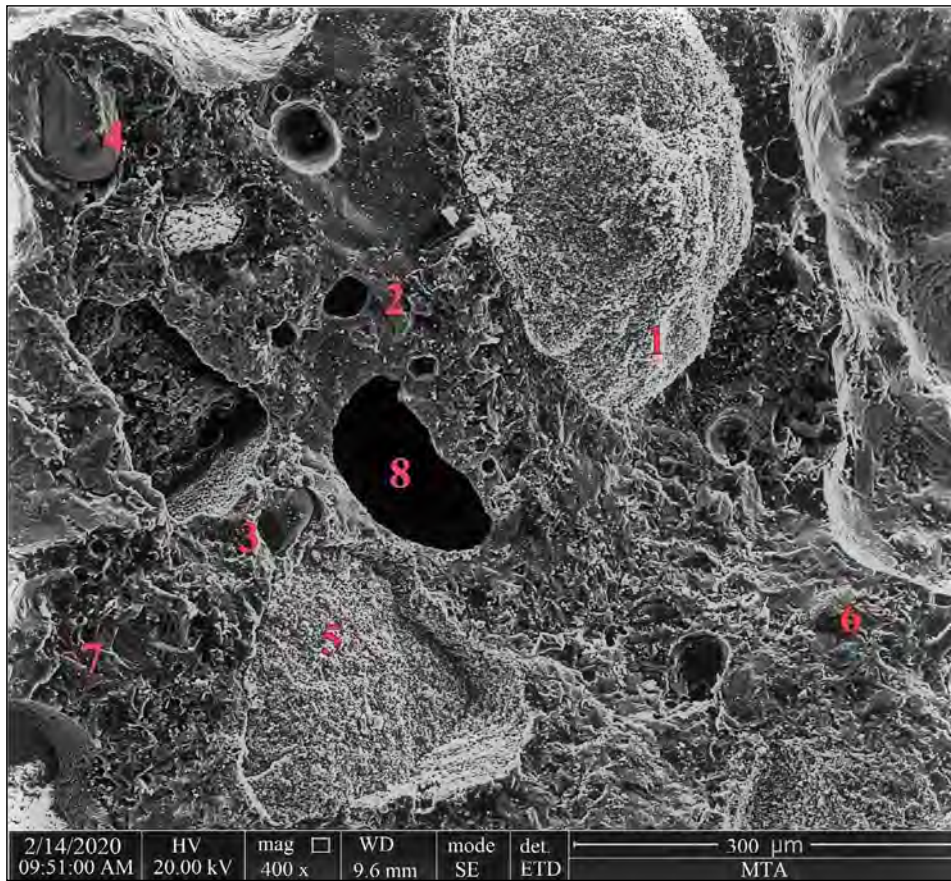


Figure 5- SEM image of the DYT product sample.

Table 6- EDS analysis of DYT product sample.

Point	O (%)	Mg (%)	Al (%)	Si (%)	Ca (%)	Na (%)	K (%)	Fe (%)	C (%)	Ti (%)
1	23.65	0.15	0.33	1.35	74.53	-	-	-	-	-
2	40.70	1.01	10.69	31.44	3.25	8.00	4.20	0.71	-	-
3	45.80	-	-	54.20	-	-	-	-	-	-
4	45.65	-	1.40	48.41	4.54	-	-	-	-	-
5	52.49	0.82	0.12	0.25	34.40	-	-	0.28	11.65	-
6	36.68	1.00	13.46	24.26	11.00	6.54	2.49	6.30	-	-
7	23.65	0.15	0.33	1.35	74.53	-	-	-	-	-

phases rich in alkali can be seen in points marked as 1, 3, 4, 5, 6 ve 8. On point marked as 10, porosity of approximately 164 nm can be seen, in many micro, meso and macro forms. According to the SEM image of the DYT-G product sample (Figure 10) and EDS analyses (Table 10), formation of inert calcium oxide (CaO) at point marked as 3, wollastonite ( $\text{CaSiO}_3$ ) and gehlenite [ $\text{Ca}_2\text{Al}(\text{AlSiO}_7)$ ] phases rich in alkali at

points 1 and 2 can be observed as the contact points. Strength decreases due to these contact points. The porosity distribution of the DYT-G product sample is determined to be quite homogeneous in the SEM imaging (Figure 11). Additionally, it is determined that the porosity ratio of the DYT-G product sample is much higher than the DYT product sample, as expected.

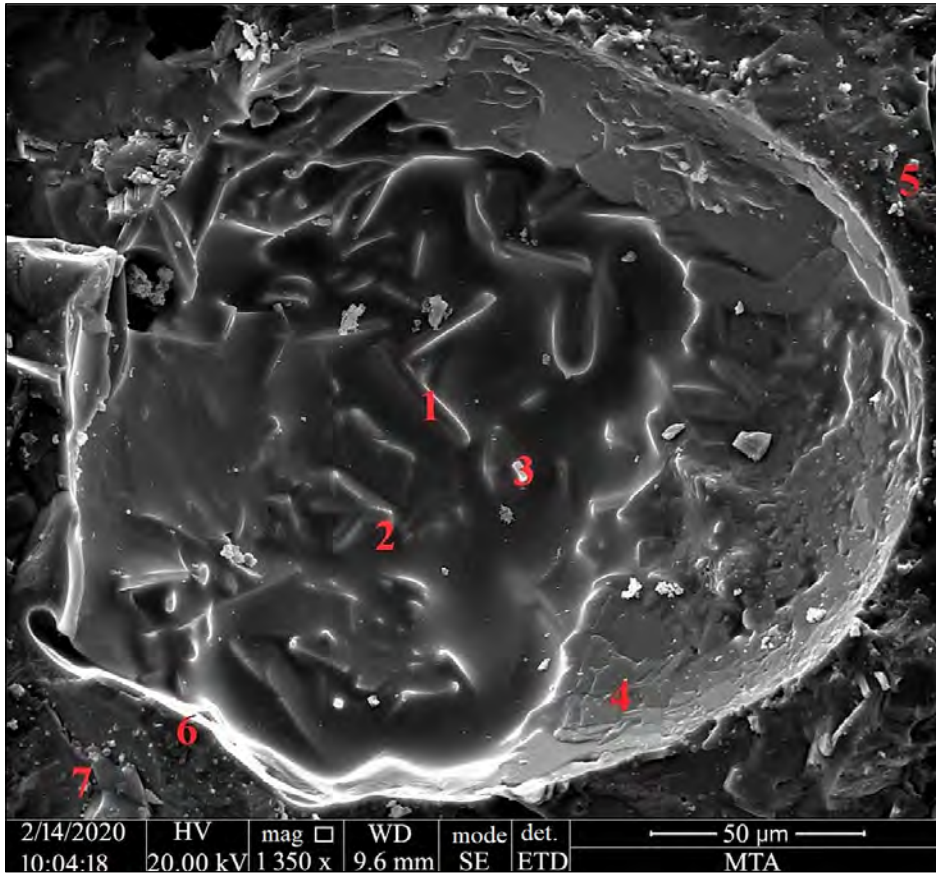


Figure 6- SEM image of the DYT product sample.

Table 7- EDS analysis of DYT product sample.

Point	O (%)	Mg (%)	Al (%)	Si (%)	Ca (%)	Na (%)	K (%)	Fe (%)	Ti (%)
1	35.57	0.94	5.72	22.26	26.08	3.58	1.86	3.42	0.58
2	37.44	0.81	11.51	27.47	8.04	7.05	3.73	3.65	0.31
3	41.55	1.09	6.88	23.03	19.04	4.67	1.60	2.09	0.05
4	41.84	-	1.02	22.38	31.60	2.07	0.25	0.85	-
5	34.22	1.49	14.12	27.99	8.03	7.62	3.85	2.69	-
6	22.12	0.96	11.50	28.69	20.41	3.81	3.69	8.02	0.82
7	29.65	2.18	11.48	27.08	14.54	6.86	3.00	4.89	0.32

#### 4. Discussion

In this study, only natural stone wastes were used and mixtures were prepared using 35% recrystallized limestone (metamorphic), 65% granite (magmatic) raw materials. According to the XRD results obtained by firing samples prepared at 1.140 - 1.150 - 1.160 °C, target phases of wollastonite and gehlenite were reached.

According to the results of the physical tests performed, comparing the samples of DYT and DYT-G with wood chip added, the flexural strength, modulus of elasticity and the apparent density of DYT-G sample was determined to be lower. True density of the samples was determined to be the same, yet their total-open porosity and water absorption values were higher. According to TS EN 14411 (Table 11) Ceramic Tile Standards, as the water absorption



Figure 7- SEM image of the DYT product sample.

Table 8- EDS analysis of DYT product sample.

Point	O (%)	Mg (%)	Al (%)	Si (%)	Ca (%)	Na (%)	K (%)	Fe (%)	Ti (%)
1	39.56	0.28	0.08	0.61	59.47	-	-	-	-
2	32.93	0.49	13.08	33.18	6.61	6.34	6.23	1.14	-

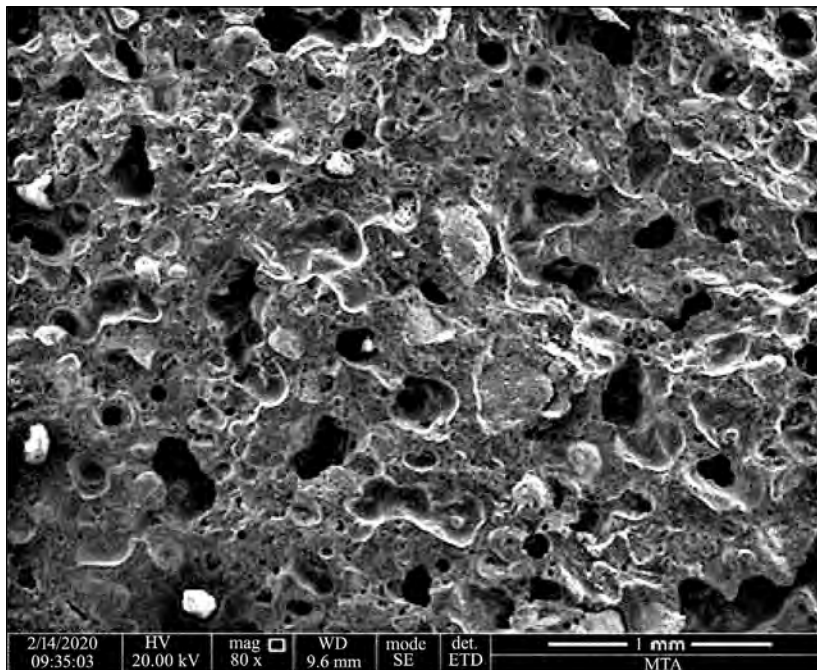


Figure 8- SEM image of the DYT product sample.

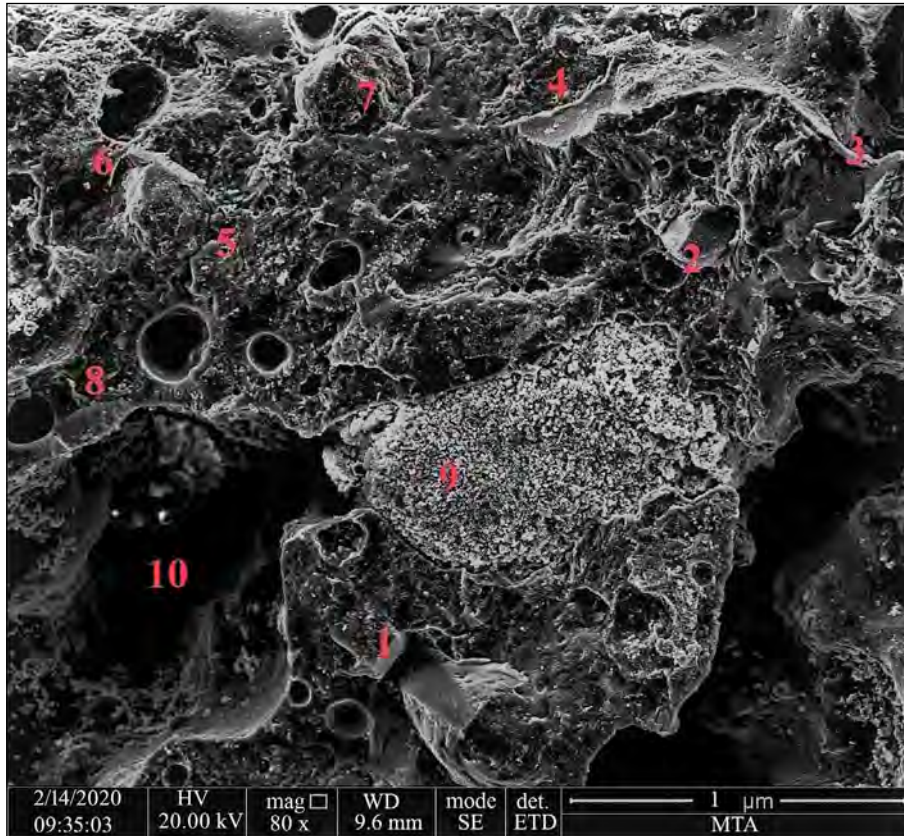


Figure 9– SEM image of the DYT-G product sample.

Table 9- EDS analysis of DYT-G product sample.

Point	O (%)	Mg (%)	Al (%)	Si (%)	Ca (%)	Na (%)	K (%)	Fe (%)	Ti (%)
1	43.05	0.68	0.27	0.77	55.23	-	-	-	-
2	33.29	1.15	11.81	22.27	21.09	6.16	1.57	2.67	-
3	46.48	-	1.57	49.26	2.68	-	-	-	-
4	36.34	1.33	12.10	25.07	7.70	7.65	3.62	5.65	0.53
5	39.49	2.29	10.72	19.71	17.68	7.15	1.02	1.94	-
6	42.10	0.71	1.17	24.36	29.06	1.55	0.42	0.63	-
7	36.38	0.72	12.64	24.75	13.91	7.12	3.06	1.42	-
8	55.44	-	1.03	42.66	0.87	-	-	-	-
9	31.05	-	14.61	26.21	12.40	6.33	4.52	4.88	-

rate DYT sample was determined to be 4.1%, in accordance with the standards, it is classified to be in the BIIa group. As the flexural strength value (22.64 MPa) is higher than the limit value of the standard (22 MPa) and single sample (20 MPa) value, it is above the values requested by the standards. According to TS EN 14411 (Table 11) Ceramic Tile Standards, as

the water absorption rate of the DYT-G sample is determined to be 6.8%, it is classified to be in the BIIIb group. Although the flexural strength value (16.5 MPa) is slightly lower than the limit values of the standard (18 MPa), as it is higher than the single sample (16 MPa) value, it is above the values determined by the standards.

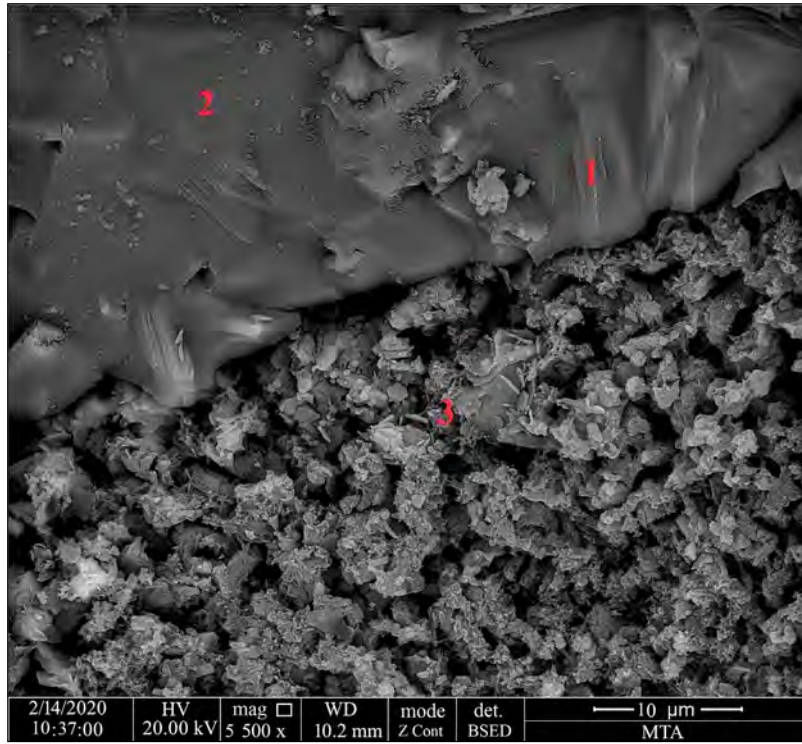


Figure 10- SEM image of DYT-G product sample.

Table 10- EDS-2 analyzes of DYT-G product sample.

Point	O (%)	Mg (%)	Al (%)	Si (%)	Ca (%)	Na (%)	K (%)	Fe (%)	Ti (%)
1	44.18	0.55	0.15	0.56	54.56	-	-	-	-
2	25.32	0.52	11.20	21.28	26.49	6.28	2.02	6.89	-
3	21.38	0.15	13.69	28.14	21.17	4.64	5.11	4.82	0.91

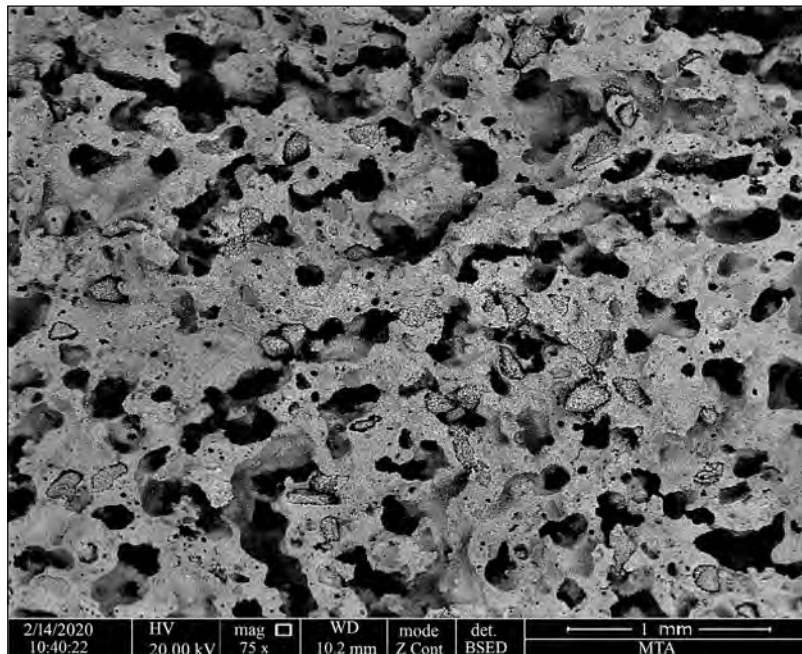


Figure 11- SEM image of the DYT-G product sample.

Table 11- Limit values of TS EN 14411 standard.

Standard Group	Water Absorption (%)	Flexural Strength (MPa)	
BIIa	$3 < w_a \leq 6$	Average at least	22
		One sample at least	20
BIIb	$6 < W_a \leq 10$	Average at least	18
		One sample at least	16

## 5. Results

The aim of this research is to obtain similar products to floor and wall tiles, completely from natural stone wastes. As a result, it is observed that anorthite, as the dominant phase in tiles, did not form through pyrolysis of natural stone wastes. A large volume of deformation is observed in the samples in anorthite formation temperature due to the melting effects of Na-feldspar and K-feldspar, contained in granite. Thus, for the temperatures above 1.160°C, no heat treatment was able to be performed. The glassy phase with high viscosity formed due to the melting effect prevented the diffusion of  $Al_2O_3$ . Therefore,  $Al_2O_3$  needed for the formation of anorthite did not react. Flexural strength values of the ceramics without the formation of anorthite were 22.64 MPa for DYT and 16.5 MPa for DYT-G. While it is undesirable for floor tiles, porosity is desired for wall tiles to adhere with mortar. Hence, porosity substance was made using wood chip additives which resulted in partial deformation in glassy phase samples of high volume formed post-firing of ceramic samples. In the light of all the aforementioned results, in contrast to producing building material solely using natural stone wastes, it is recommended only for the usage as an additive material in production of ceramic tiles. In case it is preferred to be used as a building material without the aim of tile production, it was observed that the polishing capacity of the fired samples is also good and that they can be ready for use by applying the polishing processes used in natural stones after firing. In conclusion, it is observed to be useful in disposal and re-introduction of large quantities of wastes resulting from natural stone production to the economy.

## References

ASTM C1259-15. 2015. Standard test method for dynamic Young's modulus, shear modulus, and Poisson's ratio for advanced ceramics by impulse

excitation of vibration, ASTM International, West Conshohocken, PA.

ASTM D5550-14. 2014. Standard test method for specific gravity of soil solids by gas pycnometer, ASTM International, West Conshohocken, PA.

Callebaut, K., Elsen, J., Van Balen, K., Viaene, W. 2001. Nineteenth century hydraulic restoration mortars in the Saint Michael's Church (Leuven, Belgium): natural hydraulic lime or cement?. *Cement and Concrete Research* 31(3), 397-403.

Ciullo, P. A. 1996. *Industrial Minerals and Their Uses*, Noyes Publications, New Jersey, 607.

DPT. 2001. Madencilik Özel İhtisas Komisyonu raporu Endüstriyel Hammaddeler Alt Komisyonu Toprak Sanayi Hammaddeleri çalışma grubu raporu. Devlet Planlama Teşkilatı, Ankara (unpublished).

Erol, G., Pekdemir, D. 2018. Investigation of thermal and mechanical behaviors of construction materials obtained from some natural stone waste. *Bulletin of the Mineral Research and Exploration* 157(157), 185-190.

Genç, Ş. C., Kayacı, K., Yıldırım, Y., Keskin, A., Çırpın, A. 2019. Biga yöresi zeolitik tüfitlerin karakterizasyonu ve duvar karosu bünyelerinde kullanım olanaklarının araştırılması. *Afyon Kocatepe Üniversitesi Fen ve Mühendislik Bilimleri Dergisi* 19, 310-320.

Gustavo, A. 2019. Evaluation of the effect of natural stone processing waste incorporation on red ceramics physical properties. *London Journal of Research of Engineering Research* 19(1).

Gündüz, L. 1995. Dekoratif taş endüstrisinde granit. *Endüstriyel Hammaddeler Sempozyumu*, İzmir.

Kara, A., Özer, F., Kayacı, K., Özer, P. 2006. Development of a multipurpose tile body: phase and microstructural development. *Journal of the European Ceramic Society* 26(16), 3769-3782.

Kogel, J. E., Trivedi, N. C., Barker, J. M., Krukowski, S. T. 2006. *Industrial Minerals and Rocks* (7th Edition). Society for Mining, Metallurgy, and Exploration Inc., Colorado, 1507.

Pastor, J. L., Tomás, R., Cano, M., Riquelme, A., Gutiérrez, E. 2019. Evaluation of the improvement effect of limestone powder waste in the stabilization of swelling clayey soil. *Sustainability* 11(3), 679.

Sletson, L. C., Reed, J. S. 1988. Microstructure development in a vitrified anorthite porcelain. *The American Ceramic Society Bulletin* 67(8), 1403-1408.

Sousa, S. J. G., Holanda, J. N. F. 2005. Development of red wall tiles by the dry process using Brazilian raw materials. *Ceramics International* 31(2), 215-222.

T. C. Ekonomi Bakanlığı. 2014. Doğal Taş Sektör Raporu. Ankara (published).

TS EN 12407. 2019. Natural stone test methods-petrographic examination. Turkish Standards Institute.

TS EN 14411. 2006. Ceramic tiles-definitions, classification, characteristics and marking. Turkish Standards Institute.

TS EN 15309. 2008. Characterization of waste and soil - determination of elemental composition by x-ray fluorescence. Turkish Standards Institute.

TS ISO 13320. 2009. Particle size analysis - laser diffraction methods. Turkish Standards Institute.



# Bulletin of the Mineral Research and Exploration

<http://bulletin.mta.gov.tr>



## Estimation of blast vibrations by numerical modelling and signal analysis

Güzin Gülsev UYAR AKSOY<sup>a\*</sup>, Cemalettin Okay AKSOY<sup>b</sup> and Hasan Eray YAMAN<sup>c</sup>

<sup>a</sup>Hacettepe University, Faculty of Engineering, Department of Mining Engineering, Ankara, Türkiye

<sup>b</sup>Dokuz Eylül University, Faculty of Engineering, Department of Mining Engineering, İzmir, Türkiye

<sup>c</sup>Dokuz Eylül University, Torbalı Vocational School, Department of Mining Engineering, İzmir, Türkiye

Research Article

Keywords:

Blasting, Vibration,  
Seismic Wave, Numerical  
Model, Mining.

### ABSTRACT

Seismic waves carry all the geological and geotechnical characteristics of the units they pass along the route they travel on. Therefore, seismic waves can be called the signature of the route it passes through. If the blasting point is considered as source, blast-induced seismic waves measured at a certain distance from the source can be revealed and this form can be integrated into the dynamic numerical model, the effects that will occur at any point of the model can be predicted. In this study, seismic waves induced from single-hole blast and a group blast consisting of holes with the same characteristics as a pilot blast hole were obtained using particle velocity data obtained from seismographs at certain distances and integrated into the numerical model. The data processing technique used is to estimate the theoretical group blasting data from the pilot data according to the linear superposition principle and compare with the real group blasting data to determine the nonlinear behavior effect on the blast source from the difference. When the results were examined, it was observed that the numerical model results and field measurements coincided. The results of this study will make a significant contribution to the science of rock engineering.

Received Date: 17.03.2021

Accepted Date: 24.01.2022

## 1. Introduction

Especially in large scale mining activities, controlling seismic waves caused by blasts is of great importance. These waves not only negatively impact the stability of the benches in open pits but could damage the structures in underground mining as well. In both fields of mining and in tunneling, group blasts are performed in frequent intervals, nearly up to 3 times per day. Such blasts tire the rock mass over time and cause to reduce its strength. These could lead to landslides and caved zones. Research aimed to create full scale modelling of blast vibrations were limited due to the inclusions of many parameters. Most important of these is the number of discontinuity sets, their slope and slope direction. Sing and Narendrula

(2004) have calculated the peak particle velocity (PPV) of single discontinuity set in small scale blast experiments. According to their research, the lowest PPV was determined to be 113.3 mm/s with 45° as the discontinuity slope orientation and the highest PPV was obtained at 90° which indicates the vibration transmission occurs parallel to the discontinuity set. Simangunsong and Wahyidi (2015), in addition to obtaining similar results in vibration determinations of discontinuities with different orientations and intervals, they reported a decrease in vibrations with increasing discontinuity. Zhou (2016) obtained similar results in the modeling study. Zou and Gong (2017) have reported an increase in PPV with increasing slope in bedded rocks, which correlate with the current

Citation Info: Aksoy Uyar, G. G., Aksoy, C. O., Yaman, H. E. 2022. Estimation of blast vibrations by numerical modelling and signal analysis. Bulletin of the Mineral Research and Exploration 169, 39-48. <https://doi.org/10.19111/bulletinofmre.1066943>

\*Corresponding author: Güzin Gülsev UYAR AKSOY, [gulsevaksy@hacettepe.edu.tr](mailto:gulsevaksy@hacettepe.edu.tr)

results in literature. The greatest contribution to the estimation of blast vibrations were made by Blair (2020). Blair (2020) first examines the seismic wave propagation with the dynamic finite elements methods and subsequently developed the wave model with the Monte Carlo Waveform Superposition method which takes the effects of rock anisotropy into consideration. Although in this study, no deformation module for the materials were not given; such module, the charge transport of the selected material and its ductility affect the wave propagation. To simulate the blast, load was applied to the middle of the model and with the results obtained from 4x4 m single and double discontinuity, Monte Carlo Waveform Model was created. Upon examining the normalized model, even in the 4x4 m model, an increased distance from the middle of the model results in a decrease in similarity of the wave propagation patterns between the AFEM and the polar approach results. Although blasts being performed in considerably larger areas poses a challenge in application of Blair's aforementioned study, it is a very valuable contribution to the literature.

Biggest disadvantages of such modelling studies is the challenges faced in representing the field of the full scale blast as the number, slope, direction and orientation of discontinuities are never constant. Furthermore, stress in nature is three dimensional. Blast induced seismic waves propagate in different directions in different rates. In other words, seismic waves caused by a blast, due to varying attributions different parts of a rock mass has, propagate and are absorbed in different directions and rates. Additional, it is known that rock environment shows non-linear characteristics in regions close to blasting (Uyar and Aksoy, 2019). Meaning, there are behavioral differences in measurements of the waveforms, taken from a closer and further point of distance to the blast. In closer distances, occurrences of plastic deformation (fracturing) are observed whereas in further distances these events do not occur and only elastic deformation are observed.

The main aim of this study is to estimate seismic vibrations induced by blasts from a selected distance using three dimensional dynamic finite elements method in order to overcome challenges in full field modelling. Critically, it is important to have a correct estimation of the energy in the source in order to give

correct input parameters to the numerical model. To achieve this, a nonlinear response signal is used, which is obtained by proportioning the seismic waves in the spectral media resulting from the pilot blast and the group blasting of holes, each of which is prepared as a pilot blast hole. Details of the method are given in the following chapter. Field studies to develop the method were performed in a gold mine. The model is solved by integrating the waveform at the zero point (source) obtained using the pilot and group blasts data into the 3D dynamic numerical model. Then, using the pilot blast signal, group blast was designed using the method we recommended that minimalizes the vibrations with the most suitable delay (Uyar and Ecevitoglu, 2008). The group blast done, the velocities of the particles that were caused by the blast induced seismic waves were calculated at desired distances and compared to the findings of the numerical model. The results are highly coherent. Therefore, by the results of this study, using the numerical modelling it is possible to estimate the propagation of group blast induced seismic waves and their vibrations related to the distance.

## **2. Calculation of Blast Induced Seismic Energy in the Source and Target Point**

There are two ways of input for the blast induced seismic energy to the 3D dynamic model;

- i) as peak particle velocity or acceleration rate,
- ii) as seismic waveform.

With the results obtained from the experiments of underground and ground blasts conducted for our TÜBİTAK project finalized in 2017 (Aksoy and Uyar, 2014), seismic energy of the source was produced for both cases. Studies conducted in those days aiming to realistically input the dynamic effects of the blasts performed in stability analyses of the mining slopes created using numerical models, through time, has transformed into estimating, if the energy in the blast source is known, the effects of desired distances to the blast using the 3D dynamic numerical modelling method. This means the demolishing the paradigm of using empirical equation related to the PPV - SD (peak particle velocity, scaled distance) which does not go any further than reinforcing the convention

of its usage since 1960's. Below are both methods of estimating seismic energy at the blast source and an exemplary comparative study performed with one.

2.1. Estimating Explosive Acceleration (or Particle Velocity) at the Source and Target Points

Steps of the process to be followed are given below (Aksoy and Uyar, 2014):

1. Sample explosive is placed upon the blast point.
2. A seismograph is placed on a relatively safe and close distance. The top of the seismograph could be covered (without the cover touching the device) to avoid damage inflicted by the flying debris.
3. Blast is performed and the acceleration of the closest particle to the blast zone  $A_0$  is calculated.
4. Using Equation 1, the scale coefficient  $k$  is calculated.
5. Particle-acceleration at the target point  $B_0$  is calculated.
6. Using Equation 2, absorption coefficient  $\alpha$  is calculated.
7. Using Equation 3, particle-acceleration of the actual explosive at the blast point,  $A$ , is calculated.
8. Using Equation 4, particle-acceleration of the actual explosive at the target point,  $B$ , is calculated.

Using Equation 5, limit mass of the actual explosive is calculated.

$$k = \frac{A_0^2}{m_0} \tag{1}$$

$$\alpha = \frac{\ln \frac{A_0}{B_0}}{x_0} \tag{2}$$

$$A = \sqrt{k m} \tag{3}$$

$$B = A e^{-\alpha x} \tag{4}$$

$$m_{limit} = \frac{(B_{limit} e^{\alpha x})^2}{k} \tag{5}$$

$$\alpha_e = \frac{\sum_{i=1}^n \alpha_i \Delta x_i}{\sum_{i=1}^n \Delta x_i} \tag{6}$$

In these equations the components are as follows;  $k$ : calculated scale coefficient ( $\text{g}^2 \text{kg}^{-1}$ ),  $A_0$ : particle acceleration measured at the blast point of the sample explosive ( $\text{g}$ ),  $m_0$ : mass of sample explosive ( $\text{kg}$ ),  $\alpha$ : calculated absorption coefficient ( $\text{m}^{-1}$ ),  $B_0$ : particle acceleration ( $\text{g}$ ) of the sample explosive measured at the target point,  $x_0$ : the distance between explosion point and sample explosion target point ( $\text{m}$ ),  $A$ : particle acceleration ( $\text{g}$ ), calculated at the blast point of the actual explosive,  $m$ : mass of actual explosive ( $\text{kg}$ ) (probably  $m > m_0$ ),  $B$ : calculated particle-acceleration ( $\text{g}$ ) of the original explosive at the target point,  $x$ : distance ( $\text{m}$ ) between the blast point and the actual blast target point (probably  $x > x_0$ ),  $\Delta x$ : distance between near and far stations ( $\text{m}$ ),  $\alpha_e$ : effective absorption coefficient ( $\text{m}^{-1}$ ),  $n, i$ : number of measurements,  $m_{limit}$ : the limit mass of the actual explosive ( $\text{kg}$ ),  $B_{limit}$ : selected limit particle acceleration of the actual explosive at the target point ( $\text{g}$ ).

Calculating  $\alpha_e$  in the Equation 6 at once, for far distances the energy produced by blasting induced for seismic source cannot reach is not possible. It is necessary to stay within the  $\Delta x$  spacing to record seismic signals. Due to the field conditions,  $\Delta x$ 's could have spacing in between, overlap or go beyond the line. In that case, partial measurements are made, using the Equation 2, mean values of  $\alpha$  are calculated.  $\alpha_e$  effective absorption coefficient is calculated from the distance-weighted average of the  $\alpha$  mean absorption coefficients with the help of Equation 3. In other words,  $\alpha_e$  is the distance weighted average of absorption coefficients of  $\Delta x$  spacing. In this study, the reason for calculating  $\alpha$  (absorption coefficient) is the separate calculations of  $\Delta x$  efficiencies.  $\alpha_e$  is used as the ultimate value. These equations were tried on a study, application parameters of which are given in Table 1. The study was conducted using the blast acceleration parameters obtained from a blast performed in İmbat underground coal mine in 2016. A total of 28.8 kg of explosives were used for the aforementioned blast.

Table 1- Acceleration - distance table of blasting at İmbat underground coal mine.

Geophone	Distance (m)	Acceleration (g)
13638	31.5	1.564
12270	42.0	0.835
12269	52.5	0.742
14465	63.0	0.517

$$k = \frac{A_0^2}{m_0} = \frac{1.564^2}{28.8} = 0.0849 \text{ g}^2 \text{ kg}^{-1}; \alpha = \frac{\ln \frac{A_0}{B_0}}{x_0} = \frac{\ln \frac{1.564}{0.835}}{10.5} = 0.0553 \text{ m}^{-1};$$

$$\alpha = \frac{\ln \frac{A_0}{B_0}}{x_0} = \frac{\ln \frac{1.564}{0.742}}{21} = 0.0355 \text{ m}^{-1}; \alpha = \frac{\ln \frac{A_0}{B_0}}{x_0} = \frac{\ln \frac{1.564}{0.517}}{31.5} = 0.0351 \text{ m}^{-1};$$

$$\alpha_e = \frac{0.0553 + 0.0355 + 0.0351}{3} = 0.042 \text{ m}^{-1};$$

$$A = \sqrt{k m} = \sqrt{0.0849 \times 100} = 2.9138 \text{ g};$$

$$B = A e^{-\alpha x} = 2.9138 e^{-0.042 \times 63} = 0.2067 \text{ g};$$

$$m_{limi} = \frac{(B_{limi} e^{\alpha x})^2}{k} = \frac{(0.1 e^{0.042 \times 63})^2}{0.0849} = 23.4 \text{ kg}$$

Using the blast data with the formula, the results obtained can be interpreted as the following: When the explosive amount  $m=100$  kg, an acceleration of 2.9138 g is caused at the blast point. From a  $x=63$  m distance to the blast point, an acceleration of  $B = 0.2067$  g is caused. To obtain a 0.1 g acceleration, the amount of explosives must be reduced to 23.4 kg.

### 2.2. Estimation of Seismic Waves at the Source and Target Points

To estimate the seismic waves at the source parametrically, it is necessary to gather seismic wave data using two seismographs, one placed at the closest distance (e.g. 10 m) with the possibility of saturation in the pilot blast field, the other placed in a distance to the first seismograph on the same line of path. Then, group blast routinely performed in the field for the excavation works, and measurements are repeated. Using the energy of the pilot blast, the energy that would be created by the amount of desired explosives is theoretically calculated, meaning the total seismic energy arising from the group blast is theoretically calculated. Energy caused by the actual group blast is also calculated and its ratio to the theoretical values are taken. This demonstrates how much of the energy is lesser than it is supposed to be, which represents the part measured with the seismograph, the elastic part. The remaining energy is the plastic energy used

in rock fracturing, the energy that is used as the source data in the numerical model. Therefore, for that field, the plastic energy for the desired amount of explosives and the elastic energy in the target point desired is calculated. In a change of environment, pilot blast must be repeated and the data must be reconstructed.

### 3. Field Study Using the Recommended Method

The field study is conducted on a gold mine. Prominent rocks in the field are volcanic, metamorphic and intrusive rocks. Volcanic rocks can be found in the blast zone. These data is gathered from the field.

#### 3.1. Calculation of Seismic Energy in the Source

Seismic waves caused by the group blast performed on 13.01.2021 at locations titled SV-GRUP and SV-PILOT in the Figure 1 were recorded by 4 seismographs. Seismograph locations were shown in Figure 1 with each device named after its serial number (13638, 12269, 12270 and 14465).

Design information related to the group and pilot blasts are given in Table 2, blast induced vibration, frequencies and duration data are given in Table 3.

To input a time-sequence of the blast for the numerical model, time sequences were created using the data obtained from group and pilot explosions and saves as an `ascii.txt` file. In the practical part of the study, two `ascii.txt` files were used, both of which were seismic records obtained from the gold mine, from a 10 m distance to the source. First file, is the seismic signal in which the explosive amount is 20 kg (pilot hole). Second file is the data sheet for the group blast consisting of 84 holes. Each hole in the group blast is filled with 20 kg of explosive material, same as the pilot hole.

The pilot blast is situated nearby the group blast. First, the seismic signal resulting from the pilot blast was gathered 84 times and the total signal created by the blast of the 84x20 kg explosive with a delay between the holes was produced, and then compared with the actual group blast signal. Using the difference between, theoretical signal that the desired amount of explosives would generate from the pilot blast signal. The Energy.EXE program that occurs when the program is run asks 3 questions:



Figure 1- 13.01.2021 Group and pilot blasting and seismograph locations.

Table 2- Blasting pattern of group and pilot blasts.

Blasting Area	Blasting Type	Rock Mass	Drill Hole Diameter	Drill Hole Geometry	Number of Drill Hole	Drill Hole Length	Q	Delay
sV	Pilot	Volcanic	102 mm	3 mx3.5 m	1	5-6 m	20 kg Anfo, 0.5 kg primer dynamite	42 ms delay between holes; 67 ms delay between rows
	Group		102 mm	3 mx3.5 m	84	5-6 m	20 kg Anfo, 0.5 kg primer dynamite	42 ms delay between holes; 67 ms delay between rows

Q: Explosive amount per delay

Table 3- Blasting induced measured vibration, frequency and duration data.

Seismograph	Distance m	Transversal mm/s	Vertical mm/s	Longitudinal mm/s	Vector Sum mm/s	Frequency Hz	Duration second
12270	Pilot:5	183.1	180.1	217.6	260.8	2	0.2
	Group:10	90.68	63.50	49.40	96.02	22	0.5
13638	Pilot:10	24.26	38.86	42.80	48.65	21	0.2
	Group:15	40.51	65.02	31.37	66.67	22	1
12269	Pilot:20	23.75	36.83	41.02	54.27	35	0.2
	Group:30	19.30	36.96	31.62	44.84	24	1.2
14465	Pilot:40	11.81	38.86	12.70	39.08	30	0.5
	Group:45	18.54	35.18	19.30	39.21	24	1.2
Micro	Pilot:261	0.875	1.324	1.915	2.317	7.5	1
	Group:303	2.514	3.003	3.153	3.927	12	1.5

1) Big-charge filename (no TXT):

For example: 12270-G

2) Small-charge filename (no TXT) :

For example: 12270-P

3) Multiplication factor :

For example: 84

Figure 2, shows this screen.

Energy.EXE creates 3 new files:

1) \_maxi file

For example: source\_maxi.dat

The PPV in the 12270-P.TXT file synchronized with the PPV (96.02 mm/s) in the 12270-G.dat file.

2) \_multi file

For example: source\_maxi.dat

The PPV in the 12270-P.TXT file multiplied by the Multiplication Factor (84).

3) Rapor.TXT file

Big-charge energy: Transversal Vertical Longitudinal

Small-charge energy: Transversal Vertical Longitudinal

Maximum energy: Transversal Vertical Longitudinal

Multiplier energy: Transversal Vertical Longitudinal

From the above energy levels, what percentage of the energy would be spent on elastic wave propagation and what percentage would be spent on plastic deformation can be calculated (Uyar et al., 2014).

Wave form represented by red in Figure 3 is the theoretical transversal component particle velocity data gather from the pilot blast being summed for 84 times (with delay between holes). Blue is the theoretical transversal component particle velocity data normalized to the highest PPV observed in the group blast. The amplitude expansion being only 4,7 times (96 mm/s x 84) / (1680 mm/s), rather than 84, indicates the prominence of a non-linear behavior in the environment. A majority of the energy is spent for the plastic deformation. Source energy calculated this way is integrable into the 3D dynamic numerical model as asci.txt file.

### 3.2. Three Dimensional (3D) Numerical Modelling Phase of the Study

Pilot blast, group blast and seismographic data, the locations of which were given in Figure 1 are defined in Plaxis 3D as seen in Figure 4.

The study area consists of volcanic rocks. Rock parameters used in the 3D model are given in Table 4.



Figure 2- Screenshot of running the Energy.EXE program.

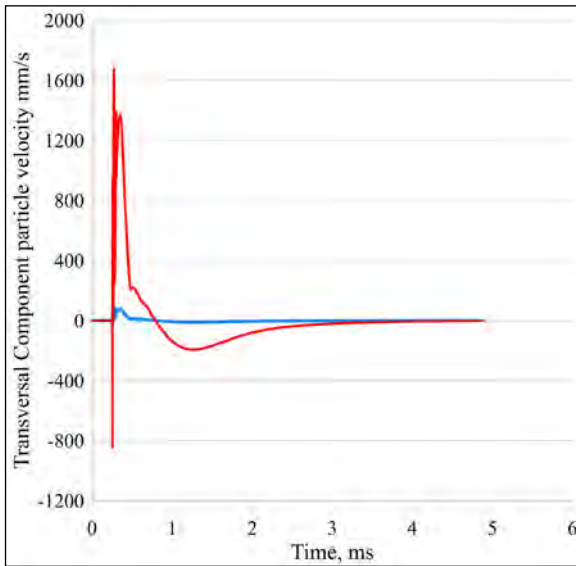


Figure 3- Seismic energy at zero point: The (red) seismic waveform obtained by linear summation of the pilot signal and calculated according to the non-linear behavior (blue). The accepted one is the blue one.

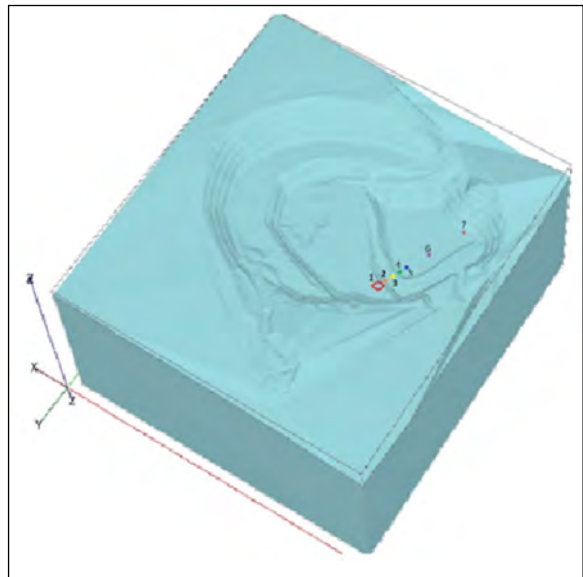


Figure 4- Group and pilot blast and seismograph locations defined in the model. No:1 blast location; No: 2, 3, 4, 5, 6, 7 seismograph locations.

Table 4- Rock parameters used in numerical modeling.

Rock Type	Deformation Modulus (MPa)	Cohesion (kPa)	Internal Friction Angle (°)	Unit Volume Weight (kN/m <sup>3</sup> )	Poisson Ratio
Volcanic Rock	553.2	667	24.34	24	0.25

Distances of seismographs to the blast area are given below;

- Seismograph 2. 10 meters; Seismograph 3. 15 meters
- Seismograph 4. 30 meters; Seismograph 5. 45 meters
- Seismograph 6. 100 meters; Seismograph 7. 200 meters

The seismic wave velocities obtained by integrating the blast source data at the blast point into the numerical model are compatible with the actual blast induced seismic waves in all components (lateral, vertical and longitudinal). This compatibility is shown in Figures 5, 6 and 7.

This was verified by testing with another source data, nevertheless, only the comparison from the gold mine was examined in this study as to save space. Upon the observation of the mentioned correlation, predictions of the numerical model at distances of 20,

30 and 40 m were given below, compared to the actual blast data (Figure 8, Figure 9 and Figure 10).

In the numerical model, total deformation amount that varies according to the distance is also shown. As seen in Figure 11, blast induced deformations are zero. The change in seismic quality factors of the blast induced seismic waves, calculated using the 10 and 40 m distanced seismograph data must also be noted (calculation of seismic quality factor using blast waves was published by us in 2020) (Aksoy and Aksoy, 2020). A variation of 0.43-0.85 in seismic quality factor is observed for the first 40 meters which subsequently increases to 3.12 past 40 meters. The capability to determine the zero deformation point by the numerical model, this point being coherent to the seismic quality factor calculations, the fact that the non-linear behavior displayed by the blast is within 40 m leads us to understand that the seismic waves past this distance display linear behavior.

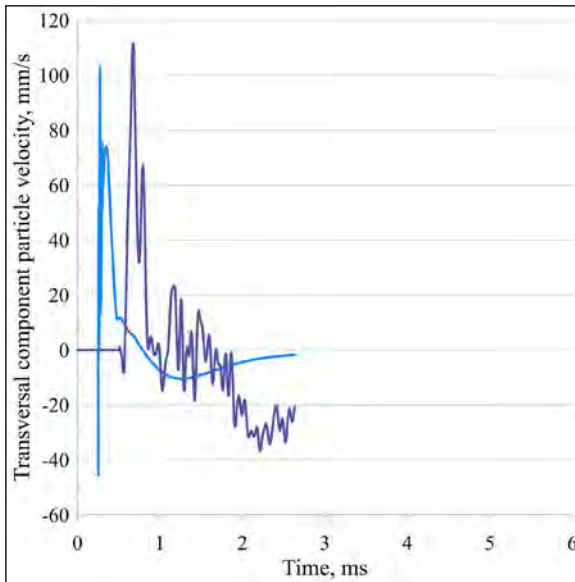


Figure 5- Comparison of the actual blast transversal component source signal and the predicted signal by numerical modeling (light blue real data vs dark blue numerical modeling data).

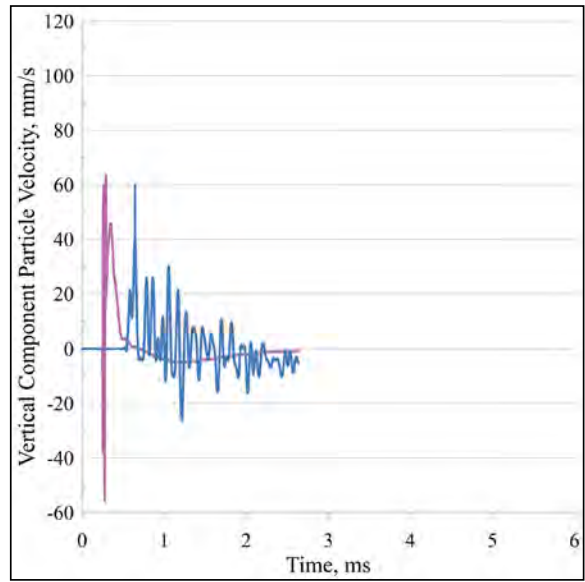


Figure 6- Comparison of the actual blast vertical component source signal and the predicted signal with numerical modeling (purple real data vs blue numerical modeling data).

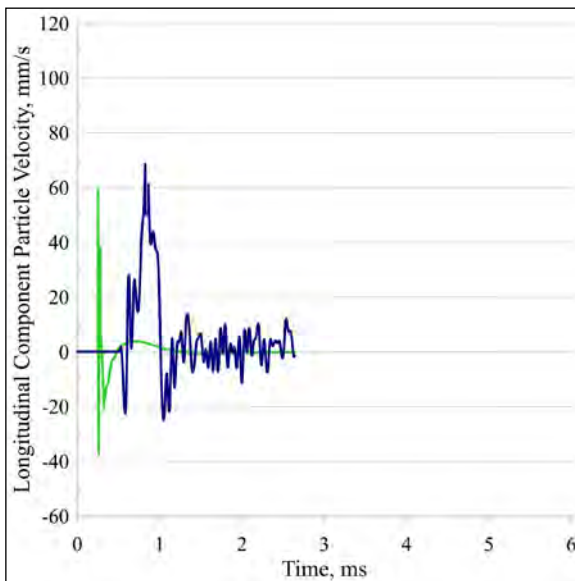


Figure 7- Comparison of actual blast longitudinal component source signal and predicted signal with numerical modeling (green true-blue numerical modeling)

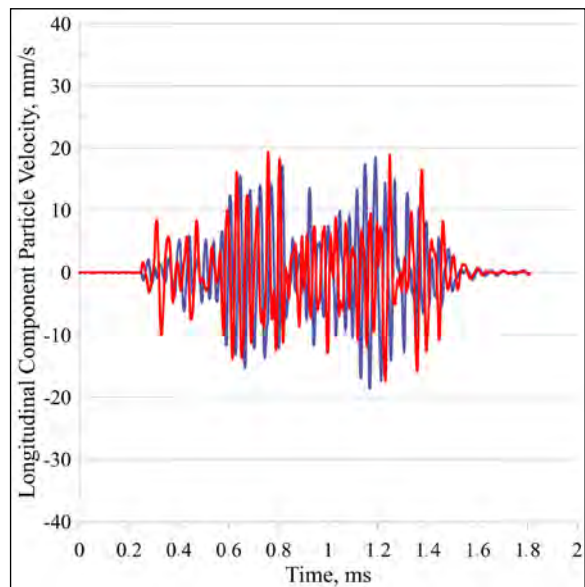


Figure 8- Numerical model predicted (red) and actual blast data (blue) (20 m from the blast).

#### 4. Results

In certain periods, one or more of the hypothesis explaining a specific event take their place in the world as Dominant Paradigm (Yazgan, 2016). Studies contrary to such paradigms or studies that examine

the views against such paradigms do not necessarily get many compliments. Studies conforming to such paradigms often reap the benefits of their adherence that acts as a reinforcement of conformity. These benefits could range from being published in an esteemed publication to receiving financial aid. Particle velocity-scaled distance hypothesis that was first put forward in the 1960s is one of such

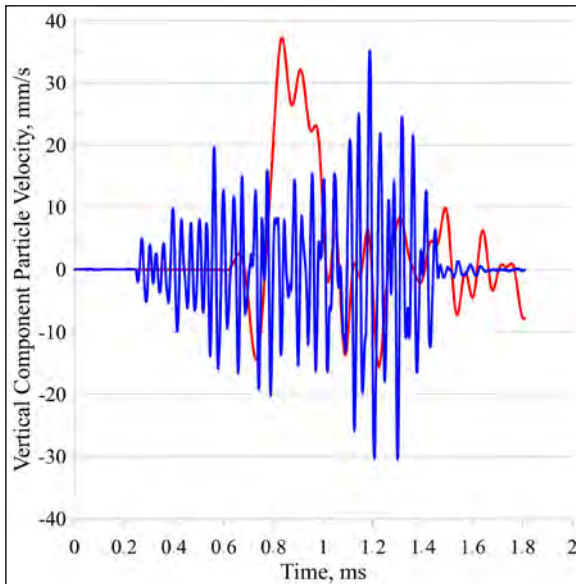


Figure 9- Numerical model predicted (red) and actual blast data (blue) (30 m from the blast).

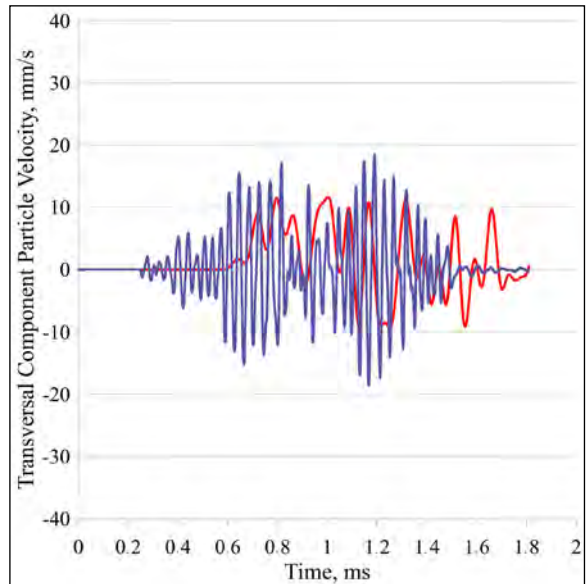


Figure 10- Numerical model predicted (red) and actual blast data (blue) (40 m from the blast).

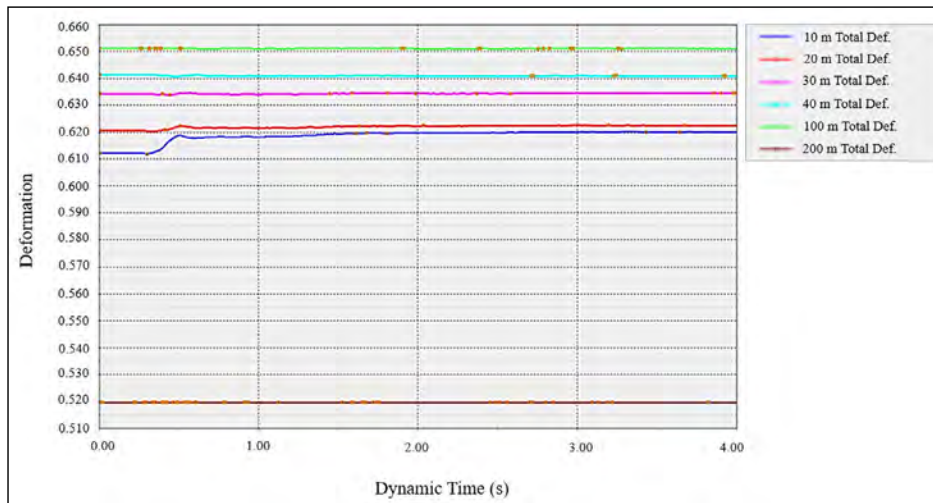


Figure 11- Total deformation amounts vary with distance in the numerical model. The x-axis shows the dynamic time (s), the y-axis shows the amount of deformation (m).

paradigms. Although it has been 60 years, since this paradigm becoming obsolete would cause chaos by disrupting the current order, empirical formulas based on explosive restraint are still used in minimizing and estimating blast-induced vibrations.

This study is very important in terms of;

- Obtaining the seismic signature caused by the seismic wave due to the pilot blast, depending on the geotechnical parameters of the study area, such as the

number of discontinuity sets, orientation, direction, groundwater and dealing with this signature,

- Obtaining the seismic energy formed in the middle of the blast, also known as the point zero, from the pilot and group blast signals.

- Feeding this signal into the 3D dynamic numerical model and estimating vibrations in the target point using defined blast parameters,

- Determining the plastic deformation area of the blast in which the blast does not display linear behavior using both numerical and seismic quality factor calculation,

- Being able to input actual blast effects into slope stability analyses in the planning stage, through estimation of dynamic blast effects.

- Allowing blast and geotechnical engineers to produce more sensitive designs.

and aims to demolish the current paradigm.

### Acknowledgements

We thank TÜMAD Lapseki Gold Mine, henceforth its executives, engineers who assisted us in the field and for the underground applications, İmbat Mining, its executives and engineers, all of whom opened their doors for us to allow the conduct of these experiments.

### References

Aksoy, G. G., Aksoy, C. O. 2020. Patlatma kaynaklı titreşimlerin tahmininde sismik kalite faktörü kullanımı. *MT Bilimsel*, 8(18), 133-145.

Aksoy, C. O., Uyar, G. G. 2014-2017. Deformasyona izin vermeyen tahkimat sisteminin geliştirilmesi. TÜBİTAK, Proje No: 114M566.

Blair, D. P. 2020. Approximate models of blast vibration in non-isotropic rock masses. *International Journal of Rock Mechanics and Mining Sciences* 128, 104-245.

Singh, S. P., Narendrula, R. 2004. Assessment and prediction of rock mass damage by blast vibrations. *International Proceeding 13th International Symposium Mine Planning and Equipment Selection, Wroclaw*, 317-322, 1-3.

Simangunsong, G. M., Wahyudi, S. 2015. Effect of bedding plane on prediction blast-induced ground vibration in open pit coal mines. *International Journal of Rock Mechanism and Mining Science* 79, 1-8.

Uyar, G. G., Aksoy, C. O. 2019. Comparative review and interpretation of the conventional and new methods in blast vibration analyses. *Geomechanics and Engineering* 18(5), 545-554.

Uyar, G. G., Aksoy, C. O., Ecevitöglü, B., Kaypak, B. 2014. Partition of elastic/plastic energy in mine blast. *International Conference of Mining, Material and Metallurgy, MMM'14*.

Uyar, G. G., Ecevitöglü, B. 2008. Waveform analysis in mitigation of blast-induced vibrations. *Journal of Applied Geophysics* 66, 25-30.

Yazgan, Y. 2016. Yaşantıların Psikolojisi ve Biyolojisi. *Remzi Kitabevi*, 285.

Zhou, J. M. 2016. The effect of joints on rock masses under blast-induced vibration. PhD Thesis, University of Hong Kong.

Zou, F., Gong, L. 2017. Experimental study on the propagation characteristics of blasting vibration in layered rock masses. *International Asia-Pacific Engineering Technology Conference, Kuala Lumpur*, 889-896, 25-26.



# Bulletin of the Mineral Research and Exploration

<http://bulletin.mta.gov.tr>



## Uludağ extensional metamorphic core complex: preliminary field observations

Gürol SEYİTOĞLU<sup>a\*</sup> and Korhan ESAT<sup>a</sup>

<sup>a</sup>Ankara University, Department of Geological Engineering, Tectonics Research Group, Gölbaşı, Ankara, Türkiye

Research Article

### Keywords:

Uludağ Core Complex,  
North Anatolian Fault,  
Eskişehir Fault, Southern  
Marmara.

### ABSTRACT

In the northern margin of Uludağ Massif in northwest Anatolia, the Bursa Detachment having top-to-the north, northeast normal sense of shear separates the lower plate high-grade metamorphic rocks of Series-A (Uludağ Group) from the upper plate low-grade metamorphic rocks of Series-B (Karakaya Complex). The deeper section of Uludağ Massif is represented by the Oligocene metagranites at the southern parts of the massif that is exposed due to the youngest high-angle Soğukpınar normal fault. The massif is a typical extensional metamorphic core complex similar to the counterparts in the west and northwest Anatolia such as the Menderes, Kazdağ, and Çataldağ core complexes due to close timing of exhumation and a similar sense of shearing.

Received Date: 20.04.2021

Accepted Date: 22.11.2021

## 1. Introduction

The Uludağ Massif and the mountain is an NW-SE trending prominent geological/geomorphological feature in the southern Marmara region in NW Türkiye (Figure 1). There is a 2442 meters elevation difference between the peak of Uludağ Mountain and the adjacent Bursa plain. The massif was mapped and the rock units were differentiated by Ketin (1947). The high-grade metamorphic rocks (Series-A) are composed of gneiss, amphibolite, and marbles. The low-grade metamorphic rocks (Series-B) comprise mica schist, phyllite, and marbles. Additionally, the Detritic Series after Ketin (1947) is composed of clastic units and limestones. As a result of further field observations, Ketin (1984) concluded that a thrust contact exists between Series-A and B, and then revised the geological map of the Uludağ Massif accordingly. Later, a nappe movement from SE to NW between Series-A and B rock units was proposed for the Uludağ massif (Şengör and Cin, 1988).

Imbach (1997) provided a more detailed description of the rock units in the Uludağ massif. The equivalent of Series-A is composed of muscovite and biotite gneiss, garnet-bearing quartzite, amphibolite, muscovite-bearing calcite-marble at the summit, and dolomite-marble with layers of kyanite-bearing tremolite schist at the northern margin of the Uludağ Massif. He also reported a post-Ordovician coral fossil. The low-grade rocks, equivalent to the Series-B, are composed of mica schist, phyllite, calcite-marble, epidote and glaucophane schist, serpentinite, and greenschist (Imbach, 1997).

Okay et al. (2008) dated the Series-A rocks from the Uludağ Group by single-zircon step-wise Pb-evaporation. Ages of gneisses in Series-A scatter strongly between Cambrian and Jurassic (Okay et al., 2008). Rocks of Series-B are differentiated as the Permian-Triassic lower and Triassic upper Karakaya Complex. Okay et al. (2008) also dated syn- and post-kinematic granites: The syn-kinematic granite called

Citation Info: Seyitoğlu, G., Esat, K. 2022. Uludağ extensional metamorphic core complex: preliminary field observations. Bulletin of the Mineral Research and Exploration 169, 49-61. <https://doi.org/10.19111/bulletinofmre.1029034>

\*Corresponding author: Gürol SEYİTOĞLU, [seyitoglu@ankara.edu.tr](mailto:seyitoglu@ankara.edu.tr)



Similar to the different views on the exhumation mechanisms of the Uludağ Massif, there are also diverse views about the strike-slip shear zones in the region. Although there is no agreement about the number of branches of the North Anatolian Fault Zone (NAFZ) in the southern Marmara region (see Seyitoğlu et al., 2016 for an evaluation), most of the classical studies accept that the Bursa area is under the influence of the NAFZ (Şengör, 1979; Şengör et al., 1985; Barka and Kadinsky Cade, 1988; Barka, 1992). However, recent studies suggest that the NE-SW trending fault zones in the Biga peninsula create an arc shape toward the east by turning to the NW-SE direction, as seen particularly by the Bursa, İnegöl, and Oylat normal faults, implying they belong to the Eskişehir Fault Zone (EFZ) (Emre et al., 2013, 2018).

In this paper, our preliminary field observations from north and south of the Uludağ massif support the interpretation that the massif is an extensional core complex, and we discuss its relationship with the NAFZ and EFZ.

## 2. Field Observations

The Bursa Fault (BF) (Emre et al., 2011a) is mapped as a single structure and is responsible for the topographical difference between Uludağ Mountain and Bursa plain. However, our field observations indicate that the BF in the north of Uludağ Massif can be divided into two sections.

The western sector of BF at the west of Yıldırım Fault (YDF) in the south of Bursa city centre is a high-angle normal fault that cuts low-angle schistosity/shear surfaces of the dolomite-marbles determined by Imbach (1997). These high-angle normal faults are developed as a normal faulted margin of the pull-apart basin under the influence of NAFZ. The NE-SW trending NAFZ, the youngest structure in the region, creates Yenişehir, eastern Bursa, and western Bursa pull-apart basins (Yılmaz and Koral, 2007; Selim and Tüysüz, 2013; Seyitoğlu et al., 2020). The western part of BF is reactivated as part of the Bursa Detachment (see below) because its surface relicts are still recognizable (Figure 1).

In the eastern sector of the BF at the east of Saitabad, the low-angle (25-30°) normal fault surfaces

are exposed where the uppermost lithology of Series-A (Ketin, 1947), the dolomite-marbles determined by Imbach (1997) create triangular facets (Figures 1, 2a and 2b).

The slicken-lines plunge down-dip and indicate a top-to-the north/northeast normal sense of shear (Figures 2c, 2d, and 3; Table 1) suggesting the eastern sector of BF is a detachment fault separating from the high-grade metamorphic rocks of Series-A (Uludağ Group) in the footwall to the low-grade metamorphic rocks of Series-B (Karakaya Complex) in the hanging wall (see also Yıldırım et al., 2005). The large outcrops of the Bursa Detachment Fault can be seen in the south of Alaçam village and Saitabad (Figures 2 and 4). This is a common feature seen in the Menderes (Bozkurt and Park, 1994; Ring et al., 2003; Seyitoğlu et al., 2004), Çataldağ (Kamacı and Altunkaynak, 2019), and Kazdağ (Yalıtırak, 2003; Kurt et al., 2010) core complexes in western Türkiye. Therefore, Bursa Detachment Fault can be regarded as the first sign that the Uludağ Massif is a typical extensional metamorphic core complex.

The deeper section of the Uludağ Massif (hereafter the Uludağ Metamorphic Core Complex - UMCC) is represented by metagranites exposed in the southern part. The final exposure of this deeper section is due to the younger south-dipping high-angle Soğukpınar Fault (SF) which is a normal fault with negligible left-lateral component (Figures 1 and 5; Table 1).

The metagranites showing the youngest AFT data ( $9.2 \pm 1.8$  Ma: Okay et al., 2008) are located on the uplifted footwall of the SF. The distinct morphological feature of the SF and the absence of strike-slip displacements on the valleys perpendicular to the fault support our field observations that the SF has a normal character. Moreover, the counterparts of SF in the west, separated by the left-lateral transfer faults, provide additional structural data that the SF is a major normal fault structure controlling step-like topography (Figure 1b). In the footwall of the SF, well-developed synthetic faults and fractures may create a misperception of near-vertical contact between the calcite-marbles and underlying metagranites (Figure 6).

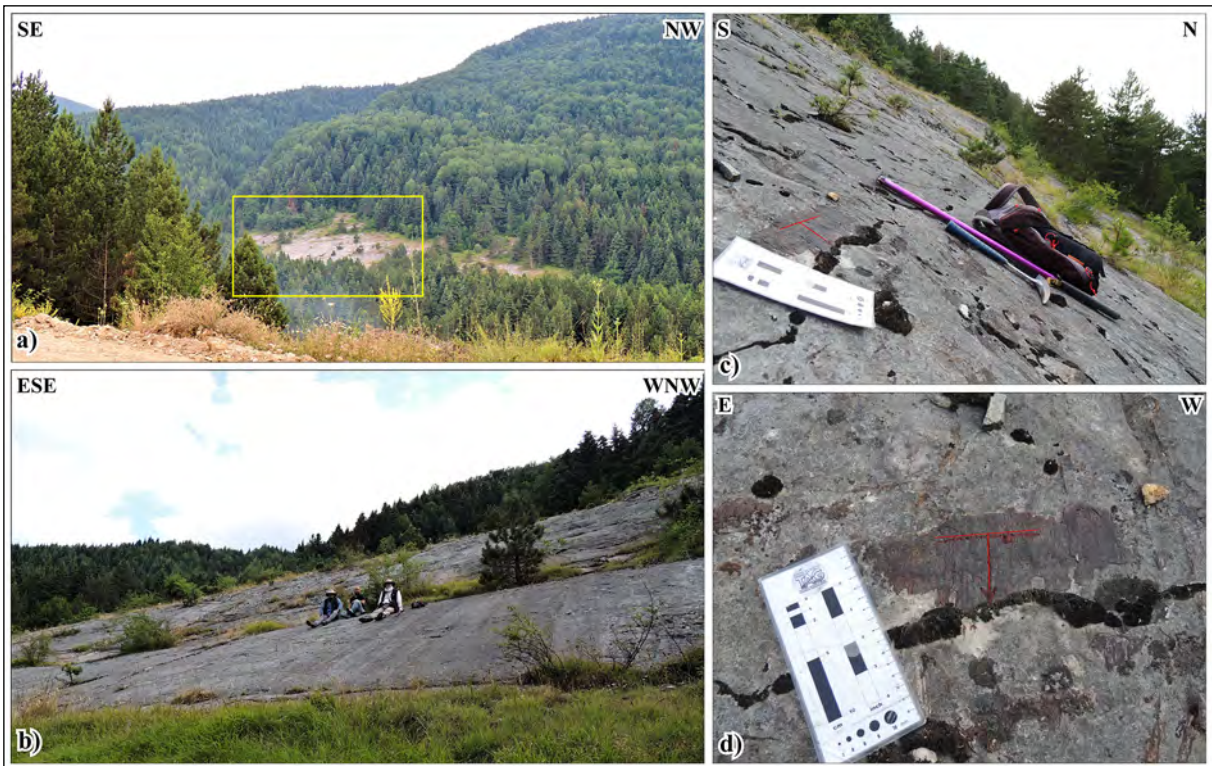


Figure 2- The Bursa detachment fault; a) its main outcrop at the south of Alaçam village, b) low angle nature of the Bursa detachment, c) the slickensides on the Bursa detachment and d) the slickensides indicating pure normal fault character. For location see Figure 1b.

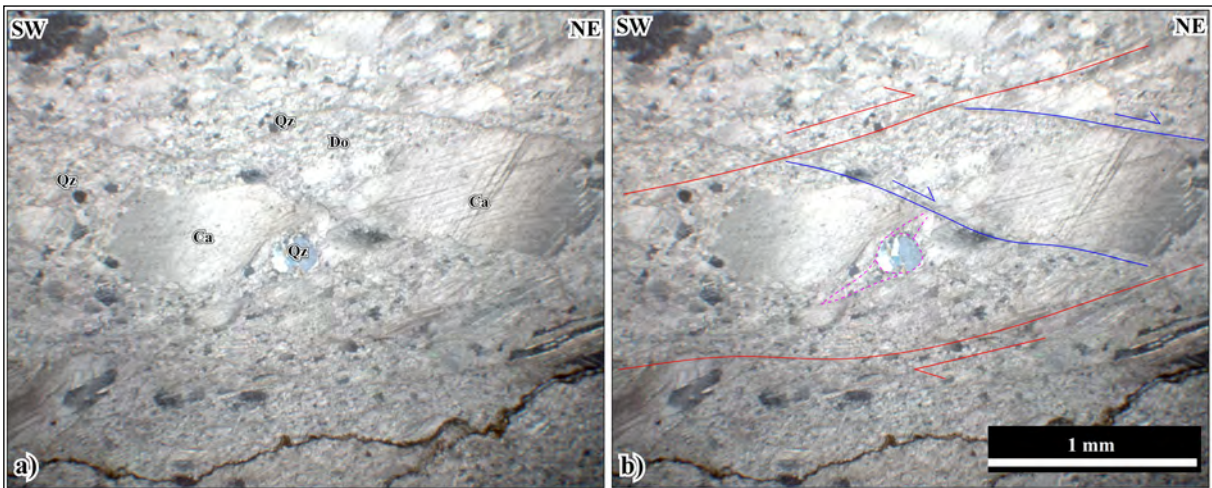


Figure 3- Oriented thin section photo from immediately under the Bursa detachment surface viewed in crossed polars; a) uninterpreted thin section (Qz: quartz, Ca: calcite, Do: dolomite), b) the overall shear zone is marked with red lines. In detail, the shear band type fragmented porphyroblast (i.e., displaced calcite porphyroblast -blue lines- interpreted after Passchier and Trouw, 2005; Figure 5.44), overprint the sigma type asymmetric porphyroblast (fuchsia colour dotted lines) probably inherited from the earlier ductile stage.

In fact, the schistosity of the calcite-marble is tilted to the NE with a 30° dip angle (Figures 6 and 7). This slight NE dipping is observable throughout the southern UMCC and the contact with the underlying metagranite is nearly parallel to this schistosity

(Figures 5a, 6, and 7). An oriented sample from the metagranite indicates a top-to-the northeast sense of shear. This might represent a granite intrusion into the ductile shear zone (Figure 8). The cross-section of the UMCC indicates that the deeper part of the



Figure 4- a) The Bursa detachment fault in the SE of Alaçam village. Insets show the oblique normal fault character of the detachment, b) the Bursa detachment in Saitabad village at Şelale location. Note that the angle of the detachment surface is getting lower towards the up. For locations, see Figure 1b. Inset indicates a close-up view of the pure normal sense of slip.

complex shows ductile shearing (metagranites) while the uppermost part shows brittle shearing along with the Bursa Detachment (Figure 1c). This overall structure strongly suggests that the Uludağ massif is an extensional metamorphic core complex (Figure 1c).

In the east of the UMCC, the İnegöl Neogene half-graben (Kaymakçı, 1991) contains several active faults. According to Emre et al. (2011a, b), the İnegöl

and Oylat normal faults combined with the SF were considered as the elements of the EFZ by Okay et al. (2008) and Emre et al. (2018).

Our field observations, however, demonstrate that the NW-SE trending active fault segments in the İnegöl basin are nearly pure right-lateral strike-slip faults evidenced by kinematic data from the fault surfaces (Table 1).

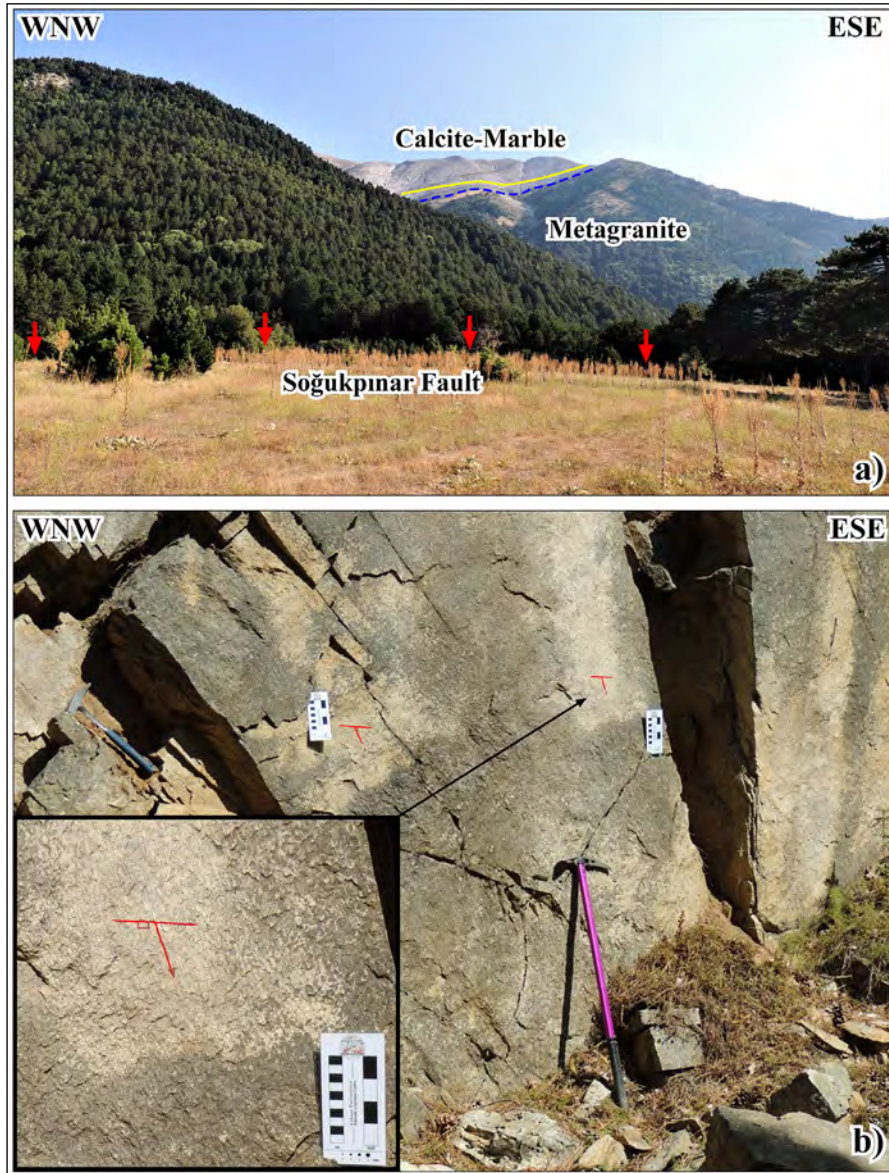


Figure 5- a) Morphological expression of the Soğukpınar normal fault. Red arrows indicate its location. The background of the photo shows the contact of calcite-marble and metagranite which is nearly parallel to the schistosity of calcite-marble dipping to NE. See Figure 1b for location, b) structural data shows normal fault character of the SF. Inset is the close-up view of the fault surface developed on metagranite.

For example, the Oylat-1 segment of the EFZ has a topographically distinct fault surface displaying right-lateral strike-slip kinematics data the entrance of the Oylat cave (Figures 1 and 9a).

The Doğanyurdu segment cuts the Neogene sedimentary units indicating that the EFZ post-dates the deposits of the Neogene İnegöl basin (Figures 1 and 9b). The Cerrah segments are located west of

İnegöl and exhibit well-developed fault surfaces displaying nearly pure strike-slip kinematics (Figures 1 and 9c). The Babasultan segment passes close to the Bursa Detachment and provides a significant fault surface NE of Sayfiye indicating its right-lateral strike-slip character (Figures 1 and 9d). The overall position of the EFZ is composed of the NW-SE trending en-echelon right-lateral strike-slip segments that reach the north of the UMCC. In other words, the

Table 1- Fault kinematic data obtained from the field. Kinematic axes have been determined by using FaultKin software (Marrett and Allmendinger, 1990; Allmendinger et al., 2012). N: Normal, RL: Right lateral, LL: Left lateral. See Figure 1b for graphical representations.

#	Latitude (°N)	Longitude (°E)	Field data					Kinematic (strain) axes					
			Fault plane		Striae		Slip	S1		S2		S3	
			Strike (°)	Dip (°)	Trend (°)	Plunge (°)		Trend (°)	Pl. (°)	Trend (°)	Pl. (°)	Trend (°)	Pl. (°)
I	40.11214	29.28819	290	30	20	30	N	195	15	285	3	24	75
			275	32	12	32	N						
			279	29	16	29	N						
			280	30	18	30	N						
II	40.11334	29.30464	240	26	13	20	N	180	19	277	19	49	63
			250	30	19	24	N						
			238	37	14	27	N						
III	40.14619	29.23621	305	53	7	49	N	22	6	114	14	269	74
IV	40.14817	29.22592	295	30	25	30	N	205	15	295	0	25	75
V	40.06108	29.17085	104	89	106	67	N	174	36	290	31	49	39
			115	88	118	60	N						
			110	88	113	53	N						
			115	88	118	54	N						
VI	39.94315	29.59160	290	85	109	13	RL	64	17	274	71	157	9
			105	80	110	27	RL						
			105	72	116	30	RL						
			95	71	108	33	RL						
			290	81	109	8	RL						
			115	79	117	8	RL						
VII	40.06526	29.44241	300	78	118	10	RL	198	1	107	44	290	46
			300	65	300	0	RL						
			334	81	153	8	RL						
VIII	40.11444	29.34139	305	77	120	19	RL	77	4	337	66	169	23
IX	39.98197	29.45140	330	42	345	13	RL	275	33	83	57	181	5
			283	87	287	50	RL						
			315	57	322	10	RL						
			320	67	326	14	RL						
X	40.17048	29.11797	278	35	350	34	N	198	9	107	3	2	80
			305	35	41	35	N						
XI	40.16811	29.09215	277	75	87	34	N	29	3	297	39	123	51
			250	50	37	33	N						
XII	40.17882	29.04836	73	78	248	22	N	13	9	245	76	104	11
			57	85	59	17	N						
			225	88	43	45	N						

Table 1- Continued.

XIII	40.18644	29.04205	310	55	82	47	N	233	9	324	5	84	79
			306	20	39	20	N						
XIV	40.11200	29.07727	139	82	143	25	LL	16	1	284	70	107	20
			143	82	146	20	LL						
			160	65	331	18	LL						
			145	63	311	25	LL						
			160	58	332	13	LL						
			148	80	196	77	LL						
			160	75	168	29	LL						
			155	80	159	20	LL						
XV	40.10759	29.07618	120	51	210	51	N	210	6	300	0	30	84
XVI	40.13230	29.02794	105	55	165	51	N	171	19	268	21	43	62
			95	80	112	59	N						
XVII	40.13995	29.02483	100	75	236	69	N	219	15	124	18	346	66
			98	80	252	68	N						
			115	63	236	59	N						
			110	68	244	61	N						
			135	45	260	39	N						
			165	55	262	55	N						
			60	60	169	59	N						
			115	53	254	41	N						
XVIII	40.10912	29.01376	150	61	324	10	LL	9	28	216	59	105	12
			145	57	321	7	LL						
			155	66	328	15	LL						
XIX	40.10754	29.00333	50	55	80	35	N	151	10	242	6	2	79
			83	52	176	52	N						
			70	65	162	65	N						
			60	45	150	45	N						
			65	53	160	53	N						

EFZ around İnegöl has a strike-slip character and there is no genetic relationship with the SF in the south of UMCC.

These observations also confirm the strike-slip kinematics of the EFZ at its northwestern edge as also demonstrated previously in the Eskişehir settlement and its southeastern edge (Seyitoğlu et al., 2015; Esat et al., 2016).

### 3. Discussion

Although further studies are needed to demonstrate ductile to brittle transition along with the Bursa Detachment in detail, available field observations presented above allow determination of the Uludağ Massif as an extensional metamorphic core complex.

In the north of UMMC, the spectacular outcrops of the Bursa detachment fault indicate top-to-the

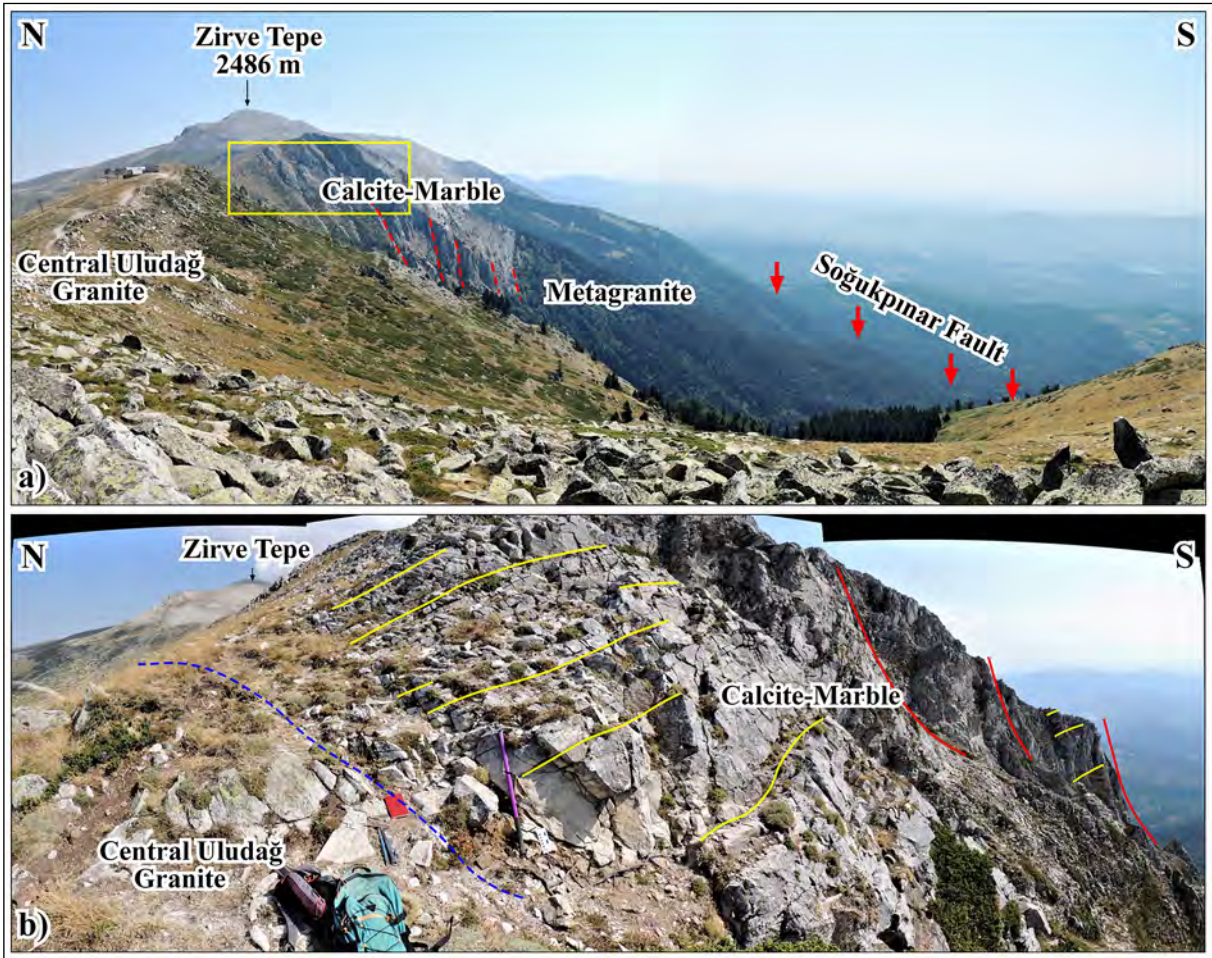


Figure 6- a) Southern margin of Uludağ and the position of Soğukpınar normal fault (red arrows). Broken red lines indicate synthetic fractures of the SF which creates a misperception of the vertical contact between calcite-marble and metagranite. Yellow rectangle shows the location of Figure 6b. For information about the location, see Figure 1b, b) a panoramic close-up view of calcite-marble indicating its schistosity slightly dipping to NE (yellow lines) and synthetic fractures of the Soğukpınar normal fault (red lines) in the footwall. The blue dashed line is the contact between Central Uludağ Granite and calcite-marble. For the location, see Figure 6a.

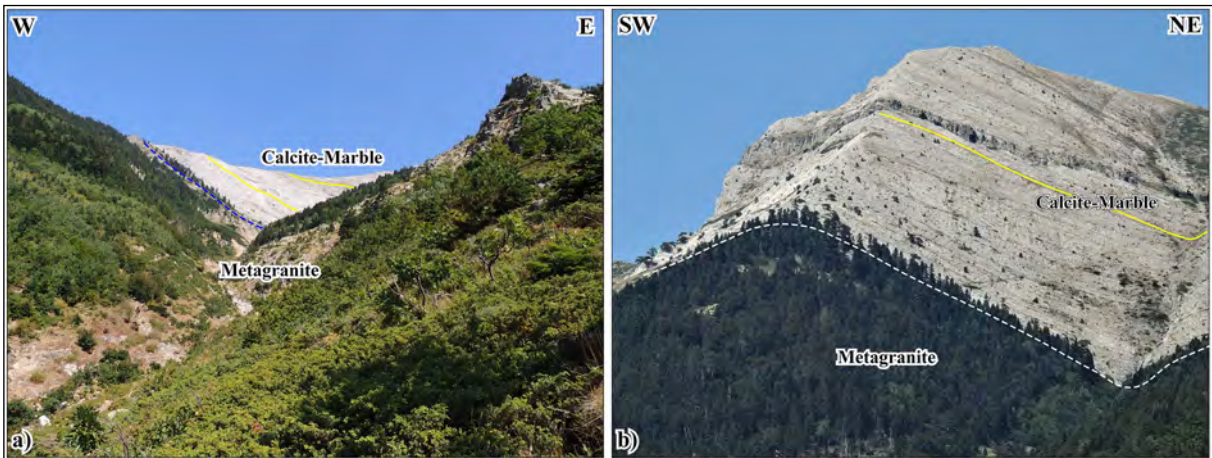


Figure 7- In the south of Uludağ, NE dipping schistosity of the calcite-marble (yellow lines) and the contact with the metagranite which is nearly parallel to the schistosity (blue and white dashed lines); a) a view from the Aras Dere valley to Zirve Tepe and b) a view from Kalemlik to Kuşaklıkaya Tepe. For locations, see Figure 1b.

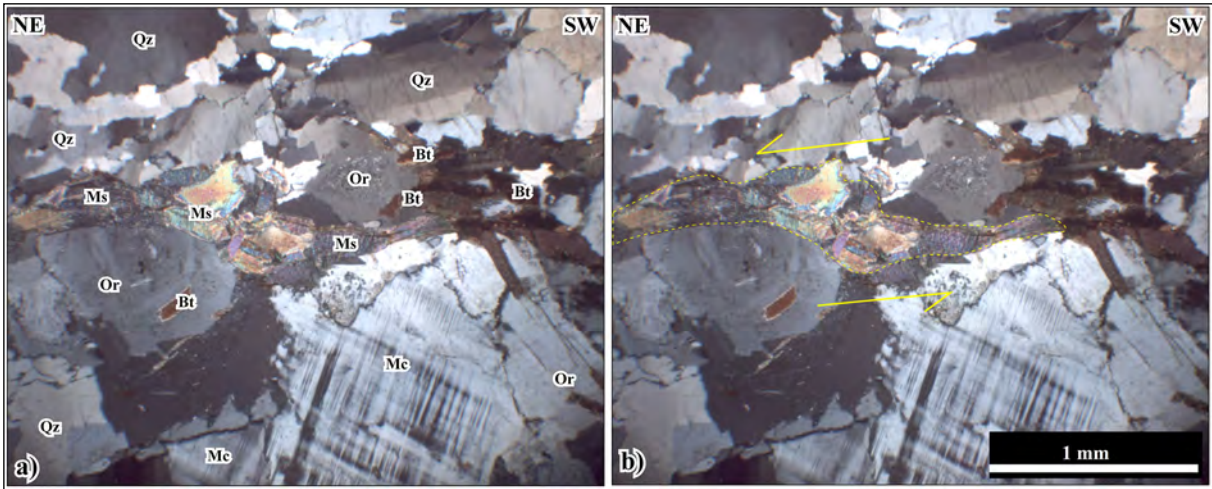


Figure 8- Oriented thin section photos from the meta-granite viewed on crossed polars; a) main minerals are quartz (Qz), orthoclase (Or), muscovite (Ms), biotite (Bi), and microcline (Mc) and b) muscovites indicate top-to-the NE sense of shear. For the location of the sample, see Figure 1b.

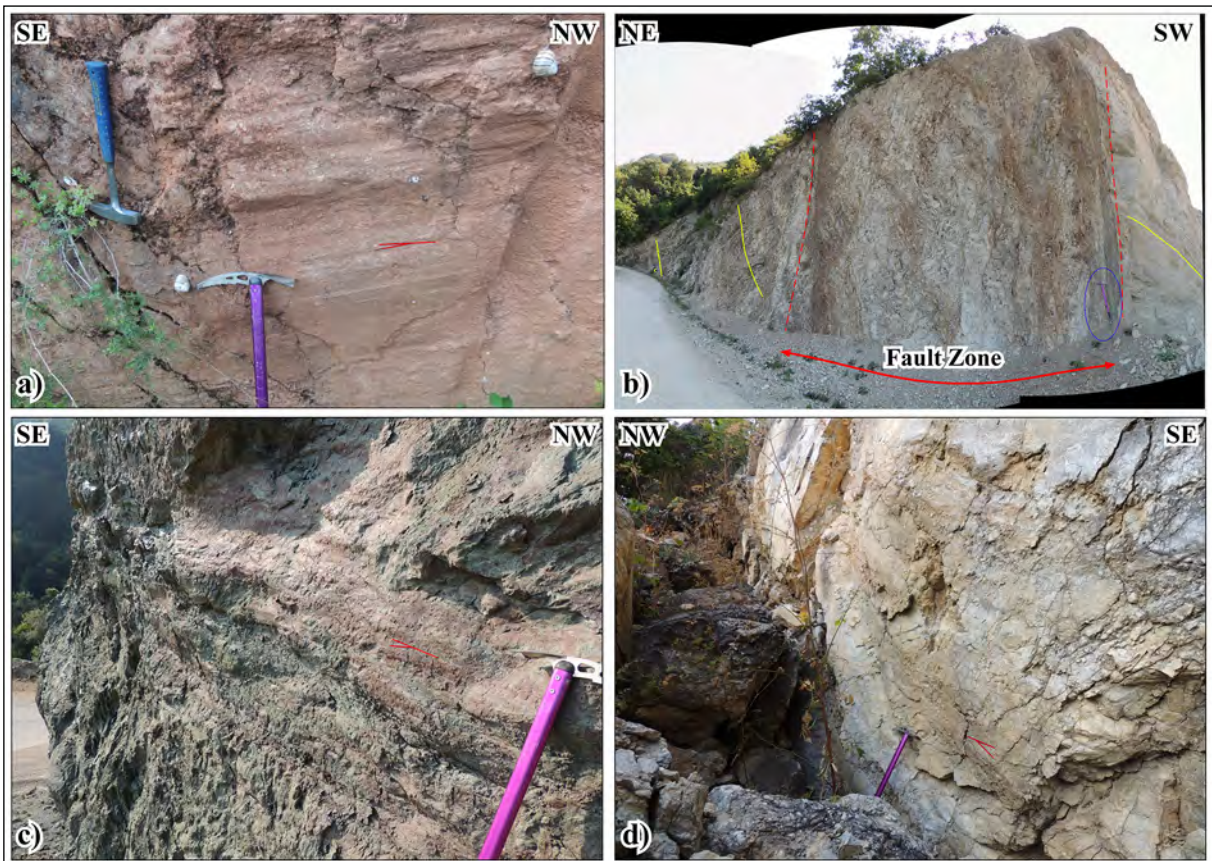


Figure 9- a) The close-up view of the fault surface having slicken-lines in the Oylat-1 segment of Eskişehir Fault Zone near the entrance of Oylat cave, b) panoramic view of the Doğanıyurdu segment of Eskişehir Fault Zone. The Doğanıyurdu segment is an NW- SE trending right-lateral strike-slip fault that clearly cuts the Neogene İnegöl basin. Yellow lines are the bedding of sedimentary unit, c) nearly pure right-lateral strike-slip data obtained from the fault surface in the NW-SE trending Cerrah-1 segment of Eskişehir Fault Zone at the SW of Cerrah village and d) close-up view of the fault surface indicating right-lateral strike-slip movement in the northwestern edge of the Eskişehir Fault Zone, the Babasultan segment at the NE of Sayfiye village. See Figure 1b for locations.

north/northeast normal sense of shear which were previously evaluated as thrust (Ketin, 1984; Şengör and Cin, 1988). Except for one sample, the AFT ages of Okay et al. (2008) are getting younger towards the detachment surface that supports the extensional nature of the Bursa Detachment Fault.

In the south of UMMC, the SF and its western counterparts are normal faults and there is no fault attributable to the right-lateral strike-slip EFZ. Moreover, the near-vertical contact between calcite-marbles and underlying metagranite is a misperception (Okay et al., 2008; Topuz and Okay, 2017) due to the well-developed synthetic faults and fractures in the footwall of a normal fault SF, thus the claim of an Oligocene ductile shear zone exhumation related to the right-lateral EFZ (Okay et al., 2008) is doubtful. Instead, a granitic intrusion might have intruded the extensional ductile shear zone creating the metagranite of the UMCC while the upper crust was under brittle conditions when the Bursa Detachment was active between the rocks of Series-A and Series-B. Available isotopic dating provided by Okay et al. (2008) indicates that extensional ductile shear must be around 38-27 Ma and this should be ceased around 27 Ma as demonstrated by the age of post-kinematic Central Uludağ Granite. It is not clear, however, whether the movement on the Bursa Detachment Fault is continuing after 27 Ma. The published AFT ages (Okay et al., 2008) indicate that Uludağ continues to uplift until 9 Ma, but this could be related to the other younger tectonic events around UMCC. Further systematic sampling and isotopic dating are necessary to clarify the uplift history of UMCC. In this stage, under the light of our field observations, it can be said that the extensional exhumation model proposed in this paper is a more convincing explanation compared to the model of Okay et al. (2008) since other extensional core complexes exist around the UMCC (see Seyitoğlu and Işık, 2015; Figure 5). One of them is the Kazdağ Core Complex which was first exhumed along with the Şelale Detachment with a top-to-the-north sense of shear and followed by top-to-the-south movements of Yeşilyurt Detachment controlling the accumulation of the Neogene sediments (Kurt et al., 2010). Another example is the Çataldağ Core Complex (Kamacı and Altunkaynak, 2019) exhumed along with the Çataldağ Detachment with a top-to-

the-north sense of shear. All these features and close isotopic ages indicate that the asymmetric Menderes Core Complex (Seyitoğlu et al., 2004; Seyitoğlu and Işık, 2015), as well as the other core complexes in NW Anatolia (the Kazdağ, Çataldağ, and Uludağ), are genetically linked. This allows for further speculation that the NW continuation of the Bursa Detachment can be seen the north of Marmara Island (Aksoy, 1996) where a low-angle detachment is visible in seismic reflection sections under the Marmara Sea (Okay et al., 1999; Figure 10). If this assumption is correct, then the Thrace basin could be classified as a supra-detachment basin.

#### 4. Results

The Bursa Fault is a low-angle normal fault and shows a detachment character developed on the dolomite-marble which is the uppermost rock unit of the Series-A (Uludağ Group). The upper plate rocks of the Bursa Detachment are composed of mica schist, phyllite, calcite-marble, epidote and glaucophane schist, serpentinite, and greenschist of the Series-B (Karakaya Complex). Spectacular outcrops of the Bursa Detachment located on the northern margin of the UMCC occur south of Alaçam village and Saitabad. They provide kinematic data of the top-to-the north/northeast sense of shear. The deeper sections are represented by the Oligocene metagranite at the southern UMCC interpreted as a syntectonic granite entering a ductile shear zone which is slightly dipping to the north below the calcite-marble at the Uludağ peak. All these features indicate that the UMCC is a typical metamorphic core complex similar to the Menderes, Kazdağ, and Çataldağ core complexes. The deeper sections of the UMCC are exposed due to the younger high-angle normal fault to the south of the UMCC. The normal SF cannot be attributed to the right-lateral EFZ because all segments of the EFZ to the east of the UMCC show a strike-slip character and run towards the north of the UMCC. Therefore, the interpretation of Okay et al. (2008) explaining the exhumation of the UMCC along the ductile shear zone of the EFZ should be re-examined. This paper presents an interpretation based on field observations regarding the nature of UMCC, further studies are necessary to clarify conflicting arguments.

## Acknowledgements

This paper is one of the results of the project titled UDAP-G-18-05: Determination of active faults that are possible earthquake sources around Bursa by geological and geophysical methods supported by the Disaster and Emergency Management Presidency of Türkiye (AFAD). We are grateful to Sinan AKISKA for the help of microscopic determinations. The earlier version of the manuscript was improved by the constructive comments of the referees, Roland OBERHANSLI, Thomas LAMONT, and Neven GEORGIEV, for which we are grateful.

## References

- Aksoy, R. 1996. Marmara Adası ve Kapıdağı Yarımadası'nın mesoskopik tektonik özellikleri. *Turkish Journal of Earth Sciences* 5, 187-195.
- Allmendinger, R. W., Cardozo, N. C., Fisher, D. 2012. *Structural Geology Algorithms: Vectors and Tensors*. Cambridge University Press, 289.
- Barka, A. 1992. The North Anatolian Fault Zone. *Annales Tectonicae* 6, 164-195.
- Barka, A., Kadinsky Cade, K. 1988. Strike-slip fault geometry in Turkey and its influence on earthquake activity. *Tectonics* 7, 663-684.
- Bozkurt, E., Park, R. G. 1994. Southern Menderes Massif: an incipient metamorphic core complex in western Anatolia, Turkey. *Journal of the Geological Society of London* 151, 213-216.
- Emre, Ö., Doğan, A., Duman, T. Y., Özalp, S. 2011a. Bursa (NK 35-12) quadrangle, 1/250000 scale of active fault map series of Turkey (serial number: 9). General Directorate of Mineral Research and Exploration, Ankara, Turkey.
- Emre, Ö., Duman, T. Y., Özalp, S. 2011b. Kütahya (NJ35-4) quadrangle, 1/250000 scale of Active Fault Map Series of Turkey (serial number: 10). General Directorate of Mineral Research and Exploration, Ankara, Turkey.
- Emre, Ö., Duman, T. Y., Özalp, S., Elmacı, H., Olgun, Ş., Şaroğlu, F. 2013. Active Fault Map of Turkey with an explanatory text 1:1.250.000 scale. General Directorate of Mineral Research and Exploration Special Publication Series 30, Ankara, Turkey.
- Emre, Ö., Duman, T. Y., Özalp, S., Şaroğlu, F., Olgun, Ş., Elmacı, H., Çan, T. 2018. Active fault database of Turkey. *Bulletin of Earthquake Engineering* 16, 3229-3275.
- Esat, K., Kaypak, B., Işık, V., Ecevitöglu, B., Seyitoğlu, G. 2016. The Ilıca branch of the southeastern Eskişehir Fault Zone: an active right-lateral strike-slip structure in central Anatolia, Turkey. *Bulletin of the Mineral Research and Exploration* 152, 25-37.
- Imbach, T. 1997. Geology of Mount Uludağ with emphasis on the genesis of the Bursa thermal waters, Northwest Anatolia, Turkey. Schindler, C., Pfister, M. (Ed.). *Active Tectonics of Northwestern Anatolia- the Marmara Poly-Project*. vdf Hochschulverlag AG an der ETH Zurich, 239-266.
- Kamacı, Ö., Altunkaynak, Ş. 2019. Cooling and deformation history of the Çataldağ Metamorphic Core Complex (NW, Turkey). *Journal of Asian Earth Sciences* 172, 279-291.
- Kaymakçı, N. 1991. Neotectonic evolution of the İnegöl (Bursa) Basin. MSc Thesis, Middle East Technical University, 73, Ankara (unpublished).
- Ketin, İ. 1947. Uludağ Masifi'nin tektoniği hakkında. *Türkiye Jeoloji Kurumu Bülteni* 1, 60-88.
- Ketin, İ. 1984. Türkiye'nin bindirmeli-naplı yapısında yeni gelişmeler ve bir örnek: Uludağ Masifi. *Ketin Sempozyumu*, 19-36.
- Kurt, F. S., Işık, V., Seyitoğlu, G. 2010. Alternative Cenozoic exhumation history of the Kazdağ Core Complex, Western Turkey. *Tectonic Crossroads: Evolving Orogens Of Eurasia-Africa-Arabia Abstracts with Programs* 36(3), Ankara, 70.
- Marrett, R., Allmendinger, R. W. 1990. Kinematic analysis of fault-slip data. *Journal of Structural Geology* 12, 973-986.
- Okay, A. I., Demirbağ, E., Kurt, H., Okay, N., Kuşçu, İ. 1999. An active, deep marine strike-slip basin along the North Anatolian fault in Turkey. *Tectonics* 18, 129-147.
- Okay, A. I., Satır, M., Zattin, M., Cavazza, W., Topuz, G. 2008. An Oligocene ductile strike-slip shear zone: the Uludağ Massif, northwestern Turkey - Implications for the westward translation of Anatolia. *Bulletin of the Geological Society of America* 120, 893-911.
- Passchier, C. W., Trouw, R. A. J. 2005. *Microtectonics*. Springer, ISBN-10: 3-540-64003-7.
- Ring, U., Johnson, C., Hetzel, R., Gessner, K. 2003. Tectonic denudation of a Late Cretaceous-Tertiary collisional belt: regionally symmetric cooling patterns and their relation to extensional faults in

- the Anatolide belt of western Turkey. Geological Magazine 140, 421-441.
- Selim, H. H., Tüysüz, O. 2013. The Bursa-Gönen depression, NW Turkey: a complex basin developed on the North Anatolian Fault. Geological Magazine 150, 801-821.
- Seyitoğlu, G., Işık, V. 2015. Late Cenozoic extensional tectonics in Western Anatolia: Exhumation of the Menderes core complex and formation of related basins. Bulletin of the Mineral Research and Exploration 151, 49-109.
- Seyitoğlu, G., Işık, V., Çemen, I. 2004. Complete Tertiary exhumation history of the Menderes massif, western Turkey: an alternative working hypothesis. Terra Nova 16, 358-364.
- Seyitoğlu, G., Ecevitoglu, B., Kaypak, B., Güney, Y., Tün, M., Esat, K., Avdan, U., Temel, A., Çabuk, A., Telsiz, S., Uyar Aldaş, G. G. 2015. Determining the main strand of the Eskişehir strike-slip fault zone using subsidiary structures and seismicity: A hypothesis tested by seismic reflection studies. Turkish Journal of Earth Sciences 24, 1-20.
- Seyitoğlu, G., Kaypak, B., Aktuğ, B., Gürbüz, E., Esat, K., Gürbüz, A. 2016. A hypothesis for the alternative southern branch of the North Anatolian Fault Zone, Northwest Turkey. Geological Bulletin of Turkey 59, 115-130.
- Seyitoğlu, G., Esat, K., Tün, M., Oruç, B., Pekşen, E., Mutlu, S., Balkan, E., Pekkan, E., Çetinkaya, D., Karaarslan, T., Kaypak, B., Çıvgın, B., Aktuğ, B., Kaya, A. M., Ecevitoglu, B. 2020. Active faults determined by the geological and geophysical methods around Bursa: New findings about the strike-slip faults cross-cutting pull-apart basins. 73<sup>rd</sup> Geological Congress of Turkey with International Participation, Ankara.
- Şengör, A. M. C. 1979. The North Anatolian transform fault: its age, offset, and tectonic significance. Journal of the Geological Society London 136, 269-282.
- Şengör, A. M. C., Cin, A. 1988. Uludağ Napı'nın alt dokanağı boyunca mezoskopik yapısal gözlemler ve napın yerleşme yönü. Türkiye Bilimsel ve Teknik Araştırma Kurumu, Proje No: TBG/824, 55, İstanbul (unpublished).
- Şengör, A. M. C., Görür, N., Şaroğlu, F. 1985. Strike-slip deformation basin formation and sedimentation: Strike-slip faulting and related basin formation in zones of tectonic escape: Turkey as a case study. Biddle, K. T., Christie-Blick, N. (Ed.). Strike-Slip Faulting and Basin Formation. Society of Economic Paleontologists and Mineralogists Special Publication 37, 227-264.
- Topuz, G., Okay, A. I. 2017. Late Eocene-Early Oligocene two-mica granites in NW Turkey (the Uludağ Massif): Water-fluxed melting products of a mafic metagreywacke. Lithos 268-271, 334-350.
- Türkecan, A., Yurtsever, A. 2002. 1/500000 scale geological map of Turkey, İstanbul Sheet No:1. General Directorate of Mineral Research and Exploration, Ankara.
- Yaltrak, C. 2003. Edremit Körfezi ve kuzeyinin jeodinamik evrimi. Doktora Tezi, İstanbul Teknik Üniversitesi, 246, İstanbul (unpublished).
- Yaltrak, C., Ceyhan, A. 2011. The synchronous geological evolution of the Northwestern Anatolian Core Complexes (Kazdağ and Uludağ) and surrounding region. 64<sup>th</sup> Geological Congress of Turkey Abstracts with Programs, Ankara, 38-39.
- Yıldırım, C., Emre, Ö., Doğan, A. 2005. Bursa ve Uludağ fayları ile Uludağ Masifi'nin neotektonik dönem yükselimi. Eskişehir Fay Zonu ve İlişkili Sistemlerin Depremselliği Çalıştayı, Abstracts with Programs, Eskişehir, 8.
- Yılmaz, M., Koral, H. 2007. Neotectonic features and geological development of the Yenişehir basin (Bursa). İstanbul Yerbilimleri Dergisi 20, 21-32.
- Yılmaz, Y. 2017. Morphotectonic development of Anatolia and surrounding regions. Çemen, İ., Yılmaz, Y. (Ed.). Active global seismology: Neotectonics and earthquake potential of the Eastern Mediterranean region. American Geophysical Union, Geophysical Monograph 225, 11-91.
- Yurdagül, A. 2004. Uludağ granitoidinin litojeokimyasal incelenmesi. Yüksek Lisans Tezi, İstanbul Üniversitesi, 140, İstanbul (unpublished).





# Bulletin of the Mineral Research and Exploration

<http://bulletin.mta.gov.tr>



## Geology, fluid inclusion characteristics and mineral resource estimation of the Güzelyayla porphyry Cu-Mo mineralization (NE Türkiye)

Mustafa Kemal REVAN<sup>a\*</sup>, Deniz GÖÇ<sup>b</sup>, Mustafa ÖZKAN<sup>c</sup>, Cüneyt ŞEN<sup>d</sup>, Rasim Taylan KARA<sup>c</sup>, Mustafa TOKOĞLU<sup>e</sup>, Semi HAMZAÇEBİ<sup>c</sup>, Rıfat Cihan SEVİM<sup>c</sup>, Fatih SEZEN<sup>f</sup>, Celaledin BAYRAKTAR<sup>f</sup> and Ömer AKGÜL<sup>f</sup>

<sup>a</sup>General Directorate of Mineral Research and Exploration, Department of Mineral Research and Exploration, Ankara, Türkiye

<sup>b</sup>MİTUS Research and Project Incorporated Company, Ankara, Türkiye

<sup>c</sup>General Directorate of Mineral Research and Exploration, Trabzon Regional Directorate, Trabzon, Türkiye

<sup>d</sup>Karadeniz Technical University, Faculty of Engineering, Department of Geological Engineering, Trabzon, Türkiye

<sup>e</sup>General Directorate of Mineral Research and Exploration, Department of Feasibility Studies, Ankara, Türkiye

<sup>f</sup>Turkish Petroleum Corporation, Ankara, Türkiye

Research Article

Keywords:

Güzelyayla  
Mineralization, Porphyry  
Cu-Mo, U-Pb Zircon,  
Sediment Geochemistry,  
Geostatistics.

### ABSTRACT

Magmatic processes that emerged with the evolution of the Neotethys ocean and associated lithospheric plates caused the formation of significant mineralization in the Tethys belt. The Eastern Pontides, which are located in the northeast of Türkiye and are a part of the Tethys metallogenic belt, are particularly rich in porphyry-type mineralization and represent an important region for Cu-Mo exploration. A large number of Cu, Pb and Zn anomalies have been determined in a large region including the Güzelyayla Cu-Mo field by stream sediment sampling. The Güzelyayla occurrence is Cu-Mo mineralization associated with andesitic/basaltic volcanic rocks and intrusive dacites crosscutting these rocks. The Güzelyayla Cu-Mo mineralization developed in the stockwork and fault-controlled silicified zones. Homogenization temperature values vary between 324 °C and 420 °C (average 374 °C). Salinity values range between 2.2 and 18.6% NaCl (average 9.1% NaCl). A concentric alteration zoning surrounding the potassic alteration indicates a gradual change in the physicochemical properties of the solutions forming the mineralization. The Güzelyayla mineralization was formed in the Eocene (50.7 ± 1.0 million years) period in the Upper Cretaceous volcanic rocks in relation to post-collisional processes in the magmatic arc environment. Contrary to previous studies, estimation zone models were created and an estimated 54.2 million tons of extracted/potential mineral resource with an average grade of 0.20% Cu and 0.014% Mo (0.26% Cu equivalent grade) was made in the Güzelyayla field.

Received Date: 02.05.2021

Accepted Date: 04.02.2022

### 1. Introduction

The Pontides, which were formed as a result of the subduction of the Neotethys Ocean along the Eurasian continental margin in the Mesozoic period, collided

with the Anatolide-Tauride platform in the Cenozoic period (Şengör and Yılmaz, 1981). As a result of these successive tectonic processes, numerous volcanogenic massive sulfide (VMS), porphyry and epithermal type mineralizations associated with calc-alkaline and

Citation Info: Revan, M. K., Göç, D., Özkan, M., Şen, C., Kara, R. T., Tokoğlu, M., Hamzaçebi, S., Sevim, R. C., Sezen, F., Bayraktar, C., Akgül, Ö. 2022. Geology, fluid inclusion characteristics and mineral resource estimation of the Güzelyayla porphyry Cu-Mo mineralization (NE Türkiye). Bulletin of the Mineral Research and Exploration 169, 63-85.  
<https://doi.org/10.19111/bulletinofmre.1074485>

\*Corresponding author: Mustafa Kemal REVAN, [kemalrevan@gmail.com](mailto:kemalrevan@gmail.com)

adakitic magmatism were formed in the Pontides. It was aimed to search for VMS and epithermal type mineralizations in the Pontides (Çağatay and Boyle, 1977; Pejatovic, 1979; Çağatay, 1993; JICA, 1998; Yiğit et al., 2000; Aslan, 2011; Karakaya et al., 2012; Akaryalı and Tüysüz, 2013; Eyüboğlu et al., 2014; Bilir, 2015; Revan et al., 2014, 2016, 2017, 2019; Revan, 2021). Scientific studies on the origins and geological environments of porphyry-type mineralization have been very limited (Doğan, 1980; Yalçınalp, 1992; Soylu, 1999; Delibaş et al., 2016, 2019; Kuşcu et al., 2019). To understand the geological events that control the formation and timing of the porphyry-type mineralization in the region, more detailed geological and geochemical studies at the deposit scale are required. Regional-scale geochemical prospecting data is an important and decisive method in the exploration of mineral resources. In particular, it plays an important role in the selection of priority target areas in explorations. A detailed geochemical sampling study (stream sediment, rock and soil) to be carried out after the selection of the target areas sheds light on the type of possible ore system in the region (Reimann et al., 2002; Zheng et al., 2014). The type of mineralization system also directly influences the selection of exploration strategies. The presence of metal anomalies and metal association is interpreted as a part of the mineralization system from which it originated and indicates target mineralization areas. The statistical analysis of the numerical data obtained from the target areas, on the other hand, has an important place in the determination or re-evaluation of mineral resources. In this context, the latest study by the General Directorate of Mineral Research and Exploration (MTA) on the Güzelyayla porphyry type mineralization in the eastern part of the Pontides and the data obtained in previous studies were examined together. The Güzelyayla mineralization is the first porphyry type occurrence discovered in the Eastern Pontides with regional prospecting geochemistry in terms of Cu and Mo resources (Nebioğlu, 1983; JICA, 1986; Güner and Güç, 1990). A large number of Cu, Pb, Zn and Au anomalies and associations have been determined as a result of geochemical sampling (stream sediment) in a large area where the Güzelyayla Cu-Mo field is located. It has been observed that some of these anomalies match exactly with the Güzelyayla mineralization area known in the

region. The existence of potential in the field has been demonstrated numerically with statistical methods prepared by creating a large number of descriptive statistical parameters of the obtained data.

The Güzelyayla Cu-Mo mineralization, which was determined as the target areas for porphyry type systems, was found as a result of the detailed geochemical sampling study carried out in the past. Also, the importance of such systematic and detailed geochemical studies in revealing the mineral resources was also emphasized in this study. The data presented in this article will be the basis for understanding the porphyry type mineralization in the region and will increase the interest in similar regions. In addition, this study has once again confirmed how important geostatistical methods are in the determination of mineralization and their possible potentials.

## 2. Geological Setting

Güzelyayla Cu-Mo mineralization is located within the Eastern Pontides volcanic belt (Figure 1). The Eastern Pontide volcanic belt is located in the northeastern part of the Anatolian Peninsula, which is a part of the Alpine-Himalayan metallogenic belt. Ketin (1966) divided the Anatolian Peninsula into four main tectonic units, aligned from north to south, as the Pontides, Anatolides, Taurides, and Border Folds, based on the orogenic development of Türkiye. Each tectonic unit has characteristic sedimentary, volcanic, plutonic, and metamorphic patterns that are related to its orogenic development. Located in the north of the northern branch of the Neotethys ocean, the Pontides are a morphological entity extending from the Gulf of Edremit in the west to the Caucasus in the east. Okay and Tüysüz (1999), who rearranged the tectonic units of the Anatolian Peninsula, named the east of the Sakarya Zone and the north of the Ankara-Erzincan Suture, as the Eastern Pontides. The Eastern Pontides is a volcanic belt consisting of Jurassic-Neogene volcanic and sedimentary rocks, ~600 km long and ~150 km wide, extending along the Eastern Black Sea coast. Due to its lithological differences, the Eastern Pontide belt is divided into two zones, generally north and south (Gedikoğlu et al., 1979; Özsayar et al., 1981; Bektaş et al., 1995; Okay and Şahintürk, 1997; Eyüboğlu et al., 2014; Liu et al., 2018). While the northern zone is mostly composed

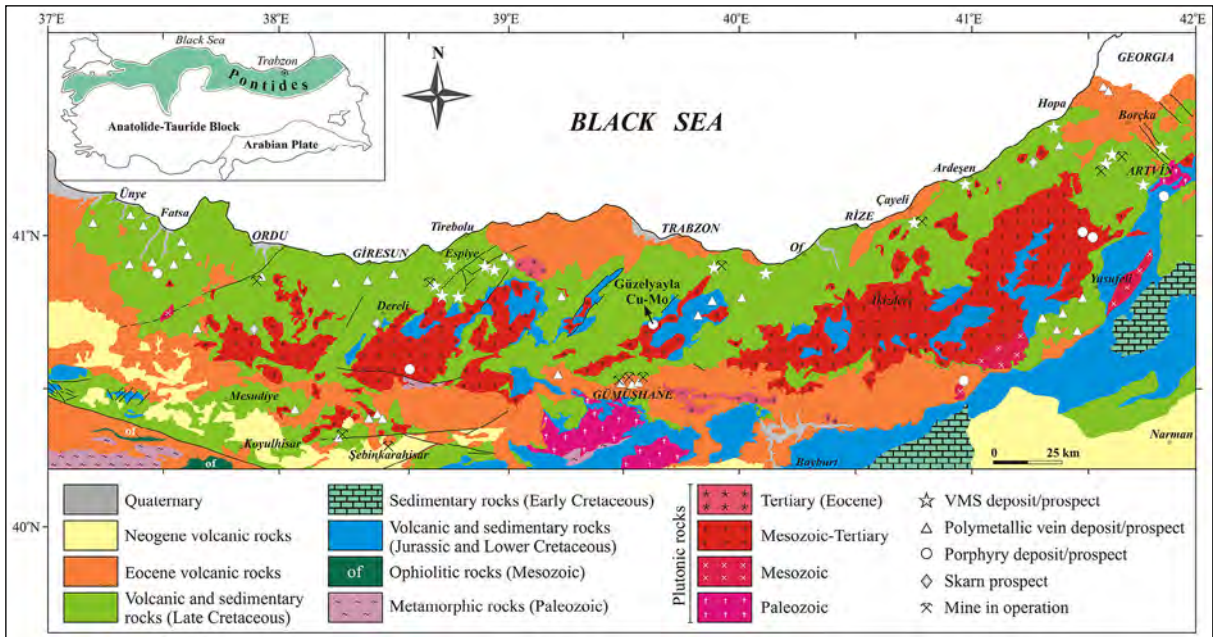


Figure 1- The locations of some important mineral deposits in Northeast Anatolia and the Güzelyayla porphyry type mineralization on the simplified regional geological map. Tectonic units of Anatolia (Ketin, 1966) are given in the upper inset.

of Late Cretaceous and Middle Eocene volcanic and volcanoclastics, the southern zone is mainly composed of pre-Late Cretaceous ophiolitic, sedimentary and lesser igneous rocks (Okay and Şahintürk, 1997). This region is restricted in the south by the Ankara-Erzincan Neotethys suture zone.

The Late Cretaceous period is represented by a volcanic arc in the Eastern Pontides (Peccerillo and Taylor, 1975; Pejatovic, 1979; Şengör and Yılmaz, 1981; Şengör et al., 1985; Robinson et al., 1995; Okay and Şahintürk, 1997; Kandemir et al., 2019). The geological evolution of the eastern Pontides during the Late Cretaceous period is related to the magmatic activity resulting from the subduction of the northern Neotethys lithosphere under the Eurasian continent. The direction and timing of the subduction are still vigorously debated. Many researchers agree that the geological evolution of the Eastern Pontides is originally related to the northward subduction of the Neotethys ocean in the Late Mesozoic period (Şengör et al., 1980; Ustaömer and Robertson, 1995; Okay and Şahintürk, 1997; Yılmaz et al., 1997; Rice et al., 2009; Dilek et al., 2010; Kandemir et al., 2019; Aydın et al., 2020). The view that the Paleotethys oceanic lithosphere was formed by southward subduction from Paleozoic to Eocene has recently gained support

(Dewey et al., 1973; Chorowicz et al., 1998; Bektaş et al., 1999; Eyüboğlu, 2010; Eyüboğlu et al., 2011a, b, 2014; Liu et al., 2018).

The Eastern Pontide volcanic belt consists of Mesozoic and Cenozoic rocks overlying a crystalline basement. The crystalline basement is a part of the Hercynian orogeny and consists of Paleozoic metamorphic rocks and Hercynian granitic intrusives in this region (Schultze-Westrum, 1961; Zankl, 1962; Yılmaz, 1976; Moore et al., 1980; Topuz et al., 2004; Kaygusuz et al., 2016). These basement rocks are overlain by a volcano-sedimentary succession ranging from Early Jurassic to Eocene (Okay and Şahintürk, 1997; Yılmaz and Korkmaz, 1999; Kandemir et al., 2019). Plutonic rocks of different ages and compositions, as well as various dykes and sills cut the entire succession. The ages of the plutonic rocks range from Carboniferous to Neogene (Delaloye et al., 1972; Okay and Şahintürk, 1997; Yılmaz et al., 1997; Kaygusuz, 2000; Arslan et al., 2004; Aydınçakır and Şen, 2013; Delibaş et al., 2016; Eyüboğlu et al., 2017, 2019; Liu et al., 2018). Plutonic rocks have a wide compositional range and are largely composed of tholeiitic and calc-alkaline granitoids and alkaline syenite/monzonites (Yılmaz and Boztuğ, 1996). The emplacement of the plutonic rocks is related to

subduction and post-collisional rifting events (Yılmaz and Boztuğ, 1996; Topuz et al., 2005; Karşlı et al., 2007; Boztuğ and Harlavan, 2008; Delibaş et al., 2016; Eyüboğlu et al., 2017, 2019; Liu et al., 2018).

### 3. Material and Method

After the macro structure and textural descriptions of the samples taken for petrographic purposes to represent the mineralizations were made, the rock cutting, etching, polishing and thin-section making and petrographic examinations were carried out in the laboratories of the MTA, Department of Mineral Analysis and Technology (MAT).

MAT of MTA was used for fluid inclusion analyses. Linkam MDSG 600 (motorized) heating and cooling system are used for fluid inclusion studies in MTA laboratories. The heating-cooling table is mounted on the Leica DM 2500 M model microscope. Objectives with 20x and 50x magnification were used for the examinations. Linkam MDSG 600 (motorized) is a fully automatic and programmable system. To be programmed, a software called Linksys32 is used in the computer environment. The temperature ranges of the Linkam table range from -196 °C to 600 °C. Heating and cooling rates increase from 0.1 °C/minute to 150 °C/minute. Liquid nitrogen (N<sub>2</sub>) is used in cooling processes. PL-A662 model PIXELINK camera is used while examining transparent samples.

Rock and sediment geochemistry was carried out in the laboratories of the Mineral Analysis Technology Department of MTA. Each rock sample was ground and sieved through 80 mesh size and turned into a 50-gram powder sample. ICP-MS instrument for gold (Au), AAS instrument for silver (Ag), and ICP-OES instrument for 10 other elements (As, Bi, Co, Cu, Mo, Ni, Pb, Sb, V, Zn) were used. For the analysis of Au (10 grams) and Ag (1 gram), the solving process was applied using the aqua regia method. For other elements (As, Bi, Co, Cu, Mo, Ni, Pb, Sb, V, Zn), 1-gram sample was weighed and dissolved in three acids (HNO<sub>3</sub> - HCl - HClO<sub>4</sub>).

### 4. Findings

#### 4.1. Research History

Güzelyayla Cu-Mo mineralization is located at 2.5 km southeast of Güzelyayla village in Maçka

district, ~30 km south of Trabzon Province. The Cu-Mo anomaly was determined in the mineralization area during the stream sediment geochemistry studies carried out in the region within the scope of the United Nations Development Project in 1973. In the following period, detailed prospecting, soil geochemistry and geological mapping studies were carried out in the field (Nebioğlu, 1983; Çınar and Yazıcı, 1985; Gülibrahimoğlu, 1985). Between 1985 and 1987, Japan International Cooperation Agency (JICA) conducted geophysical and 4969 meters of drilling in 17 locations in total (JICA, 1985, 1986, 1987). As a result of the drilling studies, 186.2 million tons of probable and proved reserves with an average grade of 0.3% Cu and 0.014% Mo were determined (JICA, 1987). To investigate the possible spread of mineralization in the northeast direction, a total of 1191 meters of drilling was carried out by MTA in four different locations from 1987 to 1990 (Güner and Güç, 1990). The data obtained about the geological settlement and geochemistry of the mineralization was examined within the scope of his doctoral study (Yalçınalp, 1992). Recent research in the field of mineralization was carried out by MTA from 2017 to 2019 within the scope of this study.

#### 4.2. Geology and Structure of Mineralized Area

Jurassic (Dogger) basalts are the oldest rocks in the mineralization area (Figure 2). Intense silicification and epidotization are typical in massive and locally amygdaloidal basalts. Late Jurassic-Early Cretaceous crystallized limestones (Gülibrahimoğlu, 1985) are in the form of blocks within the Late Cretaceous basaltic-andesitic volcanic rocks. These platform limestones belonging to the Berdiga Formation are semi-crystalline with the effect of intrusive rocks and faults and have turned into marble in places. Basalt-andesites and pyroclastics of the Çatak Formation, one of the host rocks of the porphyry type mineralization, crop out in large areas in the map area. The primary texture of the minerals in the basaltic-andesitic rocks has been obliterated by intense alteration. Chloritization and epidotization are common in basaltic-andesitic rocks close to felsic intrusives. Sediment deposits composed of siltstone, limestone and micritic mudstone are in the form of irregular lenses in the formation (Nebioğlu, 1983; Çınar and Yazıcı, 1985). Microscopically, the andesitic/dacitic rocks are

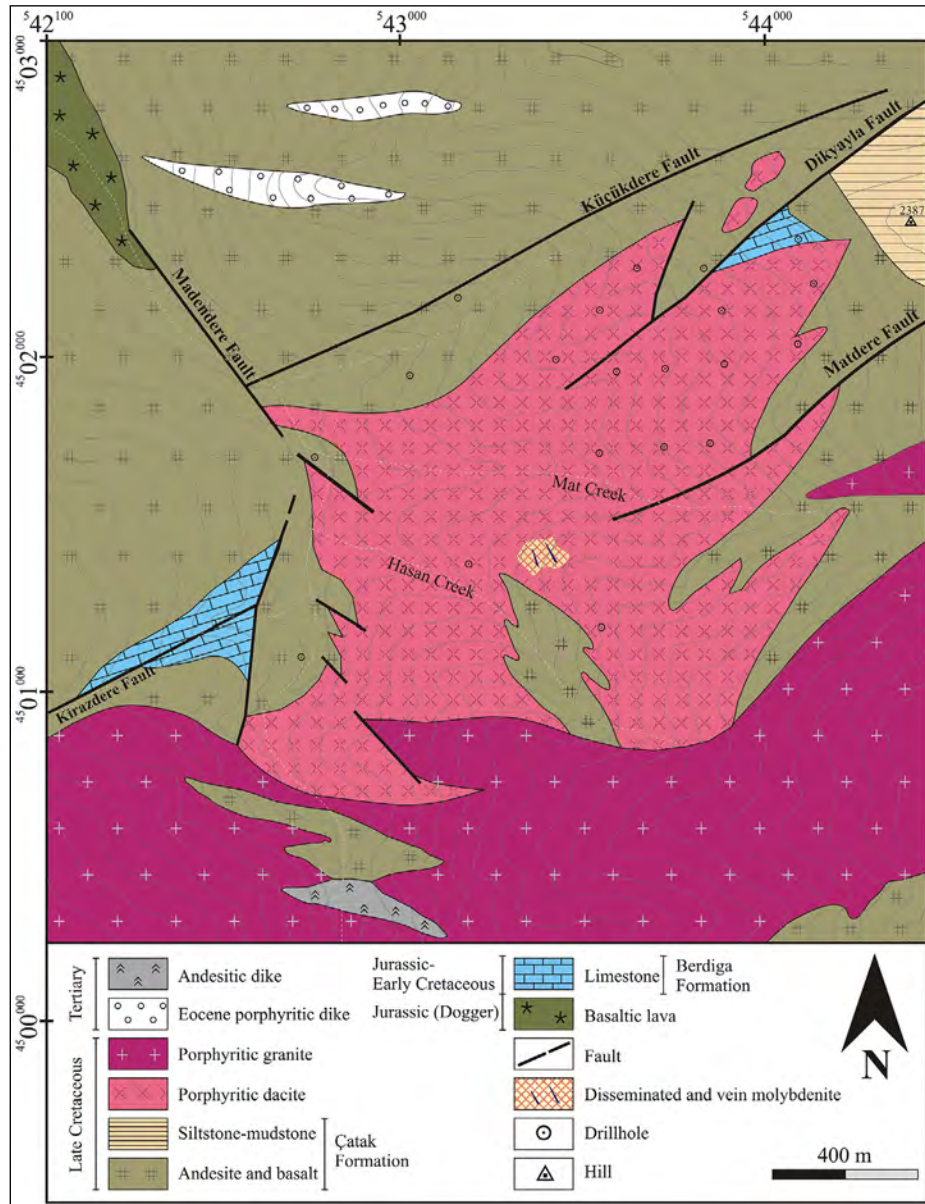


Figure 2- Geological map of the Güzelyayla Cu-Mo mineralization and distribution of important lithologies (modified from Çınar and Yazıcı, 1985 and JICA, 1986).

composed mostly of euhedral plagioclase, to lesser extent quartz phenocrysts filling interstices between other minerals. It is cut by quartz veins in place. The plagioclases are in the form of long laths and are located in the groundmass in argillized and sericitized forms. Mafic minerals are generally composed of weathered pyroxenes. The age of the Çatak Formation is Late Cretaceous (JICA, 1986; Güner and Güç, 1990). All these rock lithologies are intruded by Late Cretaceous porphyritic dacites and granites (Aydın, 2014; Delibaş et al., 2016). Porphyritic dacite has

a more fractured/jointed structure compared to the other plutonic rocks in the area, and their primary textures have largely been obliterated. The weathering products are generally sericitization, silicification, argillization and, to a lesser extent, epidotization and chloritization. This felsic intrusion is generally composed of quartz and plagioclase phenocrysts. Their plagioclase is argillized and mafic minerals are weathered. It is considered that the porphyritic dacite intrusion intruded in the form of a vertical body (JICA, 1986). Most of the mineralization in the field is in this

unit. The age data of  $81 \pm 1.1$  million years (Upper Cretaceous) were obtained from porphyritic dacites by the LA-ICP-MS U-Pb zircon method (Delibaş et al., 2016). Porphyritic granite is the largest intrusive mass outcropping in the Güzelyayla area. Porphyritic granite is commonly composed of plagioclase and quartz crystals. The mineralization is not observed in the porphyritic granite and the alteration is very weak. The mafic minerals are slightly chloritized and epidotized. Porphyritic granite cuts the volcanic and sedimentary units of the Late Cretaceous Çatak Formation in the map area. The contact relationship with the porphyritic dacite is uncertain due to the dense vegetation. However, porphyritic granite was interpreted as younger than porphyritic dacite due to the low degree of alteration (JICA, 1985). There is no radiometric age data for porphyritic granite. Age data of  $78 \pm 0.73$  million years (Upper Cretaceous) were obtained using the LA-ICP-MS, U-Pb zircon method around Turnagöl area in the northeastern part of the granitic unit (Kaygusuz et al., 2013). The latest magmatic phase is represented by Eocene granodioritic-tonalitic porphyritic dykes and andesitic dykes. Porphyritic and andesitic dykes crosscut Late Cretaceous volcanic rocks and porphyritic granite. The age of a subvolcanic porphyritic dyke representing the late-stage magmatic intrusion in the area was determined as  $53.55 \pm 0.34$  and  $51.34 \pm 0.27$  ( $^{40}\text{Ar}/^{39}\text{Ar}$  - hornblende) million years (Eocene) (Karlı et al., 2011). Andesitic dyke has a porphyritic texture and contains plagioclase, hornblende and pyroxene.

The mineralized area is located on the limb of an approximately N-S/NE-SW oriented anticline structure. The location of the porphyritic intrusions has caused some structural discontinuities (fault, fold, etc.) to form in the area. The positions of the faults are roughly parallel to each other and in the ~N45E direction. The Madendere fault, on the other hand, represents a roughly NW-SE trending fracture system. Local small faults in NE-SW direction cutting these faults were determined. It is thought that the granitic rocks in the area were emplaced along these tectonic lines. In some studies, using aerial photographs (Güner and Güç, 1990; Yalçınalp, 1992), it has been accepted that the Güzelyayla porphyry Cu-Mo mineralization is within the circular depression area.

### 4.3. Mineralization

Güzelyayla Cu-Mo mineralization was formed within Late Cretaceous porphyritic dacite and andesitic/basaltic volcanic rocks. The mineralization concentrated in the region between the Mat Dere and Hasan Dere has developed mostly in porphyritic dacites (Figure 2). The mineralization in andesitic/basaltic volcanic rocks intruded by porphyritic dacites is less developed and represents the outer parts of the mineralization center. Geochemical anomalies, distribution of alteration minerals, geophysical and drilling studies (JICA, 1986; Güner and Güç, 1990; Yalçınalp, 1992) support such a lithological distribution of the mineralization (Figure 3). In addition, skarn zones have developed at the limestone contacts with porphyritic dacite intrusions. Magnetite, chalcopyrite and pyrite enrichments are observed in these small sized skarn zones in order of abundance.

In the Güzelyayla porphyry Cu-Mo field, three types of mineralization are observed: stockwork (Figure 4a, b), disseminated (Figure 4c) and late-stage quartz veins (Figure 4d, e). The stockwork type quartz veins that crosscut the volcanic rocks with the Late Cretaceous porphyritic dacite intrusion typically contain chalcopyrite, pyrite, pyrrhotite, rutile and very rare molybdenite, while the disseminated mineralizations in the silicified zones of the porphyritic dacites are characterized by chalcopyrite, magnetite and pyrite. Covellite, chalcocite and digenite minerals observed in disseminated mineralization were interpreted as secondary minerals associated with local supergene enrichment (Delibaş et al., 2016). Late-stage quartz veins are a few centimeters thick and contain pyrite, chalcopyrite, molybdenite and sericite. Molybdenite is enriched in these late-stage quartz veins, which crosscut mostly porphyritic dacites and volcanic rocks.

Pyrite, chalcopyrite, magnetite, molybdenite, sphalerite, hematite, galena, pyrrhotite, gold, bornite, chalcocite, covellite and native copper are the ore minerals identified in the Güzelyayla porphyry Cu-Mo mineralization. Pyrite is disseminated all over the field, especially in the propylitic and sericitic zones, and in the form of infilling in quartz veins. Early and late stage phases were determined in pyrites. Magnetite is in the form of veins and disseminations in the propylitic

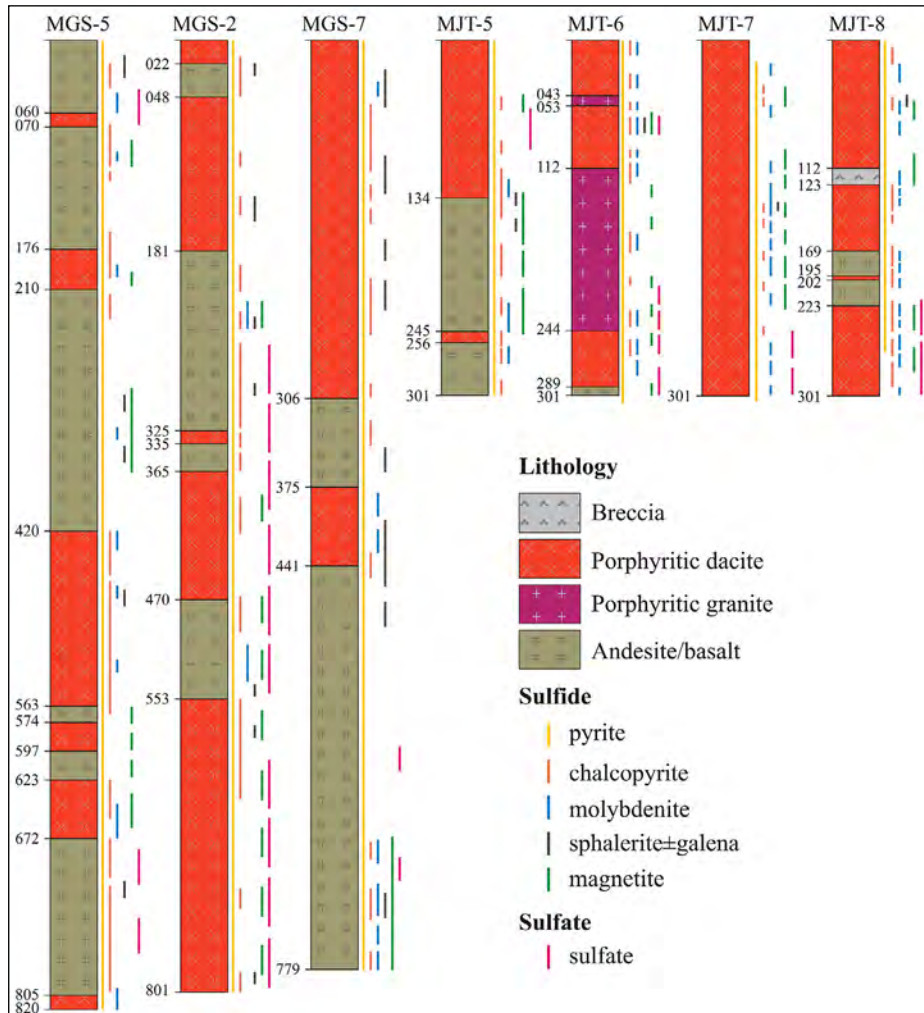


Figure 3- The main geological units and the distribution of some important related ore and gangue minerals in the representative drillings of the Güzelyayla Cu-Mo mineralization.

and potassic zone and is accompanied by very small amounts of hematite. Chalcopyrite increases towards the center of the mineralization. Molybdenite presents a distribution from the potassic zone to the propylitic zone. Sphalerite was observed in the potassic zone in the drillings. Pyrrhotite was identified as inclusions in chalcopyrites. Gold (3-7 microns in size) was identified in quartz. In microscopic examinations, it was observed that pyrite and chalcopyrite cut magnetite in many samples. Therefore, magnetite has been interpreted as one of the first minerals to form (JICA, 1986). Chalcocite, covellite and native copper were defined as secondary enrichments in the phyllic zone. Sulfate veins consisting of anhydrite and gypsum are commonly observed in the potassic zone and represent end-stage mineralization. The

relationship between paragenesis and succession of porphyry Cu-Mo mineralization is given in Figure 5.

While carbonates (calcite and dolomite) are common in the near-surface sections of the mineralization, the abundance of sulfate (gypsum and anhydrite) veins is remarkable, especially in the deep (>400m) sections. The source of abundant sulfur in porphyry deposits is problematic because of the relatively low solubility of sulfur in felsic magmas compared to mafic magmas (Sinclair, 2007). The role of mafic melts in the contribution of excess sulfur to felsic magmas has been suggested (Hattori and Keith, 2001). It was also suggested that aqueous magmas might contain abundant oxidized sulfur dissolved as sulfate (or anhydrite) (Strect and Dilles, 1998).

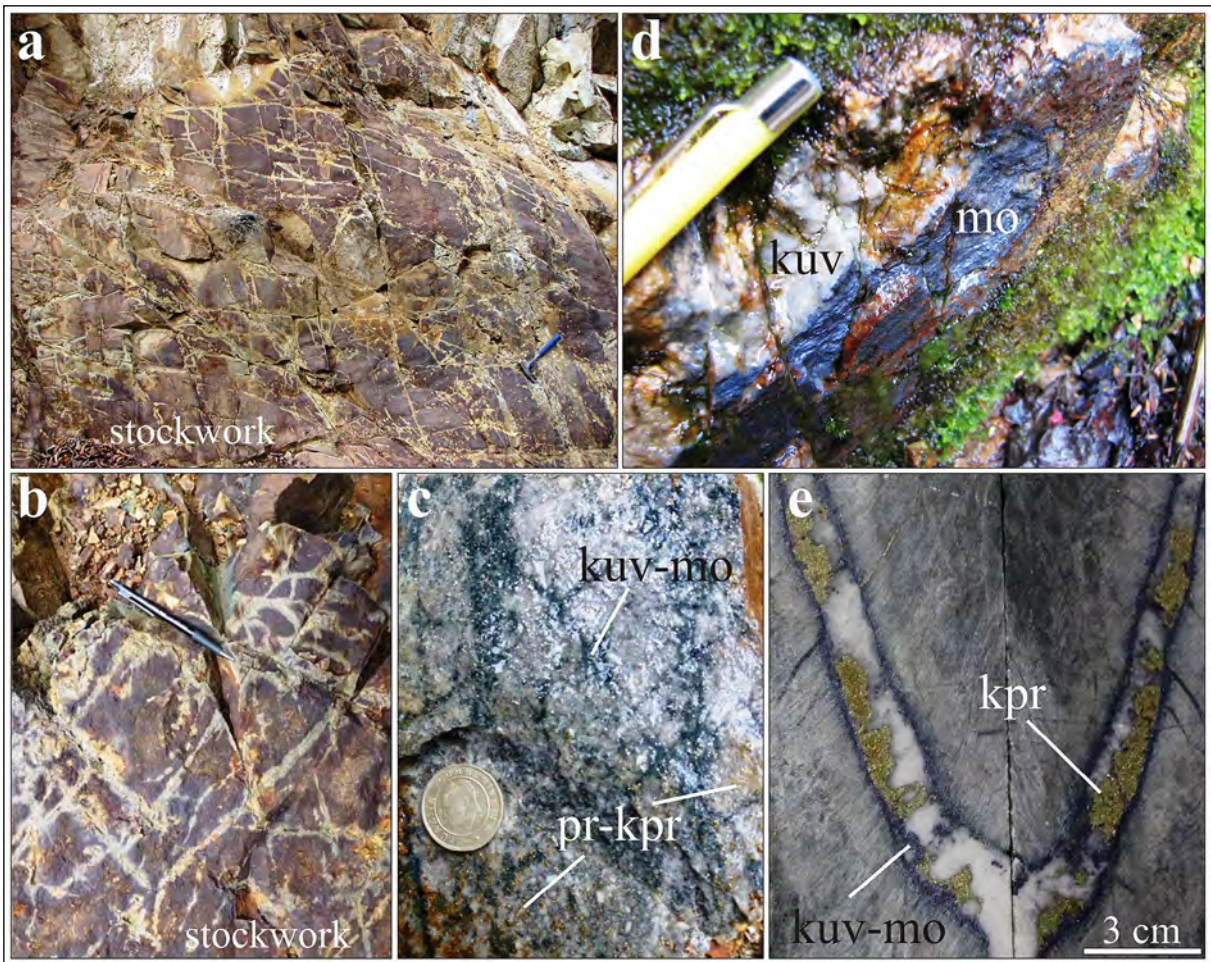


Figure 4- Mineralization types in the Güzelyayla Cu-Mo deposit; a) and b) quartz-pyrite-chalcopyrite stockwork zone developed in Late Cretaceous andesitic/basaltic volcanic rocks, c) disseminated sulfide (pyrite and chalcopyrite) and silicified mesh like sulfide (molybdenite) veins in the stockwork zones of porphyritic dacites, d) and e) late stage silicified sulfide (chalcopyrite and molybdenite) veins in porphyritic dacites. kuv-quartz; mo-molybdenite; pr-pyrite; kpr-chalcopyrite.

	First stage	Second stage	Late stage
Pyrite	---	---	---
Magnetite	---	---	---
Chalcopyrite	---	---	---
Sphalerite	---	---	---
Molybdenite	---	---	---
Galena	---	---	---
Bornite	---	---	---
Chalcocite	---	---	---
Covellite	---	---	---
Gypsum	---	---	---

Figure 5- Paragenesis and succession relationship of the Güzelyayla Cu-Mo mineralization.

Alteration minerals are largely composed of sericite, chlorite, kaolinite, pyrophyllite, and montmorillonite. Sericite-rich rocks are defined as phyllic zone, chlorite-rich rocks as propylitic zone, and rocks containing K-feldspar and biotite as potassic zone (JICA, 1987). The alteration area covers an area of 1.8 km x 1.8 km (Figure 6).

The central parts of the porphyritic dacite have been affected by potassic alteration. In the potassic zone, where thin quartz veins are common, disseminated magnetite and biotite veins and a small amount of K-feldspar are observed. The potassic zone is cut by thin quartz and sericite veins. Anhydrite is abundant in the potassic zone (Figure 7a, b). The minerals of sericitic alteration overprint porphyritic dacite and volcanic rocks. Sericitic alteration is remarkable

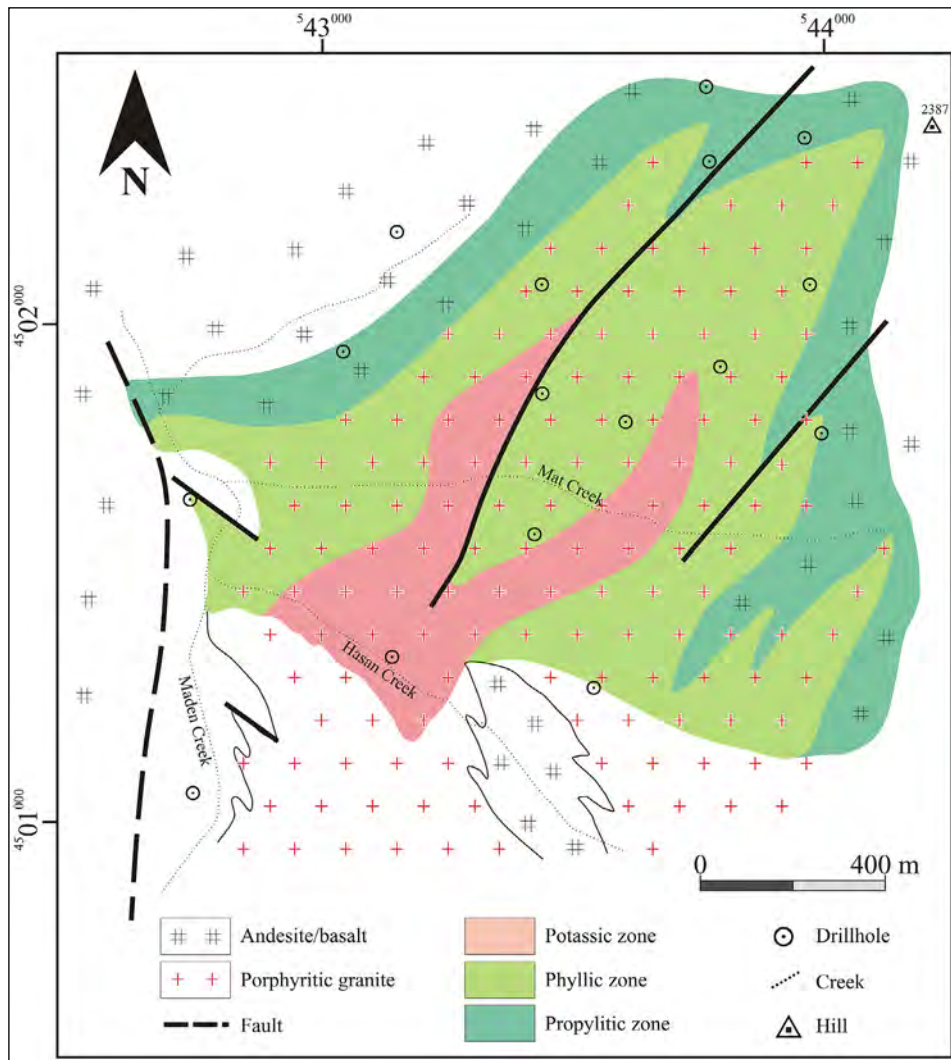


Figure 6- Alteration distribution map defined in the lithologies of the Güzelyayla Cu-Mo mineralization (modified from JICA, 1987).

with quartz, pyrite, sericite, and molybdenite veinlets (Figure 7c, d). The outermost propylitic alteration is more common in volcanic rocks. The propylitic zone contains chlorite, epidote, and magnetite. Pyritic quartz veins are common in the propylitic zone (Figure 7e, f). The argillic zone, which is characterized by kaolinite and montmorillonite, was observed only in the outer parts of the sericitic alteration zone in drillings. This alteration zoning pattern determined in the Güzelyayla Cu-Mo field is consistent with the potassic-phyllitic-propylitic (from the center to the outer parts) concentric zoning adapted by Lowell and Guilbert (1970) for porphyry systems. Alteration zoning varying from the central potassic alteration to the propylitic alteration in the outer parts indicates

that the physicochemical properties of the solutions constituting the Güzelyayla mineralization have changed gradually. The interaction of deep seated origin magmatic-hydrothermal solutions with host rocks of different permeability by rising and a decrease in the temperature and pressure of the solution are the determining features in the gradual change in the physical chemistry of ore solutions (Seedorff et al., 2005; John et al., 2010).

The geochronological (Re-Os) age of molybdenite in a quartz vein representing the stockwork zone in porphyritic dacites to reveal the formation age of the Güzelyayla porphyry system, was determined as  $50.7 \pm 1.0$  million years (Delibaş et al., 2019).

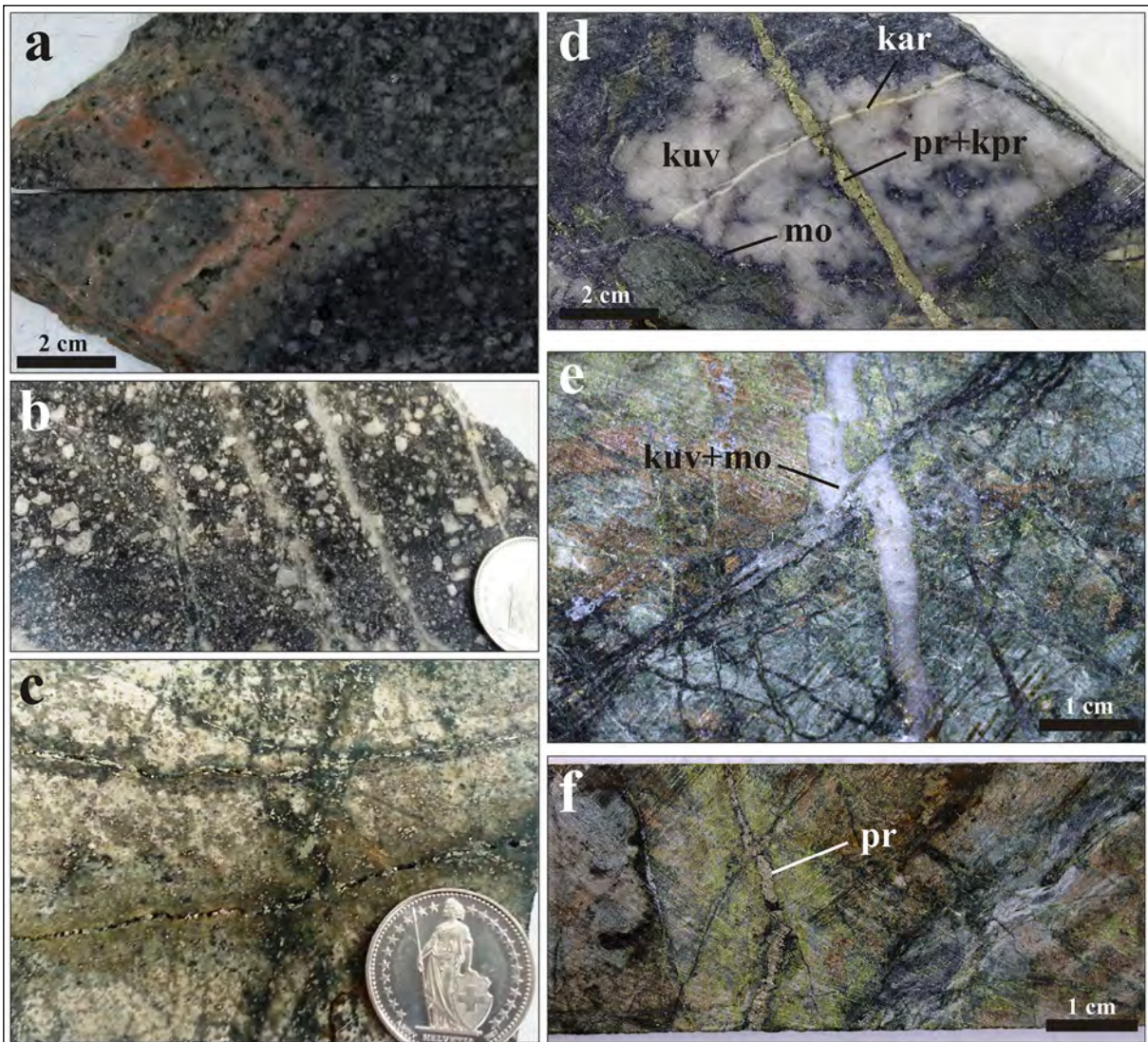


Figure 7- Some examples of alteration types identified in the Güzelyayla Cu-Mo mineralization; a), b) thin quartz and sericite veins that cut through the potassic alteration zone in porphyritic dacite, c), d) phyllic zone with veinlets of quartz, sericite, pyrite, and molybdenite in porphyritic dacite, e), and f) pyritic quartz veins observed widely as distributed in the propylitic zone of basaltic/andesitic volcanic rocks. kuv-quartz; mo-molybdenite; pr-pyrite; kpr-chalcopyrite; kar-carbonate.

#### 4.4. Fluid Inclusion Studies

To determine the homogenization temperatures of the solutions, which are effective in the formation of the Güzelyayla Cu-Mo mineralization, fluid inclusion studies were carried out in two quartz veins containing sulfide representing the stockwork zones in the ore-bearing intrusive rocks. A fluid inclusion study was carried out on quartz crystals. Primary two-phase (liquid and gas) inclusions were determined in these crystals. Inclusions are generally rod-like, polygonal and irregular in shape, and their size varies between 2 and 60 microns. Most inclusions are smaller than

20 microns. The homogenization temperatures ( $T_h$  °C) obtained as a result of microthermometric measurements made in two-phase inclusions are presented as histograms (Figure 8a). Homogenization temperature values range from 324 °C to 420 °C (average 374 °C). Salinity values vary between 2.2 and 18.6% NaCl equivalent (average 9.1% NaCl) (Figure 8b). A total of 1004 fluid inclusions were measured from 50 samples collected from quartz veins and quartz phenocrysts in porphyritic granites and dacites and andesite/basalts in fluid inclusion studies conducted within the scope of JICA-MTA

cooperation (JICA, 1986). The majority (90%) of the measurement results are clustered between 350 °C and 450 °C. Salinity values vary between 4.8 and 20.6% NaCl equivalent. Yalçınalp (1992) made a total of 209 measurements from 37 samples taken from porphyry dacite and andesitic/basaltic rocks in his doctorate study. It is observed that most of the measurement results (more than 90%) are clustered between 280 °C and 460 °C. It is observed that the fluid inclusions (homogenization temperatures and salinity) values obtained from this and previous studies are quite compatible. The formation temperatures of the Güzelyayla mineralization indicate a porphyry type formation. When a large number of fluid inclusion microthermometric measurement data compiled from porphyry systems on a global scale were examined, it was concluded that the homogenization temperatures and salinity values of ore solutions were concentrated in three fields (Tittley, 1993). Condensation fields are observed to vary from high salinity magmatic waters (Type I) to low temperature and salinity solutions diluted with meteoric waters (Type II and Type III). Hypersaline solutions with more than 30% NaCl equivalent salinity and homogenization temperature greater than 650 °C are defined as Type I. High salinity solutions with homogenization temperature between 350 °C and 550 °C are defined as Type II, and dilute solutions with less than 20% NaCl equivalent salinity and temperatures below 450 °C are defined as Type III (Figure 8b). It can be said that these fluid inclusion data compiled on a global scale are compatible with a scenario where the porphyry system includes solutions diluted by meteoric waters as it cools. When the homogenization temperatures and limited salinity values of Güzelyayla mineralization are examined, we can say that the solutions forming the mineralization are composed of dilute solutions (Type III) at relatively low temperatures. The available data indicate that the contents of ore solutions are not entirely of magmatic composition and that meteoric waters are involved.

#### 4.5. Geostatistical Evaluation of Numerical Data of the Güzelyayla Porphyry Cu-Mo Mineralization

Geostatistics constitutes the whole of the methods used in the arrangement, presentation and interpretation of the obtained numerical data. The main task of geostatistics is to organize the counting and measurement results in an easily understandable way

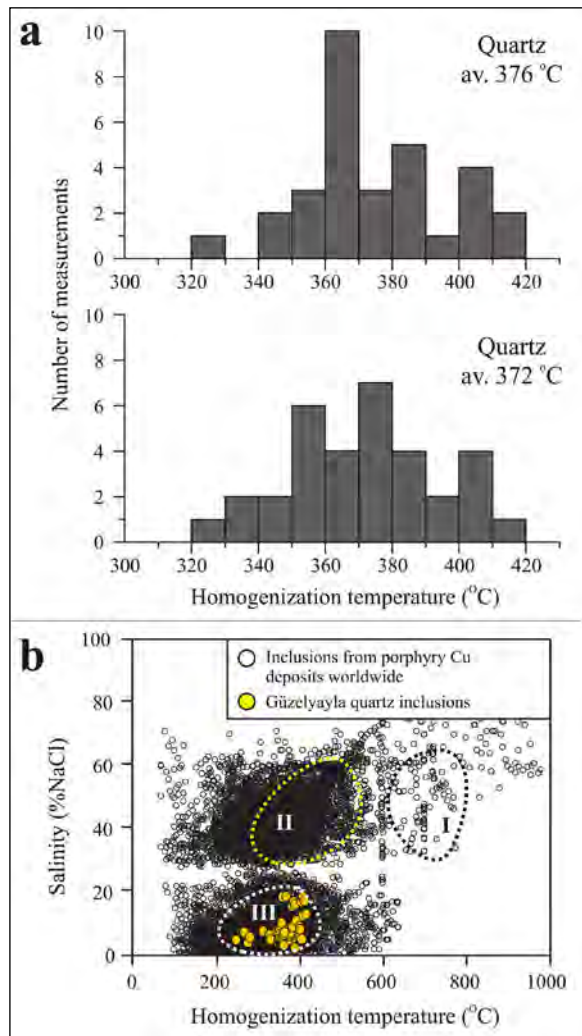


Figure 8- a) Homogenization temperature (°C) diagrams of fluid inclusions in two representative quartz samples compiled from the ore-bearing zones of the Güzelyayla Cu-Mo deposit and b) comparative presentation of the Güzelyayla Cu-Mo mineralization fluid inclusion data in the diagram (modified from Tittley, 1993 and Bodnar et al., 2014) of hydrothermal solution type formed from homogenization temperatures and salinity values compiled from porphyry type deposits. Areas I, II and III correspond to areas where homogenization temperatures and salinity values are concentrated, compiled from porphyry systems on a global scale by Tittley (1993).

and to extract information about the mass by making use of the variability in the common features of the objects that constitute a mass (Tüysüz and Yaylalı, 2005; Tütek and Gümüšoğlu, 2008). Statistically, the most useful data is the normal distribution, where the data distribution is symmetrically distributed around the arithmetic mean. However, ideal distributions are not always achieved although many methods are used

to approximate the normal distribution of values. This is one of the most common problems for geochemistry data. In such a case, appropriate and practical methods are used in calculating the threshold value to reduce the effect of extreme values.

#### 4.5.1. Geochemical Prospection

Geochemical sampling studies were carried out to reveal the existence and distribution of metal mineralizations in a wide area including Güzelyayla mineralization. In the region with a size of approximately 114 km<sup>2</sup>, a total of 160 stream sediment samples were taken and analyzed, with 1 sample per 0.7 km<sup>2</sup> area. In the analysis, the detection limit was determined as 3 ppm for Cu (copper) and Zn (zinc) elements and 5 ppm for Pb (lead). Obtained results were subjected to descriptive statistics. The table of descriptive statistics parameters of Cu, Pb and Zn elements is presented below (Table 1).

The obtained data should conform to or be close to the normal distribution (Hawkes and Webb, 1962). It was visually and mathematically tested whether the distribution of the data conformed to the normal distribution. Descriptive statistical parameters (mean, median, maximum, minimum, etc. values) were created for mathematical tests, and histograms, line and box plots were created for visual tests. In

the descriptive statistics table, the mean, median, maximum, minimum and standard deviation values of each element of the samples were given in the 95% confidence interval. Other descriptive statistical data in the table are measures of skewness and kurtosis. These values are decisive in evaluating whether the data show a normal distribution or not. In an ideal normal distribution, the mean and median should be equal, and the skewness and kurtosis coefficients should be zero. If the mean skewness coefficient of the elements is in the range of  $\pm 2$ , the distribution is considered to be normal. If the mean is greater than the median, the distribution of the data is skewed to the right (positive), and the distribution of the data is skewed to the left (negative) if the mean is less than the median (Tüysüz and Yaylalı, 2005; Güriş and Astar, 2015). The data are skewed to the right since the mean of the elements in the area where the Güzelyayla mineralization is located is greater than the median, and they do not present a normal distribution as the skewness coefficients are outside the range of  $\pm 2$  (Figure 9a). Kurtosis, on the other hand, is a parameter that shows how steep or flat the curve is in a normal distribution. In normal distribution, the kurtosis coefficient is zero. If the kurtosis coefficient is positive, the curve is steeper than the normal and flatter than normal if it is negative (Tüysüz and Yaylalı, 2005; Güriş and Astar, 2015). Since the kurtosis coefficient

Table 1- Descriptive statistical parameters of Cu-Pb-Zn elements in the stream sand samples collected from the Güzelyayla Cu-Mo mineralization and its immediate surroundings.

Element	Cu	Pb	Zn
Number of Sample	155	155	155
Minimum	7.0	5.00	21.00
Maximum	986.00	164.00	501.00
Mean	67.76	27.16	100.64
Median	42.00	20.00	90.00
Standard Deviation (SD)	102.35	19.42	56.78
Coefficient of Variation	0.14	0.71	0.56
Skewness	6.19	2.76	3.01
Kurtosis	47.95	14.91	16.03
Mean+2SD	272.47	66.00	214.22
Median+2MMS	138.60	103.92	71.40
% 25 (weighed average)	30.00	14.00	69.00
% 75 (weighed average)	84.00	40.00	123.00
% 95 (weighed average)	172.00	60.00	204.00

AMD: Absolute Median Deviation.

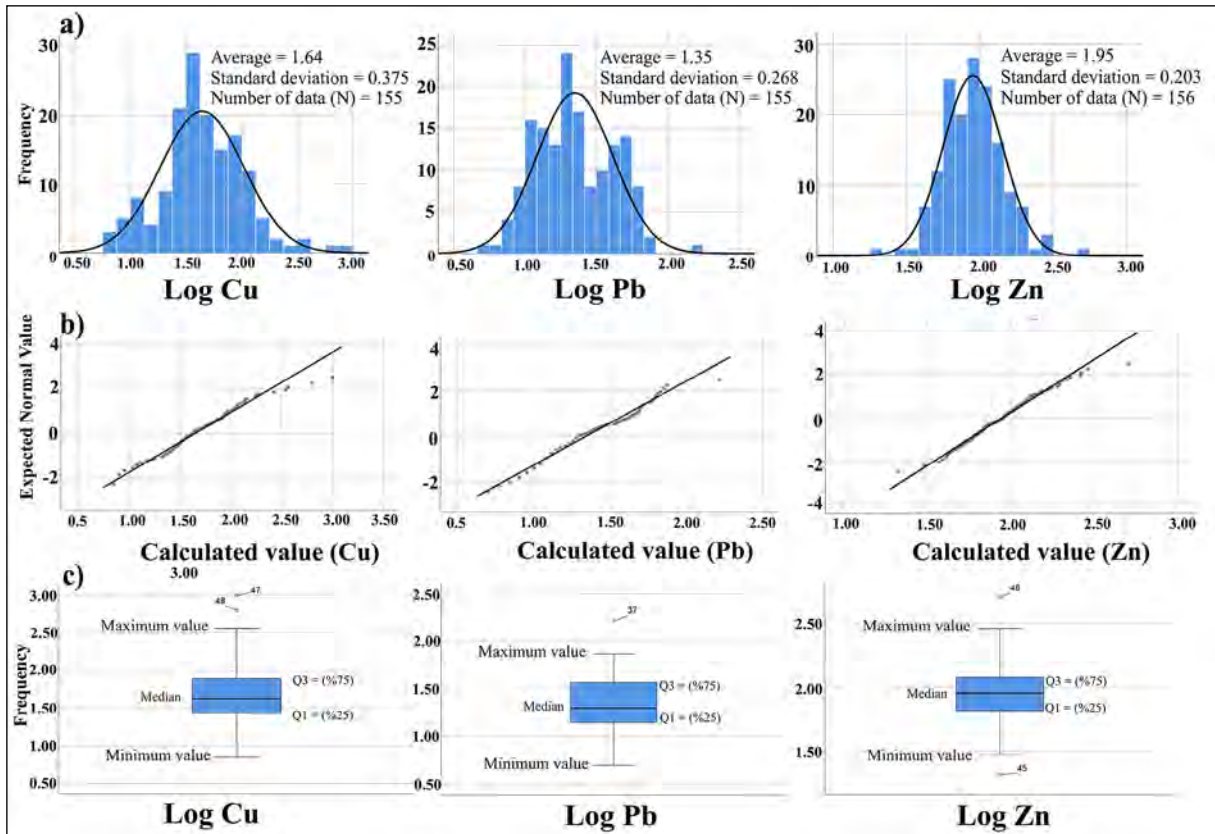


Figure 9- Visual tests of descriptive statistical data of Cu-Pb-Zn elements in the stream sand samples collected from the Güzelyayla Cu-Mo mineralization and its immediate surroundings; a) log normal distribution histograms for Cu, Pb and Zn elements, b) Q-Q diagrams for Cu, Pb and Zn elements, and c) log normal box plots for Cu, Pb and Zn elements.

of the data in the region is positive, the curve is steeper than normal.

It was also observed visually with the help of graphics whether the data set conforms to the normal distribution or not. Visual evaluation of the distributions of the samples, histograms (normal, log normal) and Q-Q (normal, log normal) and box (normal, log normal) diagrams of Cu, Pb and Zn elements subjected to descriptive statistics within 95% confidence interval were made. However, since the normal histograms of the elements do not show a normal distribution, log normal histograms, Q-Q lines and box diagrams were used to approximate the data to the normal distribution in this study. When the histogram diagrams created by taking the logarithmic values of the data belonging to Cu, Pb and Zn elements were examined, it was seen that the right-skewed data mostly approached the normal distribution, but they did not form an ideal normal ensemble (Figure 9b). A normal probability graph is also used while performing

normality analysis of data. If the samples are taken from a normally distributed stack, the values should be collected on or around a line (Kalaycı, 2006). In the log normal Q-Q diagrams of the field data, it was observed that the values of the sample populations were mostly gathered on or around a line, but did not form an ideal normal community.

Another convenient way to graphically represent groups of numerical data across their quartiles is box plots (Tukey, 1977). Box plots are used to summarize the distribution pattern of the data set, its central tendency, level of dispersion, kurtosis and skewness, and to identify outliers. With the help of this chart, the asymmetry, clustering and extreme values of the data are also easily defined (Tüysüz and Yaylalı, 2005). The line passing through the middle of the box represents the median value. The bottom of the box is the first quartile (Q1) and the top is the third quartile (Q3). The first quarter part in the box covers 25% of the data, the second quarter part covers 50% (median)

and the third quarter part covers 75% of the data. The lines drawn out of the box at the top and bottom of the box are created by extending the data up to 1.5 times the minimum (smallest value without extreme or outlier) and maximum (highest value without extreme or outlier) values (Reimann et al., 2005). It was investigated whether the data groups presented a normal distribution by creating log normal box plots of the elements subjected to descriptive statistics (Figure 9c). When the log normal box plots of the data of Cu, Pb and Zn elements are examined, it is observed that the data is skewed to the right because the line passing through the median values of the elements is closer to the minimum values of the elements, except for the log normal Zn boxplot in the log normal box plots of the elements of the log normal raw data. In the log normal box diagram, the values of Cu (2 samples), Pb (1 sample) and Zn (1 sample) elements fell to the outlier region above the maximum values, and the Zn (1 sample) element fell to the outlier region below the minimum value.

In summary, element distribution maps for Cu, Pb and Zn were created in the relevant region and anomalies were determined with the data obtained by evaluating the data sets created with the geostatistical method with the results of the stream sediment analysis of an area including the Güzelyayla mineralization (Figures 10, 11, 12). Element distribution maps are the most common and final data evaluation step in the evaluation of data in mineral exploration studies. In the creation of element distribution maps, the Inverse Distance Weighting (IDW) interpolation method of deterministic models was used. IDW is the inverse weighting of the distance between the anchor points and the point to be estimated. This method is the easiest deterministic interpolation method. To estimate the value at any unmeasured point, the IDW uses measured values near the point to be estimated. The effect of the measured values closest to the point whose value is desired to be found is more effective than the ones far from the investigated point. Therefore, it was aimed to obtain large weights from points that are close to each

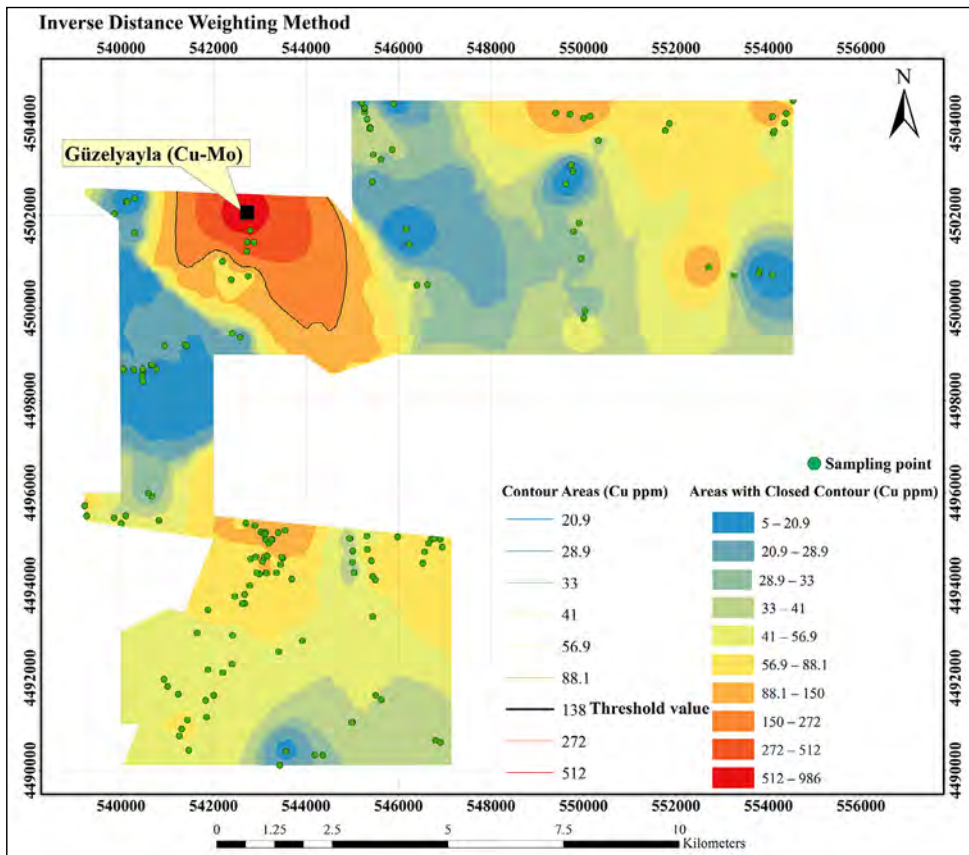


Figure 10- Cu metal anomaly map of the Güzelyayla mineralization and its surroundings, created by stream sediment geochemistry.

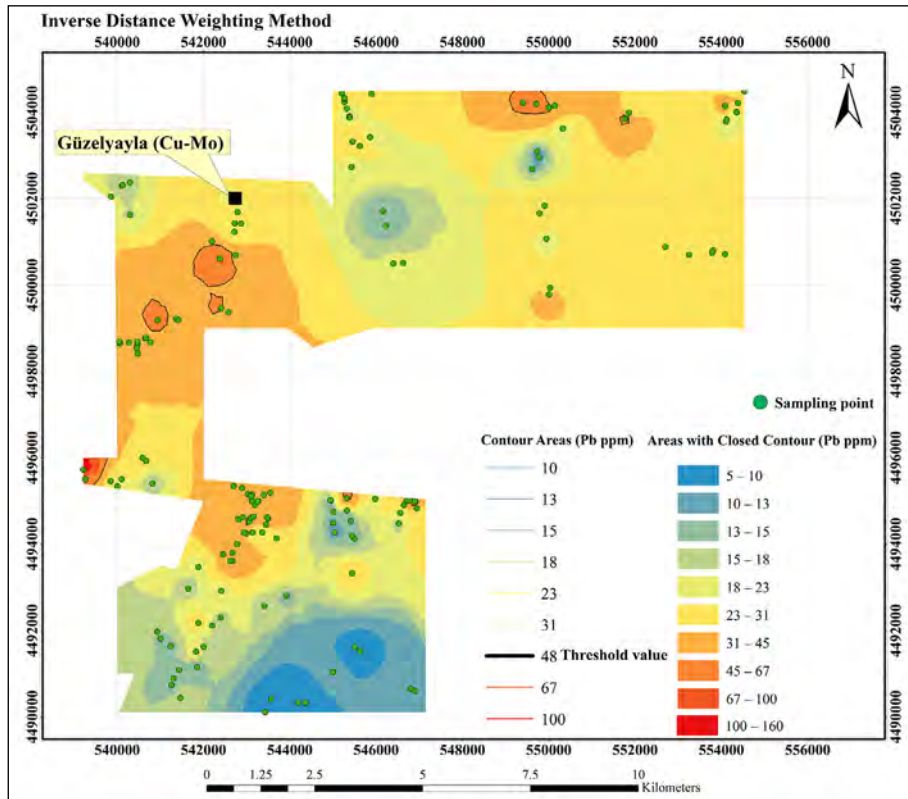


Figure 11- Pb metal anomaly map of Güzelyayla mineralization and its surroundings, created by stream sediment geochemistry.

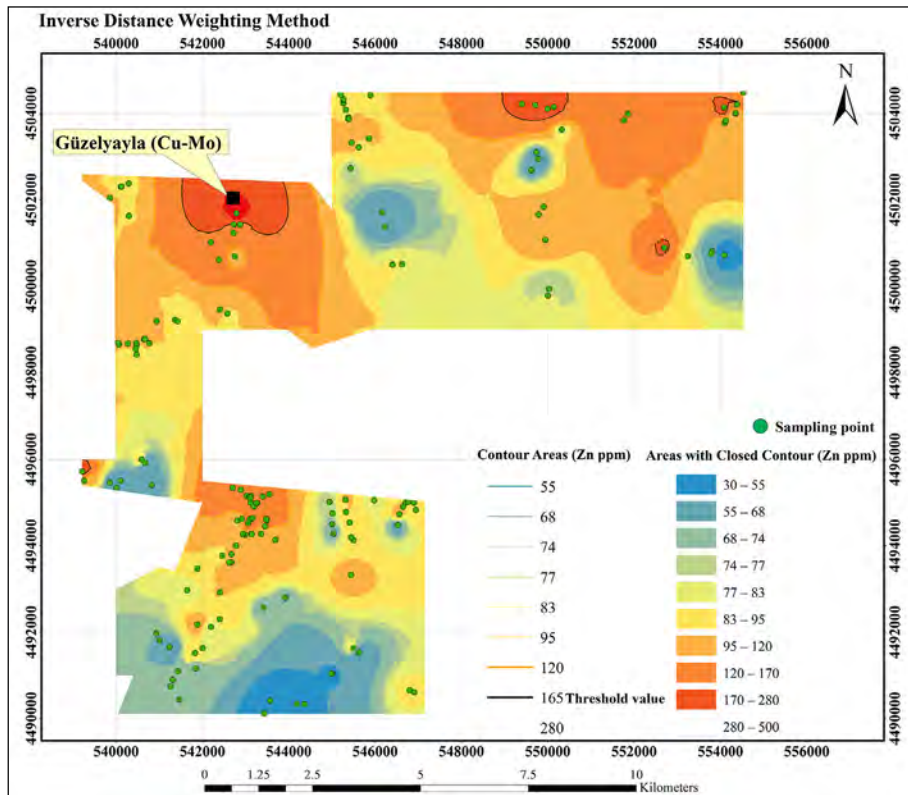


Figure 12- Zn metal anomaly map of Güzelyayla mineralization and its surroundings, created by stream sediment geochemistry.

other and to obtain small weights from points that are far from each other.

#### 4.5.2. Mineral Resource Estimation

Geological and analytical data of core drillings were used in mineral resource estimation studies of the Maçka-Güzelyayla field. Within the scope of this study, mine resource estimation studies using data compiled from 16 core drillings (Table 2) made in previous years are based on 3D block modeling principles. While the majority of the cores belonging to the drillings carried out within the scope of this study were sampled as 1 meter, sample intervals of 3 meters were preferred for the drillings of previous years and the intervals considered to be without ore were not sampled. Alphanumeric data entries (< detection limit value) denoting ranges with a grade lower than the detection limits are assigned as half of the detection limits. The summary statistical parameters prepared for the raw data collected from the Güzelyayla field and obtained as a result of the detailed search studies are given in Table 3.

The linear correlation coefficients prepared by considering the analysis data of 12 elements in the

Güzelyayla field drilling database are given in the linear correlation matrix in Table 4. In the correlation matrix, a weak to moderate positive correlation was observed between lead-zinc ( $r: 0.43$ ), silver-zinc ( $r: 0.36$ ), nickel-cobalt ( $r: 0.61$ ), antimony-arsenic ( $r: 0.56$ ), silver-antimony ( $r: 0.37$ ) and vanadium-nickel ( $r: 0.56$ ). A weak positive correlation was observed between the other elements.

Analytical data to be taken as a basis in modeling were obtained by creating a composite sample from the raw data of the field. While forming the composite sample, the sample length was determined as 2.5 meters, taking into account the vertical block size determined for the planned block model. Step compositing algorithm was used in the composite sample process and geological contacts were taken into account. Summary statistics for target metals (Mo and Cu) of 3023 composite samples created by this method are shown on the histograms presented in Figure 13, along with relative frequency graphs. Similar to raw data statistics, the histograms of shared composite data for Cu and Mo elements show rightward (positive) skewness. Grade distribution observed in composite and raw data is frequently encountered in porphyry type mineralizations.

Table 2- The summary presentation of the information about the drillings made in the Güzelyayla Cu-Mo deposit is given together with the analysis numbers used in the mine resource estimation studies.

Drilling no	Drilling year	Number of sampled well	Total Depth	Sample number		
				Mo	Cu	Ag, As, Au, Bi, Co, Ni, Pb, Sb, Zn, V
MGS	MTA - 2018 (this study)	7	4909	4909	4909	4909
MGT	MTA - 1990	4	3653	369	369	–
MJT	JICA - 1986	5	2508	504	504	–
Total		16	11070	5782	5782	4909

Table 3- Summary statistics of raw data obtained from Güzelyayla Cu-Mo deposit.

Element	Ag	As	Au	Bi	Co	Cu	Mo	Ni	Pb	Sb	V	Zn	Cu <sub>eq</sub>
Sample Number	4909	4909	4909	4909	4909	5782	5782	4909	4909	4909	4909	4909	5782
Minimum	0.5	1.5	10.0	2.5	2.5	1.5	0.0	2.5	2.5	2.5	2.5	1.5	4.0
Maximum	31	1641	300	100	78	15683	10800	109	7276	156	182	4458	48531
Median	0.5	1.5	10	2.5	8.0	443.0	18.0	6.0	6.0	2.5	18.0	55.0	564.2
<b>Mean</b>	<b>0.6</b>	<b>6.1</b>	<b>10.9</b>	<b>5.5</b>	<b>10.1</b>	<b>578.8</b>	<b>43.9</b>	<b>12.5</b>	<b>23.9</b>	<b>3.3</b>	<b>27.3</b>	<b>133.6</b>	<b>772.2</b>
Standard Deviation	0.9	32.1	8.9	9.0	6.7	591.1	260.4	17.1	137.9	5.1	25.7	263.5	1320.7
Coefficient of variation	1.33	5.27	0.81	1.62	0.66	1.02	5.93	1.37	5.77	1.52	0.94	1.97	1.71

Table 4- Correlation matrix of 12 elements in drillhole database of the Güzelyayla Cu-Mo prospect.

Element	Ag	As	Au	Bi	Co	Cu	Mo	Ni	Pb	Sb	V	Zn
Ag	1	0.26	0.15	0.07	0.08	0.24	-0.01	-0.04	0.23	0.37	-0.03	0.36
As		1	0.05	0.02	-0.02	0.22	0.02	-0.04	0.02	0.56	-0.08	0.11
Au			1	0.02	0.06	0.23	0.00	-0.01	0.09	0.04	-0.04	0.07
Bi				1	-0.03	-0.01	0.02	-0.11	0.02	0.06	-0.10	0.08
Co					1	0.35	0.02	0.61	-0.03	0.01	0.66	0.01
Cu						1	0.05	0.15	-0.02	0.13	0.10	0.03
Mo							1	0.04	-0.01	0.02	0.00	-0.04
Ni								1	-0.05	0.00	0.56	-0.06
Pb									1	0.01	-0.06	0.43
Sb										1	-0.06	0.02
V											1	-0.01
Zn												1

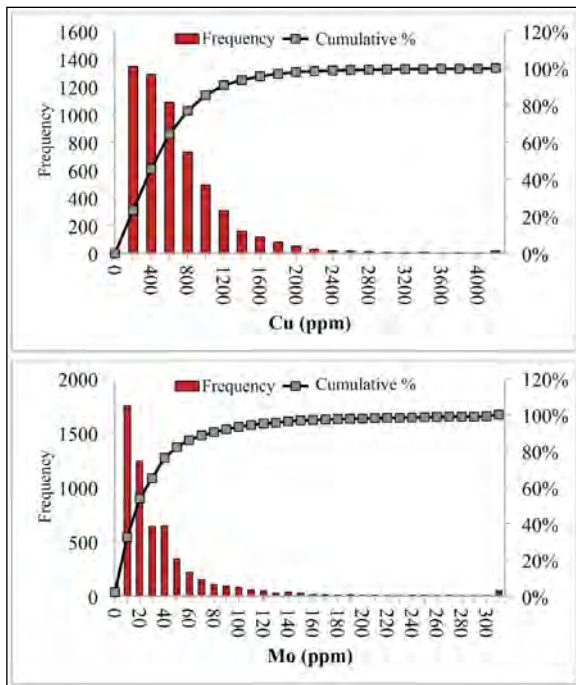


Figure 13- Composite data statistics for copper (Cu) and molybdenite (Mo) metals in the Güzelyayla mineralization.

For mineral resource estimation, 3D estimation zone models were created and by the price and metallurgical recovery assumptions made for the target metals, the copper equivalent formulation was determined as [Cu equivalent grade (%) = Cu (%) + (4.4 x Mo (%))]. In the NW-SE directional sections determined by considering the distribution of the boreholes and the ore geometry, Cu equivalent grades

equal to or higher than 0.15% were digitized. For the specified component of the Güzelyayla mineralization with the expectation of final economic extraction, the open pit boundaries determined by the Lerch-Grossman algorithm and the economic limit grade in copper equivalent (0.15% Cu equivalent grade) were taken into account.

As a result, 54.2 million tons of deduced/potential mineral resources with an average grade of 0.2% Cu and 0.014% Mo (0.26% Cu equivalent grade) were estimated in the Güzelyayla field by creating predictive zone models.

### 5. Results

The mineral deposit types associated with the closure of the Tethys oceanic basins are volcanogenic massive sulfide deposits, porphyry type Cu±Mo±Au deposits and epithermal type Au±Cu deposits. These deposits were formed as a result of subduction, collision and post-collision events, and the characteristics of the magmas with which they are associated are important in determining these processes. Among these deposits, especially porphyry type deposits are decisive in the explanation of the tectonomagmatic processes specific to the environment in which they were formed. Porphyry type formations in Tethys orogen were formed in four periods; Early Mesozoic (Triassic-Jurassic), Late Mesozoic (Cretaceous), Paleogene and Neogene periods (Richards, 2014). Except for a few

deposits, no significant porphyry type mineralization associated with the Paleozoic subduction is known. Its absence during the Paleozoic period can be explained by a later erosional removal of the deposits formed early. A large number of porphyry and associated epithermal deposits were described in the Cretaceous period. The most productive period throughout the generation is the Paleogene period. Porphyry deposits of the Paleogene period are associated with subduction (like Türkiye and Iran) or collision (Balkans, Carpathians and Tibet). Neogene deposits formed in the belt (Romania, Greece, Türkiye, Iran and Tibet) have been associated with post-subduction processes (Richards, 2014). Porphyry Cu-Mo systems in the Eastern Pontides, which are part of the Tethys belt, are typically interpreted as Early Cretaceous–Eocene (Soylu, 1999; Yiğit, 2009; Kuşçu et al., 2019; Delibaş et al., 2019). Recent studies (Kuşçu et al., 2019; Delibaş et al., 2019) indicate that the host rocks, including porphyry type mineralizations in the Eastern Pontides, were formed in an arc environment shaped by the subduction of the Neotethys ocean during the Cretaceous period. The ore formation ages of these deposits largely correspond to the Cretaceous period, except for the Güzelyayla mineralization. In the Güzelyayla area, the mineralization-related intrusions have been interpreted as the products of arc magmatism associated with the northward subduction of Neotethys subducting under the Eurasian plate (Delibaş et al., 2019). The age of the porphyritic dacites (LA-ICP-MS U-Pb zircon age  $81.4 \pm 1.1$  million years) and andesitic/basaltic volcanic rocks in which the Cu-Mo mineralization in Güzelyayla is found was determined as Late Cretaceous (Güner and Güç, 1990; Delibaş et al., 2016). However, the hydrothermal system in the Güzelyayla field was formed later from Late Cretaceous porphyritic dacite host rocks, unlike other porphyry-type deposits in the region, and corresponds to the Eocene period (molybdenite Re-Os age  $50.7 \pm 0.3$  million years) (Delibaş et al., 2019). Although the porphyry type mineralization formed during the Eocene period in the Tethys orogeny was considered to be associated with subduction and collision processes (Richards, 2014), the Güzelyayla mineralization was accepted to be associated with post-collisional processes in recent studies (Delibaş et al., 2019). In addition, it has been suggested that the Güzelyayla hydrothermal system

was formed in a tectonic environment that offers a transition from compressional to the extensional regime in a magmatic arc environment (Delibaş et al., 2019).

A large number of hydrothermal activities accompanied the Cretaceous and Eocene magmatism, which emerged with the geodynamic evolution processes of the region, and caused the formation of important mineralizations. The Güzelyayla Cu-Mo mineralization, which represents one of these mineralizations, is a part of a polycentric Cu-Mo system. The mineralization is Cu-Mo mineralization associated with andesitic/basaltic volcanic rocks and porphyritic dacite intrusives cutting these rocks. The Güzelyayla Cu-Mo occurrence is mineralization developed in the stockwork and fault-controlled silicified zones. When the ore types were examined structurally and texturally, it was evaluated that the mineralization developed in roughly three main phases. The first mineralization stage is represented by copper - magnetite - ( $\pm$ molybdenite) - containing dissemination, veinlet and brecciated zones and is associated with intense silicifications accompanied by potassic alteration. The second stage of mineralization is Cu-Mo-( $\pm$ Zn-Pb) containing veins and associated with potassic and phyllic alterations. The last stage is represented by late stage sulfate veins that cut through the whole system and is common in areas with potassic alteration. Mineral contents indicate that solutions at high temperatures initially decrease in temperature over time. When the country rock lithology, alteration features, metal content, mineralization stages and solution temperatures are evaluated together, the Güzelyayla mineralization is a porphyry Cu-Mo type formation. It would not be wrong to say that the solutions forming the Güzelyayla mineralization are composed of dilute solutions at relatively lower temperatures when compared to their global counterparts. The Güzelyayla occurrence is mineralization formed in the Upper Cretaceous volcanic rocks during the Eocene ( $50.7 \pm 1.0$  million years) period. This age value is not compatible with the LA-ICP-MS U-Pb zircon age ( $81.4 \pm 1.1$  million years) of the porphyritic dacites in which the mineralization occurs. This indicates that the Güzelyayla porphyry Cu-Mo mineralization was formed much later than the host rocks in which it was formed.

Metal anomaly maps, created with systematic and detailed stream sediment geochemistry data, have been a decisive method in determining the type of ore system in the region and the selection of the Güzelyayla Cu-Mo occurrence and mineralizations in its vicinity as target sites.

The existence of potential in the field has been demonstrated numerically with statistical methods prepared by creating a large number of descriptive statistical parameters of the obtained data. Contrary to previous studies, estimation zone models were created and an estimated 54.2 million tons of extracted/potential mineral resource with an average grade of 0.20% Cu and 0.014% Mo (0.26% Cu equivalent grade) was made in the Güzelyayla field. These determining grade and source values are in the range of values predicted for porphyry systems.

### Acknowledgements

This article includes the studies carried out within the scope of the project (project no: 2017/2018/2019-32-13-12) titled Gümüşhane ve Çevresi Metalik Maden Aramaları (Gümüşhane and Surrounding Metallic Mineral Explorations) by MTA. We would like to thank the geological engineers Abdullah DURSUN and Arif Çağrı SUBAŞI who accompanied us in the field studies carried out within the scope of the project.

### References

- Akaryalı, E., Tüysüz, N. 2013. The genesis of the slab window-related Arzular low-sulfidation epithermal gold mineralization (eastern Pontides, NE Turkey). *Geoscience Frontiers* 4, 409-421.
- Arslan, M., Kolaylı, H., Temizel, I. 2004. Petrographical, geochemical and petrological characteristics of the Güre (Giresun, NE Turkey) Granitoid. *Bulletin of Earth Sciences Application and Research Centre of Hacettepe University* 30, 1-21.
- Aslan, N. 2011. Mastra (Gümüşhane) Yatağı'nın jeolojik, mineralojik ve jeokimyasal özellikleri. MSc Thesis, Karadeniz Teknik Üniversitesi, Fen Bilimleri Enstitüsü, Trabzon, 190 (unpublished).
- Aydın, F. 2014. Geochronology, geochemistry, and petrogenesis of the Maçka subvolcanic intrusions: implications for the Late Cretaceous magmatic and geodynamic evolution of the eastern part

of the Sakarya zone, northeastern Turkey. *International Geology Review* 56, 1246-1275.

- Aydın, F., Saka, S. O., Şen, C., Dokuz, A., Aiglsperger, T., Uysal, İ., Kandemir, R., Karlı, O., Sarı, B., Başer, R. 2020. Temporal, geochemical and geodynamic evolution of the Late Cretaceous subduction zone volcanism in the eastern Sakarya Zone, NE Turkey: Implications for mantle-crust interaction in an arc setting. *Journal of Asian Earth Sciences* 192.
- Aydınçakır, E., Şen, C. 2013. Petrogenesis of the post-collisional volcanic rocks from the Borçka (Artvin) area: Implications for the evolution of the Eocene magmatism in the Eastern Pontides (NE Turkey). *Lithos* 172-173, 98-117.
- Bektaş, O., Şen, C., Atıcı, Y., Köprübaşı, N. 1999. Migration of the upper Cretaceous subduction-related volcanism towards the back-arc basin of the eastern Pontide magmatic arc (NE Turkey). *Geological Journal* 34, 95-106.
- Bektaş, O., Yılmaz, C., Taşlı, K., Akdağ, K., Özgür, S. 1995. Cretaceous rifting of the eastern Pontides carbonate platform (NE Turkey): the formation of the carbonate breccias and turbidites as evidence of a drowned platform. *Giornale di Geologia* 57, 233-244.
- Bilir, M. E. 2015. Geochemical and geochronological characterization of the Early-Middle Eocene magmatism and related epithermal systems of the Eastern Pontides, Turkey. MSc Thesis, Muğla Sıtkı Koçman Üniversitesi, Fen Bilimleri Enstitüsü, Muğla, 138 (unpublished).
- Bodnar, R. J., Lecumberri-Sanchez, P., Moncada, D., Steele-MacInnis, M. 2014. Fluid inclusions in hydrothermal ore deposits. Holland, H. D., Turekian, K. K. (Ed.). *Treatise on Geochemistry*, Second Edition, Elsevier 13, 119-142.
- Boztuğ, D., Harlavan, Y. 2008. K-Ar ages of granitoids unravel the stages of Neo-Tethyan convergence in the eastern Pontides and central Anatolia, Turkey. *International Journal of Earth Sciences* 97, 585-599.
- Chorowicz, J., Dhont, D., Adıyaman, Ö. 1998. Black Sea Pontides relationship: interpretation in terms of subduction. *International Third International Turkish Geology Symposium*, Middle East Technical University, Ankara, Turkey.
- Çağatay, M. N. 1993. Hydrothermal alteration associated with volcanogenic massive sulfide deposits: examples from Turkey. *Economic Geology* 88, 606-621.

- Çağatay, M. N., Boyle, D. R. 1977. Geochemical prospecting for volcanogenic sulfide deposits, eastern black sea region, Turkey. *Journal of Geochemical Exploration* 8(1-2), 49-71.
- Çınar, S., Yazıcı, E. N. 1985. Trabzon-Maçka-Güzelyayla Köyü Cu-Mo zuhuru ve civarına ait 1/5000 ölçekli jeoloji raporu, Maden Tetkik ve Arama Genel Müdürlüğü, Rapor No: 8025, Ankara (unpublished).
- Delaloye, M., Çoğulu, E., Chessex, R. 1972. Etude geochronometrique des massifs cristallins de Rize et de Gümüşhane, Pontides orientales (Turquie). *C. R. des Seances, SPHN, Geneve* 7, 43-52.
- Delibaş, O., Moritz, R., Selby, D., Göç, D., Revan, M. K. 2019. Multiple Porphyry Cu-Mo Events in the Eastern Pontides Metallogenic Belt, Turkey: From Early Cretaceous Subduction To Eocene Post-Collision Evolution. *Economic Geology* 114(7), 1285-1300.
- Delibaş, O., Moritz, R., Ulianov, A., Chiaradia, M., Saraç, C., Revan, M. K., Göç, D. 2016. Cretaceous subduction-related magmatism and associated porphyry-type Cu-Mo prospects in the Eastern Pontides, Turkey: New constraints from geochronology and geochemistry. *Lithos* 248(251), 119-137.
- Dewey, J. F., Pitman, W. C., Ryan, W. B. F., Bonnin, J. 1973. Plate Tectonics and the Evolution of the Alpine System. *Geological Society of America Bulletin* 84, 3137-3180.
- Dilek, Y., Imamverdiyev, N., Altunkaynak, Ş. 2010. Geochemistry and tectonics of Cenozoic volcanism in the Lesser Caucasus (Azerbaijan) and the peri-Arabian region: collision-induced mantle dynamics and its magmatic fingerprint. *International Geology Review* 52, 536-578.
- Doğan, R. 1980. The granitic rocks and related molybdenite mineralization of the Emeksen area, Espiye, NE Turkey. PhD Thesis, Durham University, Durham, UK, 334.
- Eyüboğlu, Y. 2010. Late Cretaceous high-K volcanism in the eastern Pontides orogenic belt, and its implications for the geodynamic evolution of NE Turkey. *International Geology Review* 52, 142-186.
- Eyüboğlu, Y., Chung, S. L., Santosh, M., Dudas, F. O., Akaryalı, E. 2011a. Transition from shoshonitic to adakitic magmatism in the eastern Pontides, NE Turkey: Implications for slab window melting. *Gondwana Research* 19, 413-429.
- Eyüboğlu, Y., Santosh, M., Dudas, F.O., Chung, S.L., Akaryalı, E. 2011b. Migrating magmatism in a continental arc: Geodynamics of the Eastern Mediterranean revisited. *Journal of Geodynamics* 52, 2-15.
- Eyüboğlu, Y., Dudas, F. O., Thorkelson, D., Zhu, D. C., Liu, Z. Chatterjee, N., Keewook, Y., Santosh, M. 2017. Eocene granitoids of northern Turkey: Polybaric magmatism in an evolving arc-slab window system. *Gondwana Research* 50, 311-345.
- Eyüboğlu, Y., Dudas, F. O., Zhu, D. C., Liu, Z. 2019. Late Cretaceous I- and A-type magmas in eastern Turkey: Magmatic response to double-sided subduction of Paleo and Neo-Tethyan lithospheres. *Lithos* 326-327, 39-70.
- Eyüboğlu, Y., Santosh, M., Yi, K., Tüysüz, N., Korkmaz, S., Akaryalı, E., Dudas, F. O., Bektaş, O. 2014. The Eastern Black Sea-type volcanogenic massive sulfide deposits: Geochemistry, zircon U-Pb geochronology and an overview of the geodynamics of ore genesis. *Ore Geology Reviews* 59, 29-54.
- Gedikoğlu, A., Pelin, S., Özsayar, T. 1979. Tectonic evolution of the Eastern Pontides in Mesozoic. *Geocom-I Abstracts*, 68-87.
- Gülibrahimoğlu, İ. 1985. Trabzon-Maçka güneyi yöresinin jeoloji raporu. Maden Tetkik ve Arama Genel Müdürlüğü, Rapor No: 383, 54, Trabzon (unpublished).
- Güner, S., Güç, A. R. 1990. Trabzon-Maçka-Güzelyayla yöresindeki porfiri tip Cu-Mo yatağının maden jeolojisi raporu. Maden Tetkik ve Arama Genel Müdürlüğü, Rapor No: 9191, 32, Ankara (unpublished).
- Gürüş, S., Astar, M. 2015. İstatistik. Der Yayınları, İstanbul, 421.
- Hattori, K., Keith, J. D. 2001. Contribution of mafic melt to porphyry copper mineralization: evidence from Mount Pinatubo, Philippines, and Bingham Canyon, Utah, USA. *Mineralium Deposita* 36, 799-806.
- Hawkes, H. E., Webb, J. S. 1962. *Geochemistry in Mineral Exploration*. Harper and Row 7, New York.
- JICA. 1985. Report on the cooperative mineral exploration of Gümüşhane area, phase 1. *Bulletin of the Mineral Research and Exploration Publications* 7800, 72, Ankara (unpublished).
- JICA. 1986. Report on the cooperative mineral exploration of Gümüşhane area, phase 3. *Bulletin of the*

- Mineral Research and Exploration Publications 7934, 199, Ankara (unpublished).
- JICA. 1987. Report on the cooperative mineral exploration of Gümüşhane area, follow-up report. . Bulletin of the Mineral Research and Exploration Publications 8298, 92, Ankara (unpublished).
- JICA. 1998. Report on the mineral exploration in the Espiye Area, The Republic of Turkey, Summary Report. Bulletin of the Mineral Research and Exploration Publications 10067, 119, Ankara (unpublished).
- John, D. A., Ayuso, R. A., Barton, M. D., Blakely, R.J., Bodnar, R. J., Dilles, J. H., Gray, F., Graybeal, F. T., Mars, J. C., McPhee, D. K., Seal, R. R., Taylor, R. D., Vikre, P. G. 2010. Porphyry copper deposit model, chapter B of Mineral deposit models for resource assessment. U.S. Geological Survey Scientific Investigations, Report No: 2010–5070–B, 169.
- Kalaycı, Ş. 2006. Faktör Analizi, SPSS Uygulamalı Çok Değişkenli İstatistik Teknikleri. Asil Yayın Dağıtım, Ankara.
- Kandemir, Ö., Akbayram, K., Çobankaya, M., Kanar, F., Pehlivan, Ş., Tok, T., Hakyemez, A., Ekmekçi, E., Danacı, F., Temiz, U. 2019. From arc evolution to arc-continent collision: Late Cretaceous-middle Eocene geology of the Eastern Pontides, northeastern Turkey. The Geological Society of America 131, 1889-1906.
- Karakaya, M. Ç., Karakaya, N., Küpeli, Ş., Yavuz, F. 2012. Mineralogy and geochemical behavior of trace elements of hydrothermal alteration types in the volcanogenic massive sulfide deposits, NE Turkey. Ore Geology Reviews 48, 197-224.
- Karlı, O., Chen, B., Aydın, F., Şen, C. 2007. Geochemical and Sr-Nd-Pb isotopic compositions of the Eocene Dölek and Sarıççek plutons, Eastern Turkey: Implications for magma interaction in the genesis of high-K calc-alkaline granitoids in a post-collision extensional setting. Lithos 98, 67-96.
- Karlı, O., Ketenci, M., Uysal, İ., Dokuz, A., Aydın, F., Chen, B., Kandemir, R., Wijbrans, J. 2011. Adakite-like granitoid porphyries in the eastern Pontides, NE Turkey: potential parental melts and geodynamic implications. Lithos 127, 354-372.
- Kaygusuz, A. 2000. Torul ve çevresinde yüzeyleyen kayaların petrografik ve jeokimyasal incelenmesi. Doktora Tezi, Karadeniz Teknik Üniversitesi, Fen Bilimleri Enstitüsü, Trabzon, 250.
- Kaygusuz, A., Arslan, M., Sipahi, F., Temizel, İ. 2016. U–Pb zircon chronology and petrogenesis of Carboniferous plutons in the northern part of the Eastern Pontides, NE Turkey: Constraints for Paleozoic magmatism and geodynamic evolution. Gondwana Research 39, 327-346.
- Kaygusuz, A., Sipahi, F., İlbeyli, N., Arslan, M., Chen, B., Aydınçakır, E. 2013. Petrogenesis of the late Cretaceous Turnagöl intrusion in the eastern Pontides: Implications for magma genesis in the arc setting. Geoscience Frontiers 4, 423-438.
- Ketin, İ. 1966. Tectonic units of Anatolia. Bulletin of the Mineral Research and Exploration 66, 20-34.
- Kuşcu, İ., Tosdal, R. M., Gençlioğlu-Kuşcu, G. 2019. Episodic porphyry Cu (-Mo-Au) formation and associated magmatic evolution in Turkish Tethyan collage. Ore Geology Reviews 107, 119-154.
- Liu, Z., Zhu, D., Wang, Q., Eyüpoğlu, Y., Zhao, Z.D., Liu, S., Xu, L. 2018. Transition from Low-K to High-K Calc-Alkaline Magmatism at Approximately 84 Ma In The Eastern Pontides (NE Turkey): Magmatic Response to Slab Rollback of The Black Sea. Journal of Geophysical Research-Solid Earth 123, 7604-7628.
- Lowell, J. D., Guilbert, J. M. 1970. Lateral and vertical alteration-mineralization zoning in porphyry ore deposits. Economic Geology 65, 373-408.
- Moore, W. J., McKee, E. H., Akıncı, Ö. 1980. Chemistry and chronology of plutonic rocks in the Pontide Mountains, northern Turkey. European Copper Deposits, 209-216.
- Nebioğlu, T. D. 1983. Trabzon-Maçka-Güzelyayla köyü civarındaki porfiri tip Cu-Mo zuhuruna ait ön rapor. Maden Tetkik ve Arama Genel Müdürlüğü, Rapor No: 7817, Trabzon (unpublished).
- Okay, A. I., Şahintürk, Ö. 1997. Geology of the eastern Pontides. Robinson, A. G. (Ed.). Regional and Petroleum Geology of the Black Sea and Surrounding Regions. American Association of Petroleum Geologist Memoirs 68, 291-311.
- Okay, A. I., Tüysüz, O. 1999. Tethyan sutures of northern Turkey. Durand, B., Jolivet, L., Horváth, F., Séranne, M. (Ed.). The Mediterranean Basins: Tertiary Extension within the Alpine Orogen. Geological Society of London, Special Publication 156, 475-515.
- Özsayar, T., Pelin, S., Gedikoğlu, A. 1981. Cretaceous in the eastern Pontides. Black Sea Technical University Earth Science Bulletin 1(2), 65-114.

- Peccherillo, A., Taylor, S. R. 1975. Geochemistry of upper cretaceous volcanic rocks from the pontic chain, northern turkey. *Bulletin of Volcanology* 39, 57-569.
- Pejatoviç, S. 1979. Metallogeny of The Pontide-Type Massive Sulfide Deposits. *Maden Tetkik ve Arama Genel Müdürlüğü Yayınları* 177, Ankara, 100.
- Reimann, C., Filzmoser, P., Garret, R. G. 2002. Factor analysis applied to regional geochemical data: problems and possibilities. *Applied Geochemistry* 17, 185-206
- Reimann, C., Filzmoser, P., Garrett, R. G., 2005. Background and threshold: critical comparison of methods of determination. *Science of the Total Environment* 346, 1-16.
- Revan, M. K. 2021. A review of Late Cretaceous volcanogenic massive sulfide mineralization in the Eastern Pontides, NE Turkey. *Turkish Journal of Earth Sciences* 29, 1125-1153.
- Revan, M. K., Genç, Y., Delibaş, O., Maslennikov, V. V., Nuriya, R. A., Zimitoğlu, O. 2019. Mineralogy and geochemistry of metalliferous sedimentary rocks from the Upper Cretaceous VMS deposits of the Eastern Pontides (NE Turkey). *Turkish Journal of Earth Sciences* 28, 299-327.
- Revan, M. K., Genç, Y., Maslennikov, V. V., Maslennikova, S. P., Large, R. R., Danyuhevsky, L. V. 2014. Mineralogy and trace-element geochemistry of sulfide minerals in hydrothermal chimneys from the Upper-Cretaceous VMS deposits of the eastern Pontide orogenic belt (NE Turkey). *Ore Geology Reviews* 63, 129-149.
- Revan, M. K., Hisatani, K., Miyamoto, H., Delibaş, O., Haniççi, N., Aysal, N., Özkan, M., Çolak, T., Karsh, S., Peytcheva, I. 2017. Geology, U-Pb geochronology, and stable isotope geochemistry of the tunca semi-massive sulfide mineralization, NE Turkey: implications for ore genesis. *Ore Geology Reviews* 89, 369-389.
- Revan, M. K., Maslennikov, V. V., Genç, Y., Delibaş, O., Maslennikova, S. P., Sadykov, S. A. 2016. Sulfur isotope study of the vent chimneys from the Upper Cretaceous VMS deposits of the eastern Pontide metallogenic belt, NE Turkey. *Turkish Journal of Earth Sciences* 25, 227-241.
- Rice, S. P., Robertson, A. H. F., Ustaömer, T., İnan, N., Taşlı, K. 2009. Late Cretaceous-Early Eocene tectonic development of the Tethyan suture zone in the Erzincan area, Eastern Pontides, Turkey. *Geological Magazine* 146(4), 567-590.
- Richards, J. P. 2014. A review of tectonics and metallogeny of the Tethyan orogen. *Acta Geologica Sinica* 88, 923-925.
- Robinson, A. G., Banks, C. J., Rutherford, M. M., Hirst, J. P. 1995. Stratigraphic and structural development of the Eastern Pontides, Turkey. *Journal of the Geological Society* 152, 861-872.
- Schultze-Westrum, H. H. 1961. Giresun civarındaki Aksu deresinin jeolojik profili; Kuzeydoğu Anadolu'da, Doğu Pontus cevher ve mineral bölgesinin jeolojisi ve maden yatakları ile ilgili mütalaalar. *Bulletin of the Mineral Research and Exploration* 57, 63-71.
- Seedorff, E., Dilles, J. H., Proffett, J. M., Jr., Einaudi, M. T., Zurcher, L., Stavast, W. J. A., Johnson, D. A., Barton, M. D. 2005. Porphyry deposits: characteristics and origin of hypogene features. Hedenquist, J. W., Thompson, J. F. G., Golfarb, R. J., Richards, J. R. (Ed.). *Society of Economic Geologists, Economic Geology 100th Anniversary 1905-2005*, 251-298.
- Sinclair, W. D. 2007. Porphyry deposits. Goodfellow, W. D. (Ed). *Mineral Deposits of Canada: A Synthesis of Major Deposit-Types, District Metallogeny, the Evolution of Geological Provinces, and Exploration Methods*. Geological Association of Canada, Mineral Deposits Division, Special Publication 5, 223-243.
- Soylu, M. 1999. Modeling of porphyry copper mineralization of the Eastern Pontides. PhD Thesis, Middle East Technical University, Ankara, 127.
- Streck, M. J., Dilles, J. H. 1998. Sulfur evolution of oxidized arc magmas as recorded in apatite from a porphyry copper batholith. *Geology* 26, 523-526.
- Şengör, A. M. C., Yılmaz, Y. 1981. Tethyan Evolution of Turkey: A plate tectonic approach. *Tectonophysics* 75, 181-241.
- Şengör, A. M. C., Yılmaz, Y., Ketin, İ. 1980. Remnants of a pre-Late Jurassic ocean in Northern Turkey: fragments of a Permian-Triassic Paleo-Tethys. *Geological Society of America Bulletin* 91, 599-609.
- Şengör, A. M. C., Görür, N., Şaroğlu, F. 1985. Strike slip faulting and related basin formation in zones of tectonic escape: Turkey as a case study. Biddle, T. R., Christie-Blick, N. (Ed.). *Strike-slip deformation, basin formation and sedimentation*.

- Society of Economic Paleontologists and Mineralogists, Special Publication 37, 227-264.
- Titley, S. R. 1993. Characteristics of porphyry copper occurrence in the American Southwest. Geological Association of Canada Special Paper 40, 433-464.
- Topuz, G., Altherr, R., Kalt, A., Satır, M., Werner, O., Schwarz, W. H. 2004. Aluminous granulites from the Pulur Complex, NE Turkey: a case of partial melting, efficient melt extraction and crystallisation. *Lithos* 72, 183-207.
- Topuz, G., Altherr, R., Schwarz, W. H., Siebel, W., Satır, M., Dokuz, A. 2005. Post-collisional plutonism with adakite-like signatures: the Eocene Saraycık granodiorite (Eastern Pontides, Turkey). *Contributions to Mineralogy and Petrology* 150, 441-455.
- Tukey, J. W. 1977. *Exploratory Data Analysis*. Reading 7, Addison-Wesley.
- Tütek, H., Gümüsoğlu, Ş. 2008. *İşletme İstatistiği*. Beta Basım Yayım Dağıtım AŞ, İstanbul.
- Tüysüz, N., Yaylalı, G. 2005. *Jeostatistik Kavramlar ve Bilgisayar Uygulamaları*. KTÜ Matbaası, Trabzon.
- Ustaömer, T., Robertson, A. H. F. 1995. Paleotethyan tectonic evolution of the north Tethyan margin in the central Pontides, N Turkey. Erler, A., Ercan, T., Bingöl, E., Örcen, S. (Ed.). *Geology of the Black Sea region*. Proceedings of the International Symposium on the Geology of the Black Sea Region, Ankara, Turkey, 24-33.
- Yalçınalp, B. 1992. Güzelyayla (Maçka-Trabzon) porfiri Cu-Mo cevherleşmelerinin jeolojik yerleşimi ve jeokimyası. Doktora Tezi, Karadeniz Teknik Üniversitesi, Fen Bilimleri Enstitüsü, Trabzon, 181.
- Yılmaz, C., Korkmaz, S. 1999. Basin development in the eastern Pontides, Jurassic to Cretaceous, NE Turkey. *Zentralblatt für Geologie und Paläontologie*. Teil I H10-12, 1485-1494.
- Yılmaz, S., Boztuğ, D. 1996. Space and time relations of three plutonic phase in the Eastern Pontides, Turkey. *International Geology Review* 38, 935-956.
- Yılmaz, Y. 1976. Geology of the Gümüşhane granite (petrography). İstanbul Üniversitesi, Fen Fakültesi Dergisi B(39), 157-172.
- Yılmaz, Y., Tüysüz, O., Yiğitbaş, E., Genç, Ş. C., Şengör, A. M. C. 1997. Geology and tectonic evolution of the Pontides. Robinson, A. G. (Ed.). *Regional and petroleum geology of the Black Sea and surrounding regions*. American Association Petroleum Geologist, Memoir 68, 183-226.
- Yiğit, Ö. 2009. Mineral deposits of Turkey in relation to Tethyan metallogeny: implications for future mineral exploration. *Economic Geology* 104, 19-51.
- Yiğit, Ö., Nelson, E. P., Hitzman, M. W. 2000. Early Tertiary epithermal gold mineralization, Bahcecik prospect, northeastern Turkey. *Mineralium Deposita* 35, 689-696.
- Zankl, H. 1962. Magmatismus und Bauplan des Ostpontischen Gebirges im Querprofil des Harşit-Tales, NE Anatolien. *Geologische Rundschau* 51, 218-239.
- Zheng, Y., Sun, X., Gao, S., Wang, C., Zhao, Z., Wu, S., Li, J., Wu, X. 2014. Analysis of stream sediment data for exploring the Zhunuo porphyry Cu deposit, southern Tibet. *Journal of Geochemical Exploration* 143, 19-30.





# Bulletin of the Mineral Research and Exploration

<http://bulletin.mta.gov.tr>



## Evaluation of potential rock falls with three-dimensional analysis: Example of Oltanbey and Hasanbey districts (Gümüşhane city center)

Selçuk ALEMDAĞ<sup>a\*</sup>, Rasim Taylan KARA<sup>b</sup> and Hasan Tahsin BOSTANCI<sup>c</sup>

<sup>a</sup>Gümüşhane University, Faculty of Engineering and Natural Sciences, Department of Geological Engineering, Gümüşhane, Türkiye

<sup>b</sup>General Directorate of Mineral Research and Exploration, Gümüşhane and Its Surroundings Metallic Mineral Explorations Camp, Gümüşhane, Türkiye

<sup>c</sup>Gümüşhane University, Faculty of Engineering and Natural Sciences, Department of Geomatics Engineering, Gümüşhane, Türkiye

Research Article

### Keywords:

Steel Barrier, Rockfall Inventory Map, Rocpro3D, Three Dimensional Rockfall Analysis.

### ABSTRACT

The central district campus of Gümüşhane, located on the Trabzon-Erzurum Highway, has a steep topography, and because of the effect of climatic and morphological structure, frequent rockfall events can cause loss of life and property from time to time. For these reasons, the slopes in some parts of the Oltanbey and Hasanbey districts of the central district of Gümüşhane, which pose a great threat in terms of rockfall potential, were chosen as the study area. In this study, three-dimensional rockfall analyzes were carried out using the RocPro3D program on the lines determined in the rockfall source zones with a high probability of rockfall. As a result of the analysis, it was determined that the rock blocks rolled from the O1, O2 and H1 source rock lines determined at the upper elevations of the study area threaten the settlements and road networks in Oltanbey and Hasanbey districts. With the 3D rockfall analysis, steel barrier was applied as a precautionary structure in the areas determined to be under the risk of rockfall, and the analyzes were carried out again considering the precautionary structures. By examining the results of the analyzes, the safest and most economical different barrier types have been proposed to eliminate the danger of rockfall.

Received Date: 05.05.2021

Accepted Date: 01.08.2021

## 1. Introduction

Due to its geological and geomorphological features, our country has many rockfall events, especially in the Black Sea Region. Gümüşhane city center (Figure 1), located on the Trabzon-Erzurum Highway in the Eastern Black Sea Region and located in the southern zone of the Eastern Pontide belt, is one of the places where rockfall events occur frequently.

In this study, rock masses on free, suspended or high steep slopes that threaten some parts of Oltanbey and Hasanbey districts in the central district of

Gümüşhane were examined and a rockfall inventory map was created according to the locations of the fallen blocks. Three-dimensional rockfall analyses were carried out using RocPro3D (2014) computer program in areas with high rockfall probability considering the identified source rock areas, suspended discontinuity-controlled rock masses and rockfall inventory map. According to the data obtained; rolling trajectories of rock blocks, optimum steel barrier design was made considering the maximum span distances and kinetic energies of the rolling blocks, and barrier types were determined, and precautionary structures

Citation Info: Alemdağ, S., Kara, R. T., Bostancı, H. T. 2022. Evaluation of potential rock falls with three-dimensional analysis: example of Oltanbey and Hasanbey districts (Gümüşhane city center). Bulletin of the Mineral Research and Exploration 169, 87-104. <https://doi.org/10.19111/bulletinofmre.977928>

\*Corresponding author: Selçuk ALEMDAĞ, [selcukalemdag@gmail.com](mailto:selcukalemdag@gmail.com)

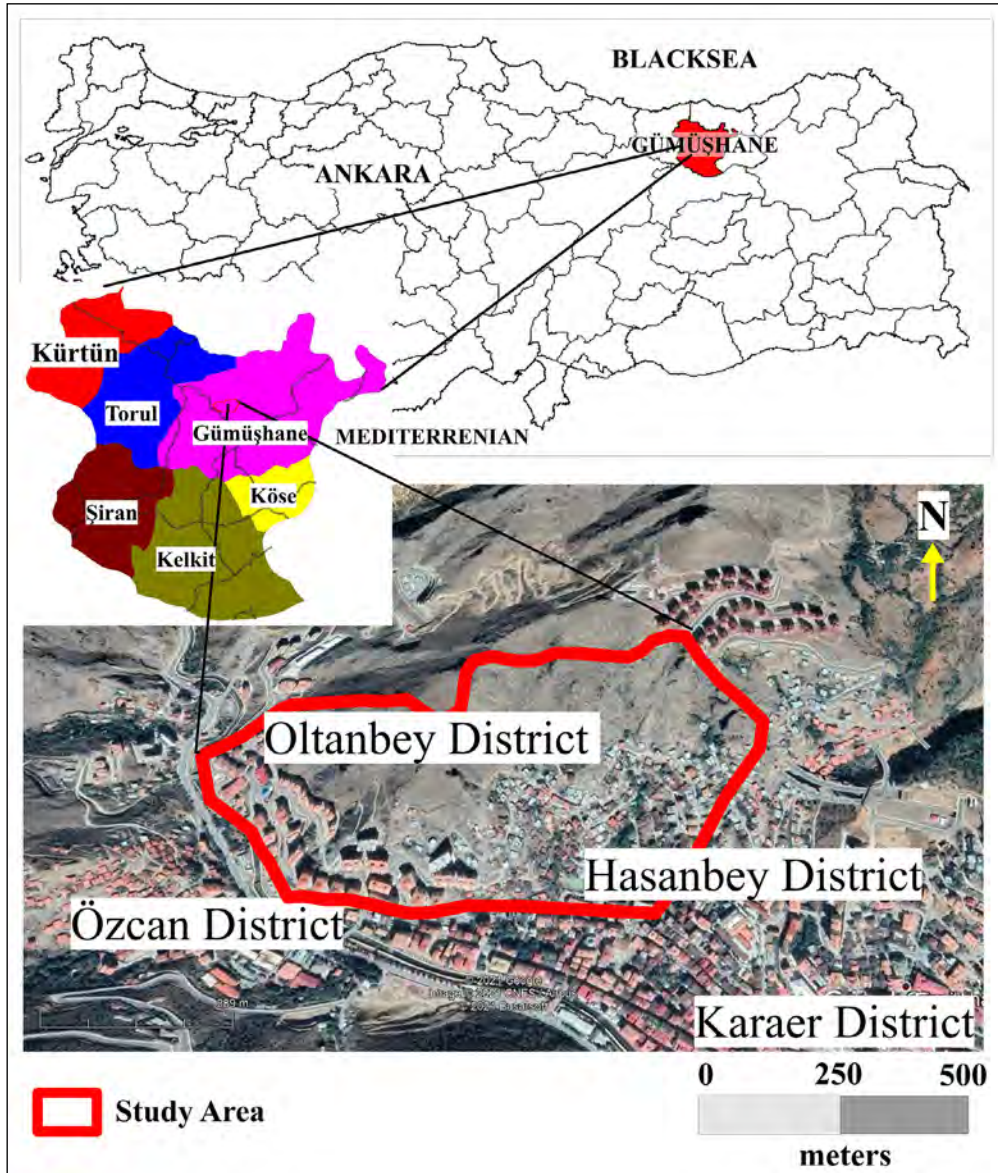


Figure 1- Location map of the study area.

were proposed considering the European Technical Approved Guide for Rockfall Prevention Kits (ETAG 27).

Many rockfall cases have been encountered in the study area so far. Although there have been loss of life and property due to rockfalls in Gümüşhane city center in the past, rockfall inventory map of Oltanbey and Hasanbey districts in Gümüşhane city center has been produced for the first time in this study, and three-dimensional rockfall analysis have been made and precautionary structures in potentially dangerous areas have been proposed.

In the region, which includes the study area, many engineering geology-based studies have been carried out so far (Tüdeş, 2001; Alemdağ vd., 2011; Tüdeş vd., 2012; Alemdağ vd., 2014; Gürocak vd., 2017).

Tüdeş (2001), in his PhD thesis study in the city center of Gümüşhane, examined the engineering properties of the rocks spreading in the settlement area. The researcher transferred parameters such as classification of rock masses, excavability, bearing capacity, seismicity of residential areas, flood assessments to the Geographical Information Systems (GIS) environment. He prepared the relevant maps in

the GIS environment and evaluated the suitability of the study area for settlement.

Alemdağ et al. (2011), the excavability properties of the Late Carboniferous aged Gümüşhane Granitoid cropping out in Gümüşhane, and its vicinity were examined and classified in terms of excavability. According to the classifications made, it was determined that moderately weathered rock masses were removable, while highly weathered rock masses were excavated. In the excavations carried out in the study areas, it was determined that moderately weathered rock masses were removed using a hydraulic breaker, while highly weathered rock masses were excavated using a shovel.

Tüdeş et al. (2012), in their study in Gümüşhane city center, are considering the engineering characteristics of the rock masses outcropping in the study area and the seismicity and flooding conditions at the regional scale, they prepared a suitability map for the city center to assist the planners in site selection and the decisions to be taken regarding land use and emphasized the importance of creating a database.

Alemdağ et al. (2014) produced a solution by using different failure methods for the formation mechanism and rehabilitation of the landslide that occurred in the Gümüşhane Granitoid located in the Mordut region of Gümüşhane city center.

Gürocak et al. (2017), to determine the possible instability mechanism due to discontinuities in the rock mass in the area where the Gümüşhane Granitoid Complex spans, by kinematic analysis method and for the subsequent instability models, the creation of GIS-based maps in ArcGIS program and by using fuzzy interpretation method, the final instability map for the study area was produced.

Three-dimensional studies on rockfall analysis have started to increase in the last ten years in the literature, and some of these studies are summarized below.

Tonini and Abellán (2014), in the study titled the use of three-dimensional (3D) point clouds in geological hazards, obtained digital elevation models with point cloud data and evaluated the importance

of these high-resolution data for the detection of geological hazards. In Lato and Vöge (2012), by using automatic mapping of rock discontinuities in 3D lidar and photogrammetry models, fracture and fracture systems of rocks and their mapping were provided. Topal et al. (2012), in their study, determined the spreading areas of the rocks that are likely to fall by performing two-dimensional (2D) RocFall analysis to determine the rockfall risk areas on the 17 profile lines selected around Kastamonu Castle (Türkiye). In Keskin (2013), the kinetic energy of the falling rocks, the distance they can travel, the jump height and speed were determined by modelling the cross-section lines created in the areas that are ruptured and in danger of rupture in the steep cliffs in the Boğaziçi (Erzincan, Türkiye) region, by modelling in the RocFall computer program. In Sarro et al. (2014), in the Son Poc rockfall (Mallorca, Spain) study, the geometry and parameters of the blocks in the existing rockfall area were revealed, all coefficients were calculated by back analysis method, and the areas at risk as a result of new rockfall events that may occur with 3D simulation were revealed. In Riquelme et al. (2015), by using 3D data, characterization of rock slopes with slope mass grading was revealed by numerical data of point clouds. In Yakar et al. (2015), they created three-dimensional, digital terrain model, orthophoto and vector maps of rockfall regions with Unmanned Aerial Vehicle (UAV) photogrammetry. As a result of the study, they have seen that high accuracy and precision data can be obtained with UAVs, they can be used for imaging hard-to-reach areas and measurements can be made in a short time. Therefore, they say that UAVs can be used in rockfall events and will play an active role in producing the necessary data for modelling the terrain. Wang et al. (2017), for automatic exposure fracture extraction from a 3D point cloud, developed different algorithms in the light of the data obtained from the lidar images and determined the areas of rockfalls that occurred or could occur. In Akın et al. (2019), in the study of evaluating the rock holding trench performance with 3D rockfall analysis; for the digital surface model, point cloud data obtained from photogrammetric images taken with an unmanned aerial vehicle created and 3D rockfall analysis were performed in RocPro3D software. It has been revealed that in general, the falling blocks were held by the trench excavated between the source zone

and the settlement, but in some parts these blocks could continue to roll past the rock holding trench. Şener (2019), according to the results of GIS-based 3D modelling of possible rockfalls using unmanned aerial vehicles around Kasımlar Village (Isparta), determined the maximum kinetic energy, maximum jump height and maximum fall speeds in possible rockfalls and prepared the base data for the design of engineering structures to prevent possible rockfalls or to minimize their effects. In Alptekin and Yakar (2020), in their study of obtaining the 3D point cloud of rock blocks using terrestrial laser scanner, laser scanning of the rock falling from a rough terrain and threatening a house was performed to obtain the 3D model in high resolution and showed that these data can be used in 3D rockfall simulations.

## 2. Geology of the Study Area

The Alibaba Formation (Figure 2), which spreads in the city center of Gümüşhane (Hasanbey, Oltanbey and Özcan Districts), starts with a thin basal conglomerate and nummulitic sandy limestones and has the characteristics of a volcano sedimentary succession that continues with andesitic-basaltic pyroclastics (Tokel, 1972). Macroscopically, basic, and intermediate volcanic rocks are gray-green in color and occasionally porphyritic, with fractures and cracks, and intense silicification, argillization,

pyritization and current alterations are observed along the fractures. Alibaba Formation overlies the Kermutdere Formation with an angular unconformity (Kaygusuz and Şen, 2011). Over these, bedded tuffs alternate with andesitic breccias. Andesite, basalt and pyroclastics, which are the subject of the study, are generally observed at the upper levels in the field (Figure 3). Considering the fossil determination of the samples taken from the clastics in the formation, the age of the unit was determined as Ypresian and Lutetian (Aydoğan, 2014). The apparent thickness of the formation is approximately 400 m, and it was deposited in shallow marine and terrestrial environments, accompanied by intense volcanic activity.

## 3. Digital Terrain Models

Topography and vegetation have a significant influence on the orientation of rockfall lines and the rolling distance of falling blocks. The main advantage of 3D analysis over 2D analysis is that the possible rolling of the falling rock blocks is determined on the digital terrain model, not on a topographic section. This feature is very useful in determining which route a block to be rolled from the source rock area can actually follow and in determining the areas where improvement methods will be applied.

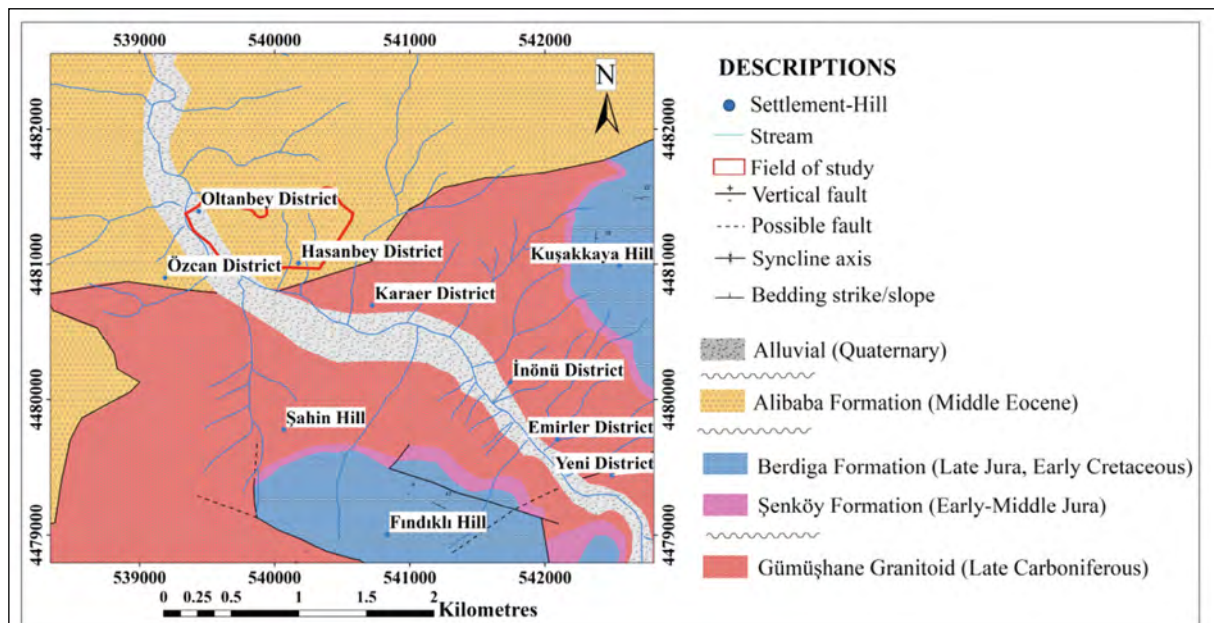


Figure 2- Geological map of the study area (modified from Kandemir, 2004).



Figure 3- a, b) Oltanbey District. Aydınlık Houses Sites Road andesites belonging to the Alibaba Formation in the field (view direction from north to south; c) Oltanbey District. Aydınlık Houses Sites and Afet Houses Sites andesites belonging to the Alibaba Formation in the field (view direction from west to east); d) Oltanbey District. Field view of andesites belonging to Alibaba Formation from Aydınlık Houses, Museum Houses Sites (view direction from south to north).

In the digital terrain model of the study area, vegetation, buildings, etc. to show small topographic changes with details and to determine healthier rolling routes, data to be obtained from medium-sized maps such as 1/25000 scale topographic maps and digital elevation models are extremely inadequate. In this study, high resolution orthophoto images and a high resolution (0.18 x 0.18 m) digital elevation model (DEM) produced from the point cloud (594.000 points) obtained in this context were used (Figure 4). The slope map (Figure 5) produced on the DEM was used to determine the source rock areas in 3D rockfall analysis, and the relief map (Figure 6) was used to visualize the areas threatened by the rolling trajectories determined in the RocPro3D program and all rasters are produced in the Turef TM39-Gauss-Krüger (ITRF 96/GRS 80) projection system.

#### 4. Rockfall Analysis

To analyse the potential rockfall areas in the Oltanbey and Hasanbey districts, which are the subject of the study area, the source rock areas should be determined. The source rock areas where rockfall can occur were determined (on the slope map) based on equation 1, which considers the resolution of the digital terrain model.

$$a = 55 \times \text{RES}^{-0.075} \quad (1)$$

The value (a) in the equation is the boundary slope value in degrees and RES is the resolution “in meters” of the digital elevation model. Considering these parameters, a value was found to be 62°. However, to stay in a safer area in terms of rockfall hazard, areas with a slope of more than 60° were accepted as the source rock area and the slope map was reclassified

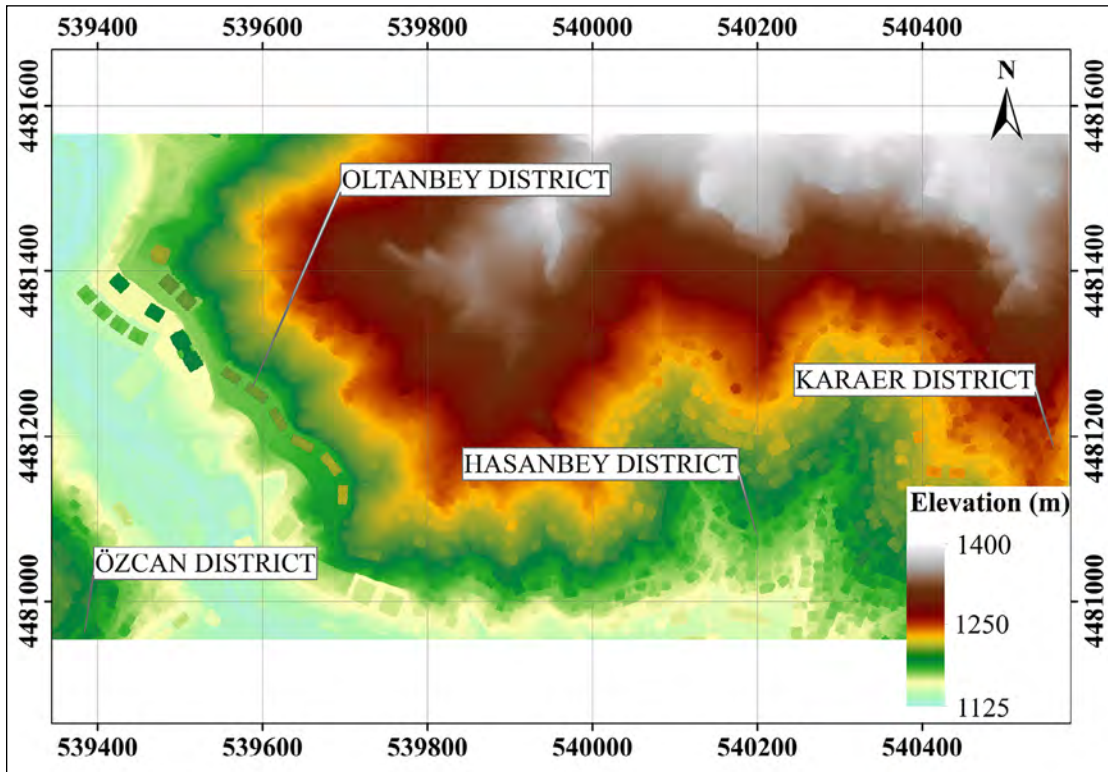


Figure 4- Digital elevation model of the study area.

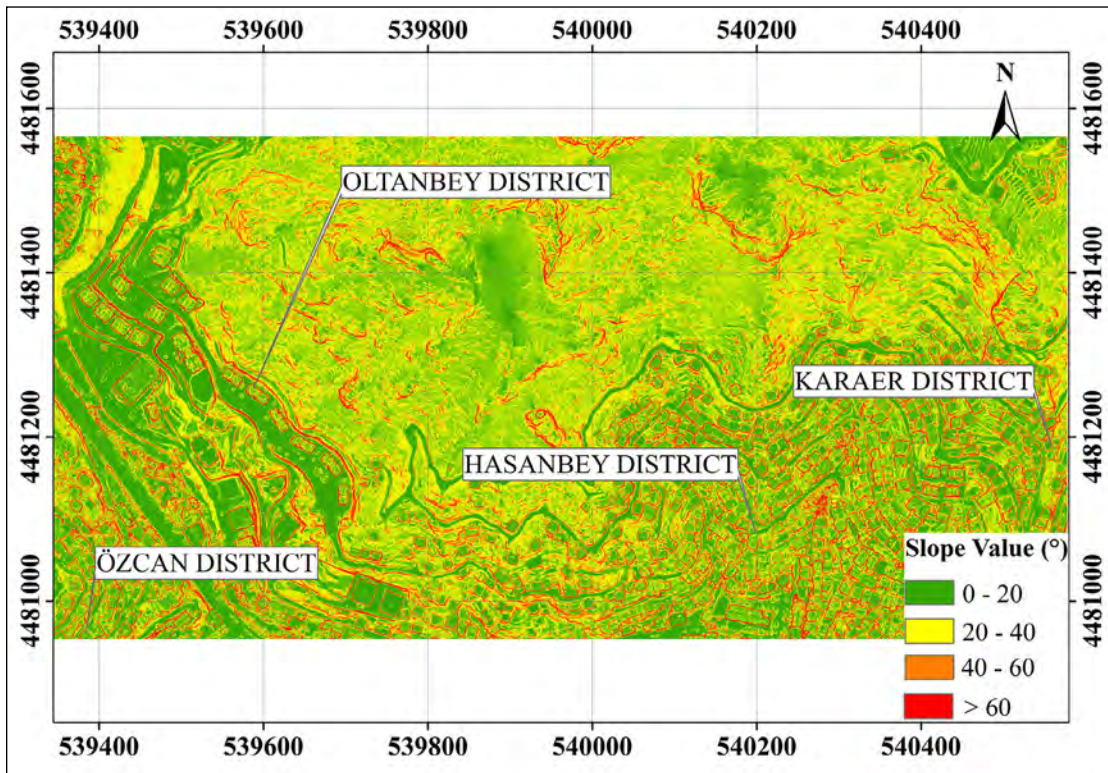


Figure 5- Slope map of the study area.

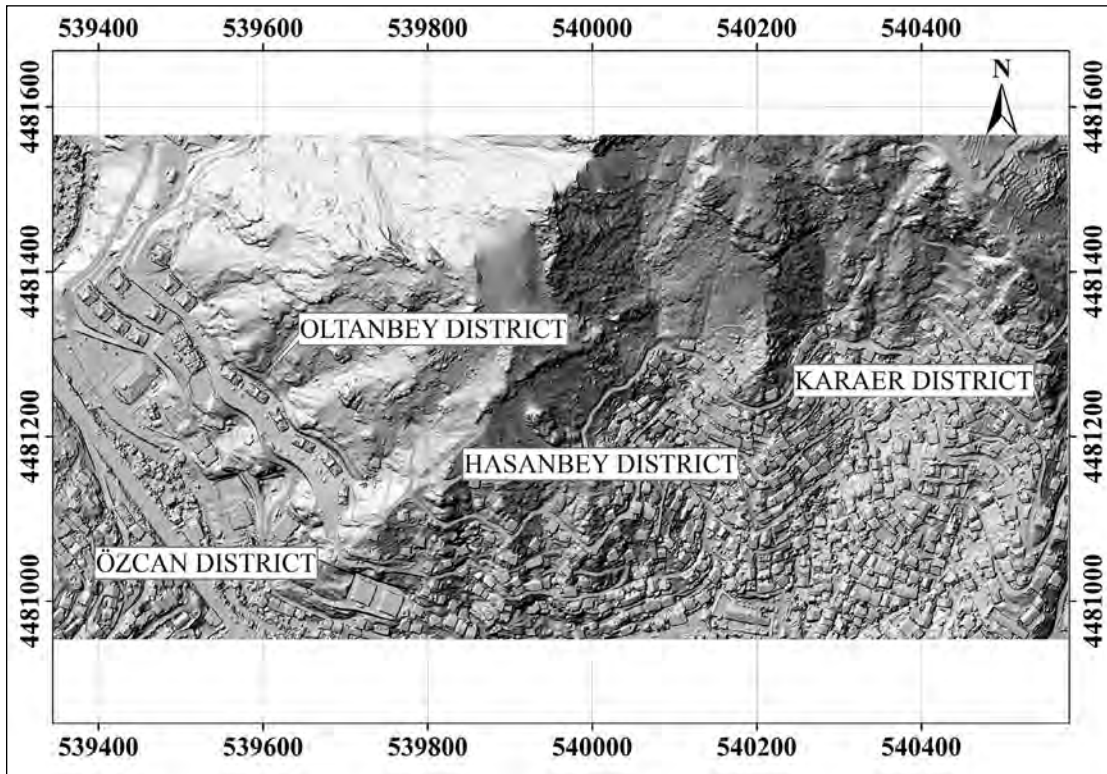


Figure 6- Relief map of the study area.

and a map showing the source rock areas was produced by transferring the borders onto the orthophoto.

By using 50 years of Disaster and Emergency (AFAD) data of the study area, orthophoto image and digital elevation model, suspended rock blocks in the active source rock areas and fallen rock blocks at lower elevations were determined and marked on the orthophoto by being detected in situ (Figure 7). In addition, rockfall events obtained through written and visual media were investigated and recorded from the past to the present, and a rockfall inventory map was obtained by processing on digital maps (Figure 8, URL-2, 2015; URL-6, 2016; URL-3, 2019; URL-5, 2019; URL-4, 2020; URL-1, 2020).

In order to model possible rockfalls in three dimensions in the study area, the locations, shapes and dimensions of the blocks were determined by considering the areas determined in the inventory map and the suspended blocks determined by field observations as well as the fallen blocks (Table 1).

Normal Return ( $R_n$ ) and Tangential Return ( $R_t$ ) parameters were obtained by trying different parameter

data input variations and simulations by back analysis method for 10 fallen blocks whose coordinates were determined by selecting on the rockfall inventory map (Figure 9). In the light of back analysis and field observations in the study area, the most suitable parameters for the study area were determined by taking the average of the values obtained from 10 andesite blocks.

The parameters to be used in the analysis of possible blocks to fall in the Alibaba Formation were determined by retrospective analysis and by using the parameter bases of the RocPro3D program using 10 block samples that had previously fallen in the field and are given in Table 2. The parameters used in Table 2 belong to the probabilistic method selected in 3D rockfall analysis, and it is the preferred method for areas where variables such as lithological, slope, and roughness conditions differ in the rolling trajectory of the rock. Based on the assumption that the values assigned to the parameters used here can change during the analysis, the software defines the range in which these values can change, and the first value assigned is changed in line with the probabilistic



Figure 7- a) Oltanbey District Museum Houses Site. Andesite blocks that have broken off from the source rock areas (view direction from southeast to northwest), b) Oltanbey District Museum Houses Site. The building hit by the andesite block from the source rock areas (view direction from north to south), c) Oltanbey District Museum Houses Site. The building hit by the andesite block from the source rock areas (view direction from west to east).

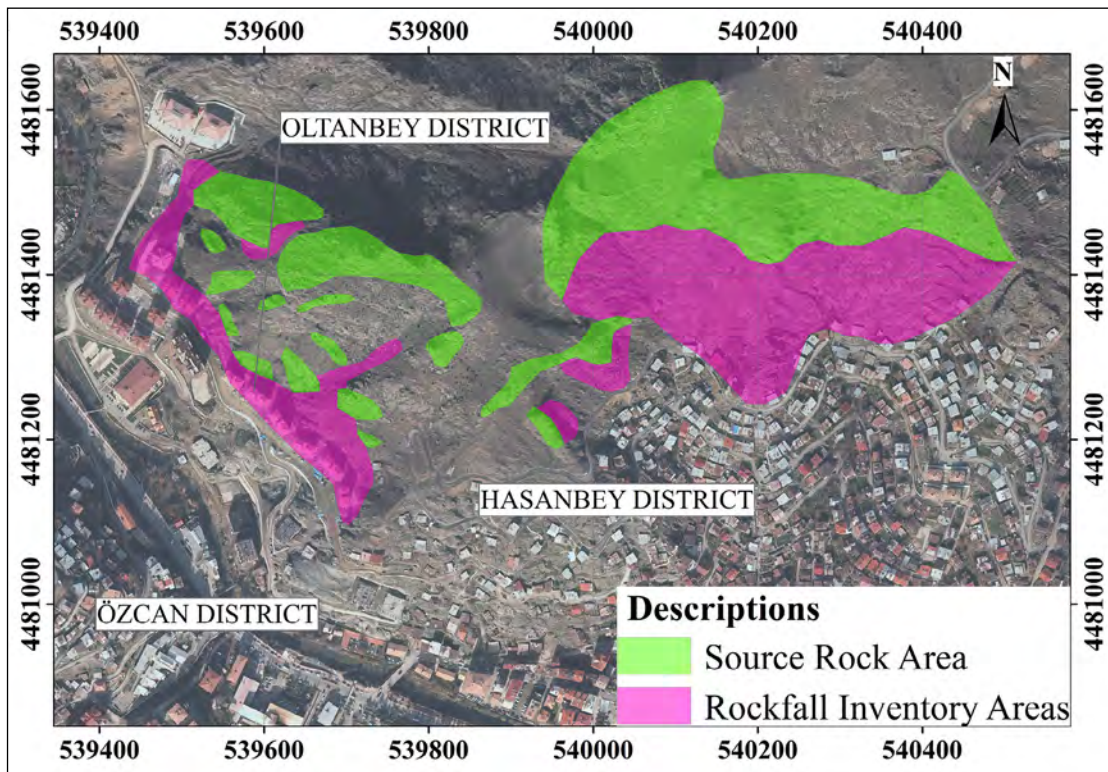


Figure 8- Source rock and rockfall inventory map determined in the study area.

Table 1- Shape and dimensions of fallen rock blocks.

Lithology	Andesite					
Sample	Falling Block Dimensions			Block Volume (m <sup>3</sup> )	Block Shape	Density (kg/m <sup>3</sup> )
	x (m)	y (m)	z (m)			
1	1.65	1.15	1.2	2.28	Quadrangular	2570
2	2.10	1.75	1.3	4.78	Quadrangular	2570
3	0.75	0.95	0.45	0.32	Quadrangular	2570
4	1.15	1.87	1.22	2.62	Quadrangular	2570
5	2.25	1.98	1.55	6.91	Quadrangular	2570

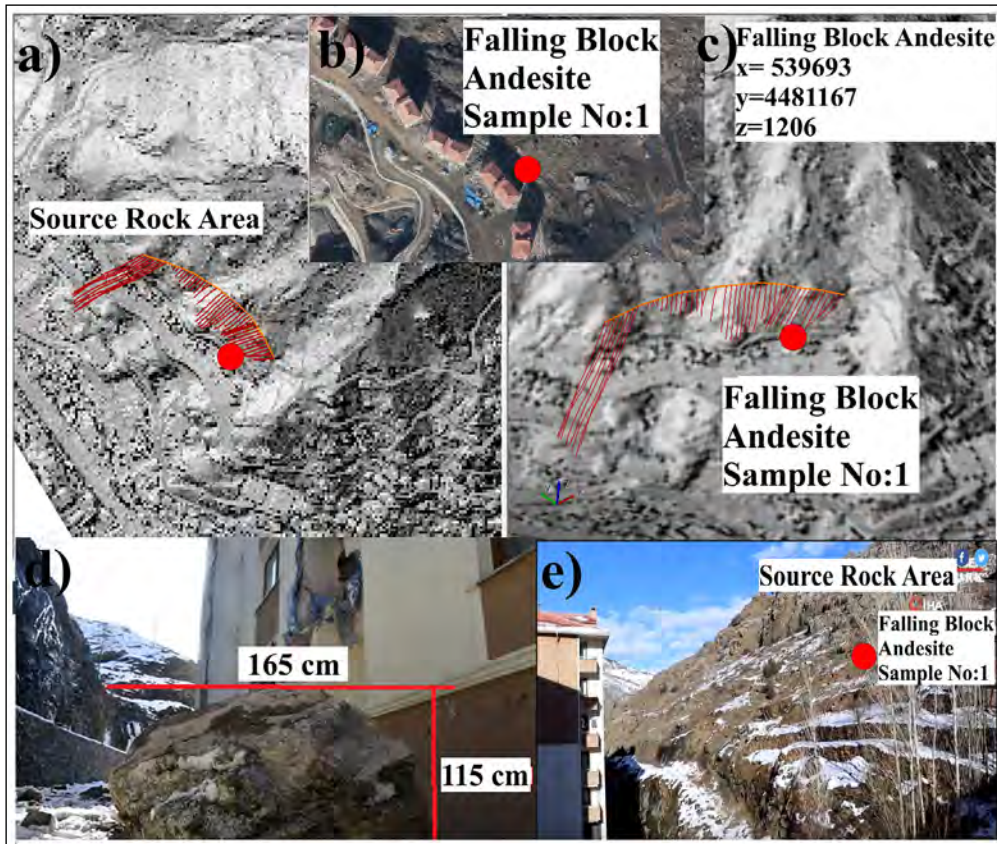


Figure 9- a) Relief map appearance of Source Rock Fields, b) orthophoto image of the fallen andesite block, c) the fallen block appears on the relief map, d) Oltanbey District. View of the andesite block striking the Museum Houses Site (view direction from west to east), e) Oltanbey District. View of the source rock areas at the upper level of the Museum Houses Site (view direction from east to west).

variables during the analysis, thus ensuring that the uncertainties arising from reasons such as speed, friction and surface heterogeneity are included in the analysis.

In the study area, the joint feature of the rock mass within the source rock areas of the Alibaba Formation and therefore the rapid development of weathering

processes caused block ruptures of different sizes in many areas in the rock mass. 3D rockfall simulation was carried out with 3 (O1, O2, H1) fall line sections created in the study area, especially in areas where the slope is high. Parameters obtained from the analysis made; are the rolling energy, jump heights and span distances of the blocks and are given in the form of graphics (Figure 10-12).

Table 2- Input parameters used in RocPro3D program.

<b>Andesite Rock Mass</b>	Sample No: 1	Sample No:2	Sample No:3	Sample No:4	Sample No:5	Sample No:6	Sample No:7	Sample No:8	Sample No:9	Sample No:10	Average
Rn	0.50	0.51	0.52	0.48	0.49	0.50	0.52	0.50	0.52	0.48	0.50
Rt	0.80	0.81	0.78	0.83	0.79	0.81	0.82	0.78	0.79	0.81	0.80
Variability $\Delta_R$ %	10	10	10	10	10	10	10	10	10	10	10
Limit Speed $V_R$ (lim) [m/s]	10	10	10	10	10	10	10	10	10	10	10
Limit Variable $\Delta_R$ (lim) %	2.1	1.9	2.0	2.0	2.0	2.0	2.0	2.0	2.0	2.0	2.0
<b>Lateral Deviation</b>											
Variability $\Delta_{Qh}$ (°)	20	20	20	20	20	20	20	20	20	20	20
Limit Speed $V_{Qh}$ (lim) [m/s]	10	10	10	10	10	10	10	10	10	10	10
Limit Variable $\Delta_{Qh}$ (lim) (°)	10	10	10	10	10	10	10	10	10	10	10
<b>Bounce Back</b>											
Variability $\Delta_{Qv}$ (°)	2.0	2.0	2.0	2.0	2.0	2.0	2.0	2.0	2.0	2.0	2.0
Limit Speed $V_{Qv}$ (lim) [m/s]	10	10	10	10	10	10	10	10	10	10	10
Limit Variable $\Delta_v$ (lim) (°)	4	4	4	4	4	4	4	4	4	4	4
<b>Coefficient of Friction</b>											
k value	0.40	0.40	0.40	0.40	0.40	0.40	0.40	0.40	0.40	0.40	0.40
Variability $\Delta_k$ (%)	10	10	10	10	10	10	10	10	10	10	10
Limit Speed $V_k$ (lim) [m/s]	10	10	10	10	10	10	10	10	10	10	10
Limit Variable $\Delta_k$ (lim) %	10	10	10	10	10	10	10	10	10	10	10
<b>Transition Parameters</b>											
Angle $\beta_{lim}$ (sudden event) (°)	2	2	2	2	2	2	2	2	2	2	2
Angle $\beta_{lim}$ (inclined position) (°)	25	25	25	25	25	25	25	25	25	25	25

#### 4.1. Source Rock Line No. O1

50 fallible rock blocks were identified for the O1 line selected in the source rock area with a high probability of rockfall from the upper elevations of Oltanbey District. As a result of the 3D analysis performed on 50 rock blocks on the O1 line, the blocks where andesite blocks move along the drainage networks show a maximum spread of around 148 m, the jump height is at most 7.5 m (Figure 10), and the highest kinetic energy generated by the rolling blocks. It was determined to be 1062 kJ. Andesite blocks approaching the settlements for the O1 line pose a high danger to the existing structures and the falling blocks spread into the settlements located at the lower levels and directly threaten the residences.

#### 4.2. Source Rock Line No. O2

50 fallible rock blocks were defined for the O2 line selected in the source rock area with a high probability

of rockfall from the upper elevations of the Oltanbey district. As a result of the 3D analysis performed on 50 rock blocks on the O2 line, it was determined that the andesite blocks moved along the drainage networks, the blocks spread out around 198 m at the most, the jump height was at most 6.5 m, and the largest kinetic energy created by the rolling blocks was 1161 kJ (Figure 11). The andesite blocks approaching the settlements for the O2 line pose a high danger to the existing structures and the falling blocks spread into the settlements located at the lower levels and directly threaten the residences.

#### 4.3. Source Rock Line No. H1

As a result of the 3D analysis performed on 50 rock blocks defined for the H1 line selected in the source rock area with a high probability of rockfall from the upper elevations of Hasanbey neighbourhood, the andesite blocks move along the drainage networks,

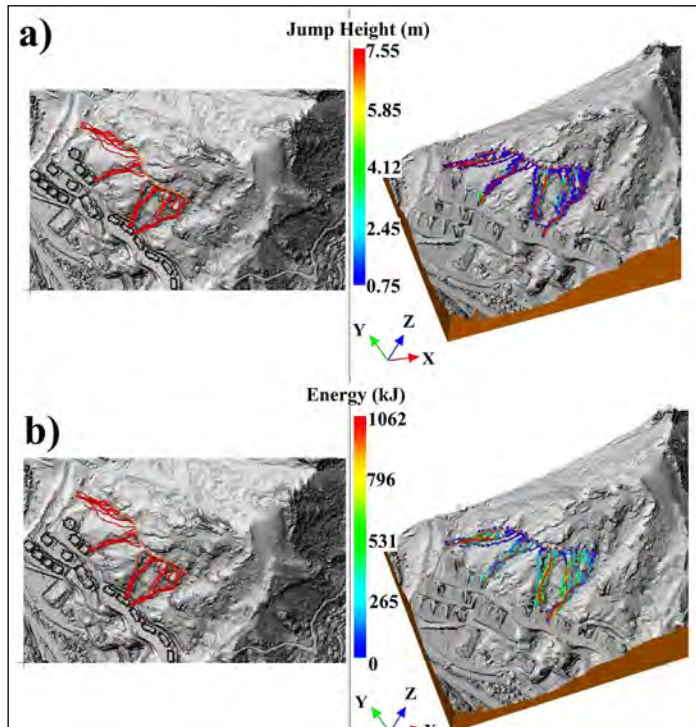


Figure 10- a) 2D, 3D maps showing the jump height and spreading route of 50 rock blocks rolled from the O1 source rock area, and b) 2D, 3D maps showing the energy and propagation route of 50 rock blocks rolled from the O1 source rock area.

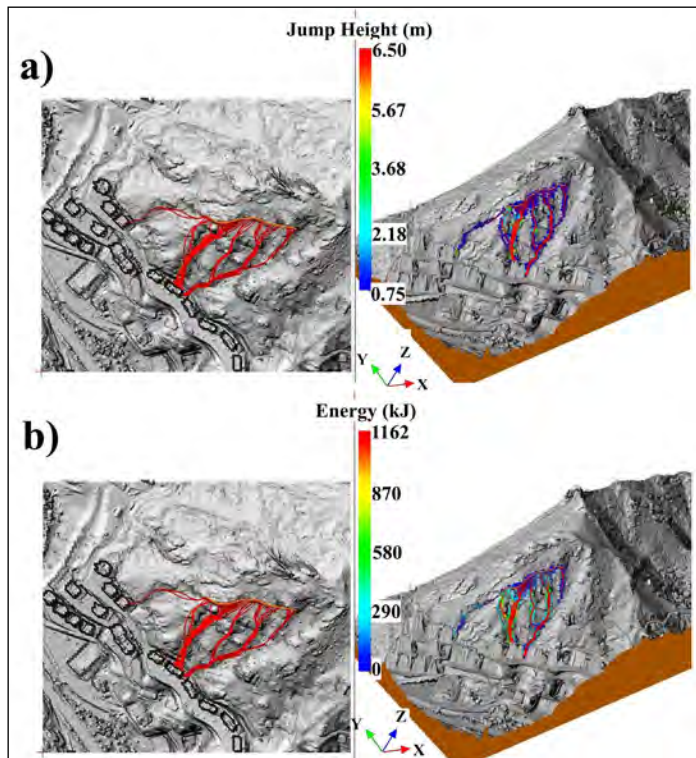


Figure 11- a) 2D, 3D maps showing the jump height and spreading route of 50 rock blocks rolled from the O2 source rock area, and b) 2D, 3D maps showing the energy and propagation route of 50 rock blocks rolled from the O2 source rock area.

the blocks spread around 176 m at most, the jump height is at most 5.35 m, and the largest kinetic energy formed by the rolling blocks was determined to be 999 kJ (Figure 12). Andesite blocks approaching the settlements for the H1 line also pose a high danger to the existing structures and threaten the residences.

### 5. Precautionary Structure Applied in Rockfall Areas

In the literature, many improvement methods (steel barrier, earth concrete embankment, combined net, trench, etc.) are applied to prevent rock blocks with high rolling probability that threaten residential areas and road routes. In this study, it was thought that the steel barrier application would be more accurate and practical due to the steep and high slope of the study area, the area to be treated consists of several source rock areas and the lack of a road network to which the construction machinery can access the improvement

area. For this reason, by determining the appropriate areas in the topography where barrier application can be made, because of the rockfall analysis made, the barrier types were determined in ETAG 27 (Maximum Energy) standards by choosing meters with the lowest bounce height and energies of the tumbling blocks and at which they are damped (Figure 13).

As a result of the rockfall analyses made on the O1, O2, H1 lines in the three source rock areas determined in the Alibaba Formation, the routes followed by the blocks falling from the O1, O2, H1 lines in the areas affecting the settlement and road networks were considered. In the selection of the barrier type and location, the locations determined by considering the topographic slopes of the spreading rolling profiles, optimum kinetic energy and jump height parameters were checked in the field and the most suitable location was determined.

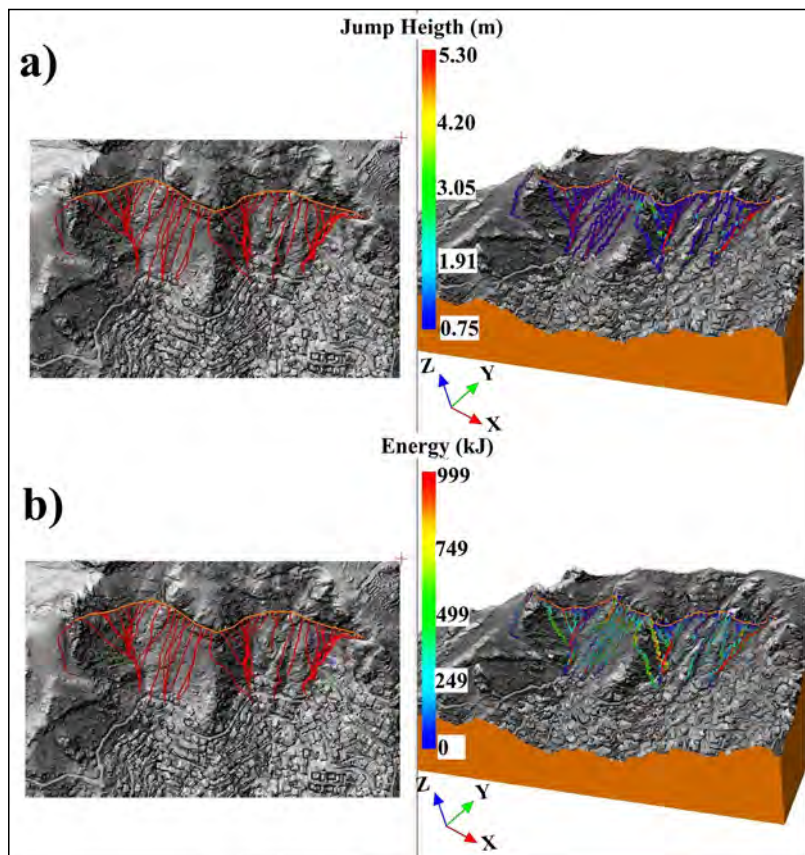


Figure 12- a) 2D, 3D maps showing the jump height and spreading route of 50 rock blocks rolled from the source rock area H1, and b) 2D, 3D maps showing the energy and propagation route of 50 rock blocks rolled from the source rock area H1.

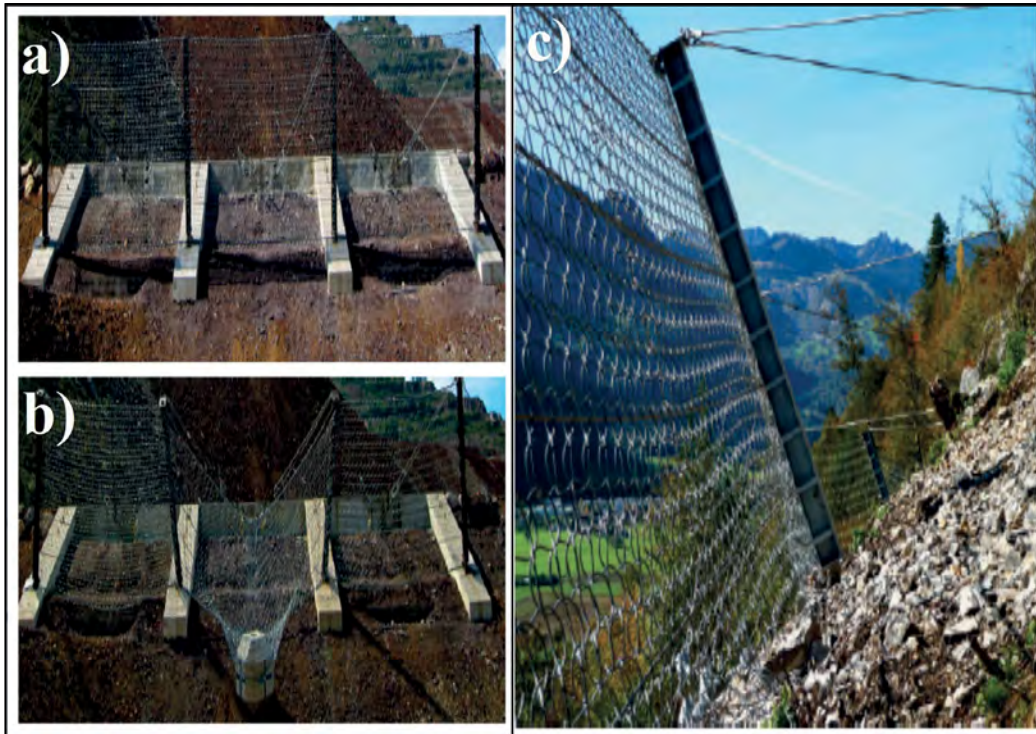


Figure 13- a) Steel barrier application example in ETAG 27 (ME) Standards (Trumer Rockfall), b) steel barrier example of preventing falling rock block in ETAG 27 (ME) standards (Trumer Rockfall), and c) steel barrier example in ETAG 27 (ME) standards (Trumer Rockfall).

### 5.1. Barrier Analysis for Blocks Falling from the O1 Source Rock Area

It was determined by the rockfall analysis that the blocks falling from the O1 source rock area threatened the settlement and road networks in the Oltanbey District. From the analysis results obtained, considering the bounce height and energy along the rolling line of the blocks, steel barrier types produced in ETAG standards; by applying the 2 m high and 500 kJ capacity class 2 barrier type in ETAG 27 (ME) standards, it was reanalysed, and it was observed that the rolling blocks were damped (Figure 14). The barrier line O1, which was applied in 3 different areas and with a total length of 238 m in sections, approximately 40 m below the source rock area in the study area, was applied to the area where the energies and jump height of the blocks falling from the source rock area were most appropriate (Figure 14). The jump height and energy graphs obtained from this analysis show that the selected barrier type is suitable and reliable for the precautionary structure.

### 5.2. Barrier Analysis for Blocks Falling from the O2 Source Rock Area

It was determined by the rockfall analysis that the blocks falling from the O2 source rock area threatened the settlement and road networks in Oltanbey District. In the light of the data obtained from the analysis results, considering the bounce height and energy along the rolling line of the blocks, from the steel barrier types produced in ETAG standards; with the application of the 3rd class barrier type with a height of 2 m and a capacity of 1000 kJ in ETAG 27 (ME) standards, it was reanalysed, and it was observed that the rolling blocks were damped (Figure 15).

The barrier line, which was applied in one piece and with a total length of 110 m, approximately 115 m below the source rock area in the study area, was applied to the area where the energies and jump height of the blocks falling from the O2 source rock area were most appropriate (Figure 15). The jump height and energy graphs obtained from this analysis show that the selected barrier type is suitable and reliable for the precautionary structure.

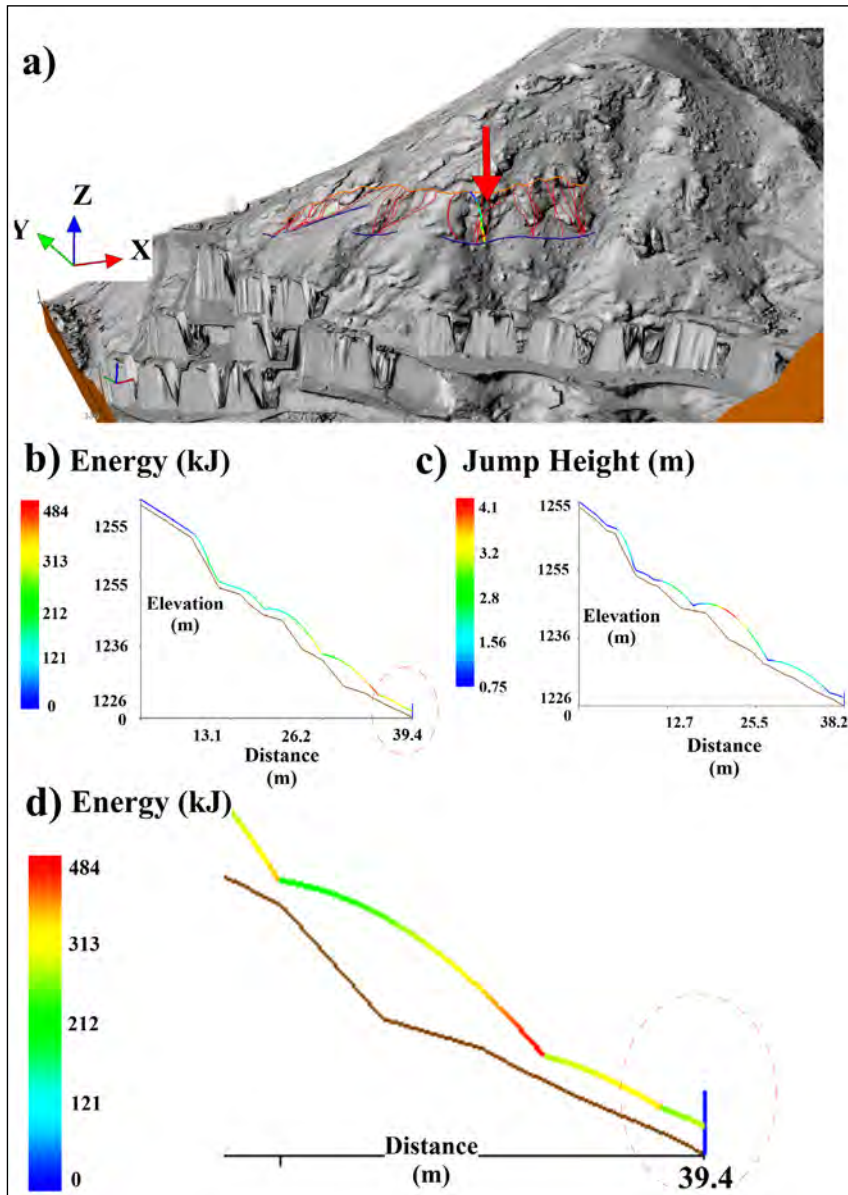


Figure 14- a) Steel barrier location and 3D rolling trajectories image at O1 rockfall line, b) barrier application energy graph on a single trajectory, c) barrier application jump height on a single trajectory, and d) close-up view of applying ETAG 27(ME) barrier to a single orbit.

### 5.3. Barrier Analysis for Blocks Falling from the H1 Source Rock Area

It was determined by the rockfall analysis that the blocks falling from the H1 source rock area threatened the settlement and road networks in Hasanbey District. From the results of the analysis, considering the bounce height and energy along the rolling line of the blocks, steel barrier types produced in ETAG standards; With the application of the 3rd class barrier type with a height of 2 m and a capacity of 500 kJ

in ETAG 27 (ME) standards, it was reanalysed, and it was observed that the rolling blocks were damped (Figure 16).

The barrier line, which was applied approximately 120 m below the source rock area in the study area, in four parts and with a total length of 300 m, was applied to the area where the energies and jump height of the blocks falling from the H1 source rock area were most appropriate (Figure 16).

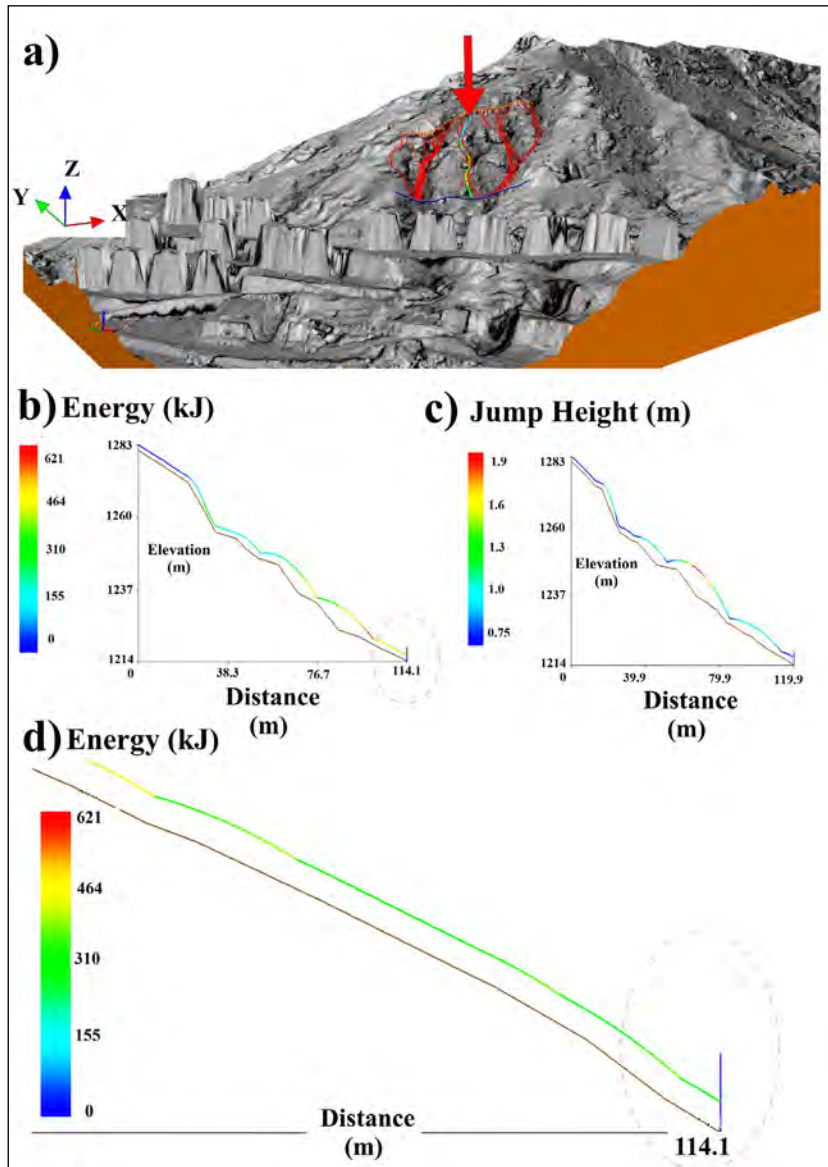


Figure 15- a) Steel barrier location and 3D rolling trajectories image at O2 rockfall line, b) barrier application energy graph on a single trajectory, c) barrier application jump height on a single trajectory, and d) close-up view of applying ETAG 27(ME) barrier to a single orbit.

The jump height and energy graphs obtained from this analysis show that the selected barrier type is suitable and reliable for the precautionary structure.

## 6. Results

In this study, the source rock areas on the high steep slopes that threaten some parts of the Oltanbey and Hasanbey districts of the central district of Gümüşhane province, along with the fallen and suspended blocks, were determined and a rockfall inventory map was

created by considering the locations of the fallen blocks. Rockfall analysis were made using the RocPro3D program on the lines determined in the source rock areas with a high probability of rockfall, and the following results were obtained.

The blocks falling from the source rock areas in the study area consist of andesite rock masses belonging to the Alibaba Formation.

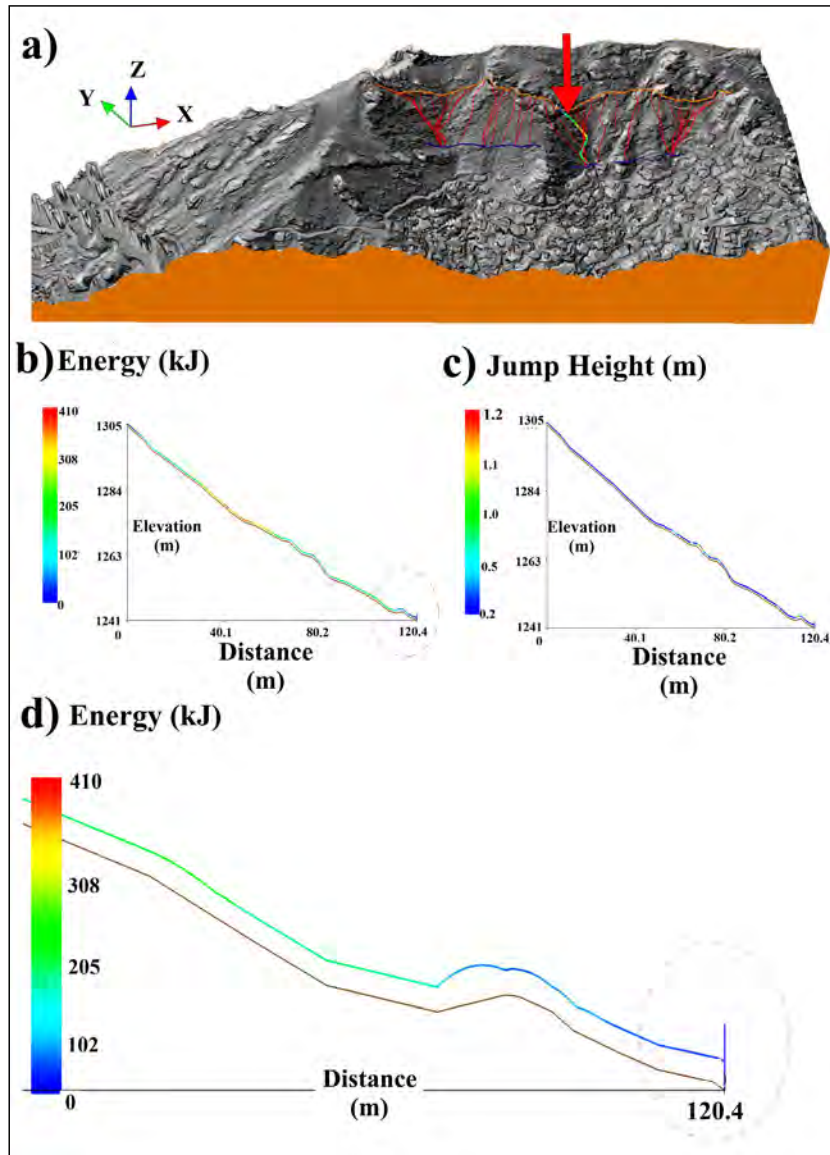


Figure 16- a) Steel barrier location and 3D rolling trajectories view at the H1 numbered rockfall line, b) barrier application energy graph on a single trajectory, c) barrier application jump height on a single trajectory, and d) close-up view of applying ETAG 27(ME) barrier to a single orbit.

In the creation of the digital terrain model of the study area, vegetation, buildings, etc. high resolution orthophoto images, digital elevation model, slope map and relief maps were used in order not to overlook the details and topographic details and to determine healthier rolling routes. All generated digital maps were produced on the Turef TM39-Gauss-Krüger (ITRF 96/GRS 80) projection system.

Based on the findings obtained from the examination of orthophoto images, the source rock areas where potential rockfall can occur for the study

area were determined as areas with a slope of  $60^\circ$  and higher, and areas with a slope of  $60^\circ$  or more on the orthophoto were limited and a map showing the source rock areas was produced.

As a result of the field studies, the locations and geometries of the fallen rock blocks were determined in the field and a rockfall inventory map was created by comparing them with the digital terrain model and orthophoto image produced previously for the study area.

It was determined that the rock blocks rolled from the O1 source rock area showed a maximum spread of 148 m, the jump height was at most 7.5 m, and the maximum kinetic energy of the rolling blocks was 1062 kJ. It has been determined that the andesite blocks rolling from the source rock area pose a high danger for the Oltanbey District at the lower elevations and the secondary road networks providing access to the district, and the falling blocks have spread into the settlements at the lower elevations. As a result of the improvement analysis, the rockfall cross-section lines were re-analysed, and it was observed that the rolling blocks were damped by applying a 2 m high and 500 kJ capacity 2nd class steel barrier in ETAG 27 (ME) standards as the barrier type.

It has been determined that the rock blocks rolled from the O2 source rock area move along the drainage networks and the blocks have a maximum spread of 198 m, the jump height is up to 6.5 m and the greatest kinetic energy created by the rolling blocks is 1161 kJ. It has been determined that the rolling andesite blocks threaten some sites and road networks in Oltanbey District and sometimes roll into the site. As a result of the improvement analysis, the rockfall cross-section lines were re-analysed, and it was observed that the rolling blocks were damped with the application of a 3rd class steel barrier with a height of 2 m and a capacity of 1000 kJ in ETAG 27 (ME) standards.

It was determined that the rock blocks rolled from the source rock area H1 move along the drainage networks, the rock blocks spread around 176 m at most, the jump height is maximum 5.35 m, and the greatest kinetic energy created by the rolling blocks is 999 kJ. It has been determined that the rolling andesite blocks threaten some sites and road networks in Hasanbey District and spread to the site from time to time. As a result of the improvement analysis, it was determined that the rolling blocks were damped in the re-analysis of the rockfall section lines with the application of a 3rd class steel barrier with a height of 2 m and a capacity of 500 kJ in ETAG 27 (ME) standards.

The rockfall source and inventory areas determined because of this study, the spreading zones of the falling blocks and the improvement results obtained by 3D rockfall analysis which must be considered in

the Gümüşhane province revision and implementation zoning plan changes will minimize and prevent future loss of life and property.

### Acknowledgements

We would like to express our gratitude to the editors and referees for their suggestions and contributions during the review and evaluation phase of the article.

### References

- Akın, M., Dinçer, İ., Orhan, A., Ok, A. Ö., Akın, M. K., Topal, T. 2019. Kaya tutma hendek performansının 3-boyutlu kaya düşme analizleriyle değerlendirilmesi: Akköy (Ürgüp) örneği. *Jeoloji Mühendisliği Dergisi* 43, 211-232.
- Alemdağ, S., Kaya, A., Gürocak, Z., Dağ, S. 2011. Farklı ayrışma derecesine sahip kaya kütlelerinin kazılabilirlik özellikleri: Gümüşhane Granitoyidi örneği. *Jeoloji Mühendisliği Dergisi* 35, 2, 135-152.
- Alemdağ, S., Akgün, A., Kaya, A., Gökçeoğlu, C. 2014. A large and rapid planar failure, causes, mechanism, and consequences (Mordut, Gumushane, Turkey). *Arabian Journal of Geosciences* 7, 3, 1205–1221.
- Aydınçakır, E. 2014. The petrogenesis of Early Eocene non-adakitic 108 volcanism in NE Turkey, Constraints on the geodynamic implications. *Lithos* 208-209, 361-377.
- Alptekin, A., Yakar, M. 2020. Kaya bloklarının 3B nokta bulutunun yersel lazer tarayıcı kullanılarak elde edilmesi. *Türkiye LİDAR Dergisi* 2(1), 01-04.
- Gürocak, Z., Alemdağ, S., Bostancı, H. T., Gökçeoğlu, C. 2017. Discontinuity controlled slope failure zoning for a granitoid complex: A fuzzy approach. *Rock Mechanics and Engineering, Surface and Underground Projects* 5, 1–25.
- Kandemir, R. 2004. Gümüşhane ve yakın yöresindeki erken-orta Jura yaşlı Şenköy Formasyonu'nun çökel özellikleri ve birikim koşulları. Doktora Tezi, Karadeniz Teknik Üniversitesi, Fen Bilimleri Enstitüsü, Trabzon, 272.
- Kaygusuz, A., Şen, C. 2011. Calc-alkaline I-type plutons in the Eastern Pontides, NE Turkey: U-Pb zircon ages, geochemical and Sr-Nd isotopic compositions, *Chemie der Erde* 71, 59-75.
- Keskin, I. 2013. Evaluation of rock falls in an urban area: the case of Boğazici (Erzincan/Turkey). *Environmental Earth Sciences* 70, 1619–1628.

- Lato, M. J., Vöge, M. 2012. Automated mapping of rock discontinuities in 3D lidar and photogrammetry models. *International Journal of Rock Mechanics and Mining Sciences* 54, 150–158.
- Riquelme, A. J., Abellán, A., Tomás, R. 2015. Discontinuity spacing analysis in rock masses using 3D point clouds, *Engineering Geology* 195, 185–195.
- RocPro3D. 2014. RocPro3D software. User's Guide, RocPro3D version 5.
- Sarro, R., Mateos, R. M., Moreno, G., Herrera, G., Reichenbach, P., Laín, L., Paredes, C. 2014. The son poc rockfall (Mallorca, Spain) on the 6th of March 2013. 3D simulation, *Landslides* 11, 493–503.
- Şener, E. 2019. İnsansız hava araçları kullanılarak olası kaya düşmelerinin coğrafi bilgi sistemleri tabanlı 3D modellenmesi: Kasımlar Köyü (Isparta-Türkiye) örneği. *Journal of Natural and Applied Sciences* 23, 2, 419-426.
- Tokel, S. 1972. Stratigraphical and volcanic history of Gümüşhane region (Kuzeydoğu Türkiye). Ph. D. Thesis. University College London.
- Tonini, M., Abellán, A. 2014. Rockfall detection from terrestrial LiDAR point clouds, a clustering approach using R. *Journal of Spatial Information Science* 8, 95-110.
- Topal, T., Akın, M. K., Akın, M. 2012. Rockfall hazard analysis for an historical castle in Kastamonu (Turkey). *Natural Hazards* 62, 255-274.
- Tüdeş, Ş. 2001. Gümüşhane kenti ve yakın çevresinin yerleşime uygunluk açısından araştırılması. Doktora Tezi, KTÜ, Fen Bilimleri Enstitüsü, Trabzon, 203.
- Tüdeş, S., Ceryan, S., Bulut, F. 2012. Geoenvironmental evaluation for planning: an example from Gumushane City, close to the North Anatolia Fault Zone, NE Turkey. *Bulletin of Engineering Geology and the Environment*. 71, 4, 679–690.
- Wang, X., Zou, L., Shen, X., Ren, Y., Qin, Y. 2017. A region-growing approach for automatic outcrop fracture extraction from a three-dimensional point cloud. *Computers and Geosciences* 99, 100–106.
- Yakar, M., Doğan, Y., Çelik, M. Ö., Alptekin, A. 2015. İHA fotoğrametresi ile kaya düşme bölgelerinin 3 boyutlu, sayısal arazi modeli, ortofoto ve vektör haritalarını oluşturulması. 10. Türkiye Ulusal Fotogrametri ve Uzaktan Algılama Birliği Teknik Sempozyumu, Aksaray.
- URL-1. 2020. [www.afad.gov.tr](http://www.afad.gov.tr). November 30, 2020.
- URL-2. 2015. [www.gumushane.gen.tr/v2/gumushanede-kaya-dusmesi-p3-aid,4514.html#galeri](http://www.gumushane.gen.tr/v2/gumushanede-kaya-dusmesi-p3-aid,4514.html#galeri). October 14, 2015.
- URL-3. 2019. [www.gumushane.gen.tr/v2/gumushane/gumushanede-dev-kayalar-apartmanin-uzerine-dustu-h22660.html](http://www.gumushane.gen.tr/v2/gumushane/gumushanede-dev-kayalar-apartmanin-uzerine-dustu-h22660.html). January 3, 2019.
- URL-4. 2020. [www.gumushane.gen.tr/v2/gumushane/gumushanede-insaat-alaninda-gocuk-meydana-geldi-h25500.html](http://www.gumushane.gen.tr/v2/gumushane/gumushanede-insaat-alaninda-gocuk-meydana-geldi-h25500.html). February 29, 2020.
- URL-5. 2019. [www.haber29.net/gumushane/dagdan-kopan-kayalar-eve-zarar-verdi-h18965.html](http://www.haber29.net/gumushane/dagdan-kopan-kayalar-eve-zarar-verdi-h18965.html). March 11, 2019.
- URL-6. 2016. [www.gumushane.gen.tr/v2/gumushane/gumushane-kayalar-park-halindeki-aracin-uzerine-dustu-h14747.html](http://www.gumushane.gen.tr/v2/gumushane/gumushane-kayalar-park-halindeki-aracin-uzerine-dustu-h14747.html). April 07, 2016.



# Bulletin of the Mineral Research and Exploration

<http://bulletin.mta.gov.tr>



## Assessment of crustal thinning and tectonic stress distribution of Gülbahçe fault zone and its surroundings (İzmir, West Türkiye) using gravity and magnetic anomalies

Oya ANKAYA PAMUKÇU<sup>a\*</sup>, Ayça ÇIRMIK<sup>a</sup>, Fikret DOĞRU<sup>b</sup>, Ece ÜNLÜ<sup>a</sup> and Barış Can MALALIÇİ<sup>c</sup>

<sup>a</sup>Dokuz Eylül University, Engineering Faculty, Department of Geophysical Engineering, İzmir, Türkiye

<sup>b</sup>Atatürk University, Oltu Vocational College, Construction, Erzurum, Türkiye

<sup>c</sup>General Directorate of Mineral Research and Exploration, Ankara, Türkiye

Research Article

### Keywords:

Bouguer Gravity Anomaly, Gülbahçe Fault Zone (GFZ), Magnetic, Microgravity, Parasnis Method.

### ABSTRACT

Gülbahçe Fault Zone (GFZ) is a significant tectonic structure and seismic source for İzmir city and its surroundings. The major earthquakes occurred at the surroundings of GFZ are 2005 Seferihisar, 2020 Samos Island-Aegean Sea and 2021 Seferihisar earthquakes. In this study, the crustal thinning and tectonic stress distribution of GFZ and its surroundings were analyzed by using the new gravity and magnetic data. The correspondence analysis was applied by appraising together the magnetic and free-air anomaly data. Moreover, the average density of the subsurface structure was calculated by applying the Parasnis method. The deviatoric stress calculation was executed and the change of the physical properties that controls the gravity and magnetic anomaly of the crustal structure of the GFZ and its surroundings from north to south was investigated. Therefore, the average density values, which were obtained from gravity anomalies, were computed as 2.59 gr / cm<sup>3</sup> in the north of the study region and it decreased to 2.06, 1.8 and 1.49 gr / cm<sup>3</sup> towards to the south. The free-air gravity anomaly values were between 0-70 mGal and the magnetic anomalies were between -450-150 nT. The deviatoric stress values were between -0.2-0.1 MPa.

Received Date: 21.06.2021

Accepted Date: 15.11.2021

## 1. Introduction

The study area is the N - S trending GFZ and its surroundings which separate Karaburun Peninsula from İzmir Gulf (Emre et al., 2005) (Figure 1). Western Anatolia including study area which is located in the Alpine - Himalayan orogenic belt, is the part of the wide - ranging compression zone between the Arabian, African and Eurasian plates (Pamukçu and Yurdakul, 2008; Çırmık et al., 2016; Çırmık et al., 2017a, b; Çırmık and Pamukçu, 2017; Doğru et al., 2017, 2018; Doğru and Pamukçu, 2019; Pamukçu et al., 2019). Western Anatolia is tectonically active and

is one of the rapidly deforming and extending areas in the world (Dewey and Şengör, 1979; Ambraseys, 1988; Taymaz et al., 1991; Bozkurt, 2001; Pamukçu and Yurdakul, 2008; Pamukçu et al., 2012, 2013). Western Anatolia has N - S trending extension from the Miocene to present (Dewey and Şengör, 1979; Şengör et al., 1985). As a result of the collision of Arabian and Eurasian plates in southeastern Anatolia, the North Anatolian and East Anatolian Fault zones occurred and the Anatolian plate has moved counter - clockwise towards the west (Şengör and Yılmaz, 1981). The westward movement of the Anatolian plate (Aktuğ and Kılıçoğlu, 2006) and the northward plunge

Citation Info: Ankaya Pamukçu, O., Çırmık, A., Doğru, F., Ünlü, E., Malaliçi, C. B. 2022. Assessment of crustal thinning and tectonic stress distribution of Gülbahçe fault zone and its surroundings (İzmir, West Türkiye) using gravity and magnetic anomalies. Bulletin of the Mineral Research and Exploration 169, 105-119. <https://doi.org/10.19111/bulletinofmre.1029265>

\*Corresponding author: Oya ANKAYA PAMUKÇU, [oya.pamukcu@deu.edu.tr](mailto:oya.pamukcu@deu.edu.tr)

of the African plate under the southern Anatolia plate along the Aegean - Cyprus subduction zone have formed the N - S trending extensional tectonics of the western Anatolia (Şengör and Yılmaz, 1981) and have caused the Anatolian block to escape to the east (Ketin, 1948; McKenzie, 1972; Barka and Kadinsky - Cade, 1988).

Emre et al. (2005) pointed out that the dominant sense of the GFZ is strike - slipe. The submarine data of Ocakoğlu et al. (2005) represented that the GFZ includes inverse fault component along the north segment and the western block of the fault is pushed on to the eastern block (Emre et al., 2005).

The previous studies (Akıncı et al., 2000; Çetiner, 2012; Pamukçu et al., 2013, 2015; Çırmık et al., 2016; Çırmık et al., 2017a, b; Malaliçi, 2019) showed that İzmir and its surroundings represent a high risk in terms of earthquakes. Particularly, the 17 October - 21 October 2005 Sığacık Bay earthquake series ( $M_1 = 5.7$ ,  $M_2 = 5.9$ ), 12 June 2017 Karaburun - Lesvos Island offshore earthquake ( $M_w = 6.3$ ) and 30 October 2020 Samos Island earthquake ( $M_w = 6.9$ ) were the most effective earthquakes for the study region. In addition, the tsunami was observed in the south of the study region immediately after 2020 Samos Island earthquake (Sözbilir et al., 2020). This seismically active region has studied since 2009 by Pamukçu et al. (2013, 2015); Çırmık et al. (2016); Çırmık et al. (2017a, b) and Malaliçi (2019). In this study, the crustal thinning and tectonic stress distributions of GFZ and its surroundings were determined by using the gravity and magnetic data which were obtained up to 2019. Within the scope of this study, the crustal structure of the risky region was examined from the gravity and magnetic data obtained from the project of Dokuz Eylül University (Project No: 2018.KB.FEN.010).

These regions, which represent magnetic and gravity anomalies caused by the complex structure of the GFZ and its surroundings, reflect the physical characteristics of the crust (Pamukçu et al., 2007, 2015). Therefore, the physical characteristics of the crust of GFZ and its surrounding were determined by using correspondence analysis of gravity and magnetic data as the first study for this study region. The mean density calculations of the subsurface structure were performed with Parasnis method by using Bouguer

anomaly and topography data. Finally, the deviatoric stress values (Turcotte and Schubert, 2002; Xu et al., 2015) were obtained by using the mean density and Bouguer gravity anomaly values. As a result, the findings related with the crustal structure and the previous studies were examined together.

## 2. Data Analysis

Gravity and magnetic data were obtained by the project founded by Dokuz Eylül University Research Foundation (Project No: DEU - BAP 2018. KB.FEN.010) and then, gravity and magnetic data were evaluated with TÜBİTAK (The Scientific and Technological Research Council of Turkey, Project No: 108Y285) project. Dokuz Eylül University Tinaztepe Campus was chosen as the base point for the gravity and magnetic measurements and the base measurements were obtained twice a day (morning and evening).

The complex gravity and magnetic anomaly fields of the GFZ and its surroundings (Figure 1) provide a record of the complex features and tectonic evolution of the underlying crust. The common approach for minimizing the interpretative uncertainties is to evaluate the correlation analyses at anomalies. There are no detailed previous gravity and magnetic studies in the study area and its surroundings. Therefore, within the scope of this study, it was aimed to better examine the crustal features of the area by analysing the crust with the correlation between gravity and magnetic anomalies.

### 2.1. The Correlation Between Free-Air and Magnetic Anomalies

The base, latitude and free-air corrections were applied to the measured microgravity data in order to obtain free-air gravity data (Figure 2). In the next step, Reduction to the Pole (RTP) was applied to the magnetic anomaly (Figure 3).

There are many studies (e.g. Von Frese et al., 1982, 1997a, b; Saleh et al., 2006; Pamukçu et al., 2007; De Ritis et al., 2010; Hinze et al., 2013; Erbek and Dolmaz, 2014; Pamuk, 2019) noticing that it is important to evaluate the alignment between gravity and magnetic anomalies in the interpretation of crustal

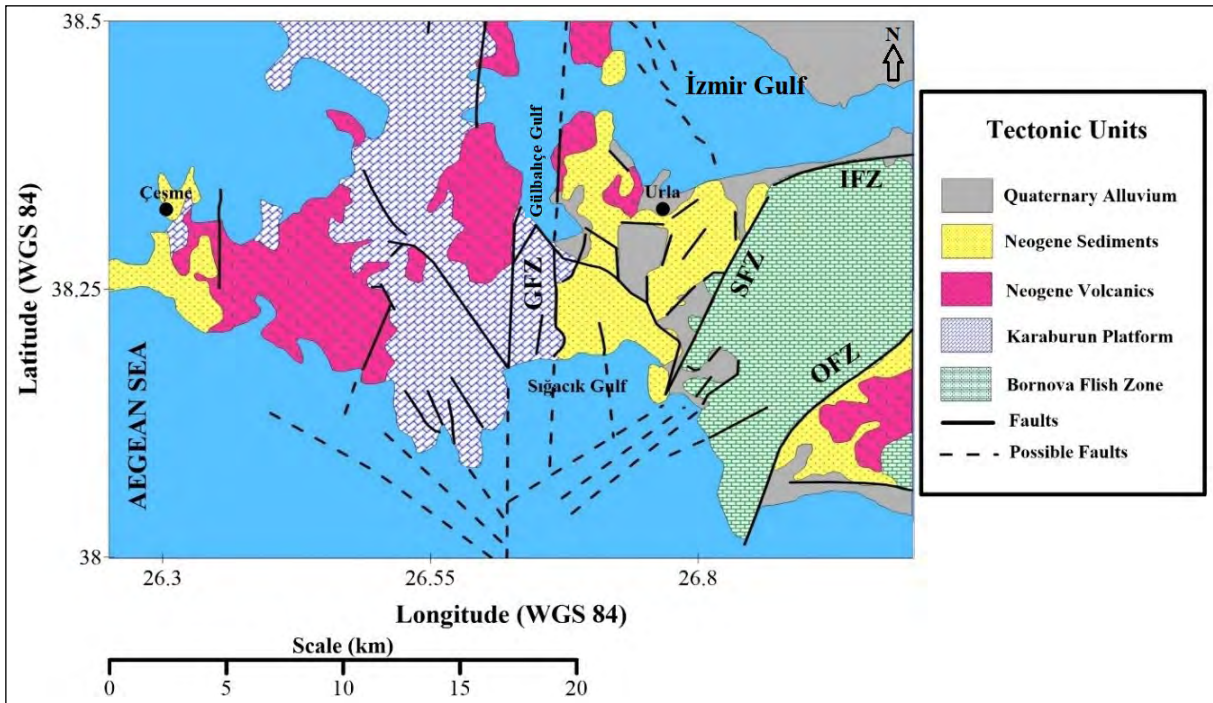


Figure 1- Simplified geological map of the study area (modified from Uzel and Sözbilir, 2008; Sözbilir et al., 2009; Uzel et al., 2012; Göktaş, 2016; Malaliçi, 2019) (GFZ: Gülbahçe Fault Zone, SFZ: Seferihisar Fault Zone, IFZ: İzmir Fault Zone, OFZ: Orhanlı Fault Zone).

properties and they pointed out that the change in crustal thicknesses can be determined by performing the correspondence analysis between gravity and magnetic anomalies.

The most important factor for gravity and magnetic data is temperature, since temperature directly affects gravity and magnetic anomalies (Von Frese et al., 1982; Pamukçu et al., 2007). In addition to these, both

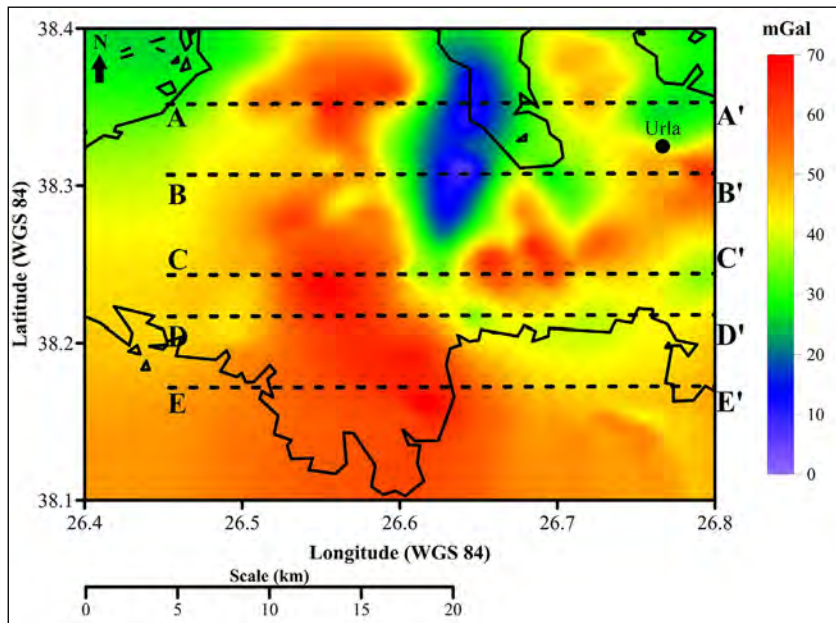


Figure 2- Free-air anomaly map of the study area.

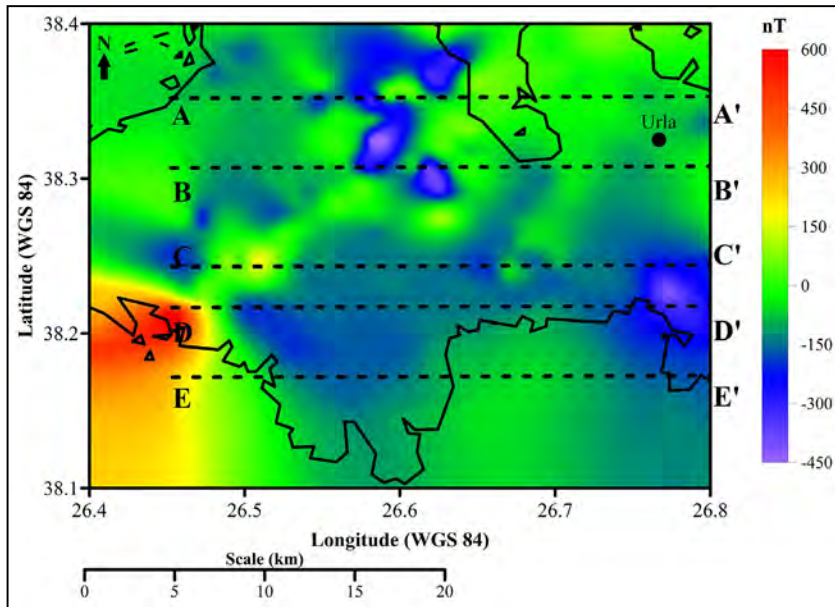


Figure 3- Reduction to the Pole (RTP) magnetic anomaly map of the study area.

surface and subsurface loads are effective on gravity. The most important parameter affecting the magnetic anomaly is the Curie temperature and depth which becomes shallower as the crust gets thinner. Thus, the amplitude of the magnetic anomaly also decreases. If this decreasing magnetic anomaly is inversely proportional to the free-air gravity anomaly including the topographic load (mass effect), then it is possible to mention the thin crust effect in that part of the study area (Von Frese et al., 1982; Pamukçu et al., 2007).

In order to perform correspondence analysis between gravity and magnetic data, five profiles were selected from free-air gravity (Figure 2) and magnetic anomaly (Figure 3) maps and the correspondence analysis of two data set were given at Figure 4.

### 2.2. The Correlation Between Complete Bouguer Gravity and Topography Anomalies

The relationship between Bouguer and topography values plays an important role in the analysis of crustal structure within the scope of isostasy (Watts, 2001; Pamukçu and Yurdakul, 2008; Arslan et al., 2010; Pamukçu and Akçığ, 2011; Doğru et al., 2018). According to the isostasy theorem, where the Bouguer anomaly increases, the topography anomaly is expected to decrease.

First order trend application was performed to the Bouguer anomalies (Figure 5). In 5 profiles seen in Figure 6, cross sections were taken from Bouguer and topography values (Figure 6) and the changes of two data set are given in Figure 7.

### 2.3. Density Determination with Parasnis Method and Calculation of Tectonic Stress

Parasnis (1952) method uses the relationship between gravity and topography variations for density determinations. The density with Parasnis method is determined as

$$\rho = \frac{0.3086 \frac{\Delta g}{\Delta h}}{0.04191} \quad (1)$$

Here  $\rho$  is density,  $\Delta g$  and  $\Delta h$  are mean gravity and topography values, respectively. The mean crustal density values of the study area were calculated (Table 1) by using Equation 1 from the topography and free-air gravity data of the profiles shown in Figure 2. The density determination was performed for D - D' profile in two steps and two density values were obtained (Table 1) due to the gravity anomaly changes in this profile (Figure 2).

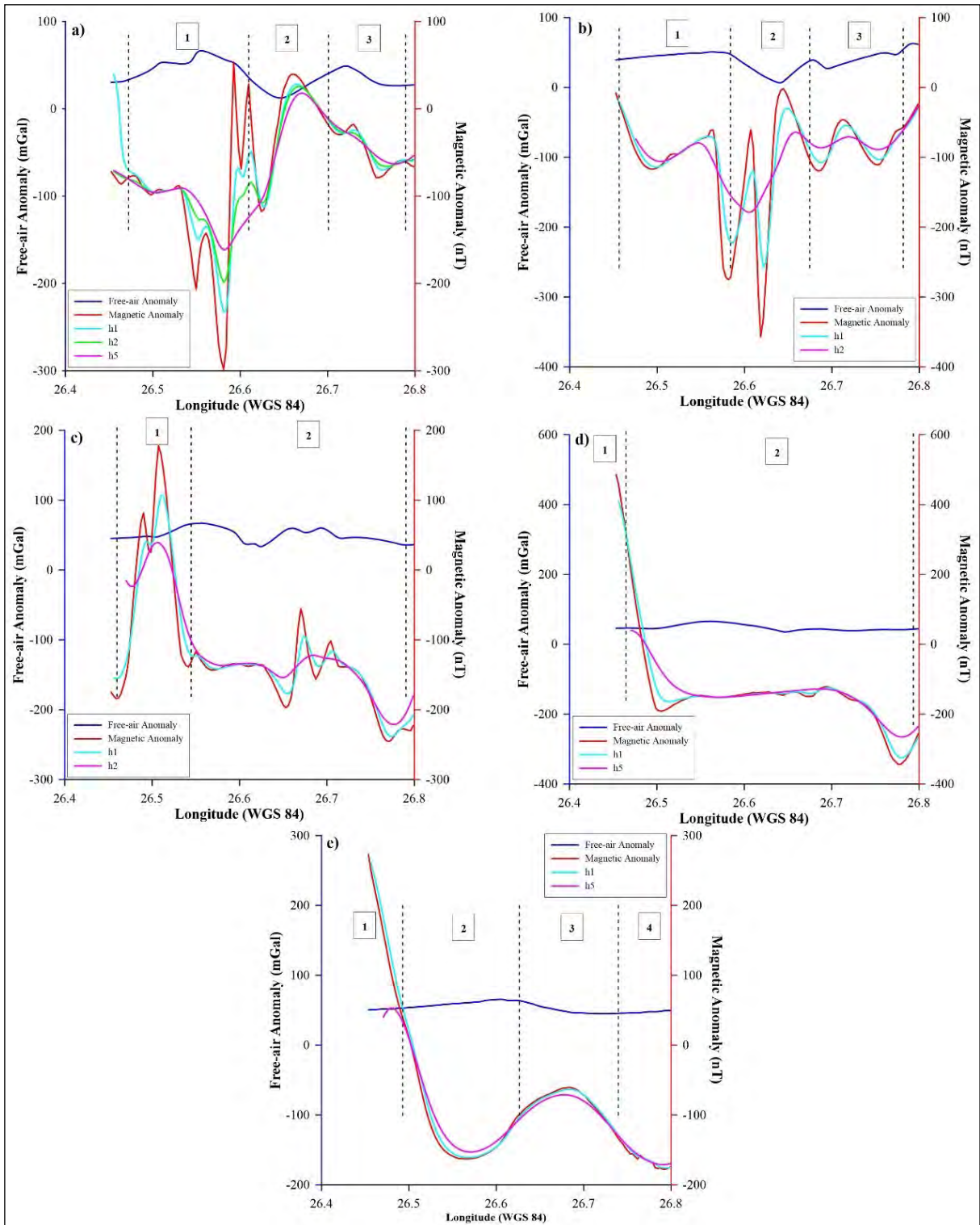


Figure 4- The correspondence analysis of the profiles taken from free-air gravity and magnetic anomaly maps; a) A - A' profile, b) B - B' profile, c) C - C' profile, d) D - D' profile, and e) E - E' profile. Blue and red lines represent free-air gravity and Reduction to the Pole (RTP) magnetic anomalies, respectively. Turquoise lines represent the upward continuation of  $h = 1$  km, green lines represent the upward continuation of  $h = 2$  km in Figure 4a, pink lines represent the upward continuation of  $h = 2$  km in 4b, 4c and  $h = 5$  km in Figure 4a, 4d, 4e.

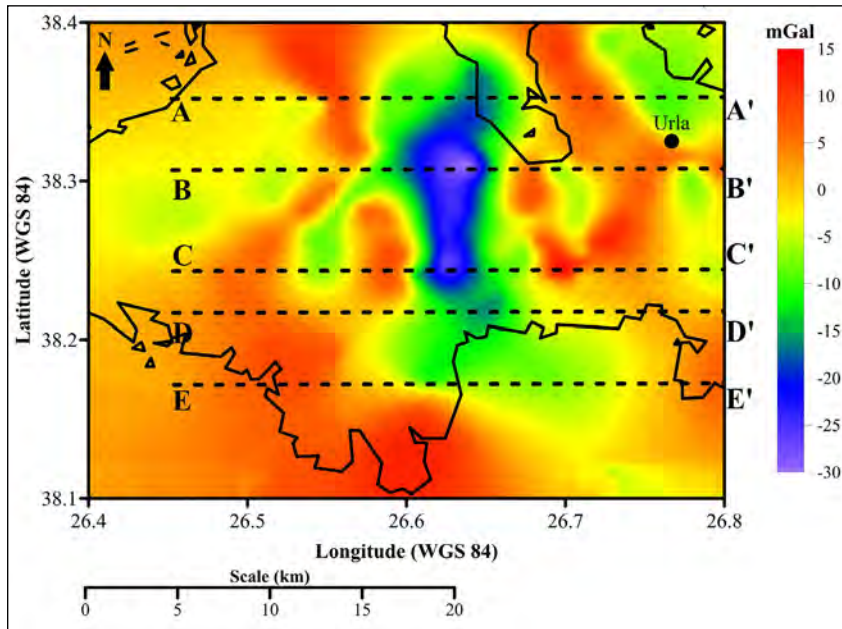


Figure 5- 1<sup>st</sup> order trend applied Bouguer gravity anomaly map and the profiles.

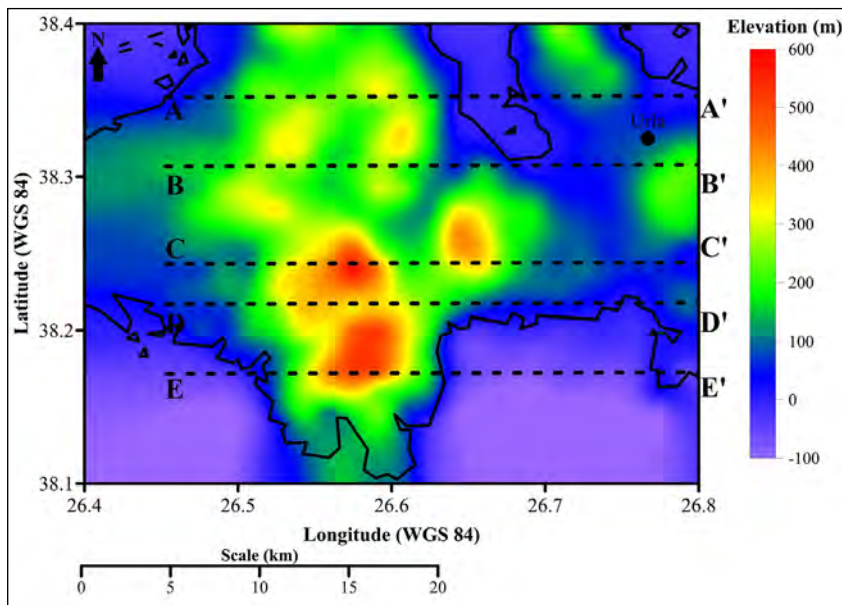


Figure 6- The topographic map and the profiles.

Table 1- The mean density values of the profiles.

Profil Name	The Mean Density values (gr / cm <sup>3</sup> )	
A - A'	2.59	
B - B'	2.06	
C - C'	2.012	
D - D'	1.40	1.80
E - E'	1.49	

The expression of lithostatic stress is given by three normal stresses and these stresses are proportional to depth. However, the lithostatic state of stress due to the isostatic equilibrium is not the same everywhere in the earth. Indeed, the horizontal normal stress consists of two components: lithostatic stress and deviatoric stress. Deviatoric stress ( $\Delta\sigma_{xx}$ ) can be based on static equilibrium on the continent (Turcotte and Schubert, 2002) and it is given by

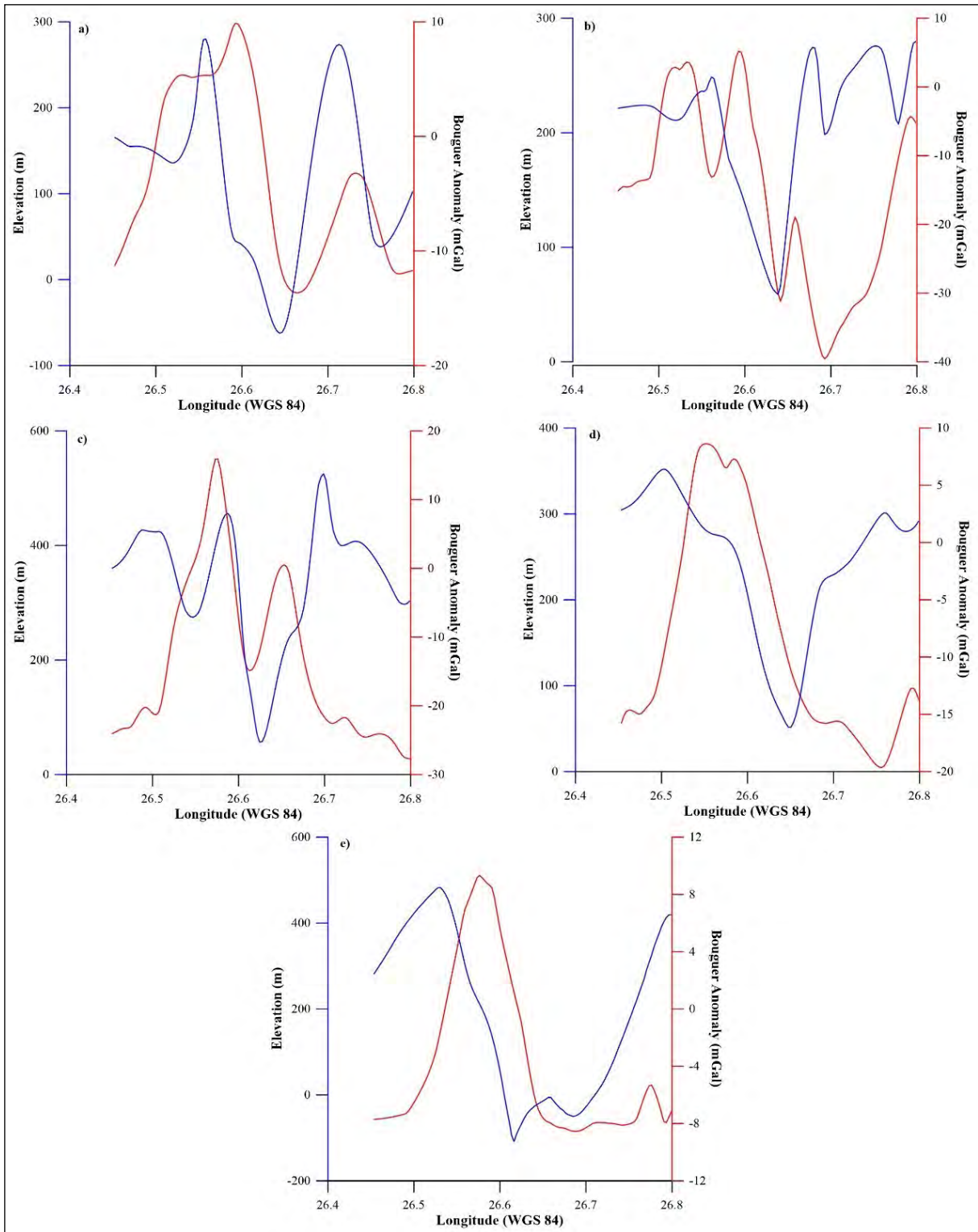


Figure 7- The profile values of the 1<sup>st</sup> order trend applied Bouguer gravity anomaly and topography maps; a) A - A' profile, b) B - B' profile, c) C - C' profile, d) D - D' profile and e) E - E' profile.

$$\Delta\sigma_{xx} = -\frac{1}{2} gh\Delta\rho \frac{\rho_c}{\rho_m} \quad (2)$$

Here,  $g$  is gravity acceleration,  $h$  is continental thickness,  $\rho_c$  and  $\rho_m$  are the density of crust and mantle, respectively. If the Bouguer plate is considered, the vertical gravity anomaly is given by (Heiskanen and Moritz, 1967);

$$\Delta g_z = -2\pi h G \Delta\rho \quad (3)$$

by using the local density value of each unit block  $\rho(x,y)$  instead of the mean density of the crust  $\rho_c$ , Equation 2 and 3 are combined and

$$\sigma_{xx} = \frac{g\rho(x,y)}{4\pi G\rho_m} \Delta g_z \quad (4)$$

is obtained. Equation 4 gives the way to find horizontal tectonic stress from the gravity anomaly (Xu et al., 2015; Pamukçu, 2017).

The deviatoric stress causes shape changes and shear stresses ascending also it controls the degree of body distortion (Aadnoy and Looyeh, 2019). Mount and Suppe (1987) pointed out that the deviatoric stress in the crust is an important unknown quantity in tectonophysics and structural geology. In the light of this knowledge, the deviatoric stress values were obtained (Figure 8) by using the mean density values calculated with Equation 4.

Additionally, the Coulomb, normal and shear stress change values of the region were calculated by using the stress values based on modelling of GNSS data and fault parameters of Çırmık et al. (2017a). These stress changes were drawn together with deviatoric stress (Figures 9, 10 and 11, respectively) for comparing the stress changes of the region.

### 3. Results

In the scope of this study, new microgravity and magnetic data were measured at GFZ and its surroundings (Figure 1) for investigating the crustal structure and tectonic stress distribution. Free-air gravity anomaly values of the region (Figure 2) change between 0 - 70 mGal. In Figure 2, the lowest values (from 0 mGal to ~25 mGal) are seen in the northern side and centre of GFZ (Figure 1) and the average values (~30 - 35 mGal) are seen at northern coasts of the study area. Besides, the lower values (0 - 35 mGal) are noticed at the southern coast of the Gulf of Gülbahçe (Figure 1). On the other hand, the southern coasts of the study region and the region between the longitudes 26.5° - 26.6° represent higher gravity values. Additionally, the free-air gravity values of the southern part of GFZ are higher than its northern part.

According to the RTP magnetic anomaly map (Figure 3) the values change from -450 nT to 600 nT

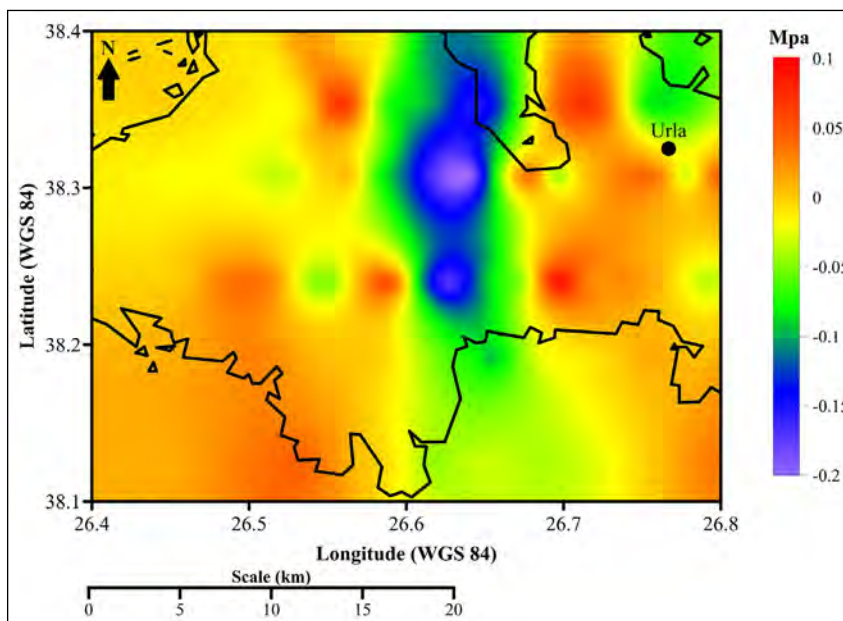


Figure 8- The deviatoric stress values obtained by gravity data and density values.

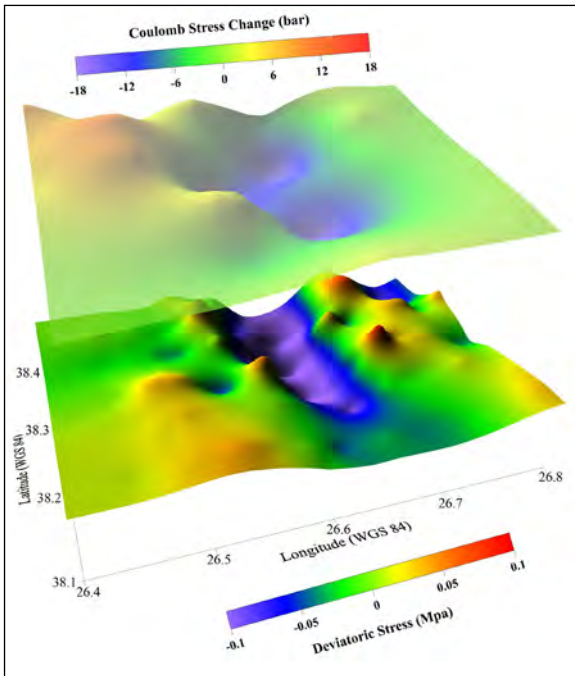


Figure 9- Coulomb stress and deviatoric stress distributions of the study area.

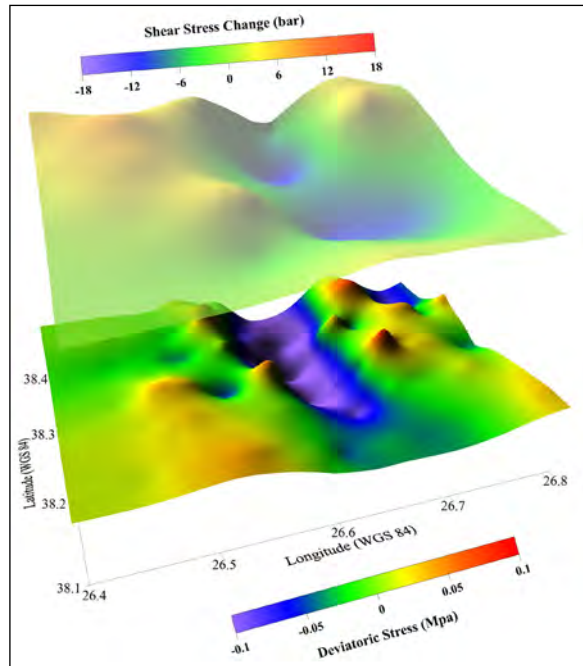


Figure 11- Shear stress and deviatoric stress distributions of the study area.

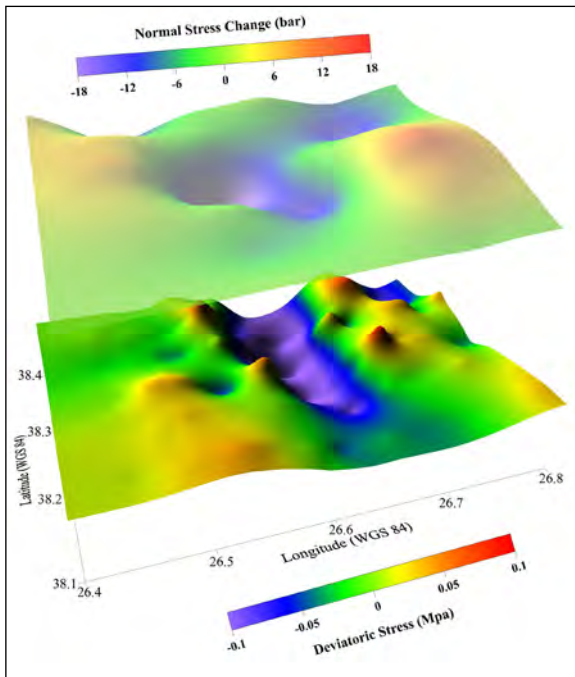


Figure 10- Normal stress and deviatoric stress distributions of the study area.

(Figure 3) but in general, the magnetic values are between 150 nT and -450 nT in the study region. While GFZ represents different (lower) gravity anomalies respect to other part of the region (Figure 2),

any anomaly difference is not seen clearly at magnetic anomaly map for GFZ (Figure 3). High positive magnetic values are remarkable between the longitudes  $26.4^{\circ}$  -  $\sim 26.47^{\circ}$  and latitudes  $38.1^{\circ}$  -  $38.2^{\circ}$  (Figure 3).

In the next step, the cross sections were taken at 5 profiles for investigating the crustal structure of GFZ and its surroundings from the RTP magnetic, upward continuation applied magnetics and free-air gravity anomalies by using the approaches of Von Frese et al. (1982) and Pamukçu et al. (2007) (Figure 4). The correspondence analysis was performed between these data. When the correlation of free-air gravity and magnetic data are examined (Figure 4), it can be said that there is a crustal thinning where the free-air gravity and magnetic data represent inverse proportions (opposite correlation) (Von Frese et al., 1982). If the regions which represent high gravity and high magnetisations are evaluated with the geological units of the region, it is seen that these regions include the volcanic (Neogene volcanic) units (Figure 1). Therefore, it can be said that the regions which represent positive correlation (direct proportion) between gravity and magnetic anomalies (Figure 4) are related with volcanic root systems in addition to topographic components.

For analysing the profiles in detail, the profiles are divided into the regions due to the changes on gravity and magnetic values (Figure 4). In Figure 4a, which contains profile values of A - A', the profile is divided into 3 regions. Free-air gravity and magnetic anomaly values in region no: 1 represent inverse (opposite) correlation. By the way, the crustal thinning is expected wherein the free-air gravity anomaly increases and magnetization decreases. In the region no: 2, while free-air gravity values decrease, the magnetic anomaly values increase. This can also be assessed by crustal thickening or by an intrusion which increases magnetization. The similar situation seen in region no: 1 is also observed in region no: 3. Therefore, it can be said that the crust is thin in the regions no: 1 and no: 3. But, the proportion of crustal thinning in the region no: 1 is greater than in no: 3. This case can be related with the high difference between the amplitude of the magnetic values of these regions. In a crustal structure affected with the same mass loading, if magnetic anomaly values are quite highly differentiated, a different mechanism most likely deformation within the crust can be expected. Figure 4b shows that the values of profile B - B' and this profile is divided into 3 regions. The values of profile B - B' (Figure 4b) are similar to the profile A - A' values (Figure 4a). In the regions no: 1 and no: 3, the free-air gravity anomaly values increase while the magnetic anomaly values decrease similar to profile A - A'. However, while free-air gravity values in region no: 2 decrease (respect to the general profile), magnetic anomaly values decrease. Therefore, it can be said that there is an important factor in the crust which reduces magnetization in this region. In Figure 4c, the profile C - C' values are seen and the profile is divided into 2 regions. In the region no: 1, high positive magnetic anomaly values are remarkable. In this area, it is possible to mention that the presence of an intrusion with high magnetization in the crust. Additionally, unlike other profiles (A and B, Figures 4a, 4b), the magnetic anomaly values decrease in the region no: 2 and free-air gravity and magnetic anomaly values change inversely. This case can be related with the crustal thinning in this area. The profile D - D' values are seen in Figure 4d and the profile is divided into 2 regions. In profile D - D' (Figure 4d), the magnetic anomaly values are high positive in the region no: 1. The magnetic anomaly values decrease

rapidly between the regions no: 1 and no: 2. Besides, the relationship between free-air gravity anomaly and decreasing magnetic anomaly in the region no: 2 (Figure 4d) is similar to profile C - C' (Figure 4c). In the region no:2 (Figure 4d), the amplitude of magnetic anomaly values of D - D' is seen more stable respect to the profiles A, B and C (Figure 4a, b, c). In Figure 4e, the profile E - E' values are drawn and the profile is divided into 4 regions. In the profile E - E' (Figure 4e), high positive magnetic anomaly amplitudes are seen in the region no: 1 as similar as in D profile (Figure 4d). In the region no:2 (Figure 4e), it is seen that while free-air gravity values are increasing and magnetic anomaly values are decreasing, this case is also observed in A and B profiles (Figures 4a, 4b). Although the free-air gravity values in the region no: 3 decreases slightly, a significant increasing and then decreasing is observed in the magnetic anomaly values. In the region no: 4, while not a clear changing is seen in the free-air gravity and the magnetic anomaly values continue to decrease. This condition can be associated with crustal thinning in this region.

In Figure 5, it is seen that 1<sup>st</sup> order trend applied Bouguer gravity anomaly values change between -30 mGal and 15 mGal. Figure 7 presents the relation between Bouguer gravity (Figure 5) and topography (Figure 6) anomalies for 5 profiles. According to isostasy theorem, if there is an inverse relation between gravity and topography data, there is a local isostatic balancing in the region (Watts, 2001; Pamukçu and Yurdakul, 2008; Çırmık et al., 2017a). In profile A - A' (Figure 7a), the relation between gravity and topography values are approximately inverse throughout the profile, therefore it can be said that there is local balancing. In profile B - B' (Figure 7b), the relation between two data set is inverse from the initial of the profile (~26.4° longitude) to 26.6° longitude and between the longitudes from 26.7° to ~26.78° so it can be said that there is a local isostatic balance in the mentioned locations. On the other hand, it can be said that there is a crustal problem (high pressure, the existence of a liquid, etc.) in the region at 26.62° longitude and its surroundings since both the Bouguer gravity and topography values decrease together. In profile C - C' (Figure 7c), the relation between two data set is inverse between the longitudes from 26.5° to ~26.54° and from 26.66° to

26.69°. Therefore, it can be said that these regions have local isostatic balancing. At similar locations (at 26.62° longitudes and its surroundings) (Figure 7c) with profile B - B' (Figure 7b), the direct relation between gravity and topographic values are seen, thus, the crustal problem is expected in this location. In the profiles D - D' (Figure 7d) and E - E' (Figure 7e), the relation between two data set is inverse generally throughout the profiles. But, this case (decreasing of the Bouguer gravity and topography values together) which shown in the regions at longitude 26.62° and its surroundings is not clear in the profiles D - D' (Figure 7d) and E - E' (Figure 7e) as seen in the profiles B - B' and C - C' (Figures 7b, c). As a result, some parts of the study area have an uncompensated mechanism.

In the other step, the deviatoric stress values (Figure 8) were obtained by using the mean density values and the Bouguer gravity anomaly values for investigating the horizontal stress distribution created by gravitational loadings. The deviatoric stress values change from -0.2 MPa to 0.1 MPa in the study region (Figure 8). Additionally, the Coulomb stress changes and its components normal and shear stress changes were calculated for investigating the changes of stress and were drawn together (Figures 9, 10 and 11) with deviatoric stress values for evaluating the changes more clearly. In Figure 9, the Coulomb stress and deviatoric stress values are negative at GFZ and its surroundings (Figure 1). In the eastern part of GFZ (at Urla and its surroundings, Figure 1) and SW of the study region, the deviatoric stress values are high positive but these regions represent average (approximately zero) Coulomb stress values (Figure 9). Controversially, NW of the study region while representing positive (higher than average) Coulomb stress values, show average (approximately zero) deviatoric stress values. SE of the study region represents similar features in both coulomb and deviatoric stress maps. In the normal stress and deviatoric stress (Figure 10) maps, it is seen that only centre of GFZ represents similar features (negative values) in both maps. The southern and northern parts of GFZ represent average normal stress values and no coherency with deviatoric stress. Besides, NE of the study region has negative normal stress values while its deviatoric stress values are high positive. Also, the normal and deviatoric stress values of SE, SW and NW of the study area are coherent with

each other (Figure 10). In Figure 11, it is seen that the shear stress values of southern and central parts of GFZ and also SE of the study area are consistent with the deviatoric stress values. Besides, the shear stress values of Urla and its surroundings are more coherent with deviatoric stress values respect to Coulomb (Figure 9) and normal stresses (Figure 10). As a general result, the area which is located between the longitude 26.6° and latitudes between 38.3° - 38.4° (GFZ and its surroundings) has negative Coulomb, normal, shear and deviatoric stress values. In Figure 8, the area between the longitudes 26.6° - 26.7° represent the highest negative deviatoric stress values. In Figure 11, it is seen that this area also has negative shear stress values (which were obtained from horizontal movements based on GNSS) and deviatoric stress values (obtained from gravity values) therefore it can be said that GFZ represents completely the sense of strike - slip fault in this area.

The decreasing of the gravity and topographic value amplitudes in the B - B' (Figure 7b) and C - C' (Figure 7c) profiles is fit with the area between the longitudes 26.6° - 26.7° which represents the highest negative deviatoric stress values seen in Figure 8. According to the isostatic compensated mechanism, while the topographic values decrease / increase, gravity value is expected to increase / decrease. In the parts of B - B' (Figure 7b) and C - C' (Figure 7c) profiles where come across with the highest negative deviatoric stress valued region (Figure 8), the isostatic compensated mechanism is not seen. Therefore, it can be thought that a physical factor may affects the density in these parts.

Additionally, the mean density estimations of the subsurface structure in the study area were calculated with Parasnis method by using Bouguer anomaly values and topography values at 5 profiles (Figure 5) (Table 1). The density, which was found as 2.59 gr / cm<sup>3</sup> in the north of the study region, decreased to 2.06, 1.8 and 1.49 gr / cm<sup>3</sup> towards to the south. Based on the detailed geological map of the study region, it can be said that this extreme density reduction may be caused by sedimentary, volcanic tuff and pyroclastic rock units (Sözbilir et al., 2009; Uzel et al., 2012). Baba et al. (2019) pointed out the existence of possible geothermal resources in the study area. The locations of the possible geothermal resources may be related

to the regions including low density and negative magnetization and uncompensated region which were found in this study.

The area which is located between the longitudes  $\sim 26.6^\circ$  -  $26.63^\circ$  and the latitude  $38.3^\circ$  (Figure 8), where is closer to region no: 2 of the B - B' profile (Figure 4b) both the gravity and magnetic values decrease. Therefore, it can be said that there is an effective factor which reduces the magnetic features in these locations and its surroundings. Additionally, this region represents negative amplitude deviatoric, coulomb shear and normal stress values (Figures 8 - 11) and high negative Bouguer anomaly values (Figure 5). In the magnetic map (Figure 3) and correspondence analysis of the profiles (Figure 4), it is seen that the magnetic anomalies reduce rapidly and represent negative amplitudes in the south of the study region. This finding is consistent with the distributions (reducing from north to south) of the mean density values of the crust (Table 1). The highest reducing (approximately  $-500$  nT) in the magnetic anomaly (Figure 4b) coincides with the location at longitude  $\sim 26.62^\circ$  (Figure 8). In this region, which has negatively high stress values, the existence of hot

crustal materials rising to shallower depths and high deformation at lower crust can be thought.

The earthquakes occurred between the years 1970 and 2020 with  $M > 4$  which were obtained from United States Geological Survey (USGS) were drawn in Figure 12. If these earthquake distributions are investigated with the deviatoric stress (Figure 12), it is seen that there is no any earthquake at the region which has high negative deviatoric stress values.

The region which has no seismicity (Figure 12) has also high negative Coulomb (Figure 9), normal (Figure 10) and shear (Figure 11) stress anomalies. Additionally, the Bouguer gravity anomalies (Figure 5) represent high negative values in this region. Therefore, it can be said that the crustal structure of the region may be ductile. Because, if the density of the crust is lower than the expected values, the form of crust is ductile, so seismicity is not expected. In addition, this idea is supported by the existence of the geothermal sources (Baba et al., 2019) and the findings related with the crust thinning (Figure 4) and the non-isostatic balance conditions (Figure 7) in the study area.

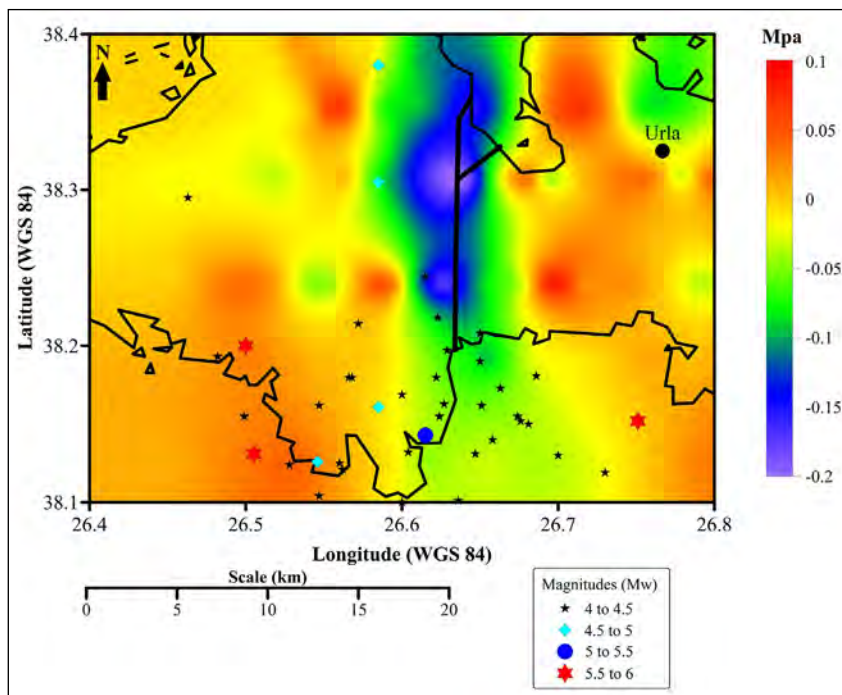


Figure 12- The deviatoric stress values with the earthquakes occurred between the years 1970 - 2020 ( $M > 4$ ). The earthquake data was obtained from United States Geological Survey (USGS, 2021; <https://earthquake.usgs.gov/earthquakes/search/>).

## Acknowledgements

In this study the microgravity and magnetic data of the projects (Project No: 2018.KB.FEN.010) funded by Dokuz Eylül University Scientific Research Project and The Scientific and the Technological Research Council of Turkey (TUBITAK) (Project No: 108Y285) were used.

## References

- Aadnoy, B., Looyeh, R. 2019. Petroleum Rock Mechanics: Drilling Operations and Well Design. Gulf Professional Publishing, 460.
- Akıncı, A., Eyidoğan, H., Göktürkler, G., Akyol, N., Ankaya, O. 2000. İzmir ili çevresinin depremselliği ve deprem tehlikesinin incelenmesi. Batı Anadolu'nun Depremselliği Sempozyumu (BADSEM 2000) İzmir, Bildiri Kitabı, 231-238 (in Turkish).
- Aktuğ, B., Kılıçoğlu, A. 2006. Recent crustal deformation of İzmir, Western Anatolia and surrounding regions as deduced from repeated GPS measurements and strain field. *Journal of Geodynamics* 41, 471-484.
- Ambraseys, N. N. 1988. Engineering seismology. *Earthquake Engineering Structural Dynamical* 17, 1-105.
- Arslan, S., Akın, U., Alaca, A. 2010. Gravite verileri ile Türkiye'nin kabuk yapısının incelenmesi. *Bulletin of the Mineral Research and Exploration* 140, 57-73.
- Baba, A., Şaroğlu, F., Akkuş, I., Özel, N., Yeşilnacar, M. İ., Nalbantçılar, M. T., Demir, M. M., Gökçen, G., Arslan, Ş., Dursun, N., Uzelli, T., Yazdani, H. 2019. Geological and hydrogeochemical properties of geothermal systems in the southeastern region of Turkey. *Geothermics* 78, 255-271.
- Barka, A. A., Kadinsky Cade, K. 1988. Strike-slip fault geometry in Turkey and its influence on earthquake activity. *Tectonics* 7, 663-684.
- Bozkurt, E. 2001. Neotectonics of Turkey- a synthesis. *Geodinamica Acta* 14, 3-30.
- Çetiner, M. 2012. İzmir ve çevresindeki mikrogravite verilerinin değerlendirilmesi. MSc Thesis, Dokuz Eylül University, The Graduate School of Nature and Applied Sciences, 78, İzmir.
- Çırmık, A., Özdağ, O. C., Doğru, F., Pamuk, E., Gönenç, T., Akgün, M., Arslan, A. T. 2016. The soil behaviours of the GNSS station. *Earth Sciences* 5(5), 70-81.
- Çırmık, A., Pamukçu, O. 2017. Clarifying the interplate main tectonic elements of Western Anatolia, Turkey by using GNSS velocities and Bouguer gravity anomalies. *Journal of Asian Earth Science* 148, 294-304.
- Çırmık, A., Doğru, F., Gönenç, T., Pamukçu, O. 2017a. The stress / strain analysis of kinematic structure at Gülbahçe Fault and Uzunkuyu Intrusive (İzmir, Turkey). *Pure and Applied Geophysics* 174(3), 1425-1440.
- Çırmık, A., Pamukçu, O., Gönenç, T., Kahveci, M., Şalk, M., Herring, T. 2017b. Examination of the kinematic structures in İzmir (Western Anatolia) with repeated GPS observations (2009, 2010 and 2011). *Journal of African Earth Sciences* 126, 1-12.
- De Ritis, R., Ventura, G., Chiappini, M., Carluccio, R., Von Frese, R. 2010. Regional magnetic and gravity anomaly correlations of the Southern Tyrrhenian Sea. *Physics of the Earth and Planetary Interiors* 181(1-2), 27-41.
- Dewey, J. F., Şengör, A. M. C. 1979. Aegean and surrounding regions: complex multi plate and continuum tectonics in a convergent zone. *Geological Society of America Bulletin Part 1* 90, 84-92.
- Doğru, F., Pamukçu, O. 2019. Analysis of gravity disturbance for boundary structures in the Aegean Sea and Western Anatolia. *Geofizika* 36(1), 53-76.
- Doğru, F., Pamukçu, O., Gönenç, T., Yıldız, H. 2018. Lithospheric structure of western Anatolia and the Aegean Sea using GOCE-based gravity field models. *Bollettino di Geofisica Teorica ed Applicata* 59(2), 135-160.
- Doğru, F., Pamukçu, O., Özsoz, I. 2017. Application of tilt angle method to the Bouguer gravity data of Western Anatolia. *Bulletin of the Mineral Research and Exploration* 155(155), 213-222.
- Emre, Ö., Özalp, S., Doğan, A., Özaksoy, V., Yıldırım, C., Göktaş, F. 2005. İzmir yakın çevresinin diri fayları ve deprem potansiyelleri. Maden Tetkik Arama Genel Müdürlüğü, Rapor No: 10754, Ankara (unpublished).
- Erbek, E., Dolmaz, M. N. 2014. Geophysical researches (gravity and magnetic) of the Eratosthenes Seamount in the eastern Mediterranean Sea. *Acta Geophysica* 62(4), 762-784.
- Heiskanen, W. A., Moritz, H. 1967. Physical geodesy. *Bulletin Geodesique* 86, 491-492.

- Hinze, W. J., Von Frese, R. R. B., Saad, A. H. 2013. Gravity and Magnetic Exploration Principles, Practices and Applications. Cambridge University Press, 502.
- Göktaş, F. 2016. Ildır Körfezi güneyindeki bölgenin Neojen stratigrafisi Çeşme Yarımadası, Batı Anadolu. Türkiye Jeoloji Bülteni 59(3), 299–321 (in Turkish).
- Ketin, İ. 1948. Über die tektonisch - mechanischen Folgerungen aus den grossen Anotolischen Erdbeben des letzten Dezeniums. Geologische Rundschau 36, 77-83.
- Malaliçi, B. C. 2019. Gülbahçe fayı ve çevresinin jeodinamik yapısının irdelenmesi. MSc Thesis, Dokuz Eylül University, The Graduate School of Nature and Applied Sciences, 77, İzmir.
- McKenzie, D. 1972. Active tectonics of the Mediterranean region. Geophysical Journal of the Royal Astronomical Society 30, 109-185.
- Mount, V. S., Suppe, J. 1987. State of stress near the San Andreas fault: implications for wrench tectonics. Geology 15(12), 1143-1146.
- Ocakoglu, N., Demirbağ, E., Kuşçu, İ. 2005. Neotectonic structures in İzmir Gulf and surrounding regions (western Turkey): evidences of strike-slip faulting with compression in the Aegean extensional regime. Marine Geology 219(2-3), 155-171.
- Pamuk, E. 2019. Investigating edge detection, Curie point depth, and heat flow using EMAG2 magnetic and EGM08 gravity data in the northern part of Eastern Anatolia, Turkey. Turkish Journal of Earth Sciences 28(6), 805-821.
- Pamukçu, O. 2017. Stress analysing with gravity data. 3. International Conference on Engineering and Natural Science, 3 - 7 May 2017, Budapest, 600-602.
- Pamukçu, O. A., Akçığ, Z. 2011. Isostasy of the Eastern Anatolia (Turkey) and discontinuities of its crust. Pure and Applied Geophysics 168(5), 901-917.
- Pamukçu, O., Yurdakul, A. 2008. Isostatic compensation in Western Anatolia with estimate of the effective elastic thickness. Turkish Journal of Earth Sciences 17, 545-557.
- Pamukçu, O., Akçığ, Z., Demirbaş, Ş., Zor, E. 2007. Investigation of crustal thickness in eastern Anatolia using gravity, magnetic and topographic data. Pure Applied Geophysics 164, 2345-2358.
- Pamukçu, O., Gönenç, T., Çırmık, A., Pamukçu, Ç., Ertürk, N. 2019. The geothermal potential of Büyük Menderes Graben obtained by combined 2.5 - D normalized full gradient results. Pure and Applied Geophysics 176(11), 5003-5026.
- Pamukçu, O., Gönenç, T., Çırmık, A., Sındırgı, P., Kaftan, I., Akdemir, Ö. 2015. Investigation of vertical mass changes in the south of İzmir (Turkey) by monitoring microgravity and GPS/GNSS methods. Journal of Earth System Science 124(1), 137-148.
- Pamukçu, O., Gönenç, T., Yurdakul, A., Kahveci, M. 2013. Sismik riski yüksek olan İzmir - Karaburun'un güneyinde yapılmış mikrogravite ve GPS çalışmaları. Jeofizik 18, 59-66.
- Pamukçu, O., Gönenç, T., Yurdakul, A., Özyalın, Ş., Sözbilir, H. 2012. Application of boundary analysis and modelling methods on Bouguer gravity data of the Gediz Graben and surrounding area in Western Anatolia and its tectonic implications. Journal of the Balkan Geophysical Society 15, 19-30.
- Parasnis, D. S. 1952. A study of rock densities in English Midlands. Geophysical Journal International 6, 252–271.
- Saleh, S., Jahr, T., Jentzsch, G., Saleh, A., Abou Ashour, N. M. 2006. Crustal evaluation of the northern Red Sea rift and Gulf of Suez, Egypt from geophysical data: 3-dimensional modeling. Journal of African Earth Sciences 45(3), 257–278.
- Sözbilir, H., Softa, M., Eski, S., Tepe, Ç., Akgün, M., Pamukçu, O., Çırmık, A., Utku, M., Özdağ, C. Ö., Özden, G., Özçelik, Ö., Evlek, D. A., Çakır, R., Baba, A., Uzelli, T., Tatar, O. 2020. 30 October 2020 Sisam (Samos) Earthquake (Mw: 6.9) Evaluation Report, Dokuz Eylül University Earthquake Research and Application Center (in Turkish).
- Sözbilir, H., Sümer, Ö., Uzel, B., Ersoy, Y., Erkül, F., İnci, U., Helvacı, C. Özkaymak, Ç. 2009. 17 - 20 Ekim 2005 - Sığacık Körfezi (İzmir) depremlerinin sismik jeomorfolojisi ve bölgedeki gerilme alanları ile ilişkisi, Batı Anadolu. Türkiye Jeoloji Bülteni, 52 (2), 217–238 (in Turkish).
- Şengör, A. M. C., Yılmaz, Y. 1981. Tethyan evolution of Turkey: a plate tectonic approach. Tectonophysics 75, 181-241.
- Şengör, A. M. C., Görür, N., Şaroğlu, F. 1985. Strike - slip faulting and related basin formation in zones of tectonic escape: Turkey as a case study. Special Publications of the Society of Economic Palaeontologists and Mineralogists 37, 227–264.

- Taymaz, T., Jackson, J., McKenzie, D. P. 1991. Active tectonics of the North and Central Aegean Sea. *Geophysical Journal International* 106, 433–490.
- Turcotte, D. L., Schubert, G. 2002. *Geodynamics*. Cambridge University Press, 456.
- USGS (United States Geological Survey earthquake catalog). <https://earthquake.usgs.gov/earthquakes/search/>. 1 June 2021.
- Uzel, B., Sözbilir, H. 2008. A first record of strike - slip basin in western Anatolia and its tectonic implication: The Cumaovası basin as an example. *Turkish Journal of Earth Sciences* 17, 559–591.
- Uzel, B., Sözbilir, H., Özkaymak, Ç. 2012. Neotectonic evolution of an actively growing superimposed basin in western Anatolia: the inner bay of Izmir, Turkey. *Turkish Journal of Earth Sciences* 21(4), 439-471.
- Von Frese, R. R. B., Hinze, W. J., Braile, L. W. 1982. Regional North American gravity and magnetic anomaly correlations. *Geophysical Journal International* 69, 145-761.
- Von Frese, R. R., Jones, M. B., Kim, J. W., Kim, J. H. 1997*a*. Analysis of anomaly correlations. *Geophysics* 62(1), 342-351.
- Von Frese, R. R., Jones, M. B., Kim, J. W., Li, W. S. 1997*b*. Spectral correlation of magnetic and gravity anomalies of Ohio. *Geophysics* 62(1), 365-380.
- Watts, A. B. 2001. *Isostasy and Flexure of the Lithosphere*. Cambridge University Press, 458.
- Xu, C., Wang, H. H., Luo, Z. C., Ning, J. S., Liu, H. L. 2015. Multilayer stress from gravity and its tectonic implications in urban active fault zone: a case study in Shenzhen, South China. *Journal of Applied Geophysics* 114, 174-182.





# Bulletin of the Mineral Research and Exploration

<http://bulletin.mta.gov.tr>



## Analysis of the stress distribution of North Anatolian Fault Zone for the part between Amasya-Tokat cities

Ayça ÇIRMIK<sup>a\*</sup>, Ufuk AYDIN<sup>b</sup>, Oya ANKAYA PAMUKÇU<sup>a</sup> and Fikret DOĞRU<sup>c</sup>

<sup>a</sup>Dokuz Eylül University, Faculty of Engineering, Department of Geophysical Engineering, İzmir, Türkiye

<sup>b</sup>Atatürk University, Faculty of Engineering, Department of Civil Engineering, Erzurum, Türkiye

<sup>c</sup>Atatürk University, Oltu Vocational Collage, Construction, Erzurum, Türkiye

Research Article

### Keywords:

GNSS, Regional Absorption Coefficient, Coulomb Stress / Strain Analysis.

### ABSTRACT

Tectonic forces formed in the continental crust, cause permanent changes in stress, compression and deformation. The amplitudes of earthquake waves vary with the stress/strain distribution in the crust. In this study, the change of stress/strain and regional absorption coefficient, which is effective in tectonic forces caused by elastic deformation energy accumulating in the brittle crust over time, was investigated. The study area is the middle part of the North Anatolian Fault Zone and the area formed by Ezinepazarı fault zone and Merzifon fault zone. In this area, Coulomb stress analysis was carried out by using the focal mechanism solution values of the earthquake that occurred in Yoldere - Erbaa, Tokat on October 9, 2015 ( $M_L=5.1$ ). In order to examine the deformation caused by this earthquake in and around the study area, Global Navigation Satellite System (GNSS) data were evaluated and the velocities of these stations were calculated using GNSS data of these stations for the years 2013-2014-2015-2016. Also, regional absorption coefficients were determined by using earthquake data. As a result, Coulomb stress analysis results, velocity values distribution obtained from GNSS data and absorption findings obtained from seismological study were evaluated together.

Received Date: 01.07.2021

Accepted Date: 02.11.2021

## 1. Introduction

The internal force fields that cause the distortion in the bodies can be approximately estimated based on the deformation generated by the displacement of the blocks during an earthquake. The kinematics of continental deformation are shown by the horizontal and vertical variation amounts derived by monitoring the temporal changes of the coordinates, which allow an estimate of the internal stress/strain amount in the tectonic forces of such deformation. Increasing of the effective stresses causes stresses, thus earthquakes in the deformed areas of the fault zone (Chinnery,

1963). Many researchers have investigated Coulomb stress variation (Harris and Simpson, 1992; Stein et al., 1992; Çırmık, 2014; Çırmık et al., 2016; Çırmık and Pamukçu, 2017; Çırmık et al., 2017; Affandi et al., 2019). Changes in stress or strain in the crust affect not just the velocity of seismic waves created during the earthquake, but also the amplitudes of those waves. There are numerous factors that affect seismic absorption in the crust, and changing conditions have a major impact (Toksöz and Johnston, 1981). The lithological structure and stress/strain state of the environment influence the absorption of earthquake

Citation Info: Çırmık, A., Aydın, U., Pamukçu A. O., Doğru, F. 2022. Analysis of the stress distribution of North Anatolian Fault Zone for the part between Amasya-Tokat cities. Bulletin of the Mineral Research and Exploration 169, 121-133. <https://doi.org/10.19111/bulletinofmre.1022323>

\*Corresponding author: Ayça ÇIRMIK, [ayca.cirmik@deu.edu.tr](mailto:ayca.cirmik@deu.edu.tr)

energy that causes continental crust deformation in the time-distance environment (reduction in wave amplitude - increase). The rate of decrease in the wave amplitude gives a good idea of the absorption (Aki, 1969). In our country and around the world, many studies on absorption have been undertaken (Aki and Chouet, 1975; Aydın and Kadirov, 2008; Ugalde et al., 2010; Aydın, 2014, 2016). Pamukçu et al. (2015) investigated vertical mass movements in the south of İzmir. Furthermore, using the Coulomb software (Toda et al., 2011), Çırmık et al. (2017) studied the kinematic structure of the Gülbahçe fault. The impact area of the earthquakes nearest to the region was calculated initially in this context. Then, using the software Gamit/Globok (Herring et al., 2015), the GNSS data of Continuously Operating Reference Stations (CORS-TR) and the probable velocity structure in the region was estimated.

Within the context of this study, stress and strain distributions were calculated in Amasya-Tokat provinces and the surrounding region, and absorption analysis was undertaken for the same region. The relationship between the absorption study results and the Coulomb stress variation within the crust was investigated, and the seismicity was compared.

## 2. Tectonics of the Study Area

Seismic activity in Anatolia, the North Anatolian Fault Zone (NAFZ), the Aegean Graben System (AGS), the East Anatolian Fault Zone (EAFZ), the East Anatolian Compression Zone, the Hellenic Cyprus Arc, and the Central Anatolian Plain Region, six basic seismic regimes are used to express it. From the Saros Gulf to Karlıova, the NAFZ is around 1200 kilometers long (Figure 1). The NAFZ (Ketin, 1948; Şengör, 1979; Şengör and Natal'in, 1996; Şengör et al., 2005) is one of the world's most active strike-slip faults. The NAFZ connects the Aegean Taphrogene with the Eastern Anatolian High Plateau and extends parallel to the Black Sea for about 100 kilometers (Taymaz et al., 1991; Koçyiğit et al., 2001; Şengör et al., 2005). The Ezinepazarı fault (Şaroğlu et al., 1987) is a 250-kilometer-long fault that originates in the NAFZ and continues southwest through the Ezinepazarı, Amasya, and Sungurlu districts, ending

near Delice (Şaroğlu et al., 1987). The Merzifon fault is a 30-kilometer-long E-W directional fault that runs along the Merzifon plain from the south (Arpat and Şaroğlu, 1975; Şaroğlu et al., 1987) (Figure 1)

## 3. Method

### 3.1. Coulomb Analysis

Coulomb v3.3 software (Toda et al., 2011) is used to calculate displacement, stress, and strain at any depth caused by faults. Calculations in this software are performed in an elastic half-space environment containing the uniform, isotropic elastic properties specified by Okada (1992). In the Coulomb criterion, if the Coulomb stress ( $\sigma_f$ ) exceeds a certain value, the collapse that occurs on a surface is indicated by the following equation:

$$\sigma_f = \tau_\beta - \mu (\sigma_\beta - p) \quad (1)$$

The shear stress at the failure surface is  $\tau_\beta$ , the normal stress is  $\sigma_\beta$ , the pore water pressure is  $p$ , and the friction coefficient is  $\mu$  (Toda et al., 2011).

As a result, the overall effect of the shear stress and the normal stress change values equal the Coulomb stress variation estimated for a medium.

### 3.2. Absorption Analysis

The method of decay of seismic wave amplitudes overtime was utilized to find out the regional absorption coefficient. The following formula is used to calculate the amplitude decrease (absorption) (Aki and Richards, 1980),

$$A(x, t) = A_0^{(kx-wt)} \quad (2)$$

Where  $A_0$ ;  $x=0$  represents the amplitude (focal amplitude) at time  $t=0$  and distance  $x=0$ ,  $w$  is the angular frequency, and  $k$  is the number of waves. Absorption can be defined in terms of frequency or number of complex waves (Toksöz and Johnston, 1981).

The logarithm of the decrease in the amplitude of the harmonic wave expresses the absorption of the medium.  $A_{x_1}$ ; the amplitude at  $x_1$  distance,  $A_{x_2}$  the amplitude at  $x_2$  distance and ( $x_1 > x_2$ ), the absorption

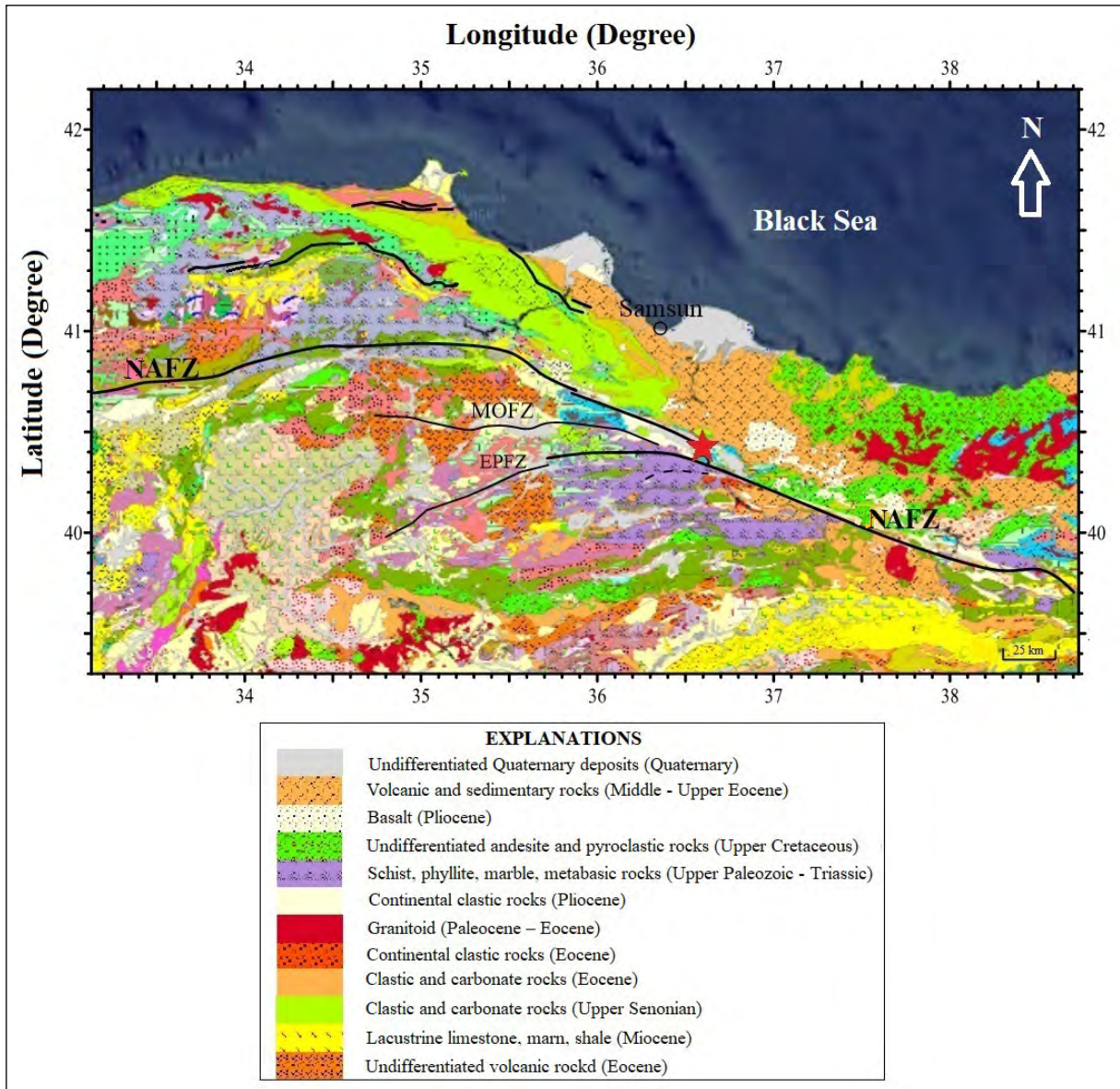


Figure 1- General tectonic and geological structure of the study region and its surroundings (modified from <http://yerbilimleri.mta.gov.tr/anasayfa.aspx>). NAFZ: The North Anatolian Fault Zone, MOFZ: Merzifon Ovacık Fault Zone, EPFZ: Ezinepazarı Fault Zone. The red star represents the epicenter of the earthquake that occurred on October 9th, 2015 ( $M_L=5.1$ ).

coefficient (Chopra and Alexeev, 2004) is defined as follows.

$$\delta = \frac{1}{x_2 - x_1} \ln \left( \frac{A(x_1)}{A(x_2)} \right) \quad (3)$$

$$A_x = A_0 e^{-\delta x} \quad (4)$$

#### 4. Data and Findings

An earthquake with a magnitude of  $M_L=5.1$  and a focal depth of roughly 5 km occurred near Yoldere - Erbaa (Tokat) on 09 October 2015, according to data

from the Boğaziçi University Kandilli Observatory Earthquake Research Institute (KOERI, 2015). According to the KOERI's estimated intensity map, the intensity value was  $I_0=V$  in the epicenter (Erbaa) and  $I_0=IV$  in Tokat province. The earthquake epicenter is located over the NAFZ. The largest earthquake in the region since 1900 ( $M = 7.0$ ) struck Erbaa - Tokat on December 20, 1942 (KOERI, 2015). The stress and strain values caused by the 9 October 2015 Yoldere - Erbaa (Tokat) ( $M_L = 5.1$ ) earthquake were computed

by Coulomb v3.3 software using the earthquake focal mechanism solution data (Table 1) provided by KOERI (Figure 2, 3).

In the other step of the study, GNSS data belonging to the CORS-TR stations were used to examine the tectonic effects of the earthquake ( $M_L=5.1$ ) that occurred in Yoldere-Erbaa district of Tokat province on 9<sup>th</sup> October 2015 (Figure 4). 61 days of data from the GNSS stations namely; TOK1 (Tokat, City Center), RDIY (Tokat, Reşadiye), GIRS (Giresun, City Center), FASA (Ordu, Fatsa), SAM1 (Samsun, City Center), VEZI (Samsun, Vezirköprü) and CORU (Çorum, City Center) including 30 days (9<sup>th</sup> September) before and 30 days (9<sup>th</sup> November) after earthquake data were evaluated with Gamit/Globk (Herring et al., 2015) software. The process was made by taking the Eurasia plate fixed. The International GNSS Service (IGS) stations; BUCU, GLSV, ISTA,

MATE, MIKL, NICO, PENC, TUBI, and ZECK were chosen, and ITRF 2014 was utilized as the International Terrestrial Reference System (ITRF). Table 2 shows the GNSS data evaluation strategy as well as the GNSS data assessment technique.

The time series (Figure 5) were constructed for the date range corresponding to the 252<sup>nd</sup> and 313<sup>th</sup> days, and the date of 9<sup>th</sup> October 2015, which coincides with the 282<sup>nd</sup> day of 2015. The Eurasian plate was fixed in the next step of this stage by analyzing the GNSS data of these stations for the years 2013, 2014, 2015, and 2016, as well as their velocities (Figure 6).

Data from the Boğaziçi University Kandilli Observatory, as well as the Ministry of Public Works and Settlement (Ministry of Environment, Urbanization, and Climate Change)'s KVK (Kavak, Samsun), RSDY (Reşadiye, Tokat), and TOKT

Table 1- The source parameters used in the Coulomb v3.3 software (Toda et al., 2011).

Poisson Ratio	Young Module (bar)	Coefficient of Friction	Institute Name	Strike Angle (°)	Dip Angle (°)	Rake Angle (°)	Depth (km)
0.25	$8 \times 10^5$	0.4	KOERI	280	86	178	5

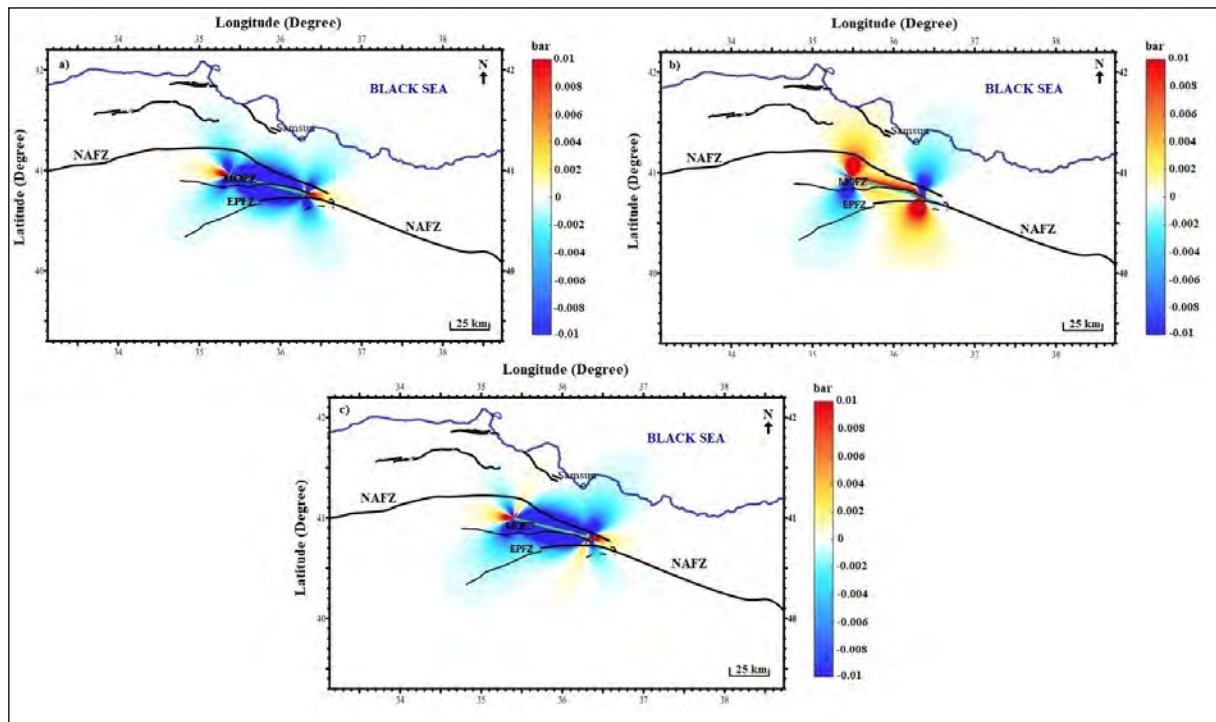


Figure 2- a) Shear stress, b) normal stress, and c) Coulomb stress values calculated by the earthquake focal mechanism data of KOERI (blue color: stress release, red color: stress loading).

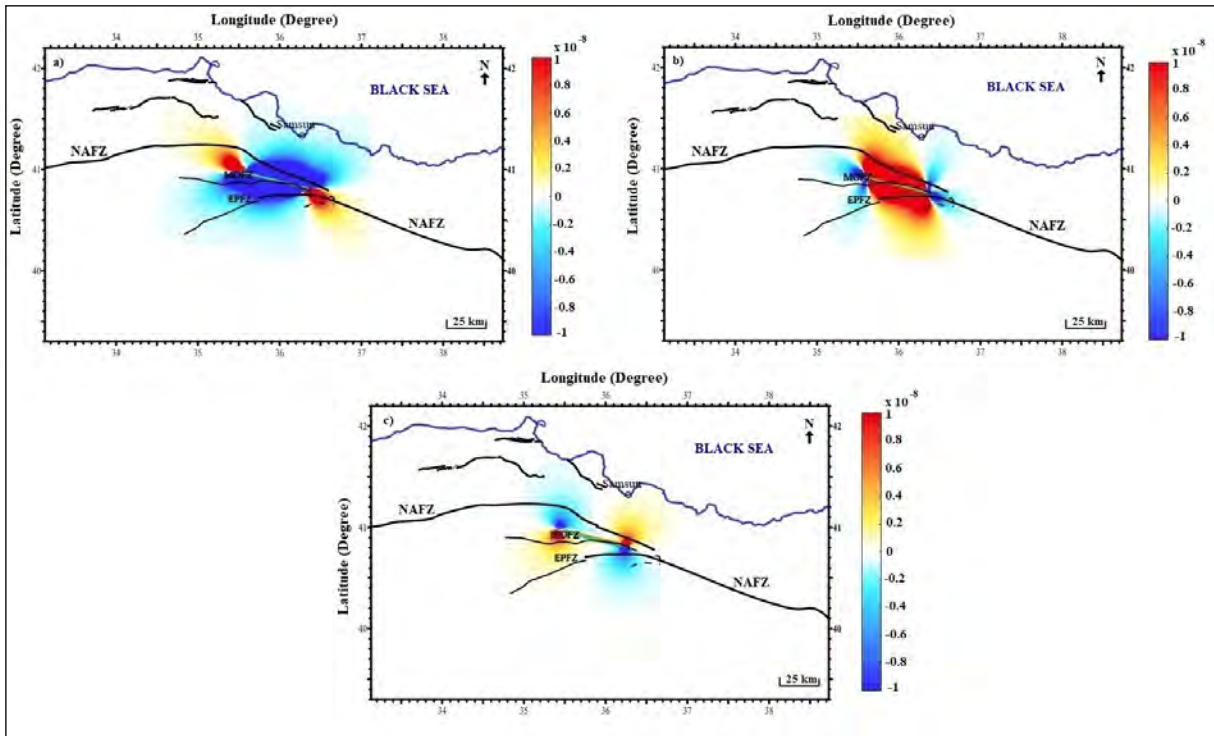


Figure 3- The strain a) XX, b) YY, and c) ZZ component variations calculated by using the earthquake focal mechanism data of KOERI.

Table 2- The processing strategy of GNSS data.

Software	Gamit/Globk Version 10.71
Data range	30 sec./24 hours Daily data
Process days	9 <sup>th</sup> September – 9 <sup>th</sup> November 2015 (between 252 <sup>th</sup> - 313 <sup>th</sup> days of 2015)
Cut-off angle	10°
Ephemeris Data	IGS final orbital and IGS ERP folders
Antenna Phase Centre Data	The weighted phase center model was associated with the high angle (PCV-antmod.dat).
The parameters of Troposphere	VMF1 (Vienna Mapping Function) was used. Zenith delay parameters were calculated every 2 hours.
International Terrestrial Reference System	ITRF 2014
Stabile Stations	Eurasia fixed reference system was used. BUCU, GLSV, ISTA, MATE, MIKL, NICO, PENC, TUBI, and ZECK stations were chosen as IGS reference stations.
Final Coordinate Calculation	61 days GNSS data were combined with GLOBK.

(Tokat) stations, were used in the absorption analysis (Figure 7). A total of 192 mass wave data from three stations (KVK, RSDY, and TOKT) were used in the study, which included the effects of all three faults in the area (Figure 7). These data were used to calculate the absorption values of Pg and Sg waves (Figure 8). The study included earthquakes with magnitudes ranging from 3 to 5.1 and focal depths ranging from 1.2 to 32 km, with the epicenter distances of

these earthquakes being around 150 km. For each of the three sites, regional absorption values and coefficients of Pg and Sg waves were determined. Figure 8 shows the calculated Pg and Sg absorption values for the earthquakes at the three stations. The regional absorption coefficients were calculated using these values (Table 3) and the regional absorption coefficients' lateral tomography images are presented in Figure 9.

**5. Discussion**

The evaluation of GNSS data and Coulomb stress/strain calculations in and around the Merzifon Fault and Ezinepazarı Fault zone within the scope of the study region in the NAFZ were done in the first part of this study. It was observed that the amplitude values were generally low in and around the region where the earthquake occurred, based on the stress and strain results (Figure 2) obtained with the Coulomb v3.3 software using the earthquake focal mechanism solutions values (Table 1) specified by KOERI for the Yoldere - Erbaa (Tokat) ( $M_L = 5.1$ ) earthquake on October 9, 2015.

According to the stress analysis results, stress is released in the blue sections and loaded in the red sections in the shear stress (Figure 2a), normal stress (Figure 2b), and Coulomb stress (Figure 2c) variations. In the shear stress values (Figure 2a), it is seen that there is stress loading at the east and west

ends of the fault, where the red color dominates, and stress releases at the northern and southern ends of the fault, where the blue color dominates. According to the normal stress values (Figure 2b), the stress is loaded in the northwest and southeast sections of the fault, and the tension is released in the NE - SW segment. The energy originating from the earthquake generates stress loading at both ends of the fault and stress release in the northern and southern sections of the fault, as seen in the Coulomb stress values which contain the overall effect of shear and normal stress (Figure 2c). In addition, the change values in the strain's XX (Figure 3a), YY (Figure 3b), and ZZ (Figure 3c) components were assessed as part of this study. Negative amplitude strain occurs in the north and south of the fault, while positive amplitude strain occurs at both ends of the fault, according to the XX component of the strain induced by the earthquake (Figure 3a). In the YY component of the strain (Figure 3b), it is seen that negative amplitude values occur

Table 3- The coordinates of the stations and the Pg, Sg regional absorption coefficients.

Station	Longitude (°)	Latitude (°)	Amount	$\delta P_g$ (km/1)	$\delta S_g$ (km/1)	$\delta S_g / \delta P_g$	Location
KVK	36.0463	41.0807	60	0.0203	0.0248	1.2216	SAMSUN
RSDY	37.3273	40.3972	57	0.029	0.0238	0.8207	TOKAT
TOKT	36.5445	40.3173	75	0.0106	0.0131	1.2359	TOKAT
TOTAL	-----	-----	192	-----	-----		

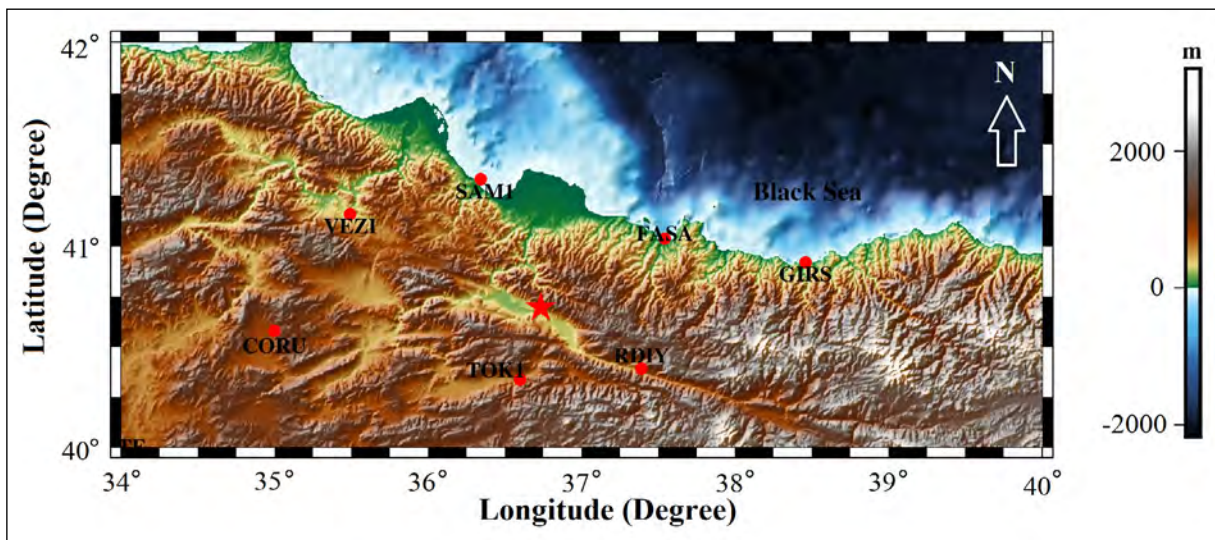


Figure 4- The view of the CORS-TR stations located near the epicenter (Erbaa district of Tokat province) of the 9<sup>th</sup> October 2015 ( $M_L=5.1$ ). Red dots: the locations of GNSS stations of CORS-TR, red star: the epicenter of the 9<sup>th</sup> October 2015 ( $M_L=5.1$ ) earthquake.

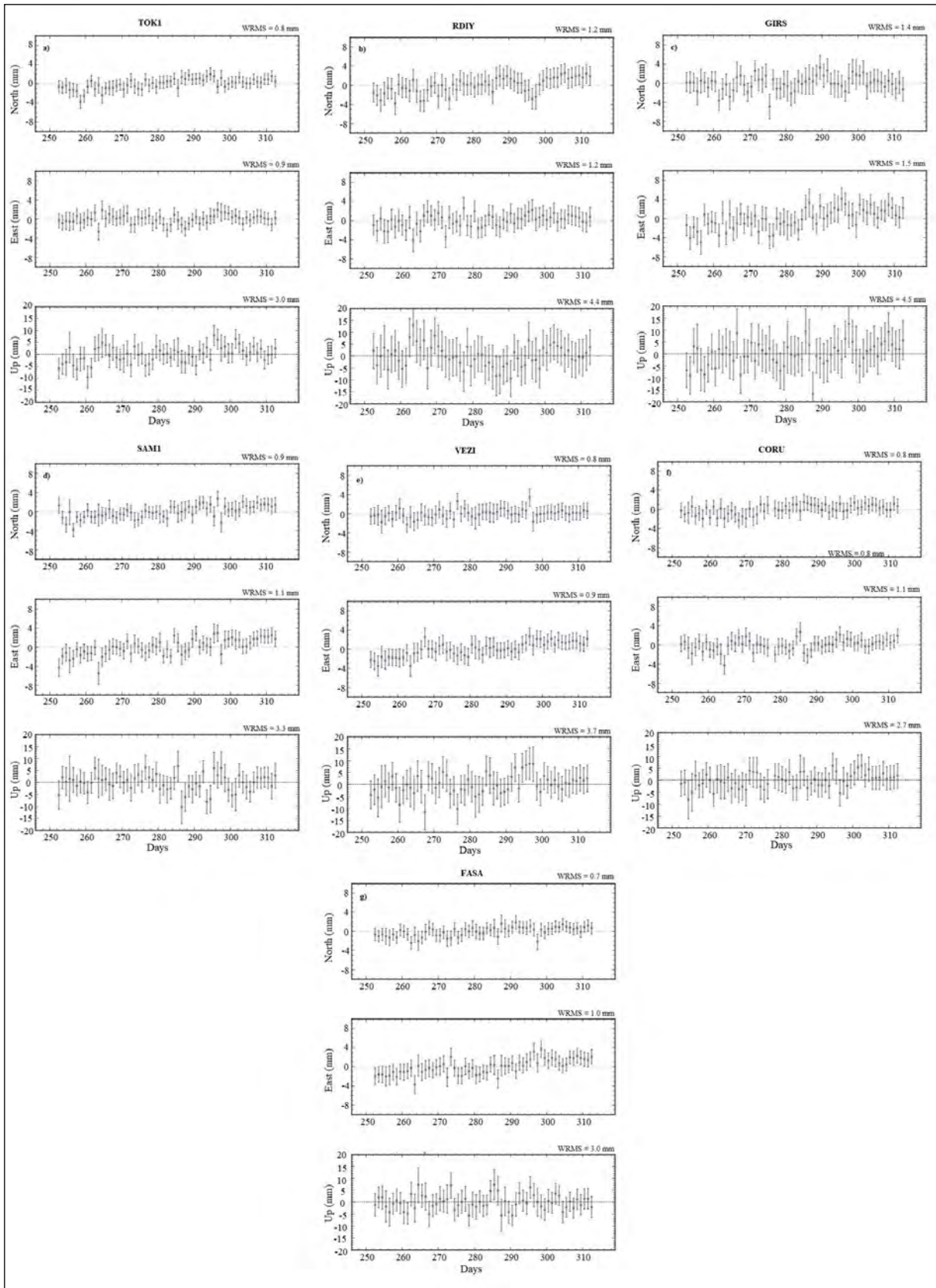


Figure 5- The north, east and up components of the time series for the 252<sup>nd</sup> - 312<sup>th</sup> days of 2015 of the stations a) TOK1, b) RDIY, c) GIRS, d) SAM1, e) VEZI, f) CORU, and g) FASA.

at both ends of the fault, whereas positive amplitude values occur in the north and south. In the ZZ component, negative amplitude values occur at both northwestern and southeastern of the fault.

In the other step, the deformation of GNSS stations induced by this earthquake was investigated with the time series (Figure 5). As a general result, it was found that the Yoldere - Erbaa earthquake on 9<sup>th</sup> October 2015 ( $M_L = 5.1$ ) did not generate significant deformation in the region. However, in the time series of TOK1 (Figure 5a), it is seen that there is a movement at the coseismic period (282<sup>th</sup> Julien day) at the northern component. A movement was also detected in the eastern component at the CORU (Figure 5f). It can be said that the Tokat - Erbaa earthquake ( $M_L=5.1$ ) caused deformation in the northern component at TOK1 station which is closest to the epicenter. For investigating the reason of the movement at CORU (Figure 5f), which location is not close to the epicenter (Figure 4), the tectonism of this region needs to be studied in detail.

In the other step of the study, the velocities of the GNSS stations were calculated for the years 2013, 2014, 2015, and 2016 (Figure 6). In Figure 6, it is seen that the velocities of SAM1, FASA and GIRS stations were slower than the velocities of VEZI,

CORU, TOK1, and RDIY stations. The directions of the velocity vectors of the stations are towards NW in general. According to the differences in the velocity vector directions, it is seen that the north component of the velocity of CORU is less dominant than the other stations (Figure 6). The velocities of CORU (Çorum, City Center) and TOK1 (Tokat, City Center) are faster than other GNSS stations in the region, as seen in Figure 6. The difference in velocity vector direction at the CORU station can be interpreted as the tectonic structure of the region in which CORU is located is different from the region of TOK1.

According to the findings of the study area, it can be said that the crustal motion is stable. There are two possible explanations for this event. First, an elastic deformation in the study area might be explained by the accumulation of energy or the fact that this area is more rigid than others. Another option is that the data was collected from stations that were relatively unaffected by the earthquake since they were located far from the epicenter. Therefore, GNSS measurements on the bedrock representing the kinematic mechanism should be pre-planned in the study area to determine the underground deformation more precisely and in detail, or continuous GNSS stations should be used to continually monitor this tectonism.

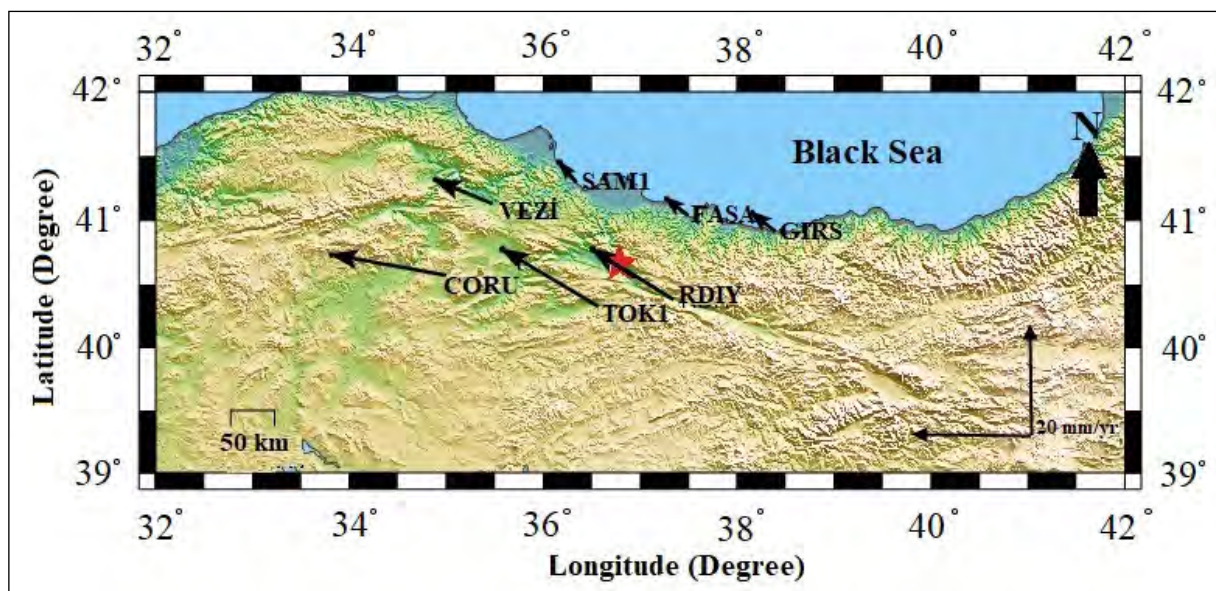


Figure 6- The velocity vectors estimated with the Eurasian plate fixed using GNSS data of CORS - TR stations between the years 2013-2016. The epicenter of the 9<sup>th</sup> October 2015 ( $M_L = 5.1$ ) earthquake is shown by a red star

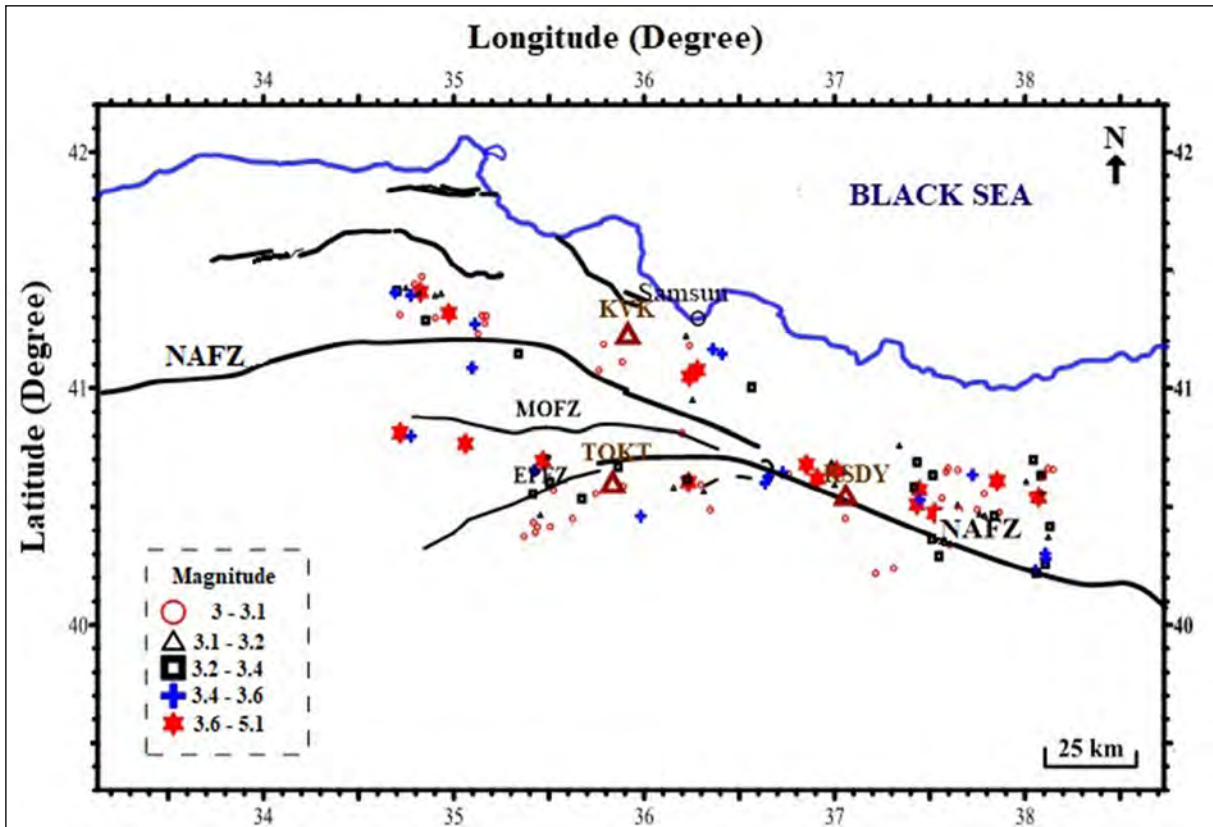


Figure 7- The locations of the stations (KVK, TOKT, RSDY) and the distribution of earthquakes used in the absorption analysis. Burgundy triangles represent the locations of the stations. NAFZ: North Anatolian Fault Zone, MOFZ: Merzifon Ovacık Fault Zone, EPFZ: Ezinepazarı Fault Zone.

Seismic waves are affected not only by the elastic parameters, lithological, and chemical properties of the medium but also by changes in the medium's stress/strain properties (Aydın, 2011). A decrease in absorption is caused by an increase in the underground pressure. One of the elements controlling absorption is pressure and/or stress as the first order (Aydın, 2011). The internal stress/strain distribution and regional absorption variation, which are effective in tectonic forces created by elastic deformation energy accumulating in the brittle crust over time, were explored in another step of the study in light of this knowledge. For KVK, TOKT, and RSDY stations, absorption values (Figure 8) and absorption coefficients (Figure 9) were calculated. The highest  $P_g$  and  $S_g$  absorption values in the region were obtained from KVK (Figure 8a) and RSDY (Figure 8b) station, whereas TOKT (Figure 8c) station had the lowest absorption values. The regional absorption coefficient ( $\delta_p$  and  $\delta_s$ ) values in KVK and RSDY stations are

greater than the values in the TOKT station. (Figure 9). The RSDY station has the highest  $P_g$  and  $S_g$  absorption (Figure 8b) and regional absorption coefficients values (Figure 9a, and 9b). Therefore, it can be said that the crustal structure of RSDY and its surroundings have intense faulting mechanism than the crustal structure of KVK and its surroundings. The reason of lower values of TOKT station (Figure 8 and Figure 9) than others can be explained by the fact that the location of the TOKT is close to the MOFZ and EPFZ, as seen in Figure 9. In addition, the lowest findings (Figure 9) show that TOKT and its surroundings are under more pressure than the other two stations. These findings show that the compression impact is stronger in the region between NAFZ and EPFZ than other regions and lower compression affects Reşadiye (Tokat) and its surroundings.

When the Coulomb stress values obtained from the Coulomb analysis are compared with the locations of the seismology stations used in the study (Figure 10),

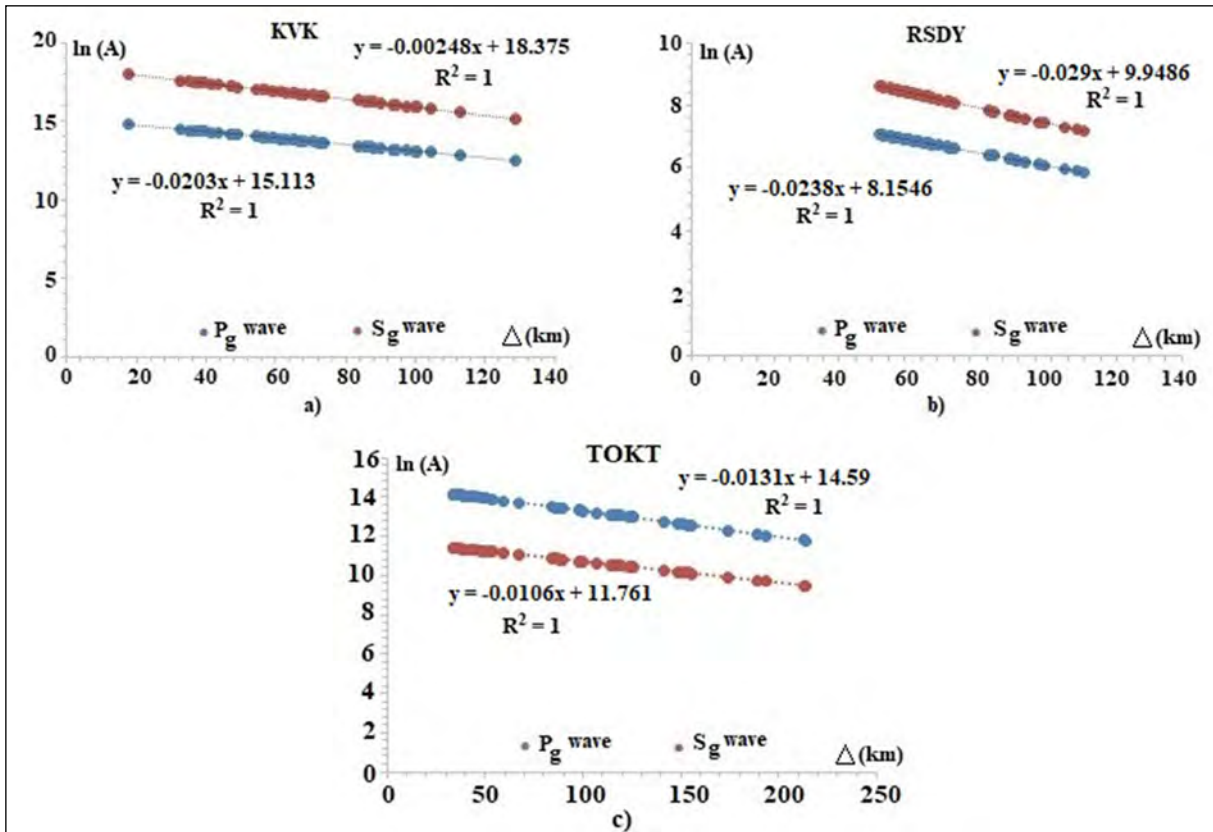


Figure 8-  $\ln(A) - \Delta$  (km) graphs and  $P_g - S_g$  absorption values of the stations; a) KVK, b) RSDY and c) TOKT.

it is observed that the TOKT station is located in the stress relaxation region caused by the 9<sup>th</sup> October 2015 earthquake, while RSDY and KVK stations are outside the impact area.

## 6. Results

According to the stress and strain values calculated with the Coulomb software using the earthquake focal mechanism solutions values of the 9<sup>th</sup> October 2015 Yoldere-Erbaa (Tokat) ( $M_L = 5.1$ ) earthquake, the shear, normal, and Coulomb stress values are changing between  $-0.01 - 0.01$  bars. The XX, YY and ZZ components of the strain values have values ranging from  $-1 \cdot 10^8$  to  $1 \cdot 10^8$ . As a result, the amplitude of the stresses and strains caused by the earthquake are generally low in and around the region where the earthquake occurred.

The  $\delta p$  absorption coefficients ranging from 0.01 to 0.03 and  $\delta s$  absorption coefficients ranging from 0.0135 to 0.025 of the lateral tomography of

the study area. According to the regional absorption coefficients, it can be said that the stress accumulation surrounding and under the crust of the TOKT station, where the absorption was the least, are greater than the other two stations. It can be deduced that pressure is accumulated, particularly around the MOFZ and EPFZ and their surroundings.

While the velocity is 20 mm per year for NAFZ and its surroundings, it is far below 20 mm per year at sites (SAM1, FASA, GIRS) located in the north of the NAFZ. The fact that the stations located in the north of the NAFZ (SAM1, FASA, GIRS) have slower velocities than the others (VEZI, RDIY, CORU, TOK1) can be obtained with the effect of the sense of NAFZ (right-lateral strike-slip fault).

## Acknowledgements

This research was conducted as part of the Atatürk University Scientific Research Projects (Project No: 8443), which was a collaborative effort between

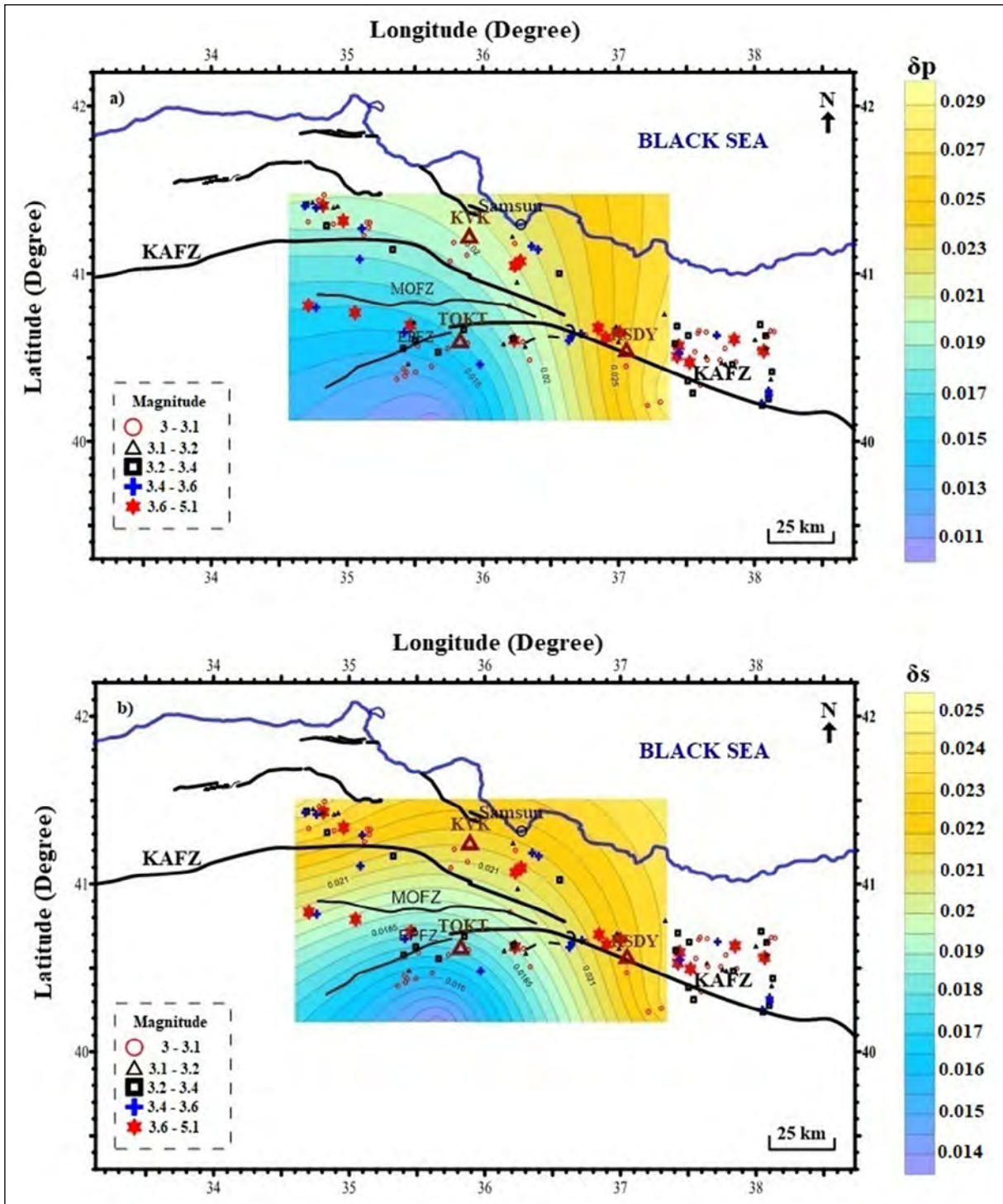


Figure 9- Obtained from the station; a)  $\delta\rho$  regional absorption coefficients, and b) the lateral tomography of  $\delta\sigma$  regional absorption coefficients. NAFZ: North Anatolian Fault Zone, MOFZ: Merzifon Ovacık Fault Zone, EPFZ: Ezinepazarı Fault Zone.

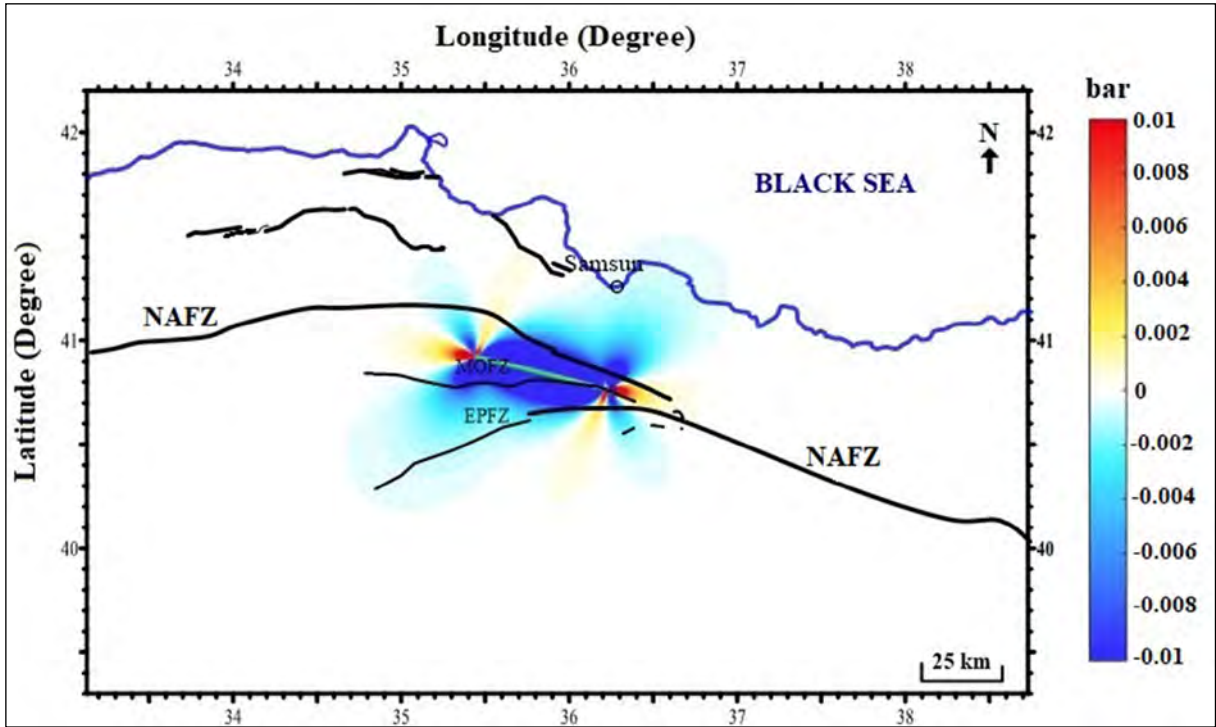


Figure 10- Coulomb stress changes on the study field. NAFZ: North Anatolian Fault Zone, MOFZ: Merzifon Ovacık Fault Zone, EPFZ: Ezinepazarı Fault zone.

Atatürk University and Dokuz Eylül University. GNSS data used in the study were provided from the CORS-TR system is operated by the General Directorate of Maps and the General Directorate of Land Registry and Cadastre. Generic Mapping Tools (GMT) were used to create some figures (Wessel et al., 2019). We'd like to express our gratitude to the three referees for their time and participation in the article's development.

## References

- Affandi, A. K., Sailah, S., Ardiansyah, S., Wafiazizi, M. 2019. An analysis of Coulomb stress change and triggering interaction toward seismic activities in the area West Sumatera within January 2000 - June 2018. *Journal of Physics, Conference Series*, 1282.
- Aki, K. 1969. Analysis of the seismic coda of local earthquakes as scattered waves. *Journal of Geophysical Research* 74(2), 615-631.
- Aki, K., Chouet, B. 1975. Origin of coda waves: source, attenuation, and scattering effects. *Journal of Geophysical Research* 80(23), 3322-3342.
- Aki, K., Richards, P. G. 1980. *Quantitative Seismology: Theory and Methods*. Freeman, San Francisco.
- Arpat, E., Şaroğlu, F. 1975. Türkiye'deki bazı önemli genç tektonik olaylar. *Türkiye Jeoloji Kurumu Bülteni* 18(1), 91-101.
- Aydın, U. 2011. Erzincan - Muş - Oltu (Erzurum) arasındaki yüzey kayaçlarının soğurma özelliklerinin incelenmesi. *Doktora Tezi, Çukurova Üniversitesi, Fen Bilimleri Enstitüsü*, 136, Adana.
- Aydın, U. 2014. Crustal stresses and seismodynamic characteristics in the upper crust. *Open Journal of Earthquake Research* 3(04), 143.
- Aydın, U. 2016. Relationships between geotectonic and seismodynamic characteristics of the crust in the Eastern Anatolia. *Acta Geodaetica et Geophysica* 51(1), 69-79.
- Aydın, U., Kadirov, A. 2008. Erzincan ve çevresinde P dalgası soğurulması. *Sakarya Üniversitesi Fen Bilimleri Enstitüsü Dergisi* 12(1), 1-8.
- Chinnery, M. 1963. The stress changes that accompany strike - slip faulting. *Bulletin of the Seismological Society of America* 53(5), 921-932.
- Chopra, S., Alexeev, V. 2004. A new approach to enhancement of frequency bandwidth of surface seismic data. *First Break* 22(8).
- Çırmık, A. 2014. Determining the deformations in Western Anatolia with GPS and gravity measurements.

- Doktora Tezi, Dokuz Eylül Üniversitesi, Fen Bilimleri Enstitüsü, 196, İzmir.
- Çırmık, A., Pamukçu, O. 2017. Clarifying the interplate main tectonic elements of Western Anatolia, Turkey by using GNSS velocities and Bouguer gravity anomalies. *Journal of Asian Earth Sciences* 148, 294-304.
- Çırmık, A., Özdağ, O. C., Doğru, F., Pamuk, E., Gönenç, T., Pamukçu, O., Akgün, M., Arslan, A. T. 2016. The soil behaviors of the GNSS station. *Earth Sciences* 5(5), 70.
- Çırmık, A., Doğru, F., Gönenç, T., Pamukçu, O. 2017. The stress/strain analysis of kinematic structure at Gülbahçe Fault and Uzunkuyu Intrusive (İzmir, Turkey). *Pure and Applied Geophysics* 174(3), 1425-1440.
- Harris, R. A., Simpson, R. W. 1992. Changes in static stress on southern California faults after the 1992 Landers earthquake. *Nature* 360(6401), 251-254.
- Herring, T. A., King, R. W., Floyd, M. A., McClusky, S. C. 2015. Introduction to GAMIT/GLOBK, Release 10.6., Massachusetts Institute of Technology, Cambridge.
- KOERI (Boğaziçi University Kandilli Observatory Earthquake Research Institute, Kandilli Rasathanesi Deprem Araştırma Enstitüsü). 2021. 09 Ekim 2015 Yoldere-Erbaa (Tokat) Depremi. <http://www.koeri.boun.edu.tr/sismo/2/wp-content/uploads/2015/10/09-Ekim-2015-Yoldere-Erbaa-Tokat-Depremi-1.pdf>. 1 Mart 2021.
- Ketin, I. 1948. Über die tektonisch-mechanischen Folgerungen aus den grossen anadoluischen Erdbeben des letzten Dezenniums. *Geologische Rundschau* 36(1), 77-83.
- Koçyiğit, A., Yılmaz, A., Adamia, S., Kuloshvili, S. 2001. Neotectonics of East Anatolian Plateau (Turkey) and Lesser Caucasus: implication for transition from thrusting to strike-slip faulting. *Geodinamica Acta* 14(1-3), 177-195.
- Okada, Y. 1992. Internal deformation due to shear and tensile faults in a half-space. *Bulletin of Volcanology* 47, 239-246.
- Pamukçu, O., Gönenç, T., Çırmık, A., Sındırgı, P., Kaftan, I., Akdemir, Ö. 2015. Investigation of vertical mass changes in the south of İzmir (Turkey) by monitoring microgravity and GPS/GNSS methods. *Journal of Earth System Science* 124(1), 137-148.
- Stein, R. S., King, G. C., Lin, J. 1992. Change in failure stress on the southern San Andreas fault system caused by the 1992 magnitude= 7.4 Landers earthquake. *Science* 258(5086), 1328-1332.
- Şaroğlu, F., Emre, Ö., Boray, A. 1987. Türkiye'nin diri fayları ve depremsellikleri. Maden Tetkik ve Arama Genel Müdürlüğü, Rapor No: 8174, Ankara.
- Şengör, A. 1979. The North Anatolian transform fault: its age, offset and tectonic significance. *Journal of the Geological Society* 136(3), 269-282.
- Şengör, A. C., Natal'in, B. A. 1996. Turcic-type orogeny and its role in the making of the continental crust. *Annual Review of Earth and Planetary Sciences* 24(1), 263-337.
- Şengör, A., Tüysüz, O., İmren, C., Sakıncı, M., Eyidoğan, H., Görür, N., Le Pichon X., Rangin, C. 2005. The North Anatolian fault: a new look. *Annual Review of Earth and Planetary Sciences* 33, 37-112.
- Taymaz, T., Jackson, J., McKenzie, D. 1991. Active tectonics of the north and central Aegean Sea. *Geophysical Journal International* 106(2), 433-490.
- Toda, S., Stein, R. S., Sevilgen, V., Lin, J. 2011. Coulomb 3.3 graphic-rich deformation and stress-change software for earthquake, tectonic, and volcano research and teaching-user guide. US Geological Survey Open - file report: 1060(2011), 63.
- Toksöz, M. N., Johnston, D. H. 1981. *Seismic Wave Attenuation*. Society of Exploration Geophysicists, Tulsa, Okla, 2.
- Ugalde, A., Carcolé, E., Vargas, C. A. 2010. S-wave attenuation characteristics in the Galeras volcanic complex (southwestern Colombia). *Physics of the Earth and Planetary Interiors* 181(3-4), 73-81.
- Wessel, P., Luis, J. F., Uieda, L., Scharroo, R., Wobbe, F., Smith, W. H. F., Tian, D. 2019. The generic mapping tools version 6. *Geochemistry, Geophysics, Geosystems* 20, 5556-5564.





# Bulletin of the Mineral Research and Exploration

<http://bulletin.mta.gov.tr>



## Formation and tectonic evolution of structural slices in eastern Kargı Massif (Çorum, Türkiye)

Cihan YALÇIN<sup>a\*</sup>, Nurullah HANILÇI<sup>b</sup>, Mustafa KUMRAL<sup>c</sup> and Mustafa KAYA<sup>c</sup>

<sup>a</sup>Republic of Türkiye Ministry of Industry and Technology, General Directorate of Industrial Zones, Ankara, Türkiye

<sup>b</sup>Istanbul University-Cerrahpaşa, Department of Geological Engineering, İstanbul, Türkiye

<sup>c</sup>Istanbul Technical University, Department of Geological Engineering, Faculty of Mines, İstanbul, Türkiye

Research Article

### Keywords:

Central Pontides, Tectonic Slice, Accretionary Complex, Geodynamic, Kargı, Çorum.

### ABSTRACT

The closure of Tethys Ocean has led to shaping the Central Pontides together with different types of rocks. In the east of Kargı (Gökçedoğan), which is located in the Central Pontides, allochthonous rocks of Late Palaeozoic- Early Cenozoic age and autochthonous units exist together, and allochthonous rocks present various tectono-stratigraphical sequences. Distinctive tectonic slices developed in the area as a consequence of the thrusting of the Permian carbonates from the north towards the south over the Middle Jurassic accretionary Complex (Kunduz Metamorphites) that form the basement of the area, and also because of the thrusting of the units of the Kirazbaşı Complex (ophiolitic melange) and Mesozoic carbonate rocks over this basement from the south towards the north because of the closure of Tethys Ocean. This paper presents whole-rock geochemical data, which suggest that the metabasites and the ophiolitic basalts are tholeiitic. The Jurassic metabasites from the Kunduz Unit and basalts from ophiolitic melange are characterized by the mid-ocean ridge basalt (MORB) and within plate tholeiites. This paper highlights the occurrence of the tectonic slices in the area is closely related to the tectonic evolution of the Tethys Ocean.

Received Date: 02.07.2021

Accepted Date: 02.02.2022

## 1. Introduction

The Pontides comprise an east-west trending mountain belt in the northern Türkiye and are accepted as a 1500 km long part of the Alpine-Himalayan belt by Ketin (1966). The Pontides separated from the edge of Southern Eurasia in Late Barremian or Aptian times, during the subsidence of the Black Sea Basin (Finetti et al., 1988; Görür, 1988; Robinson et al., 1996; Rice et al., 2006; Hippolyte et al., 2010; Nikishin et al., 2015). Later that sequence deformed by colliding with Kırşehir and Anatolide-Taurid microcontinents with the closure of branches of the Tethys Ocean (Şengör

and Yılmaz, 1981; Şengör et al., 1982; Okay et al., 1994; Lefebvre et al., 2013).

The Pontide Belt is commonly classified as the western, the central, and the eastern Pontides (Okay et al., 1994), and is also divided into the İstanbul, the Istranca, and the Sakarya zones. Due to the closure of Paleotethys Ocean and Intra-Pontide Ocean, the suture zones formed in this belt (Okay et al., 2013).

The Central Pontides consist of metamorphic, magmatic, oceanic, and sedimentary rock groups, ranging in age from Late Paleozoic to Early Cenozoic

Citation Info: Yalçın, C., Hanılçı, N., Kumral, M., Kaya, M. 2022. Formation and tectonic evolution of the tectonic slices in the eastern Kargı Massif (Çorum, Türkiye). Bulletin of the Mineral Research and Exploration 169, 135-154.  
<https://doi.org/10.19111/bulletinofmre.1067604>

\*Corresponding author: Cihan YALÇIN, [cihan.yalcin@sanayi.gov.tr](mailto:cihan.yalcin@sanayi.gov.tr)

(Robertson, 2002; Robertson and Ustaömer, 2004; Robertson et al., 2006; Okay et al., 2006, 2013; Okay and Nikishin, 2015; Aygül et al., 2015b, 2016).

Pre-Jurassic high pressure-low temperature (HP/LT) metamorphic rock units and younger ophiolitic rock units outcropping in the wide areas in the south of the Central Pontides are the products of the subduction-accretionary complex which emerged with the closure of Tethys ocean (Okay et al., 2006, 2013; Marroni et al., 2014; Aygül et al., 2015a, 2015b, 2016; Çelik et al., 2016, 2018). This zone has been referred as being tectonic complexes and as metamorphic complexes (Domuzdağ, Kunduz, Çangaldağ, Saka, Middle Jurassic Accretionary Complex) by many researchers (Tüysüz, 1990; Ustaömer and Robertson,

1997; Yılmaz et al., 1997; Okay et al., 2006, 2013; Çelik et al., 2016; Altherr et al., 2020). These areas which include Middle Jurassic and Cretaceous Accretionary Complex are also named as Central Pontide Supercomplex (Figure 1a) (Okay et al., 2013; Marroni et al., 2014; Okay and Nikishin, 2015) or Central Pontide Structural Complex (CPSC) (Tekin et al., 2012; Çimen et al., 2016, 2017, 2018). The area has undergone metamorphism in greenschist facies in general with the emplacement of Tethyan ophiolites (Okay and Göncüoğlu, 2004). This change was reported to occur in the Albian stage under low pressure and temperature conditions (LP, LT) in consideration of the results obtained by finding the  $107.0 \pm 4.6$  Ma –  $114.1 \pm 3.3$  Ma age from the metamorphic rocks in greenschist facies (Okay et al., 2013).

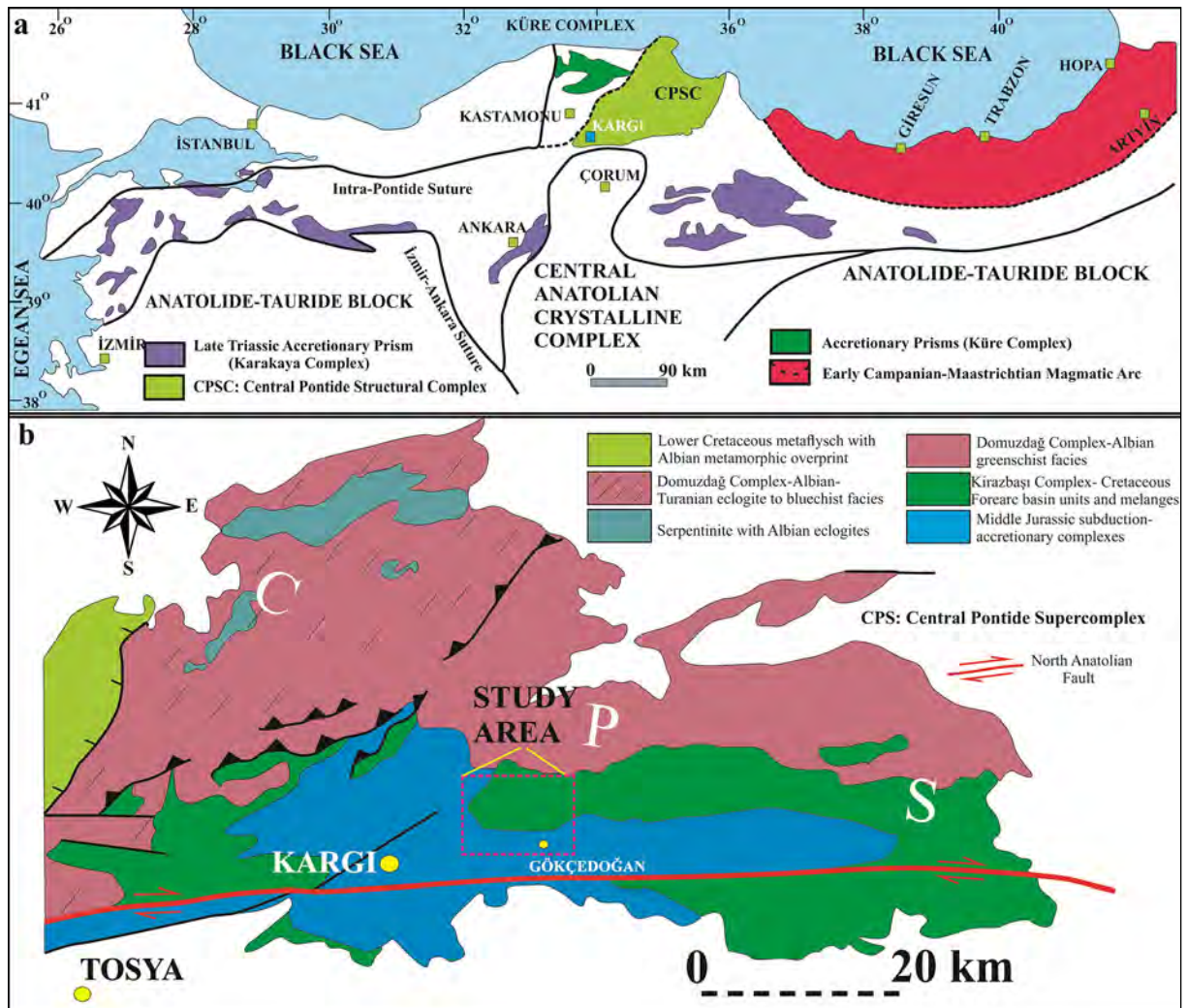


Figure 1- a) Position of the study area between Türkiye's structural zones (Göncüoğlu, 2010; Eyüboğlu et al., 2014; Çimen et al., 2017; Günay et al., 2018), and b) position of the study area in the Central Pontide Supercomplex (Tüysüz, 1990; Okay et al., 2013, 2014; Aygül et al., 2016).

After the age determination studies carried out in the before-mentioned supercomplex in recent years, 3 distinctive units are identified; 1: Middle Jurassic subduction/accretionary complex in the south part; 2: Kirazbaşı Complex formed by an ophiolitic melange and; 3: Domuzdağ Complex with varying metamorphism conditions towards the north have been identified in the eastern Kargı area (Figure 1b) (Aygül et al., 2016). Çelik et al. (2016) conducted an age determination of  $^{40}\text{Ar}/^{39}\text{Ar}$  from the amphiboles of Jurassic metabasites in the Accretionary Complex and determined that the cooling age is in between  $159.4 \pm 0.4$  Ma and  $163.5 \pm 0.8$  Ma. Owing to the coexistence of allochthonous rocks and autochthonous units of Late Palaeozoic–Early Cenozoic age range in the area, there are various tectono-stratigraphical sequences in the east of Kargı (Gökçedoğan).

Uğuz and Sevin (2009) reported that the allochthonous rocks are formed by lower and upper tectonic slices in the area and that the metamorphic rocks (Bekirli Formation) are autochthonous. Some researchers argue that the metamorphic complexes identified in the Central Pontides have allochthonous nature (Ustaömer and Robertson, 1997, 1999; Okay et al., 2006, 2013; Çimen et al., 2016). Certain kinds of stratigraphic sequences have been formed in the study area together with the thrust of Palaeozoic and Mesozoic carbonate rocks over the units which belong to the Middle Jurassic accretionary Complex and the Kirazbaşı Complex (Okay et al., 2013). Geological mapping, new geochemical data, and isotopic age data in the Central Pontides in recent years have revealed different geodynamic models (Okay et al., 2014; Aygül et al., 2015b; Gücer et al., 2016; Çimen et al., 2016, 2017, 2018; Günay et al., 2018). For this reason, more detailed mapping studies should be done and associated with these regions. In addition, there are Cyprus type and Besshi type massive sulphide mineralizations associated with mafic tholeiitic volcanism, metavolcaniclastics, and metaclastics also there are arc-back arc geochemical signatures in the Central Pontides (Çakır, 1995; Altun et al., 2015; Çimen et al., 2016; Akbulut et al., 2016; Günay et al., 2018, 2019; Yalçın, 2018).

This study describes for the first time the tectonic slices formed by Gökçedoğan and adjacent lithostratigraphic units, a detailed geology map, and

a structural element map with a scale of 1/25.000. The main objective of this paper is to exhibit the relationship of the rocks in the field. Then we model their tectonic evolution with the help of geochemical analysis of basalts in different ages within the detailed geological information.

## 2. Geology

The Küre volcanogenic massive sulphide (VMS) Cu deposit (Kastamonu), established in the Central Pontides is held in the Cyprus type (Ustaömer and Robertson, 1997; Çakır, 1995; Altun et al., 2015; Akbulut et al., 2016) or Besshi type (Koç et al., 1995). Another VMS deposit is located 54 km north of the study area was observed within the metamorphic rocks in the Çangaldağ complex (Dönmez et al., 2013; Günay et al., 2018). Yalçın (2018) identified that stratiform type Cu-Zn mineralization occurred in metamorphic rocks on Gökçedoğan (Kargı-Çorum) and explained the formation of the ore. Geological informations declared that the mineralization is metamorphosed VMS deposit and is complementary to the Besshi-type Cu-Zn deposits (Yalçın, 2018). Günay et al. (2019) identified Zeybek VMS deposit in the Central Pontides near the study area. Detailed geological maps and supporting geochemical data will constantly be required, as the relevant VMS deposits in this province are recognized.

Various types of Paleozoic, Cenozoic and Quaternary rock groups showing structural and stratigraphic contacts are present in the study area (Figure 2). Different tectono-stratigraphic sequences have occurred in the region where carbonate rocks are thrust not only to units belonging to the ophiolitic mélangé (Figure 3a, b) but also to the Kunduz Metamorphics of the ophiolitic mélangé (Figure 3c, d).

### 2.1. Allochthonous Units

Allochthonous rock groups are extensively observed in the study area and are represented by the Kunduz metamorphites and the ophiolitic melange. All these rocks are covered by the Permian and Jurassic-Cretaceous carbonate rocks. Allochthonous rocks overlain by autochthonous units.

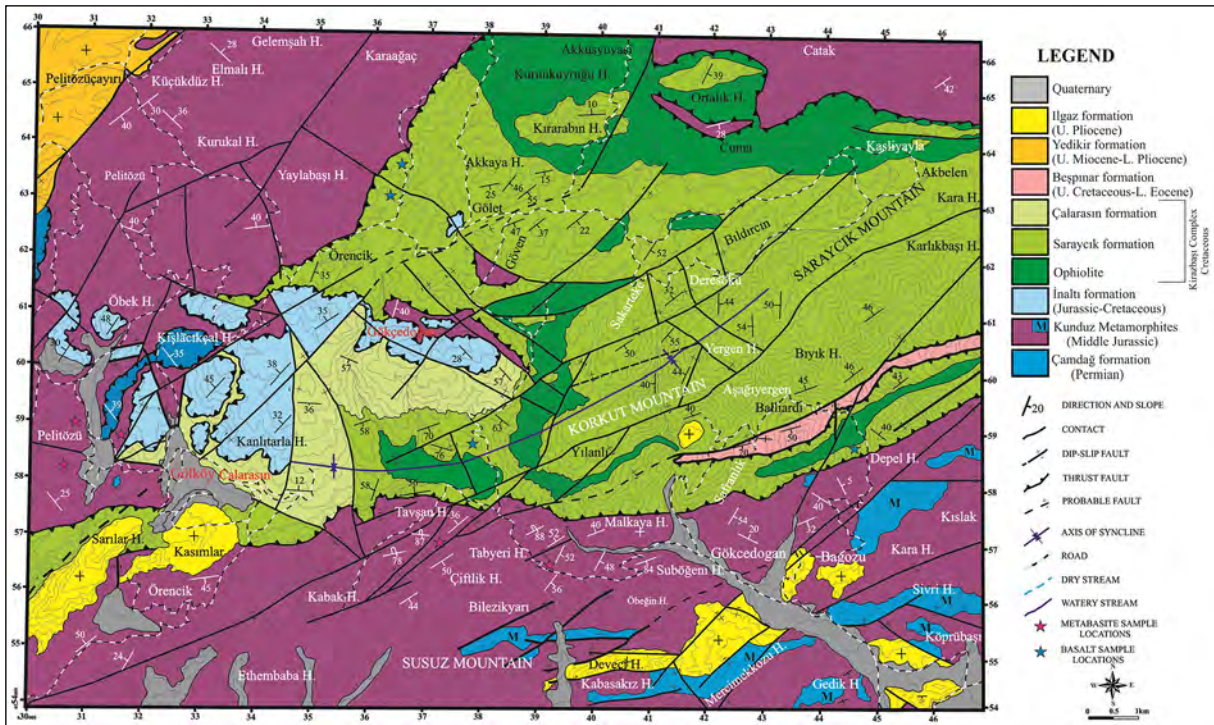


Figure 2- Geology map of the study area.

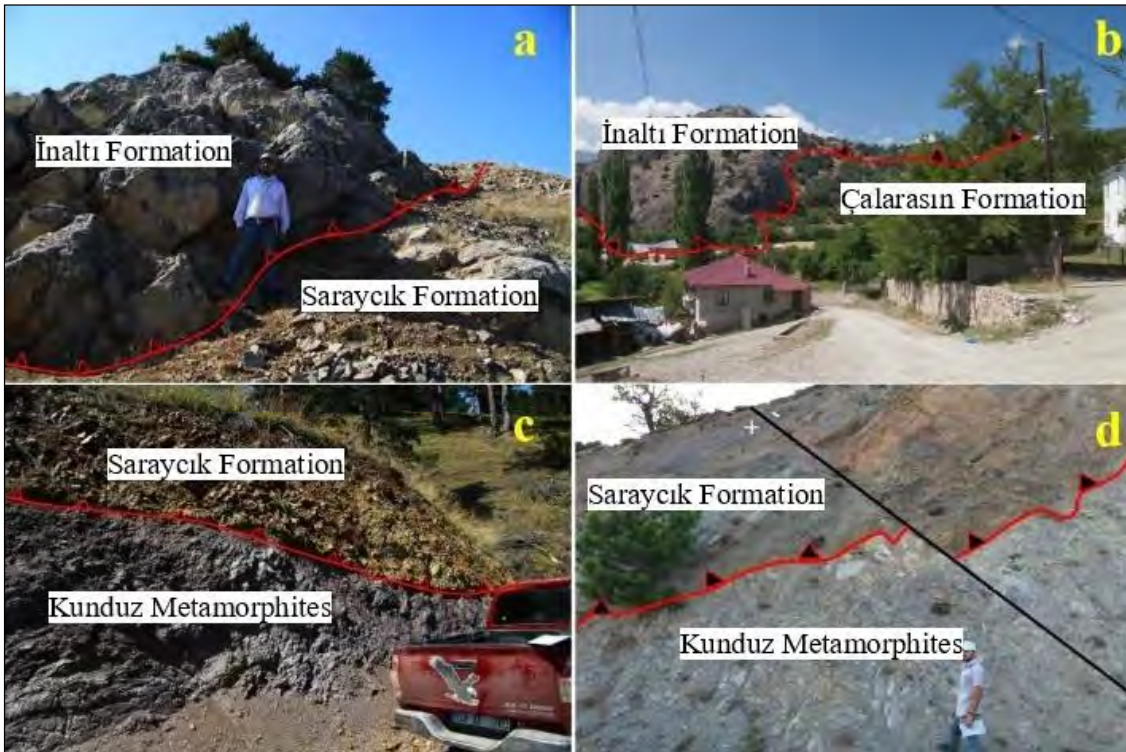


Figure 3- Observed thrusts in the study area; a) carbonate rocks belonging to the İnaltı Formation thrusting onto the Saraycık Formation west of Gölet, looking northwest from the southeast, b) thrusting of carbonate rocks belonging to the İnaltı Formation to the Çalarasin Formation in the neighborhood of Çalarasin and around Gölköy, looking northwest from the southeast, c) thrusting of Saraycık Formation to Kunduz metamorphites in the northeast of Gökçedöğan plateau, looking northwards from the south, and d) thrusting of Saraycık Formation to Kunduz metamorphites southeast of Kasımlar, looking northwards from the south).

### 2.1.1. Kunduz Metamorphites

Kunduz Metamorphites which form the basement of the area and is composed of metamorphic rocks (Tüysüz, 1990) expands over a large part of the study area (Figure 2). It is composed mainly of mica-rich metasandstone, quartzite, phyllite, metabasite, mica schist, gneiss, marble blocks, amphibole schist and metachert, (Yılmaz and Tüysüz, 1984). Middle Jurassic age has been determined for this unit located in the accretionary complex belonging to the Central Pontide Supercomplex (Marroni et al., 2014; Okay et al., 2013; Okay and Nikishin, 2015) and this unit can be correlated with Bekirli Formation described by Yılmaz and Tüysüz (1984). Martin Complex, which is showing geological features similar to Kunduz Metamorphites, consists of an interlayers of metabasite and chert, which is composed of similar lithologies and possibly deposited in an oceanic environment (Okay et al., 2013).

This unit is overlain by Middle Eocene Beşpınar Formation with angular unconformity near the study area (Uğuz and Sevin, 2009) and by ophiolitic melange, Jurassic-Cretaceous İnaltı Formation, and Permian Çamdağ Formation with a tectonic contact (Figure 2).

### 2.1.2. Ophiolitic Melange (Kirazbaşı Complex)

Ophiolitic Melange which belongs to the Kirazbaşı Complex (Tüysüz, 1990; Rice et al., 2006; Aygül et al., 2016) is composed of Kargı Ophiolite, Saraycık and Çalarasın Formation. Kargı Ophiolite consists of dunite, serpentinite, spilitic lava on gabbro (Yılmaz ve Tüysüz, 1984; Uğuz and Sevin, 2009), Saraycık Formation consists of metadiabase, metabasalt, radiolarite, chert, mudstone and pelagic limestones (Yılmaz and Tüysüz, 1984; Okay et al., 2006; Rice et al., 2006) and Çalarasın Formation consists of thin bedded, siltstone intercalated with sandstone-shale and mudstone alternation (Yılmaz and Tüysüz, 1984) respectively. The contact relations between these units are tectonic in some areas and generally lateral-vertical transition. On the other hand, the ophiolite and ophiolitic melange units in the accretionary complexes in the Central Pontides are also defined as the Kızılırmak Ophiolite or the Kirazbaşı Complex (Tüysüz, 1990; Yılmaz et al., 1997; Ustaömer and Robertson, 1997; Tüysüz and Tekin, 2007).

Yılmaz and Tüysüz (1984) stated that the fossils in the carbonate rocks within the mélangé are of Upper Cretaceous age. The ophiolitic melange is tectonically overlain by Paleozoic metamorphosed carbonates and Mesozoic carbonate rocks and this unit overlies Kunduz metamorphites and Beşpınar Formation with a tectonic contact (Figure 2).

### 2.1.3. İnaltı Formation

İnaltı Formation is composed of fossiliferous limestones and recrystallized limestones which was named as İnaltı limestone for the first time by Ketin and Gümüş (1963) is observed in the study area around Gök köy, Gökçedoğan plateau, Öbek hill, Gölet plateau, in the north of Çalarasın neighbourhood and around Kanlıtarla Hill (Figure 2). The age of the unit which has a massive appearance and contains plenty of fossil was determined as Jurassic-Cretaceous by Sütçü et al. (1994), as Late Jurassic by Aydın et al. (1995) and as Late Jurassic-Early Cretaceous by Derman and Sayılı (1995) and Tüysüz (1999). Contact relations of the Formation are primarily tectonic and the unit thrusts over ophiolitic melange and Kunduz Metamorphites with tectonic contact. Since its relationship with Permian aged recrystallized limestones is not observed in the study area, the base contact relationship has not been determined.

### 2.1.4. Çamdağ Formation

The Permian Çamdağ Formation consists mainly of neritic limestone and recrystallised limestone (Özgül et al., 1981; Uğuz and Sevin, 2009). Its main outcrops lie in Kışlacıkçal hill, in the north of Pelitözü neighbourhood and in the west of Kozulca (Figure 2). The age of the sequence which is also seen in marble levels due to metamorphism is Permian (Uğuz and Sevin, 2009). Contact relations of the unit are primarily tectonic. Since the base levels of Permian aged carbonates could not be traced, the base contact relationship could not be determined in the study area. The unit thrusts over Kunduz Metamorphites in the north of Pelitözü and in the west of Pelitözü plateau with tectonic contact (Figure 2).

## 2.2. Autochthonous Units

The autochthonous units overlie the units older than themselves with angular unconformity. They

are Beşpınar Formation, Yedikır Formation, Ilgaz Formation and Quaternary clastics.

The Beşpınar Formation consists mainly of sandstone, conglomerate, limestone and marl (Yılmaz and Tüysüz, 1984), and observed along the NE-SW direction starting from the northern Safranlık ridge to the Tirindıran hill in the study area (Figure 2). The unit is tectonically overlain by the allochthonous Saraycık Formation to the north of the Safranlık ridge. The age of the unit was determined as Upper Cretaceous-Lower Eocene (Yılmaz and Tüysüz, 1984) and this unit can be correlated Kadıkızı Formation described by Rice et al. (2006) whose age is Middle Eocene by the age of the nummulites.

The Yedikır Formation, consisting of sandstone, marl, and limestone, was named by Gümüüşsu (1980). It is observed to the NW of the study area and overlies the Kunduz metamorphites and the Çamdağ Formation with the angular unconformity. The age of the unit has been determined as Upper Miocene-Lower Pliocene by Genç et al. (1991).

The Upper Pliocene Ilgaz Formation consists of sandstones, conglomerates, and siltstones (Hakyemez et al., 1986; Türkecan et al., 1991). This unit unconformably overlies ophiolitic melange rocks and

the Kunduz Metamorphites in the south of the field area.

Slope debris and alluvium are composed of unconsolidated mixtures of gravel, block, sand, silt, and clay.

### 2.3. Tectono-stratigraphy

Allochthonous units, which are made up of rock associations representing various geotectonic environments, present various stratigraphic sequences in accordance with their structural locations (Figure 4). These sequences have been identified as three different tectonic slices: Gök köy Tectonic Slice (GTS), Pelitözü Tectonic Slice (PTS), and Ophiolitic Melange Slice (OMS) (Figure 5). The metamorphic basement rocks located in accretionary complexes in the Central Pontides is tectonically overlain by ophiolite and ophiolitic melange units (Yiğitbaş et al., 1990; Okay et al., 2006; Tüysüz and Tekin, 2007; Tüysüz, 2017). In addition, Paleozoic and Mesozoic carbonate rocks thrusts over the Kunduz Metamorphites and Ophiolitic Melange in the study area. These imbrication structures led to different tectono-stratigraphic sequences.

The GTS is represented by the tectonic contacts of Kunduz Metamorphites, the Ophiolitic Melange, and the İnaltı Formation (Figure 6). The PTS has

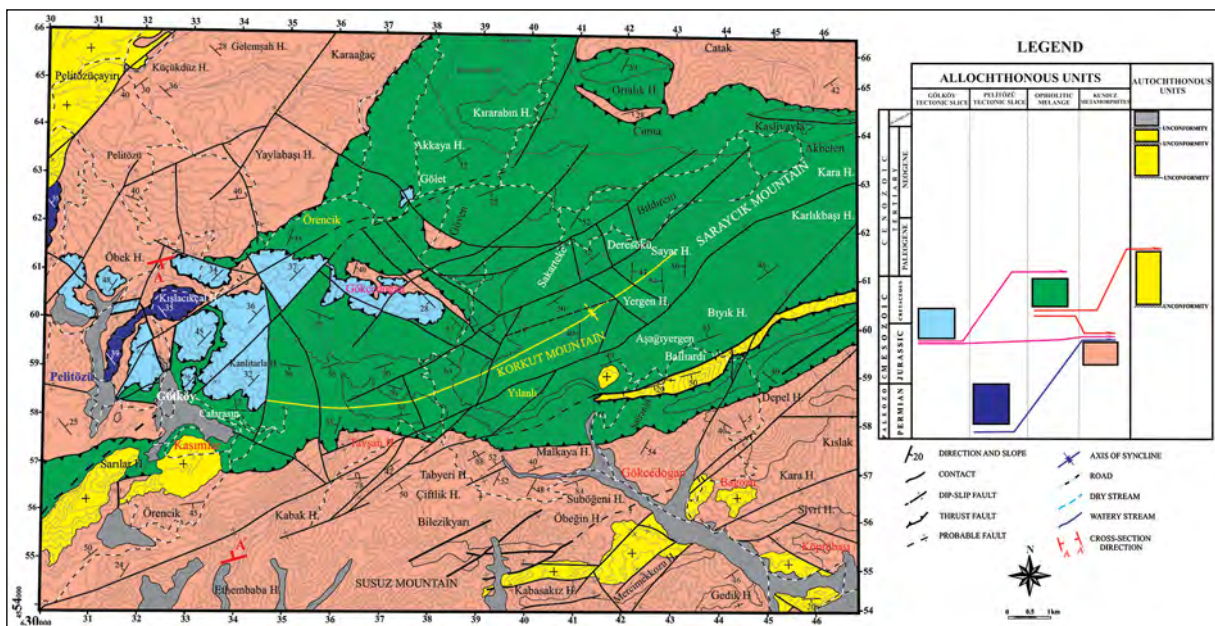


Figure 4- Structural map of the study area.

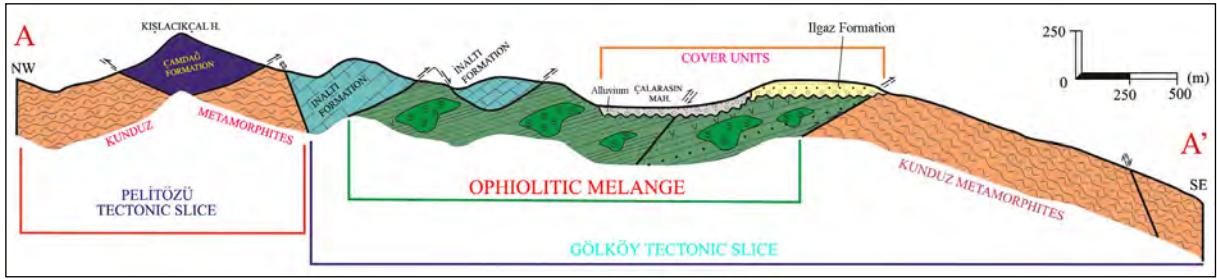


Figure 5- Cross-section through the study area.

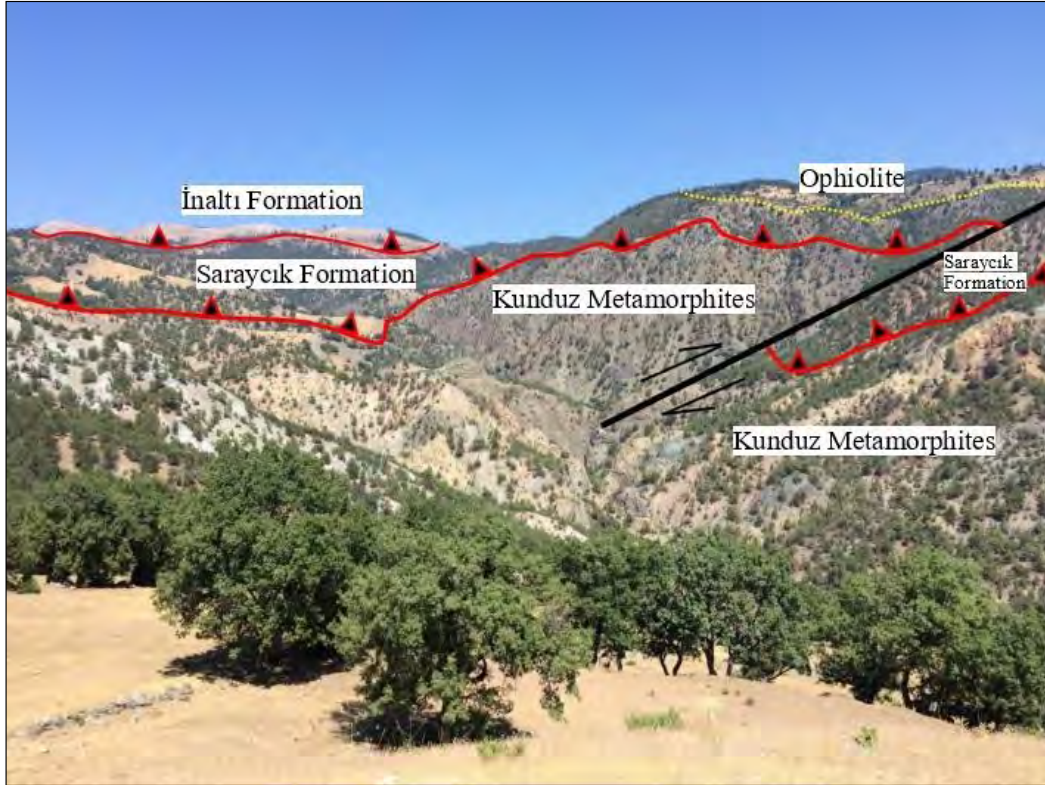


Figure 6- General view of the units forming the Gökkyö tectonic slice in the field (looking northwards from Malkaya Hill).

been formed by Çamdağ Formation and Kunduz Metamorphites (Figure 7) and the OMS has been formed by Ophiolitic Melange, Beşpınar Formation, and Kunduz Metamorphites (Figure 8) via tectonic contacts.

### 3. Sampling and Analytical Methods

In the study area, 9 metabasites from Kunduz Metamorphics and 14 basalt samples from ophiolitic melange were collected due to the presence of basalts of different origin in the study area. X-ray Fluorescence (XRF) and Inductively Coupled Plasma

Mass Spectrometry (ICP-MS) analyses of the samples were performed at Istanbul Technical University Geochemistry Research Laboratory (ITU-JAL).

Geochemical analysis of the samples was performed via BRUKER S8 TIGER model X-ray fluorescence spectrometer (XRF) and PerkinElmer ELAN 6000 DRC-e model Inductively Coupled Plasma-Mass Spectrometry (ICP-MS). Before the ICP-MS analysis, milled samples were completely decomposed in an acid mixture on BERGHOF speed wave TM MWS-3+ model microwave device. Also, to validation of XRF, microwave digestion, and ICP-

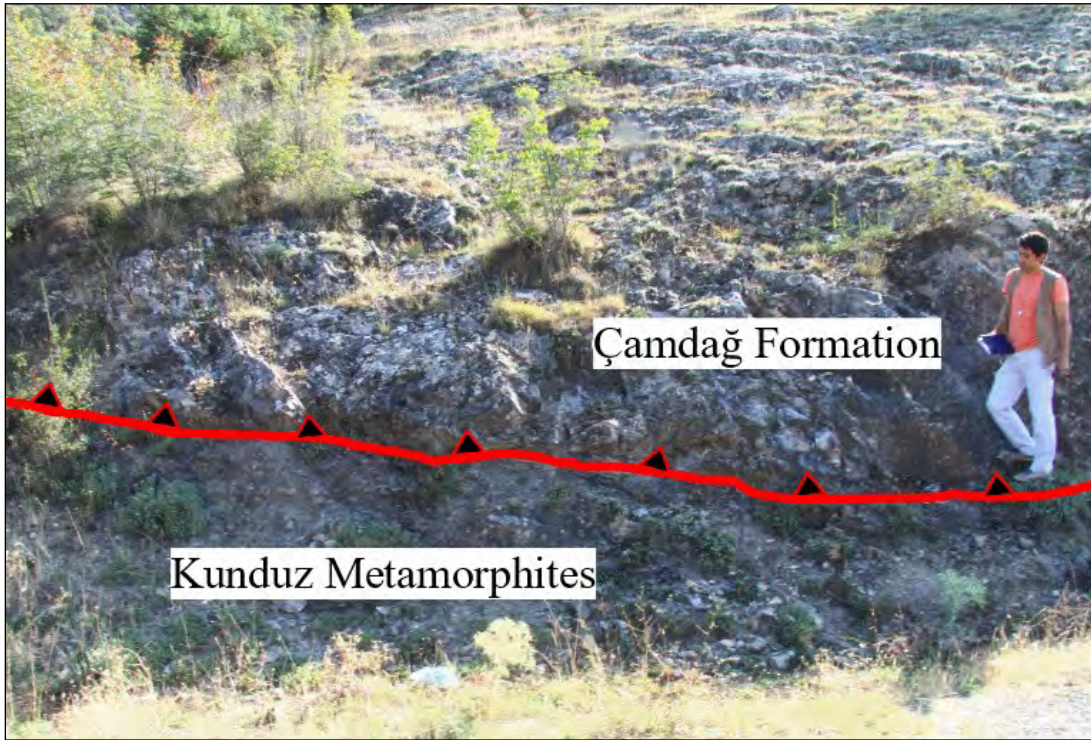


Figure 7- General view of the units forming the Pelitözü tectonic slice (looking eastward from the west at southern of Kışlacıkçal Hill).

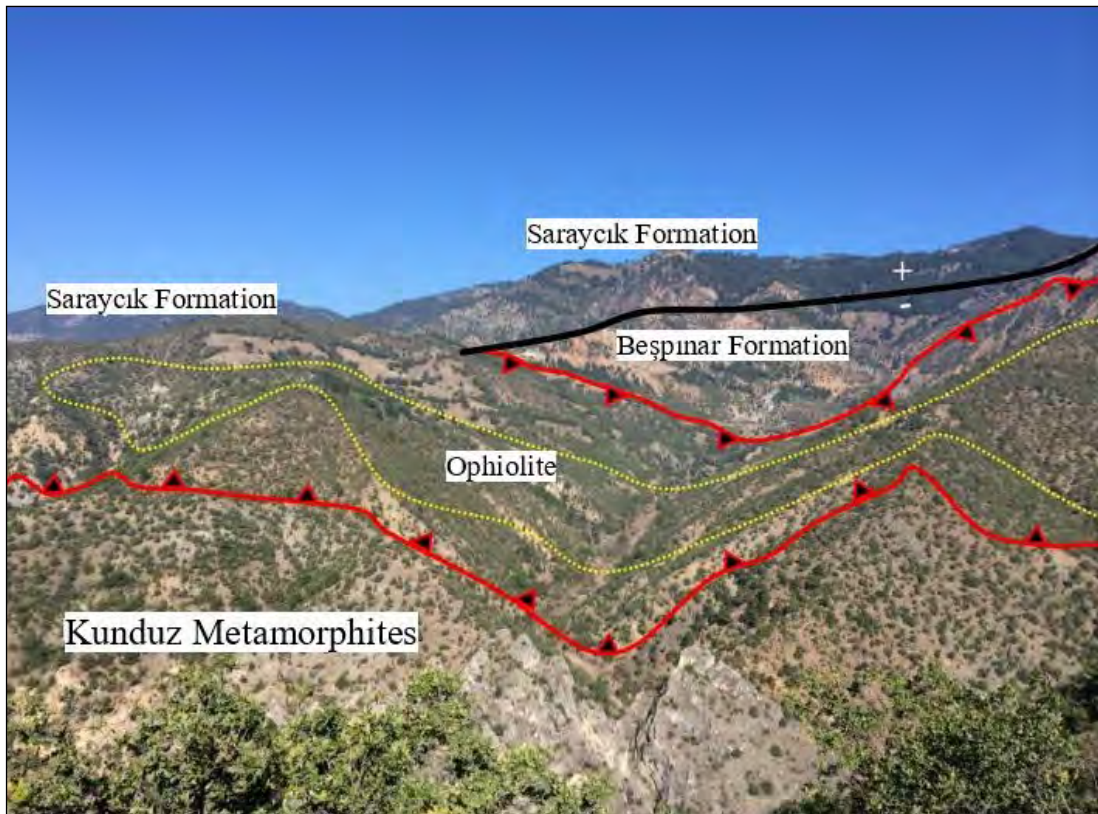


Figure 8- General view of the tectonic slice formed by Ophiolitic Melange (looking northwards from the south at southern of Safranlık Hill).

MS methods the certified reference material (CRM) was used.

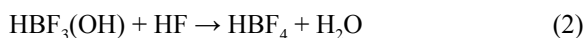
The reagents were all of the certified analytical-grade purity. Pure water was obtained with Zeneer UP 900 model water purification system. The maximum resistivity of pure water was 18.3  $M_{\Omega\text{cm}}$ . Hydrochloric acid (HCL) 37% (w/v), nitric acid (HNO<sub>3</sub>) 65%, (w/v), hydrofluoric acid (HF) 38-40% (w/v) and boric acid (H<sub>3</sub>BO<sub>3</sub>) were supplied by Merck. The mix standard solution of 10 mg/l of yttrium (Y), thorium (Th), lanthanum (La), samarium (Sm), and ytterbium (Yb,) and as 225 an internal standard, 1000 mg/l of rhenium (Re) solution were supplied by PerkinElmer. The CRM is (GSP-2) from the United States Geological Survey (USGS).

Samples were crushed by a jaw crusher. The material was then dried in an oven at 105 °C for 24 hours. After the drying process, the grain sizes of 10-15 g samples were reduced to 177  $\mu\text{m}$  by using RETSCH (RS-200) model milling device. The milling process was carried out for 1-2 min at 1250 rpm. All dried and powdered samples were stored in a desiccator to protect them from humidity.

XRF analysis was used to determine major oxides and niobium (Nb), zirconium (Zr). The milled samples were pressed, pelleted then analyzed to determine major and some of trace elements concentration by using XRF (Detection limits for S8 TIGER XRF; Y-Th: 0.3 ppm).

Microwave digestion process was effectuated in two steps. The microwave digestion steps were performed with the described program (power 90%, temperature 180 °C, pressure 20-30 bar, ramp time 10 minutes, hold time 20-25 minutes). In the first step which all samples were decomposed; approximately 100-200 mg of milled sample was weighed to high-pressure digestion on teflon vessel. Then, 8 ml of aqua regia (3:1, HCl: HNO<sub>3</sub>) and 1 ml of HF were added to each vessel. Subsequently, the vessels were closed tightly and placed in the microwave device. When the first step finished, the vessels were cooled and carefully opened at the fume hood. In the second step, the excess of HF was removed to prevent damage to glass and quartz parts of ICP-MS equipment. For this

purpose, 6 ml of H<sub>3</sub>BO<sub>3</sub> 5% (w/v) solution was added to each vessel. Then, the vessels were closed tightly and placed in the microwave. The damaging effect of HF has been eliminated after the occurrence of the following reaction (Equations 1 and 2) ;



After the second step finished, the vessels were cooled and carefully opened. Each digested sample was transferred by washing pure water to a 50 mL volumetric flask. Thus, solutions of samples were obtained. By the same digestion method, the same acid mixture was added to the empty vessel to prepare the blank solution for ICP-MS analysis.

ICP-MS analysis was used to determine Y, Th, La, Sm, and Yb. As an internal standard, 50  $\mu\text{g/l}$  of Re solution was added to the sample solutions which were obtained by microwave digestion. The calibration standards were prepared from the stock mix solutions. The calibration points of graphs were 5, 10, 50 and 100  $\mu\text{g/l}$ . Calibration graphs were linear and the square of the correlation coefficient ( $R^2$ ) was at least 0,999 for each element. Solutions of standards, sample, and CRM were diluted and they were analyzed three times. Relative standard deviation (RSD) % values were kept below 5% throughout the analysis. Also, after all three samples, contamination was checked by analyzing the blank solution (Detection Limits for ELAN DRC-e ICP-MS; Y-Th-La-Sm-Yb: 0.0005 ppb).

#### 4. Petrography

Metabasites crop out in and around Pelitözü and west of Gökçedoğan districts. Although the weathered surface of metabasites is gray, greenish-gray and dark green, the freshly fractured surface is green, greenish-white, and gray (Figure 9a, b). The metabasites around Pelitözü are thickly bedded (Figure 9a), while the metabasites west of Gökçedoğan are thinly bedded (Figure 9b). The metabasites of western Gökçedoğan are still extremely well foliated correlated to the metabasites around Pelitözü (Figure 9b). Banded pyrite levels are farther prevalent in this zone and limonitic zones are still observed depending on the mineralization.

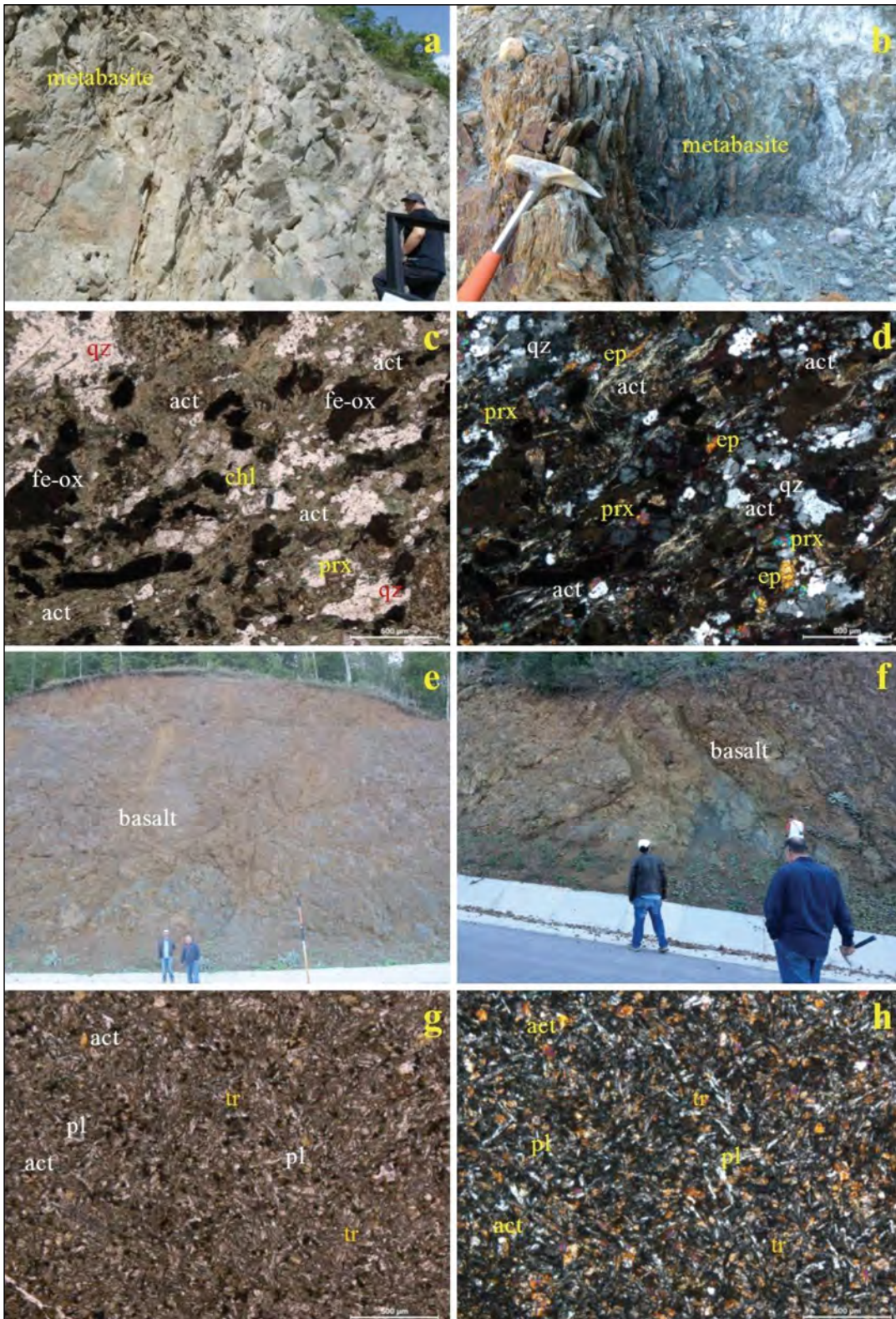


Figure 9- a), b) Field view of metabasites belonging to the Kunduz metamorphites, c), d) polarizing microscope images of metabasites belonging to the Kunduz metamorphites, e), f) field view of basalts belonging to the Ophiolitic Melange, g), h) polarizing microscope images of basalts belonging to the Ophiolitic Melange, Abbreviations: (act) actinolite, (Fe-ox) iron oxide, (prx) pyroxene, (chl) chlorite, (ep) epidote, (qz) quartz, (pl) plagioclase, (tr) tremolite.

In the petrographic study of the metabasites in the Kunduz metamorphics, it was seen that the major mineral was actinolite. In supplement, pyroxene, quartz, muscovite, epidote minerals, and Fe-oxide are still staged in the rock (Figure 9c, d). Actinolite minerals were oriented by the deformation effect and nematoblastic and fibroblastic textures developed in the rock. In general, as a result of the alternation of quartz and actinolite, it was ascertained that the grano-nematoblastic texture was predominant in the rock (Figure 9c, d).

The weathering color of the pillow basalts outcropping around the Devebağırđığı creek is gray and brown. Basalts show a relatively thick sequence in this district. Since it is in the zone adjacent to the thrust zone, crushed zones have developed within the unit (Figure 9d, e).

In the petrographic examination of basalts applying to the ophiolitic melange, mineral paragenesis consists of plagioclase, tremolite, actinolite, and volcanic glass. The main texture in basalts is in the form of pilotaxitic character (Figure 9g, 9h).

## 5. Whole Rock Geochemistry

In order to reveal the origins and geotectonic positions of the rocks major, trace and rare earth

element analysis of the data obtained from metabasite of the Kunduz Metamorphites (Table 1, 2, 3) and from the basalt belonging to ophiolitic melange (Table 4, 5, 6) was carried out and presented in diagrams.

In the Zr/Ti versus Nb/Y diagram (Pearce, 1996) metabasite and basalt samples plot in the basalt area (Figure 10). Protoliths of the Kunduz metamorphites and basalts from the ophiolitic melange exhibit the tholeiitic character in Nb/Yb versus TiO<sub>2</sub>/Yb diagram (Pearce, 2008) (Figure 11). The TiO<sub>2</sub>/Yb and Nb/Yb ratios of metabasites are greater than basalts. Metabasites represent deep melting in the ocean island basalt (OIB) area. Basalts of the ophiolitic melange are settled in the normal mid-ocean ridge basalt (NMORB) area in this diagram and display shallow melting (Figure 11).

Chondrite normalized trace element trends display enrichment in the Light Rare Earth Elements (LREE's e.g., La, Ce, Nd) for metabasites of the Kunduz Metamorphites relative to basalts belonging to the Ophiolitic mélangé. The Heavy Rare Earth Elements (HREE's e.g., Er, Tm, Yb, Lu) exhibits almost flat trends for each unit (Figure 12).

The metabasites of Kunduz Formation and the basalts of ophiolitic melange display with MORB

Table 1- Major oxide analysis results of the metabasites belonging to the Kunduz Metamorphites.

Sample	K2-13	K2-28	KGD-303	KGD-336	KGD-565	KGD-567	KGD-622	KGD-626	KGD-627
Latitude ( <sup>0</sup> N)	36.800	39.420	39.430	39.374	42.551	42.655	30.987	36.003	36.003
Longitude ( <sup>0</sup> E)	56.816	56.728	56.910	56.885	57.016	57.029	58.800	63.818	63.815
<b>Major Oxides (%)</b>									
SiO <sub>2</sub>	41.16	44.49	44.18	47.59	46.59	39.34	42.63	45.12	46.64
Al <sub>2</sub> O <sub>3</sub>	11.06	12.07	11.62	10.59	13.58	12.72	12.46	13.01	11.07
Fe <sub>2</sub> O <sub>3</sub>	14.32	13.93	14.61	13.24	15.50	14.36	15.06	14.89	12.82
MgO	9.94	9.21	9.18	10.52	11.41	10.74	10.77	9.61	8.97
CaO	10.19	10.86	11.87	10.66	10.50	9.80	9.66	7.84	10.08
Na <sub>2</sub> O	2.86	2.74	2.46	2.72	1.34	2.58	2.67	2.58	2.21
K <sub>2</sub> O	0.29	0.08	0.05	0.07	0.23	0.48	0.08	0.40	0.32
TiO <sub>2</sub>	1.67	1.64	1.32	1.94	4.56	3.52	2.18	2.92	3.69
P <sub>2</sub> O <sub>5</sub>	0.19	0.14	0.15	0.05	0.45	0.75	0.25	0.36	0.39
MnO	0.21	0.21	0.22	0.23	0.30	0.29	0.21	0.23	0.28
Cr <sub>2</sub> O <sub>3</sub>	0.41	0.03	0.05	0.00	0.21	0.00	0.03	0.00	0.00
LOI	7.51	3.48	3.24	3.07	3.90	5.08	3.78	2.66	1.96
TOTAL	99.8	98.88	99.68	99.68	99.57	99.67	99.78	99.62	99.56

Table 2- Trace element analysis results of the metabasites belonging to the Kunduz Metamorphites.

Trace Elements (ppm)	K2-13	K2-28	KGD-303	KGD-336	KGD-565	KGD-567	KGD-622	KGD-626	KGD-627
Sc	98.35	81.05	141.79	97.10	140.68	107.22	79.32	80.91	52.30
Y	27.47	25.01	23.38	23.16	22.48	27.82	23.80	23.05	23.24
Th	0.57	0.49	0.45	0.10	1.42	1.75	0.64	0.56	0.17
Li	19.06	12.05	12.47	9.91	15.45	13.43	42.84	13.85	1.75
Be	0.80	0.90	0.90	0.24	1.30	1.04	0.55	1.02	0.61
Ga	16.27	16.34	14.01	11.98	17.39	17.91	16.20	14.16	1.84
V	374.00	356.00	6188.00	509.00	781.00	6365.00	0.00	0.00	651.00
As	73.00	63.72	34.82	17.96	42.10	45.01	23.21	7.54	48.72
Se	7.59	6.33	0.00	0.61	25.28	5.49	2.00	0.00	0.00
Rb	4.92	1.57	0.19	0.58	2.95	4.79	0.94	4.48	1.13
Ag	0.41	0.34	1.01	0.53	0.00	0.00	0.11	0.40	0.52
Cd	1.20	2.36	0.86	0.13	0.17	0.04	0.10	0.05	0.29
In	0.08	0.08	0.07	0.04	0.07	0.04	0.05	0.11	0.00
Cs	0.60	0.09	0.00	0.10	0.11	0.76	0.08	0.80	0.49
Nb	6	7	6	3	8	7	6	6	7
Tl	0.03	0.04	0.00	0.00	0.00	0.00	0.00	0.00	0.00
Zr	82	86	80	74	106	131	140	158	156
Ti	10009	9830	7912	11628	27332	21098	13066	17502	22117
Hf	1.14	1.13	0.90	0.79	1.83	1.68	0.36	6.81	0.00
Ir	0.01	0.01	0.01	0.00	0.01	0.00	0.01	0.02	0.00
Sb	0.54	0.95	0.94	0.45	0.55	3.58	0.65	5.99	0.21
Sn	1.25	1.05	0.84	0.59	1.98	0.90	2.30	2.73	0.53
Te	0.06	0.07	0.10	0.08	0.05	0.06	0.07	0.09	0.08
Ta	0.40	0.44	0.50	0.39	0.41	0.56	0.38	0.49	0.50
Nb/Y	0.21	0.27	0.25	0.12	0.35	0.25	0.25	0.25	0.30
Zr/Ti	0.008	0.008	0.010	0.006	0.003	0.006	0.010	0.090	0.007
Nb/Yb	6.02	7.20	5.92	3.07	3.29	3.79	4.57	3.05	3.74
TiO <sub>2</sub> /Yb	1.67	1.68	1.30	1.98	1.87	1.90	1.66	1.48	1.97

Table 3- Rare earth element analysis results of the metabasites belonging to the Kunduz Metamorphites.

REE (ppm)	K2-13	K2-28	KGD-303	KGD-336	KGD-565	KGD-567	KGD-622	KGD-626	KGD-627
La	6.62	6.26	5.64	9.45	17.95	22.56	7.07	9.85	6.05
Ce	17.08	15.57	14.16	14.70	39.86	49.64	17.10	24.75	12.10
Pr	2.33	2.10	2.05	2.95	5.14	6.47	3.52	5.80	2.01
Nd	11.59	10.62	9.96	9.09	23.09	29.30	15.20	25.55	10.03
Sm	3.41	3.20	2.95	2.15	5.52	6.82	5.34	9.28	6.01
Eu	1.17	1.19	1.10	0.88	2.02	2.59	1.95	3.31	1.01
Gd	4.87	4.63	4.34	3.36	6.83	8.47	7.49	12.85	3.01
Tb	0.78	0.75	0.67	0.70	0.88	1.06	1.58	2.62	1.00
Dy	5.17	4.82	4.22	4.45	4.85	5.85	8.60	14.13	4.02
Ho	1.06	0.99	0.87	1.07	0.88	1.08	2.13	3.53	1.01
Er	3.05	2.84	2.45	2.94	2.39	2.88	5.44	8.83	3.02
Tm	0.41	0.38	0.33	0.48	0.29	0.34	0.92	1.48	0.61
Yb	0.99	0.97	1.01	0.98	2.43	1.85	1.31	1.97	1.87
Lu	0.33	0.30	0.29	0.43	0.23	0.25	0.84	1.39	0.31

Table 4- Major oxide analysis results of the basalts belonging to ophiolitic melanges.

Sample	K2-37	K2-38	K3-39	K2-43	K2-44	K2-45	K2-46	K2-47	KGD-625	KGD-629	KGD-913A	KGD-913B	KGD-913C	KGD-914
Latitude ( <sup>0</sup> N)	36.471	36.471	36.471	36.457	36.457	36.457	36.457	36.457	36.601	36.617	36.581	36.581	36.581	36.640
Longitude ( <sup>0</sup> E)	63.186	63.186	63.186	63.122	63.122	63.122	63.122	63.122	63.810	63.791	63.845	63.845	63.845	63.726
Major Oxides (%)														
SiO <sub>2</sub>	41.55	40.67	40.68	42.20	44.37	45.01	44.80	46.22	43.52	46.78	43.18	44.11	45.11	44.19
Al <sub>2</sub> O <sub>3</sub>	11.66	11.99	10.10	10.31	10.92	10.85	10.41	11.97	10.91	10.31	10.10	10.22	10.30	13.03
Fe <sub>2</sub> O <sub>3</sub>	17.54	21.20	18.01	17.37	16.92	17.21	12.68	16.98	18.52	20.14	18.38	19.20	18.04	16.11
MgO	5.06	5.99	4.40	5.94	6.50	8.05	7.02	7.41	5.69	5.66	7.90	6.79	6.67	8.50
CaO	12.39	8.72	14.19	9.70	10.52	10.27	12.75	12.00	10.45	6.61	9.71	8.28	8.55	10.38
Na <sub>2</sub> O	2.27	2.19	2.78	2.72	2.84	2.21	3.42	3.65	2.66	2.83	3.16	3.22	3.71	3.31
K <sub>2</sub> O	1.44	0.94	0.04	0.31	0.44	0.57	0.14	0.07	0.07	0.15	0.15	0.14	0.14	0.09
TiO <sub>2</sub>	3.07	3.28	2.86	1.17	1.01	1.24	1.47	1.94	3.70	3.37	3.65	3.70	3.59	3.33
P <sub>2</sub> O <sub>5</sub>	0.26	0.29	0.21	0.10	0.10	0.17	0.19	0.09	0.39	0.35	0.43	0.44	0.41	0.17
MnO	0.21	0.20	0.21	0.19	0.15	0.29	0.13	0.14	0.25	0.29	0.30	0.30	0.31	0.23
Cr <sub>2</sub> O <sub>3</sub>	0.00	0.00	0.00	0.04	0.06	0.06	0.04	0.06	0.00	0.01	0.01	0.00	0.00	0.04
LOI	3.39	4.23	6.24	7.03	4.02	3.87	4.8	4.23	2.97	2.06	2.23	2.99	2.03	4.49
TOTAL	98.83	99.70	99.74	99.84	99.85	99.79	99.86	99.77	99.12	99.55	99.18	99.40	98.86	99.85

Table 5- Trace element analysis results of the basalts belonging to ophiolitic melanges.

Trace Elements (ppm)	K2-37	K2-38	K3-39	K2-43	K2-44	K2-45	K2-46	K2-47	KGD-625	KGD-629	KGD-913A	KGD-913B	KGD-913C	KGD-914
Sc	106.65	102.85	131.36	153.70	108.98	90.08	86.40	86.41	81.39	72.04	84.14	162.14	209.83	162.24
Th	0.33	0.36	0.25	0.10	0.49	0.19	0.16	0.11	0.72	0.56	0.60	0.55	0.60	0.11
Li	17.18	27.36	12.12	22.96	12.44	14.39	21.20	15.68	9.32	11.58	5.04	14.70	9.17	10.16
Be	0.86	2.09	1.31	0.46	0.51	0.74	1.14	0.64	1.29	1.09	1.62	1.58	1.49	0.94
Ga	20.02	23.15	17.33	15.14	16.44	16.98	15.20	12.67	24.20	15.11	19.44	21.46	17.21	10.37
As	49.31	26.53	56.58	72.66	64.57	55.90	31.85	54.35	11.44	14.96	20.32	24.52	25.11	21.97
Se	3.60	0.00	4.77	0.00	0.29	1.02	0.00	1.39	0.00	0.00	8.06	7.04	3.20	1.29
Rb	23.86	19.09	1.25	2.75	3.55	3.81	1.71	1.18	1.20	1.61	1.57	2.39	1.77	0.99
Sr	81.55	74.67	76.87	56.73	139.55	124.29	126.18	153.50	39.62	70.42	85.78	58.59	69.65	45.13
In	0.11	0.04	0.07	0.05	0.05	0.05	0.00	0.04	0.12	0.20	0.13	0.13	0.14	0.03
Cs	0.83	1.12	0.20	0.19	0.22	0.29	0.26	0.15	0.12	0.18	0.20	0.16	0.15	0.11
Ba	61.58	19.39	25.75	53.02	23.27	84.19	15.33	42.62	12.52	16.65	16.96	6.06	6.23	0.00
Tl	0.01	0.02	0.00	0.00	0.00	0.00	0.00	0.00	0.00	0.00	0.00	0.00	0.00	0.00
Pb	7.68	37.85	6.90	7.51	12.20	4.69	30.14	12.82	7.16	3.78	5.15	0.00	0.00	0.00
V	611	711	599	311	283	296	109	146	659	0	0	0	0	0
Hf	5.91	6.12	4.87	1.52	1.28	1.92	2.52	1.10	8.09	7.16	8.58	7.67	7.87	2.24
Ir	0.03	0.03	0.02	0.02	0.01	0.01	0.01	0.01	0.02	0.02	0.03	0.03	0.03	0.01
Sb	0.19	0.23	0.22	0.18	0.19	3.20	0.15	0.13	1.04	0.18	0.72	0.60	1.86	0.61
Sn	2.80	2.39	1.56	1.05	0.77	0.98	1.13	0.86	3.44	3.08	2.77	1.87	1.94	0.82
Te	0.06	0.22	0.05	0.09	0.04	0.07	0.05	0.05	0.10	0.07	0.03	0.05	0.07	0.04
Ta	0.21	0.30	0.50	0.40	0.12	0.24	0.40	0.39	0.51	0.54	0.31	0.27	0.13	0.22
Y	47.71	63.19	45.65	24.71	18.24	23.00	23.48	15.54	62.92	47.83	56.29	105.11	110.89	34.28
Nb	7	5	6	4	6	4	3	4	5	5	6	6	6	3
Zr	231	239	223	78	59	96	109	146	248	241	263	259	249	230
Ti	18401	19660	17142	7012	6053	7432	8811	11628	22177	20199	21878	22177	21518	19960
Nb/Y	0.14	0.07	0.13	0.16	0.32	0.17	0.12	0.25	0.07	0.10	0.10	0.05	0.05	0.08
Zr/Ti	0.012	0.012	0.013	0.011	0.009	0.012	0.012	0.012	0.011	0.011	0.012	0.011	0.011	0.011
Nb/Yb	1.21	0.72	1.05	1.16	1.71	0.99	0.62	0.64	0.78	0.77	0.94	0.90	0.88	0.46
TiO <sub>2</sub> /Yb	0.52	0.47	0.49	0.33	0.28	0.30	0.30	0.31	0.57	0.51	0.56	0.55	0.52	0.51

Table 6- Rare earth element analysis results of the basalts belonging to ophiolitic melanges.

REE (ppm)	K2-37	K2-38	K3-39	K2-43	K2-44	K2-45	K2-46	K2-47	KGD-625	KGD-629	KGD-913A	KGD-913B	KGD-913C	KGD-914
La	5.54	7.74	5.56	2.14	3.42	3.07	3.18	1.45	12.67	9.34	8.70	10.74	10.61	3.90
Ce	17.94	24.05	17.22	9.12	8.38	9.55	10.95	4.96	29.94	24.61	25.24	36.48	38.08	12.84
Pr	3.02	3.79	2.90	1.32	1.18	1.47	1.68	0.77	7.17	5.74	5.23	6.51	6.75	2.21
Nd	16.26	20.27	15.85	7.83	6.03	8.10	9.26	4.44	31.42	25.48	25.53	35.44	37.01	11.73
Sm	5.54	6.70	5.24	2.71	2.02	2.69	2.94	1.58	11.27	9.18	8.83	12.00	12.58	3.90
Eu	1.86	2.21	1.78	1.10	0.89	0.98	1.15	0.61	3.93	3.19	2.94	3.88	4.11	1.46
Gd	8.03	10.04	7.55	3.96	3.00	3.84	4.11	2.39	15.67	12.70	12.67	17.05	17.73	5.62
Tb	1.39	1.69	1.31	0.69	0.50	0.65	0.68	0.42	3.18	2.62	2.33	2.86	3.04	0.94
Dy	9.09	11.18	8.43	4.46	3.25	4.27	4.37	2.81	17.28	14.22	14.23	18.86	20.02	6.05
Ho	1.90	2.34	1.77	0.91	0.68	0.88	0.91	0.61	4.39	3.51	3.30	3.95	4.21	1.27
Er	5.63	6.88	5.14	2.61	1.98	2.55	2.64	1.78	11.30	8.78	9.21	11.72	12.45	3.66
Tm	0.80	0.97	0.72	0.36	0.28	0.36	0.37	0.25	1.97	1.49	1.41	1.69	1.80	0.53
Yb	5.80	6.97	5.72	3.46	3.51	4.06	4.81	6.25	6.43	6.49	6.41	6.69	6.80	6.53
Lu	0.79	0.90	0.69	0.30	0.26	0.33	0.34	0.24	1.91	1.40	1.36	1.65	1.76	0.48

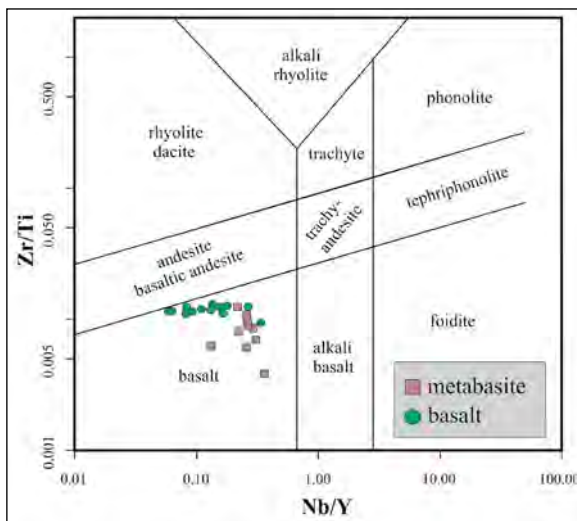


Figure 10- Positions of metabasites and basalts in the Nb/Y-Zr/Ti diagram (Pearce, 1996).

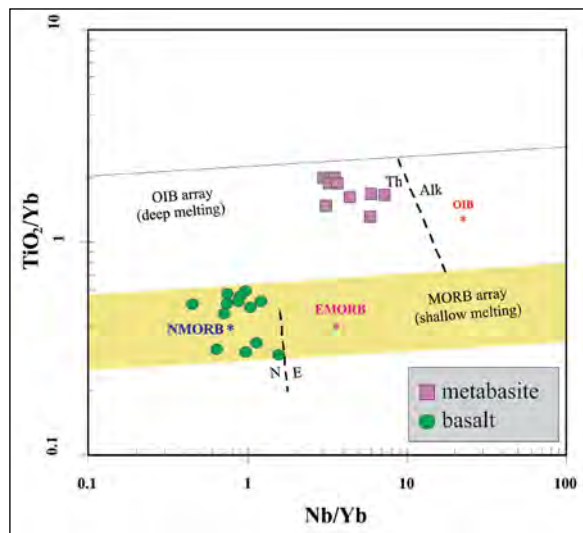


Figure 11- Nb/Yb-TiO<sub>2</sub>/Yb diagram belonging to metabasites and basalts (Pearce, 2008).

and within-plate tholeiites character, based on the Ti versus Zr diagram of Pearce (1982) (Figure 13). The metabasites from the Kunduz Unit and the basalts from the melange exhibit MORB and within-plate characteristics. The data suggest that they most probably represent fragments of accreted oceanic lithosphere including MORB and intra-plate volcanic edifices.

## 6. Discussion

The various types and ages of rock groups that range from Paleozoic to Quaternary were observed in the Central Pontide Supercomplex (Okay et al., 2013; Marroni et al., 2014; Okay and Nikishin, 2015). Metamorphic basement rocks, belonging to the Kunduz Formation, are interpreted as a marginal basin complex located in the southern side of Eurasia before the Late Jurassic (Ustaömer and Robertson, 1997, 1999; Robertson, 2002) (Figure 14a).

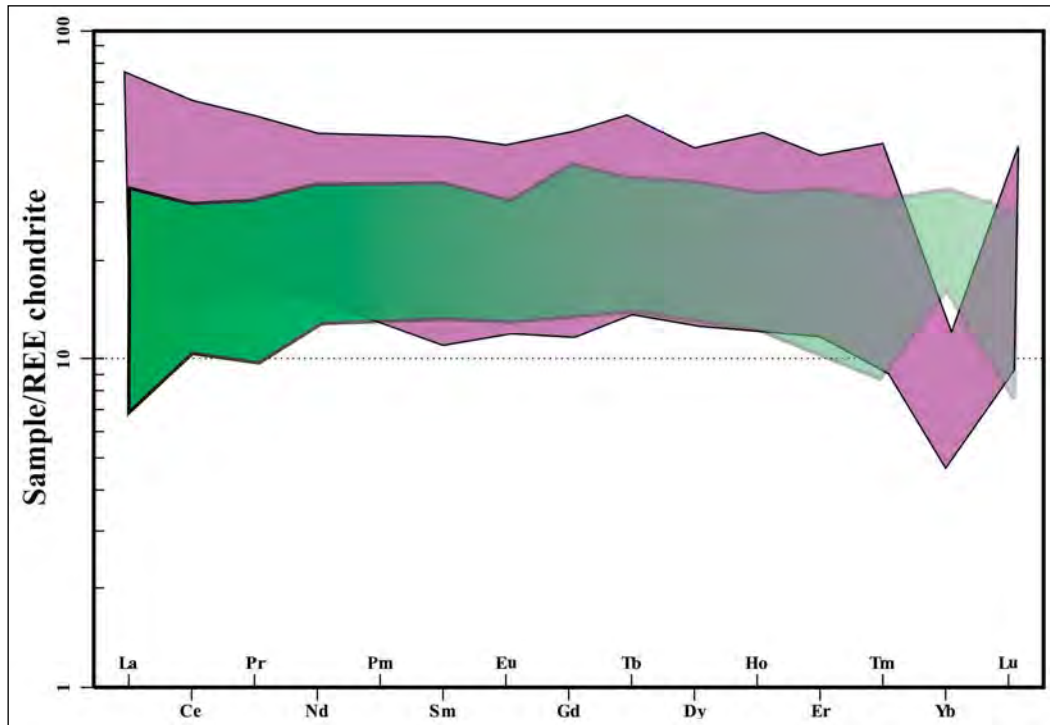


Figure 12- Chondrite-normalized REE diagrams (Sun and McDonough, 1989).

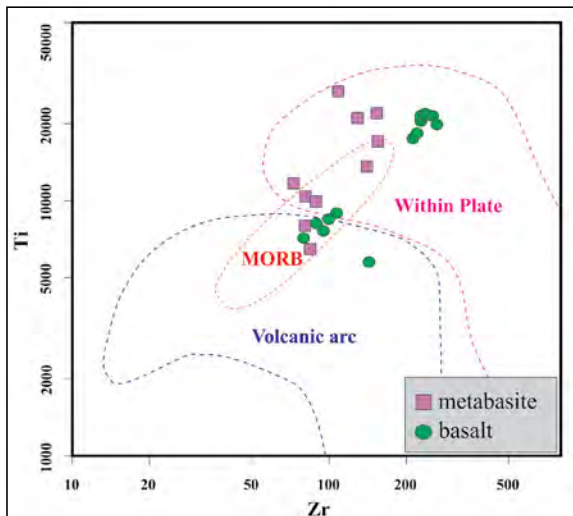


Figure 13- Ti-Zr diagram of metabasites (Pearce, 1982).

It is suggested that the age of metamorphism of the metabasites within Kunduz Formation is Late Jurassic (Aygül et al., 2016; Çelik et al., 2016) by the way of  $^{40}\text{Ar}/^{39}\text{Ar}$  method which yield robust plateau ages. Geochemical data reveals that protoliths of the metabasites have tholeiitic composition and are characterized with the MORB and within plate tholeiites. High pressure and low temperature (HP-LT) metamorphism occurred in Albian (Okay et al., 2013)

in the area which was thrust into an accretionary prism area due to the northward subduction of the Tethys oceanic crust (Çelik et al., 2011; Topuz et al., 2012; Marroni et al., 2014; Okay et al., 2013). The geochemistry of basalts in the Kirazbaşı Melange show MORB to within plate-type settings (Rice et al., 2006). In this study, the basalts have tholeiitic character and they coincide with the MORB and within plate areas as the geotectonic position as referred by Rice et al. (2006).

Permian limestone deposited on carbonate platforms in shallow areas located in the southern side of Eurasia (Yılmaz and Tüysüz, 1988) were thrust over Kunduz Metamorphites (Figure 14b) with the Domuzdağ-Saraycıkdağı Complex in the area from north to south in Upper Jurassic (Ustaömer and Robertson, 1999) with the closure of Tethys oceanic crust. With this thrusting, which has been related to the northwards subduction (Okay et al., 2013; Akbayram et al., 2013; Marroni et al., 2014; Tüysüz, 2017), regional metamorphism developed in the Albian (Okay et al., 2013). As a result of this thrusting, The Pelitözü tectonic slice, which presents a specific tectono-stratigraphical sequence from bottom to top was formed in the study area (Figure 14b). After the

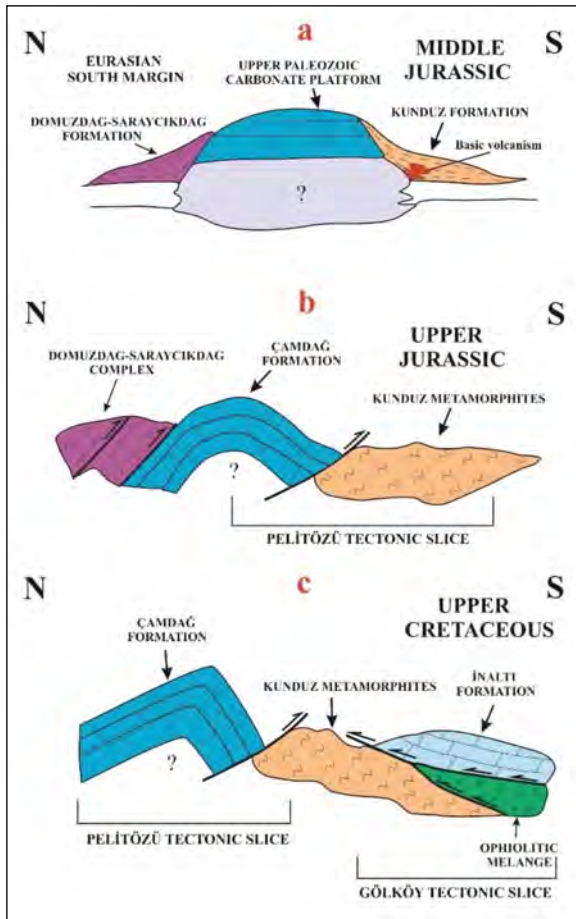


Figure 14- Structural evolution of the tectonic slices in the study area; a) Middle Jurassic period, b) Upper Jurassic period, and c) Upper Cretaceous period.

transgression that started in the Jurassic, a carbonate platform occurring in the Pontides (Ketin and Gümüş, 1963; Tüysüz, 1985) formed the İnaltı Formation. This unit thrust over both the Kirazbaşı ophiolitic Melange and metamorphic basement as a result of the subduction to the northwards and collision (Figure 14c). This tectono-stratigraphic sequence also formed the Gökölü tectonic zone. Rice et al. (2006) stated that in the Akkaya and Yuvasaray regions of the Central Pontides, there is a northward kinematic orientation within the Upper Cretaceous-Lower Cenozoic units, whereas the Kirazbaşı Ophiolitic Melange tends to thrust similar the north. As a result of the geological mapping studies, it was understood that the units belonging to ophiolitic melange in the study area have both north and south thrust planes (Figure 2), and they are compatible with the kinematic analysis proposed by Rice et al. (2006).

Middle Jurassic accretionary complex (Kunduz Metamorphites) formed with the continuation of subduction (Okay et al., 2013). The rocks located in this area had metamorphism under the conditions of high pressure and low temperature (HP, LT) in Albian (Okay et al., 2013). It has been reported that a similar structure exists in the southern part of the Kargı Massif (Yığıtbaş et al., 1990; Okay et al., 2006; Tüysüz and Tekin, 2007). A large part of the study area to the east of Kargı consists of rocks belonging to ophiolitic melange overlying the metamorphic basement with tectonic contact.

The Gökölü tectonic slice was formed by the northerly thrusting (Rice et al., 2006), related to the northward's subduction (Okay et al., 2013; Akbayram et al., 2013; Marroni et al., 2014; Tüysüz, 2017), of Kirazbaşı complex (ophiolitic melange) and Mesozoic carbonate rocks over the metamorphic rocks forming the basement of the area. The distance between the Pontides, Taurid-Anatolide and Kırşehir blocks probably decreased in the Paleocene and continued to exist until the Early-Middle Eocene (Okay et al., 2017). The thrust faults in Central Pontides started in the Late-Eocene and (Kaymakçı et al., 2009; Espurt et al., 2014; Hippolyte et al., 2016). Yılmaz and Tüysüz (1984) stated that during the subduction of oceanic lithosphere towards the north in Late Cretaceous, the slices in the Atlantic-type continental margin located in the north-end moved towards the south, and argued that later in the Paleocene-Early Eocene, the direction of the movement of retro-thrust was towards the north due to the compression in the south. However, in the study area, there is no evidence that carbonate rocks thrust after the Eocene. However, when the contact relations are examined, it is determined that the ophiolitic melange is thrust over the Upper Cretaceous-Lower Eocene Beşpınar Formation (Figure 2). This situation hereby indicates that the thrusting postdates Early Eocene.

Uğuz and Sevin (2009) asserted that the allochthonous rocks in the area are formed of lower and upper tectonic slices and that the metamorphic rocks have autochthonous character.

## 7. Results

In the study area, not only ophiolite or ophiolitic melange tectonically exists on the metamorphic belt, it has been determined that carbonate units of different ages are also tectonically located on these imbrication zones. The tectonic slices formed in this study have been defined as PTS, GTS, and OMS for the first time.

The whole rock geochemistry studies explain that Kunduz metamorphites and basalts from the ophiolitic melange exhibit the tholeiitic character. Their chondrite-normalized trace element patterns show enrichment in LREE (La, Ce, Nd) for metabasites of the Kunduz Metamorphites relative to basalts belonging to the ophiolitic mélangé. In addition, HREE (Er, Tm, Yb, Lu) exhibits almost flat trends for each unit.

## Acknowledgements

This study is a part of a Ph.D. thesis that was prepared in the Graduate School of Science and Engineering of İstanbul University was supported by TÜBİTAK project no: 113Y536.

## References

- Akbayram, K., Okay, A. I., Satır, M. 2013. Early Cretaceous closure of the Intra-Pontide Ocean in western Pontides (northwestern Turkey). *Journal of Geodynamics* 65, 38-55.
- Akbulut, M., Oyman, T., Çiçek, M., Selby, D., Özgenç, I., Tokçaer, M. 2016. Petrography, mineral chemistry, fluid inclusion microthermometry and Re–Os geochronology of the Küre volcanogenic massive sulfide deposit (Central Pontides, Northern Turkey). *Ore Geology Reviews* 76, 1-18.
- Altherr, R., Topuz, G., Marschall, H., Zack, T., Ludwig, T. 2020. Evolution of a tourmaline bearing lawsonite eclogite from the Elekdağ area (Central Pontides, N Turkey): Evidence for infiltration of slab-derived B-rich fluids during exhumation. *Contributions to Mineralogy and Petrology* 148, 409-425.
- Altun, Y., Yılmaz, H., Siner, I., Yazar, F. 2015. The secrets of massive sulfide deposits on mid-ocean ridge and Küre-Magaradoruk copper deposit. *Bulletin of the Mineral Research and Exploration* 150, 51–65.
- Aydın, M., Demir, O., Özçelik, Y., Terzioğlu, N., Satır, M. 1995. A geological revision of İnebolu, Devrekani Ağılı and Küre areas: new observations in PaleoTethys–NeoTethys sedimentary successions. Erler, A., Ercan, T., Bingöl, E., Örcen, S. (Ed.). *Geology of the Black Sea Region*, General Directorate of Mineral Research and Exploration, 33–38.
- Aygül, M., Okay, A. I., Oberhansli, R., Ziemann, M. A. 2015a. Thermal structure of lowgrade accreted Lower Cretaceous distal turbidites, the Central Pontides, Turkey: insights for tectonic thickening of an accretionary wedge. *Turkish Journal of Earth Sciences* 24, 461–474.
- Aygül, M., Okay, A. I., Oberhansli, R., Schmidt, A., Sudo, M. 2015b. Late Cretaceous infant intra-oceanic arc volcanism, the Central Pontides, Turkey: petrogenetic and tectonic implications. *Asian Journal of Earth Sciences* 111, 312-327.
- Aygül, M., Okay, A. I., Oberhansli, R., Sudo, M. 2016. Pre-collisional accretionary growth of the southern Laurasian active margin, Central Pontides, Turkey. *Tectonophysics* 671, 218–234.
- Çakır, Ü. 1995. Asıköy-Toyköndü (Küre-Kastamonu) masif sülfid yataklarının jeolojik özellikleri. *Bulletin of the Mineral Research and Exploration* 117, 29–40.
- Çelik, Ö. F., Chiaradia, M., Marzoli, A., Özkan, M., Billor, Z. 2016. Jurassic metabasic rocks in the Kızılırmak accretionary complex (Kargı region, Central Pontides, Northern Turkey). *Tectonophysics* 672–673, 34–49.
- Çelik, Ö. F., Marzoli, A., Marschik, R., Chiaradia, M., Neubauer, F. 2011. Early–Middle Jurassic intra-oceanic subduction in the İzmir–Ankara–Erzincan Ocean, Northern Turkey. *Tectonophysics* 509, 120–134.
- Çelik, Ö. F., Marzoli, A., Marschik, R., Chiaradia, M., Mathur, R. 2018. Geochemical, mineralogical and Re–Os isotopic constraints on the origin of Tethyan oceanic mantle and crustal rocks from the Central Pontides, northern Turkey. *Mineralogy and Petrology* 112, 25–44.
- Çimen, O., Göncüoğlu, M. C., Sayit, K. 2016. Geochemistry of the metavolcanic rocks from the Çangaldağ Complex in the Central Pontides: implications for the Middle Jurassic arc-back-arc system in the Neotethyan Intra-Pontide Ocean. *Turkish Journal of Earth Sciences* 25, 491–512.
- Çimen, O., Göncüoğlu, M. C., Simonetti, A., Sayit, K. 2017. Whole-rock geochemistry, zircon U–Pb and Hf isotope systematics of the Çangaldag pluton: evidences for middle Jurassic Continental

- Arc magmatism in the central Pontides, Turkey. *Lithos* 290, 136–158.
- Çimen, O., Göncüoğlu, M.C., Simonetti, A., Sayit, K. 2018. New zircon U-Pb LA-ICP-MS ages and Hf isotope data from the Central Pontides (Turkey): geological and geodynamic constraints. *Journal of Geodynamics* 116, 23–36.
- Derman, A. S., Sayılı, A. 1995. İnalıtı Formation: a key unit for regional geology. In: Erler, A., Ercan, T., Bingöl, E., Örcen, S. (Eds.). *Geology of the Black Sea Region, General Directorate of Mineral Research and Exploration*, 104–108.
- Dönmez, C., Günay, K., Yıldız, H., Şahin, Ş. 2013. Gökırmak ve Devrettepe-Hanönü (Kastamonu) Cu cevherleşmesi. *MTA Doğal Kaynaklar ve Ekonomi Bülteni* 127, 16.
- Espurt, N., Hippolyte, J. C., Kaymakçı, N., Sangu, E. 2014. Lithospheric structural control on inversion of the southern margin of the Black Sea Basin, Central Pontides, Turkey. *Lithosphere* 6(1), 26-34.
- Eyüboğlu, Y., Santosh, M., Keewook, Yi., Tüysüz, N., Korkmaz, S. 2014. The Eastern Black Sea-type volcanogenic massive sulfide deposits: geochemistry, zircon U-Pb geochronology and an overview of the geodynamics of ore genesis. *Ore Geology Reviews* 59, 29-54.
- Finetti, I., Bricchi, G., Del Ben, A., Pipan, M., Xuan, Z. 1988. Geophysical study of the Black Sea. *Bolletino di Geofisica ed Applicata* 30, 197–324.
- Genç, Ş., Kurt, Z., Küçükmen, Ö., Cevher, F., Saraç, G. 1991. Merzifon (Amasya) dolayının jeolojisi, General Directorate of Mineral Research and Exploration, Report No: 9527, Ankara (unpublished).
- Göncüoğlu, M. C. 2010. Introduction to the geology of Turkey: geodynamic evolution of the Pre-Alpine and Alpine Terranes. *Bulletin of the Mineral Research and Exploration* 1–69.
- Görür, N. 1988. Timing of opening of the Black Sea Basin. *Tectonophysics* 147, 247–262.
- Gücer, M. A., Arslan, M., Sherlock, S., Heaman, L. M. 2016. Permo-Carboniferous granitoids with Jurassic high- temperature metamorphism in Central Pontides, Northern Turkey. *Mineralogy and Petrology* 110, 943-964.
- Gümüşsu, M. 1980. Amasya ili, Merzifon ve Suluova İlçeleri kömür jeolojisi. General Directorate of Mineral Research and Exploration, Report No. 7063, Ankara.
- Günay, K., Dönmez, C., Oyan, V., Yıldırım, N., Çiftçi, E. 2018. Geology and geochemistry of sediment-hosted hanönü massive sulfide deposit (Kastamonu – Turkey). *Ore Geology Reviews* 101, 652–674.
- Günay, K., Dönmez, C., Oyan, V., Baran, C., Çiftçi, E., Parlak, O., Yıldırım, N., Deng., XH, Li C., Yıldırım, E., Özkümüş, S. 2019. Geology, geochemistry and Re-Os geochronology of the Jurassic Zeybek volcanogenic massive sulfide deposit (Central Pontides, Turkey). *Ore Geology Reviews* 111, 102994.
- Hakyemez, Y., Barkurt, M. Y., Bilginer, E., Pehlivan, Ş., Can, B. 1986. Yapraklı-İlgaz-Çankırı-Çandır dolayının jeolojisi, General Directorate of Mineral Research and Exploration, Report No: 7966, Ankara.
- Hippolyte, J. C., Müller, C., Kaymakçı, N., Sangu, E. 2010. Dating of the Black Sea Basin: new nannoplankton ages from its inverted margin in the Central Pontides (Turkey). In: Sosson, M., Kaymakçı, N., Stephenson, R., Bergerat, F., Starostenko, V. (Ed.). *Sedimentary Basin Tectonics from the Black Sea and Caucasus to the Arabian Platform. Geological Society of London, Special Publications* 340, 113–136.
- Hippolyte, J. C., Espurt, N., Kaymakçı, N., Sangu, E., Müller, C. 2016. Cross-sectional anatomy and geodynamic evolution of the Central Pontide orogenic belt (northern Turkey). *International Journal of Earth Sciences* 105, 81–106.
- Kaymakçı, N., Özçelik, Y., White, S. H., Van Dijk, P. M. 2009. Tectono-stratigraphy of the Çankırı Basin: late Cretaceous to early Miocene evolution of the Neotethyan suture zone in Turkey. *Geological Society of London, Special Publications* 311(1), 67-106.
- Ketin, İ. 1966. Tectonic units of Anatolia (Asia Minor). *Bulletin of the Mineral Research and Exploration* 66, 23–34.
- Ketin, İ., Gümüş, A. 1963. Sinop-Ayancık arasında III. Bölgeye dahil sahaların jeolojisi. *Turkish Petroleum Corporation, Report No: 288, Ankara.*
- Koç, Ş., Ünsal, A., Kadioğlu, Y. 1995. Küre (Kastamonu) cevherleşmelerini içeren volkanitlerin jeolojisi, jeokimyası ve jeotektonik konumu. *Bulletin of the Mineral Research and Exploration* 117, 41-54.
- Lefebvre, C., Meijers, M. J. M., Kaymakçı, N., Peynircioğlu, A., Langereis, C. G. 2013. Reconstructing the geometry of central Anatolia during the late Cretaceous: large-scale Cenozoic rotations and deformation between the Pontides and Taurides. *Earth and Planetary Science Letters* 366, 83-98.

- Marroni, M., Frassi, C., Göncüoğlu, M. C., Di Vincenzo, G., Pandolfi, L. 2014. Late Jurassic amphibolite facies metamorphism in the Intra- Pontide Suture Zone (Turkey): an eastward extension of the Vardar Ocean from the Balkans into Anatolia?. *Journal of the Geological Society of London* 171, 605–608.
- Nikishin, A. M., Okay, A., Tüysüz, O., Demirer, A., Wannier, M. 2015. The Black Sea basins structure and history: new model based on new deep penetration regional seismic data. Part 2: Tectonic history and paleogeography. *Marine Petroleum Geology* 59, 656–670.
- Okay, A. I., Göncüoğlu, M. C. 2004. Karakaya Complex: a review of data and concepts. *Turkish Journal of Earth Sciences* 13, 77–95.
- Okay, A. I., Nikishin, A. M. 2015. Tectonic evolution of the southern margin of Laurasia in the Black Sea region. *International Geology Reviews* 57, 1051-1076.
- Okay, A. I., Altıner, D., Sunal, G., Aygül, M., Akdoğan, R. 2017. Geological evolution of the central Pontides. Simmons, M. D., Tari, G., Okay, A. I. (Ed.). *Petroleum Geology of the Black Sea*. Geological Society of London, Special Publications 464(1), 33.
- Okay, A. I., Gürsel, S., Sherlock, S., Altıner, D., Tüysüz, O. 2013. Early Cretaceous sedimentation and orogeny on the active margin of Eurasia: Southern Central Pontides, Turkey. *Tectonics* 32, 1247–1271.
- Okay, A. I., Gürsel, S., Tüysüz, O., Sherlock, S., Keskin, M. 2014. Low-pressure-high-temperature metamorphism during extension in a Jurassic magmatic arc, Central Pontides, Turkey. *Journal of Metamorphic Geology* 32, 49-69.
- Okay, A. I., Şengör, A. M. C., Görür, N. 1994. Kinematic history of the opening of the Black Sea and its effect on the surrounding regions. *Geology* 22 (3), 267-270.
- Okay, A. I., Tüysüz, O., Satır, M., Özkan-Altıner, S., Altıner, D. 2006. Cretaceous and Triassic subduction-accretion, HP/ LT metamorphism and continental growth in the Central Pontides, Turkey. *Geological Society of America Bulletin* 118, 1247–1269.
- Özgül, N., Turşucu, A., Özyardımcı, N., Şenol, M., Bingöl, İ. 1981. Munzur dağlarının jeolojisi. General Directorate of Mineral Research and Exploration, Report No: 6995, 136, Ankara (unpublished).
- Pearce, J. A. 1982. Trace element characteristics of lavas from destructive plate boundaries, andesites: orogenic andesites and related rocks. Thorpe R. S. (Ed.). *John Wiley and Sons, Chichester*, 525-548.
- Pearce, J. A. 1996. A user's guide to basalt discrimination diagrams, Trace Element Geochemistry of Volcanic Rocks: Applications for Massive Sulphide Exploration. Wyman, D. A. (Ed.). *Geological Association of Canada, Short Course Notes* 12, 79–113.
- Pearce, J. A. 2008. Geochemical fingerprinting of oceanic basalts with applications to ophiolite classification and the search for Archean oceanic crust. *Lithos* 100, 14–48.
- Rice, S. P., Robertson, A. H. F., Ustaömer, T. 2006. Late Cretaceous–Early Cenozoic tectonic evolution of the Eurasian active margin in the Central and Eastern Pontides, northern Turkey. Robertson, A. H. F., Mountrakis, D. (Ed.). *Tectonic Development of The Eastern Mediterranean Region*. Geological Society of London, Special Publication 260, 413-445.
- Robertson, A. H. F. 2002. Overview of the genesis and emplacement of Mesozoic ophiolites in the Eastern Mediterranean Tethyan Region. *Lithos* 65, 1-67.
- Robertson, A. H., Ustaömer, T. 2004. Tectonic Evolution of The Intra-Pontide Suture Zone in The Armutlu Peninsula, NW Turkey. *Tectonophysics* 381, 175–209.
- Robertson, A. H. F., Ustaömer, T., Parlak, O., Ünlügenç, Ü. C., Taşlı, K. 2006. The Berit transect of the Tauride thrust belt, S Turkey: Late Cretaceous–Early Cenozoic accretionary/collisional processes related to closure of the Southern Neotethys. *Journal of Asian Earth Sciences* 27, 108-145.
- Robinson, A., Rudat, J. H., Banks, C. J., Wiles, R. L. F. 1996. Petroleum geology of the Black Sea. *Marine and Petroleum Geology* 13, 195–223.
- Sun, S. S., McDonough, W. F. 1989. Chemical and isotopic systematics of oceanic basalts: implications for mantle composition and processes. *Geological Society of London, Special Publication* 42, 313-345.
- Sütçü, Y. F., Barkurt, M. Y., Bilginer, E., Kurt, Z., Pehlivan, Ş. 1994. Boyabat-Vezirköprü arasındaki jeolojisi. General Directorate of Mineral Research and Exploration, Report No, 9884, Ankara.
- Şengör, A. M. C., Yılmaz, Y. 1981. Tethyan evolution of Turkey: a plate tectonic approach. *Tectonophysics* 75, 181-241.

- Şengör, A. M. C., Yılmaz, Y., Ketin, İ. 1982. Remnants of a pre-late Jurassic ocean in northern Turkey: fragments of Permian-Triassic Paleo-Tethys?. *Geological Society of America Bulletin* 93, 932-936.
- Tekin, U. K., Göncüoğlu, M. C., Pandolfi, L., Marroni, M. 2012. Middle Late Triassic radiolarian cherts from the Arkotdag melange in northern Turkey: implications for the life span of the northern Neotethyan branch. *Geodinamica Acta* 25, 305-319.
- Topuz, G., Göçmengil, G., Rolland, Y., Çelik, Ö. F., Zack, T. 2012. Jurassic accretionary complex and ophiolite from northeast Turkey: no evidence for the Cimmerian continental ribbon. *Geology* 41, 255-258.
- Türkecan, A., Hepşen, N., Papak, I., Akbaş, B., Dinçel, A. 1991. Seben-Gerede (Bolu)-Güdül-Beypazarı (Ankara) ve Çerkeş-Orta-Kurşunlu (Çankırı) yörelerinin (Koroğlu dağları) jeolojisi ve volkanik kayaların petrolojisi, General Directorate of Mineral Research and Exploration, Report No: 9193, Ankara (unpublished).
- Tüysüz, O. 1985. Kargı Masifi ve dolayındaki tektonik birliklerin ayırıcı ve araştırılması (petrolojik inceleme), PhD Thesis, İstanbul University, Institute of Science and Technology, 431.
- Tüysüz, O. 1990. Tectonic evolution of a part of the Tethyside orogenic collage: the Kargı Massif, northern Turkey. *Tectonics* 9, 141-160.
- Tüysüz, O. 1999. Geology of the cretaceous sedimentary basins of the western Pontides. *Geological Journal* 34, 75-93.
- Tüysüz, O. 2017. Cretaceous geological evolution of the Pontides, *Geological Society of London, Special Publications* 464(1), 69.
- Tüysüz, O., Tekin, U. K. 2007. Timing of imbrication of an active continentalmargin facing the northern branch of Neotethys, Kargı Massif, Northern Turkey. *Cretaceous Research* 28, 754-764.
- Uğuz, M. F., Sevin, M. 2009. 1/100.000 Ölçekli Türkiye Jeoloji Haritaları, No:115, General Directorate of Mineral Research and Exploration, Ankara (in Turkish).
- Ustaömer, T., Robertson, A. H. F. 1997. Tectonic-sedimentary evolution of the northtethyan margin in the central Pontides of northern Turkey. Robinson, A. G. (Ed.). *Regional and Petroleum Geology of the Black Sea and Surrounding Region. American Association of Petroleum Geologists Memoir* 68, 255-290.
- Ustaömer, T., Robertson, A. H. F. 1999. Geochemical evidence used to test alternative plate tectonic models for the pre-Upper Jurassic (Palaeotethyan) units in the Central Pontides, N Turkey. *Geological Journal* 34, 25-53.
- Yalçın, C. 2018. Geology and formation of the Gökçedoğan (Kargı-Çorum) Cu±Zn mineralisation. PhD Thesis, İstanbul University, Institute of Graduate Studies in Science and Engineering, 301 (in Turkish).
- Yılmaz, Y., Tüysüz, O. 1984. Kastamonu-Boyabat-Vezirköprü-Tosya arasındaki bölgenin jeolojisi (Ilgaz-Kargı masiflerinin etüdü). *Maden Tetkik ve Arama Genel Müdürlüğü Yayınları*, Ankara (in Turkish).
- Yılmaz, Y., Tüysüz, O. 1988. Kargı masifi ve dolaylarında Mesozoyik tektonik birliklerin düzenlemeleri sorununa bir yaklaşım. *Turkish Association of Petroleum Geologist Bulletin* 1(1), 73-86 (in Turkish).
- Yılmaz, Y., Tüysüz, O., Yiğitbaş, E., Genç, S. C., Şengör, A. M. C. 1997. Geology and tectonic evolution of the Pontides. Robinson, A. G. (Ed.). *Regional and Petroleum Geology of the Black Sea and Surrounding Region. Bulletin of American Association Petroleum Geology* 68, 183-226.
- Yiğitbaş, E., Tüysüz, O., Serdar, H. S. 1990. Yığışım prizması ve melanj gelişimine bir örnek: Orta Pontidler. *Türkiye 8. Petrol Kongresi*, Ankara, Türkiye, 25-26 (in Turkish).

# BULLETIN OF THE MINERAL RESEARCH AND EXPLORATION

2022

169

ISSN : 0026-4563

E-ISSN : 2651-3048



## CONTENTS

### Research Articles

Some thoughts on the morphotectonic development of the Denizli region.....1 Yücel YILMAZ	1
Recovery of Cu-Ce from copper slag by using flotation and chemical methods.....17 Bekir BAŞKURT, M. Tayhan SERDENGEÇTİ, Kaan ÖZÇELİK and Hüseyin BAŞTÜRKÇÜ	17
Investigation of thermal transformation of composite material obtained from granite and recrystallized limestone natural stone wastes .....27 Gökhan EROL and Devrim PEKDEMİR	27
Estimation of blast vibrations by numerical modelling and signal analysis .....39 Güzin Gülsev UYAR AKSOY, Cemalettin Okay AKSOY and Hasan Eray YAMAN	39
Uludağ extensional metamorphic core complex: preliminary field observations.....49 Gürol SEYİTOĞLU and Korhan ESAT	49
Geology, fluid inclusion characteristics and mineral resource estimation of the Güzelyayla porphyry Cu-Mo mineralization (NE Türkiye)...63 Mustafa Kemal REVAN, Deniz GÖÇ, Mustafa ÖZKAN, Cüneyt ŞEN, Rasim Taylan KARA, Mustafa TOKOĞLU, Semi HAMZAÇEBİ, Rıfat Cihan SEVİM, Fatih SEZEN, Celaledin BAYRAKTAR and Ömer AKGÜL	63
Evaluation of potential rock falls with three-dimensional analysis: Example of Oltanbey and Hasanbey districts (Gümüşhane city center)...87 Selçuk ALEMDAĞ, Rasim Taylan KARA and Hasan Tahsin BOSTANCI	87
Assessment of crustal thinning and tectonic stress distribution of Gülbahçe fault zone and its surroundings (İzmir, West Türkiye) using gravity and magnetic anomalies.....105 Oya ANKAYA PAMUKÇU, Ayça ÇIRMIK, Fikret DOĞRU, Ece ÜNLÜ and Barış Can MALALİÇİ	105
Analysis of the stress distribution of North Anatolian Fault Zone for the part between Amasya - Tokat cities .....121 Ayça ÇIRMIK, Ufuk AYDIN, Oya ANKAYA PAMUKÇU and Fikret DOĞRU	121
Formation and tectonic evolution of structural slices in eastern Kargı Massif (Çorum, Türkiye) .....135 Cihan YALÇIN, Nurullah HANILÇI, Mustafa KUMRAL and Mustafa KAYA	135
Acknowledgements.....155	155
Bulletin of the Mineral Research and Exploration Notes to the Authors .....157	157

Phone : +90 (312) 201 10 00

Fax : +90 (312) 287 91 88

Adress : MTA 06530 - Ankara - TURKEY

www.mta.gov.tr

## ACKNOWLEDGEMENTS

We would like to thank the honored reviewers whose names are written below contributing to the Bulletin of the Mineral Research and Exploration during the article review process between 30<sup>th</sup> of November 2021 and 22<sup>nd</sup> November 2022 in the name of the Executive Publication Editorial.

Mustafa AFŞİN (Türkiye)	Ye E. FENG (USA)	Vijaya RAO (India)
Joseph AISABOKHAE (Nigeria)	Anke FRIEDRICH (Germany)	Moumtaz RAZACK (France)
Taylan AKIN (Türkiye)	Emmanuel FRITSCH (France)	Leigh H. ROYDEN (USA)
İsmail AKKAYA (Türkiye)	Luca GASPERINI (Italy)	Ladislaus RYBACH (Switzerland)
Nicholas ARNDT (France)	Gönenç GÖÇMENGİL (Türkiye)	Çağdaş SAĞIR (Türkiye)
Abdelmalek ATIA (Algeria)	Tolga GÖNENÇ (Türkiye)	Hakim SAİBİ (United Arab Emirates)
Ahmet Emin ATİK (Türkiye)	Murat GÜL (Türkiye)	Gülcan SARP (Türkiye)
Ulaş AVŞAR (Türkiye)	Fatma GÜLTEKİN (Türkiye)	Hossain Md. SAYEM (Bangladesh)
Harun AYDIN (Türkiye)	Recep GÜNEY (Türkiye)	Ülkü SAYIN (Türkiye)
Guru BALAMURUGAN (India)	Ömer Feyzi GÜRER (Türkiye)	Christopher SCHIFFLECHNER (Germany)
Emil BAYRAMOV (Azerbaijan)	Martina HAVELCOVÁ (Czech Republic)	Viladkar SHRINIVAS (India)
Özcan BEKTAŞ (Türkiye)	Fatma HOŞÇEBİ (Türkiye)	Adile Melis SOMAY ALTAŞ (Türkiye)
Daniel BERNOULLI (Switzerland)	Hakan HOŞGÖRMEZ (Türkiye)	M. Lütfi SÜZEN (Türkiye)
Foued BOUAICHA (Algeria)	Tahir Serkan IRMAK (Türkiye)	Eren ŞAHİNER (Türkiye)
Mehmet BUĞDAYCI (Türkiye)	Mostafa KAMEL (Egypt)	Şehnaz ŞENER (Türkiye)
Ersin BÜYÜK (Türkiye)	Hüseyin KARAKUŞ (Türkiye)	Çetin ŞENKUL (Türkiye)
Aydın BÜYÜKSARAÇ (Türkiye)	Hakan KARSLI (Türkiye)	Servet TİMUR (Türkiye)
Oya CENGİZ (Türkiye)	Orhan KARSLI (Türkiye)	Ahmet TURAN (Türkiye)
Dornadula CHANDRASEKHARAM (India)	Bülent KAYPAK (Türkiye)	Koray ULAMIŞ (Türkiye)
Kimon CHRISTANIS (Greece)	Bedri KURTULUŞ (Türkiye)	Emin ULUGERGERLİ (Türkiye)
Emine CİCİOĞLU SÜTÇÜ (Türkiye)	György LESS (Hungary)	İnan ULUSOY (Türkiye)
Ziyadin ÇAKIR (Türkiye)	Adrian LISTER (United Kingdom)	Yusuf URAS (Türkiye)
Ömer Faruk ÇELİK (Türkiye)	Sape A. MIEDEMEA (Netherlands)	Mehmet UTKU (Türkiye)
Günay ÇİFCİ (Türkiye)	Soumyajit Mukherjee MUKHERJEE (India)	Bruno VALENTİM (Portugal)
Kaan Hakan ÇOBAN (Türkiye)	Faruk OCAKOĞLU (Türkiye)	Noël VANDENBERGHE (Belgium)
İbrahim ÇOBANOĞLU (Türkiye)	Safianou OUSMANOU (Cameroon)	Orlando VASELLI (Italy)
Güldemin DARBAŞ (Türkiye)	Erdinç ÖKSÜM (Türkiye)	Alaaddin VURAL (Türkiye)
Michael DIEDERICH (Germany)	Kemal Mert ÖNAL (Türkiye)	Vivek WALIA (Taiwan)
Ünal DİKMEN (Türkiye)	Selim ÖZALP (Türkiye)	Leyuan WU (China)
Feyza DİNÇER (Türkiye)	Çağlar ÖZER (Türkiye)	İrfan YEŞİLNACAR (Türkiye)
Doğa DOĞAN (Türkiye)	Emre Aytuğ ÖZSOY (Türkiye)	Ahmet YILDIZ (Türkiye)
Fikret DOĞRU (Türkiye)	Serkan ÖZTÜRK (Türkiye)	Hüseyin YILMAZ (Türkiye)
Derman DONDURUR (Türkiye)	Özcan ÖZYILDIRIM (Türkiye)	Yücel YILMAZ (Türkiye)
Günseli ERDEM (Türkiye)	Eleftheria PAPANITRIU (Greece)	Sabah YILMAZ ŞAHİN (Türkiye)
Ahmet Cem ERKMAN (Türkiye)	Spyridon PAVLIDIS (Greece)	Erdinç YİĞİTBAŞ (Türkiye)
Orkun ERSOY (Türkiye)	Johannes PIGNATTI (Italy)	Elena YURIEVNA ZAKREVSAYA (Russia)
Daniel ESHIMIYAKHE (Nigeria)	Maksim Igorevich PROTASOV (Russia)	Cengiz ZABCI (Türkiye)
Joan ESTERLE (Australia)	Asif QURESHI (India)	Uğur ZAMAN (Türkiye)
İslam FEJZA (Kosovo)	Sankaran RAJENDRAN (Qatar)	



## Publication Rules for the “Bulletin of the Mineral Research and Exploration”

### 1. Purposes

- To contribute to the establishment of scientific communication issues in earth sciences both in Turkey and internationally.
- To contribute to economic (mining, oil and gas, geothermal etc.), environmental and social (geoheritage etc.) studies in Turkey and in the World.
- To make the earth science scientific research and applications made by the MTA on publicly known,
- To use the bulletin as an effective tool in the international publication exchange by keeping it at a high level in terms of quality, scope and format,

### 2. Scope-Attribute

In order for manuscripts to be published in the Bulletin of the Mineral Research and Exploration, they must have at least one of the following qualifications:

#### 2.1. Research Articles and Reviews

##### 2.1.1. Original Scientific Researches

- Such articles cover original scientific research and its results that contribute to the fundamental issues of earth sciences, research and evaluation of underground resources, and examine the environmental problems in terms of earth sciences,
- It covers research that apply new approaches and methods in solving problems related to earth sciences.

##### 2.1.2. Review Articles

- They cover studies that compile previous research on subjects of earth sciences with a critical approach and put forward a new opinion on that subject.

#### 2.2. Criticism and Response Articles

- Articles that criticize all or part of an article of the bulletin in the latest issue are published in the following first issue, if submitted within six months at the latest from the date of publication digitally.
- Before the publication, review articles are sent to the responsible author of the criticized article to make a response.
- If the criticism is not responded within foreseen time, the criticism letter is published alone, subsequent replies are not published. Replies are not allowed to be re-criticized.

- In criticizing and replying, scientific discussion and ethical rules should be followed. Criticism and response manuscripts should not exceed four pages, including figures, if available.

### 2.3. Brief Notes

- In “Brief Notes” section of the Bulletin of the Mineral Research and Exploration, the brief, objective and concise articles reflecting the data obtained from scientific researches and applications carried out in the area of earth sciences or new findings related to previously unknown geosciences in Turkey are given place.
- The articles arranged in the “Brief Notes” section are published without waiting in the first or in the second issue the latest, after the date they are sent to the Chair of the Editorial Board in order to ensure rapid communication.
- Articles requested to be published in the “Brief Notes” section should not exceed four pages, including all figures and tables.

### 3. Submission and Acceptance for Manuscripts

- The manuscripts submitted to be published in the Bulletin of the Mineral Research and Exploration should be prepared in ENGLISH in accordance with the Publishing Rules of the Bulletin of the Mineral Research and Exploration, and submitted via electronic application at <http://dergi.mta.gov.tr/index.php>.
- The manuscript must not have been previously published partially or completely elsewhere (except in abstract form).
- Manuscripts submitted with the request for publication in the Bulletin of the Mineral Research and Exploration should not exceed 30 pages, including all illustrations. The articles exceeding 30 pages can be published if deemed appropriate by referees and editors.
- In the submitted manuscript, the number of figures and tables should be given in proportion to the main text in a ratio of 1/3.
- Corresponding author is asked to suggest at least three referees for the evaluation of the manuscript. (The proposed referees and the authors should not have any joint work within the last two years).

- Manuscripts that do not comply with the Publishing Rules for the Bulletin of the Mineral Research and Exploration in terms of quality and form are directly returned without being examined in terms of content.
- Manuscripts deemed appropriate in terms of format are sent to at least two expert referees for review by the Editorial Board of the Bulletin of the Mineral Research and Exploration.
- Authors should make the referee corrections and suggestions sent to them within 20 days and upload to the system.
- Comments from referees are evaluated by the Editors and associated editors. Manuscripts deemed necessary to be corrected are sent back to the authors with a request for correction. Whether the suggested corrections have been made or not is checked by the Editorial Board.
- In the revision proposals given by the editors and referees, if there are suggestions that are not accepted by the author and have not been corrected, a report explaining the reason for rejecting these suggestions by the author should be sent to the Editorial Board together with the corrected copies.
- After the last control at the printing stage, the pre-print of the manuscript is sent to the authors in pdf format and the printing control is requested.
- Articles, not accepted for publication are not returned to the authors, for the unpublished articles, a letter is written to the responsible author indicating the reason for rejection.

#### **4. Language and Period of Publication**

- The Bulletin of the Mineral Research and Exploration is published three times a year, each issue as being in English (printed and online) and in Turkish (online) languages.
- The spelling rules of the Turkish Language Association are valid for the spelling rules for the Turkish issue. However, in spelling of the words related to earth sciences, the spelling forms of technical terms are used in accordance with the decision of the Editorial Board (For example; underground, ground, earth's crust, etc.).

#### **5. Spelling Draft**

- The text of the manuscripts to be sent for the first review with the request to be published in the

Bulletin of the Mineral Research and Exploration should be written in A4 (29.7 x 21 cm) size, word format, Times New Roman 10 pt., normal with 2.0 line spacing.

- At the bottom, top, left and right of the page 2.5 cm indent must be left. Formulas that require the use of special letters and symbols should be presented in computer media.
- In all subtitles, the initials of all words must be capital. First degree headings to be used in the article should be written in Times New Roman, 10 pt., bold and left aligned by giving numbers. Secondary headings should be written in Times New Roman, 10 pt., normal font and left aligned by giving numbers. Third-degree headings should be written in Times New Roman, 10 pt., italic font and left-aligned by giving numbers. Fourth-order headings should be written in Times New Roman, 10 pt., italic, aligned to the left, without giving numbers, and the text should continue after the title without a colon and a paragraph (see example article: [www.dergi.mta.gov.tr](http://www.dergi.mta.gov.tr)).
- One blank line should be left after paragraphs in the text.
- Paragraph headings should be written 0.5 mm indentation.
- One article should respectively contain;
  - Title
  - Author's Name and Surname and \* sign
  - Abstract
  - Keywords
  - Introduction
  - Main Text
  - Discussion
  - Results
  - Acknowledgements
  - Reference sections.
- Line and page numbers must be added to the article text.

#### **5.1. Title of the Article**

- The title should reflect the subject of the article as briefly, clearly and adequately as possible. Subjects that are not sufficiently covered in the article should not be included in the title. The first letter of the title

should be capitalized and the other words should be in lowercase letters (except for proper names) in Times New Roman, 10 pt. and bolded.

### **5.2. Author Name, Address and E-Mail Address**

- The first name of the authors should be in lowercase (except the first letter), and the surname should be in capital letter and without any title.
- Only the name of the organization should be specified in the occupational address after the name and surname of the authors (position should not be specified).
- ORCID number should be taken from [www.orcid.org](http://www.orcid.org) and placed under the address.
- In articles written by more than one author, numbers should be placed on surnames of the authors, the address information should be included in the bottom line with a single line spacing. In this section, the corresponding author of the article should be indicated by using an asterisk (\*) and the corresponding author's e-mail, telephone and other contact information must be provided.
- Abbreviations should not be used in writing the author's name and address. Addresses should be given in Turkish in Turkish publication (online) and in English in English publication (printed).

### **5.3. Abstract**

- Abstract should be written at a level that can be understood without referring to the other parts of the article.
- The abstract should be organized as a brief presentation of the sections in the article, reflect the purpose of the article, be informative, and should be written in a way to emphasize new data and results on the subject.
- Short and simple sentences should be used in writing the abstract.
- In the abstract, there should not be any reference to other parts and illustrations of the article or to other articles.
- Information not mentioned in the main text should not be included in the abstract.
- The abstract should not exceed approximately 200 words and should be written as a single paragraph.
- Abstract should be written in Times New Roman, 10 pt., normal text with single line spacing.

- “ABSTRACT” should not be placed for the articles to be included in “Brief Notes” section.
- The English abstract should be given under the heading “ABSTRACT”.

### **5.4. Keywords**

In order to facilitate searches, five keywords that will indicate the general content of the article should be selected and specified in this section. Words used in the title should not be repeated.

### **5.5. Introduction**

- In this section, the necessary information for preparatory and facilitative to understand the article such as the purpose of the study, its location, methods of study and previous reviews on the subject should be given.
- If an unusual way is followed in naming, classification and abbreviations within the text of the manuscript, its reason should be stated in this section.
- Each of the topics to be included in this section can create a separate paragraph or a subtitle can be given for each of them when necessary (e.g. method, material, terminology and etc.).
- This section can again be used when reminder information is needed to facilitate the understanding of the article (e.g. statistical information, formulas, experimental or application methods and etc.).

### **5.6. Main Body of Article**

- Constitutes the main body of the article.
- In this section, the data, findings and opinions that are intended to be transferred to the reader on the subject are mentioned.
- The data used in other parts of the article such as “Abstract”, “Discussions”, “Results” originate from this part.
- Care should be taken not to deviate from the purpose stressed in the “Introduction” section of the article when dealing the topics. Information that does not contribute to the achievement of the purpose of the article or that is not used to reach the conclusion should not be included.
- All data used in this section and all opinions put forward should be proven by the findings obtained from the studies or based on a source by reference.

- The way and method to be followed in handling the topics vary according to the characteristics of the topics covered.
- Subject headings in necessary numbers with different stages should be used in this section.

### 5.7. Discussions

- The data and findings objectively conveyed in the “Main Text” section of the article should be discussed by the author in this section. Discussions should be separate from the “Results” section.

### 5.8. Results

- New data and findings obtained from the review that constitutes the subject of the article should be stated concisely and concretely in this section.
- Subjects that are not adequately addressed and / or covered in the main text should not be included in this section.
- The results can be given as items in order to emphasize the research results and make the expression understandable.

### 5.9. Acknowledgements

- In this section, important contributions in the realization of the study, which is the subject of the article, are indicated. An attitude that will distract this section from its main purpose should not be taken in the Acknowledgements.

Contribution should be stated as short and concise as possible to the persons and/or organizations that provided assistance (reading, writing, language assistance, etc.) during the research, and should not take an attitude that would distract this section from its main purpose.

### 5.10. References

- In this section, only the documents mentioned in the article should be included in complete.
- Abbreviations should be avoided in naming the publications and journals.
- The mentioned documents should be written in Times New Roman and 9 pt.
- The first line of the references should be written as justified to the left margin of the page, and the other lines should be written by giving a hanging indent value of 1.25.

- The references should be listed in alphabetical order, taking into account the surnames of the authors.
- If one author has more than one work in the same year, lowercase alphabet letters should be used right after the year of publication and the letters should be italic (e.g. Saklar, 2011*a, b*).
- If more than one document of the same author is cited, first his / her single-name publications in chronological order, then double-names according to the chronological order, and then multi-names according to chronological order should be given.

#### *For example:*

- Corradini, C. 2007. The conodont genus *Pseudooneotodus* Drygant from the Silurian and Lower Devonian of Sardinia and the Carnic Alps (Italy). *Bollettino-Societa Paleontologica Italiana* 46 (2/3), 139-148.
- Corradini, C., Serpagli E. 1999. A Silurian conodont biozonation from late Llandovery to end Pridoli in Sardinia (Italy), In Serpagli (Ed.), *Studies on conodonts: Proceedings of the 7th European Conodont Symposium*. *Bollettino della Società Paleontologica Italiana* 37 (2-3) (1998), 255-273.
- Corradini, C., Corriga, M. G. 2010. Silurian and lowermost Devonian conodonts from the Passo Volaja area (Carnic Alps, Italy). *Bollettino della Società Paleontologica Italiana* 49 (3), 237-253.
- Corradini, C., Corriga, M. G. A. 2012. Pridoli – Lochkovian conodont zonation in Sardinia and the Carnic Alps: implications for a global zonation scheme. *Bulletin of Geosciences* 87 (4), 635-650.
- Corradini, C., Leone, F., Loi, A., Serpagli, E. 2001. Conodont Stratigraphy of A Highly Tectonised Silurian-Devonian Section in The San Basilio Area (Se Sardinia, Italy). *Bollettino Della Societa Paleontologica Italiana* 40 (3), 315-323, 1 Pl.
- Corradini, C., Pondrelli, M., Serventi, P., Simonetto, L. 2003. The Silurian cephalopod limestone in the Monte Cocco area (Carnic Alps, Italy): conodont biostratigraphy. *Revista Española de Micropaleontologia* 35 (3), 285-294.

Corradini, C., Corriga, M. G., Männik, P., Schönlaub, H. P. 2015. Revised conodont stratigraphy of the Cellon section (Silurian, Carnic Alps). *Lethaia* 48 (1), 56-71.

- If documents of different authors with the same surname are mentioned, they should be written in alphabetical order, considering their first names.
- If documents of different author(s) with the same surname are mentioned in the same year, they should be cited as given below. Same publication rule should be applied for the single author.

***For example:***

“Usta, M., Yetiş, C., Nazik, A. 2018. Anamur (Mersin) dolayının stratigrafisi ve Kambriyen yaşlı kuvarsitler ile dolomitlerin endüstriyel hammadde potansiyeli. Çukurova Üniversitesi Fen ve Mühendislik Bilimleri Dergisi 35, 6, 11-22, Adana”

should be cited as (Usta, M. et. al., 2018)

“Usta, D., Ateş, Ş., Çoban, M., Deveci, Ö, Sağlam, F.M. 2014. Adıyaman-Sincik-Hilvan arasındaki bölgenin stratigrafisi ve kaya türü özellikleri. 67. Türkiye Jeoloji Kurultayı Bildiri Özleri, Ankara, 98-99”

should be cited as (Usta, D. et. al., 2018)

“Usta, M. 2018. Anamur (Mersin) dolayının stratigrafisi ve Kambriyen yaşlı kuvarsitler ile dolomitlerin endüstriyel hammadde potansiyeli. Çukurova Üniversitesi Fen ve Mühendislik Bilimleri Dergisi 35, 6, 11-22, Adana”

should be cited as (Usta, M., 2018)

“Usta, D. 2014. Adıyaman-Sincik-Hilvan arasındaki bölgenin stratigrafisi ve kaya türü özellikleri. 67. Türkiye Jeoloji Kurultayı Bildiri Özleri, Ankara, 98-99”

should be cited as (Usta, D., 2018)

- If the document is in a periodical publication (if it is an article), information about the document is given in the following order: Authors ‘ surname, first letters of the authors’ first names. Year of publication. The name of the article. The name of the publication in which the article was published, volume number and / or issue number with the first letters in capital, the numbers of the first and last page of the document.

Punctuation marks like comma and etc. after journal names should not be used.

- In the examples below, the information about the mentioned documents is organized according to different document types, taking into account the punctuation marks.

***For example:***

Gürsoy, M. 2017. Munzur Dağları Alt Miyosen çökelleri mollusk topluluğu ve paleoekolojisi (Doğu Anadolu, Türkiye). *Maden Tetkik ve Arama Dergisi* 155, 75-99.

Pamir, H. N. 1953. Türkiye’de kurulacak bir Hidrojeoloji Enstitüsü hakkında rapor. *Türkiye Jeoloji Bülteni* 4 (1), 63-68.

Robertson, A. H. F. 2002. Overview of the genesis and emplacement of Mesozoic ophiolites in the Eastern Mediterranean Tethyan region. *Lithos* 65, 1-67.

- If the document is a book: authors’ surnames, authors’ first names. Year of publication. Title of the book with capital letters. The name of the publishing organization or the name of the publication in which the document was published, the volume and / or issue number, and the total number of pages of the book should be specified, respectively.

***For example:***

Einsele, G. 1992. *Sedimentary Basins*. Springer Verlag, 628.

Ketin, İ., Canitez, N. 1956. *Yapısal Jeoloji*. İTÜ, 308.

Meriç, E. 1983. *Foraminiferler*. Maden Tetkik ve Arama Genel Müdürlüğü Eğitim Serisi, 26, 280.

- If the document is published in a book containing the articles of various authors, the usual order for the document included in a periodical publication is followed until the end of the document title. Then the editors’ surnames and initials and the abbreviation of the editor word “Ed.” is written in parentheses. Then, the title of the book in which the document is located is written with the first letters in capital letters. Name of publishing organization. The place of publication, the volume number of the publication in which the document was published, and the numbers of the first and last pages of the document should be written.

**For example:**

Anderson, L. 1967. Latest information from seismic observations. Gaskell, T. F. (Ed.). The Earth's Mantle. Academic Press. London, 335-420.

Göncüoğlu, M. C., Turhan, N., Şentürk, K., Özcan, A., Uysal, S., Yalınız, K. 2000. A geotraverse across northwestern Turkey. Bozkurt, E., Winchester, J. A., Piper, J. D. A. (Ed.). Tectonics and Magmatism in Turkey and the Surrounding Area. Geological Society of London. Special Publication, 173, 139-162.

- If it is desired to specify the name of a book in which the writings of various authors are collected as a document; following the surnames and names of the book's editors, in parentheses the "Ed." statement is written. Year of publication. Title of the book with capital letters. The name of the publishing organization or the name of the publication in which the document was published, the volume and / or issue number and the total number of pages of the book should be specified.

**For example:**

Gaskel, T. F. (Ed.). 1967. The Earth's Mantle. Academic Press, 520.

- If the document is "published abstract", information about the document is given in the following order: Authors' surnames, authors' first names. Year of publication. Name of the document (paper). The name, date and place of the meeting where the paper is published, and the first and last page numbers in the book containing the abstract should be written.

**For example:**

Öztunalı, Ö., Yenyol, M. 1980. Yunak (Konya) yöresi kayaçlarının petrojenezi. Türkiye Jeoloji Kurumu 34. Bilim Teknik Kurultayı, Ankara, 36.

Yılmaz, Y. 2001. Some striking features of the Anatolian geology. 4. International Turkish Geology Symposium, 24-28 Eylül 2001, Adana, 13-14.

- If the mentioned document has not been published like report, lecture notes and etc., the word "unpublished" should be written at the end of the information about the document in parentheses after the information about the document is given

in the usual order for the document in a periodical publication.

**For example:**

Akyol, E. 1978. Palinoloji ders notları. EÜ Fen Fakültesi Yerbilimleri Bölümü, 45, İzmir (unpublished).

Özdemir, C., Biçen, C. 1971. Erzincan ili, İliç ilçesi ve civarı demir etütleri raporu. Maden Tetkik Arama Genel Müdürlüğü, Rapor No: 4461, 21, Ankara (unpublished).

- For unpublished courses, seminars and similar notes, the course organizer after document name. The place of the meeting. Title of the book and relevant page numbers should be given.

**For example:**

Walker, G.R., Mutti, E. 1973. Turbidity facies and facies associations. Society for Sedimentary Geology Pacific Section Short Course. Anaheim. Turbitides and Deep Water Sedimentation, 119-157.

- If the document is a thesis; author's surname, initial of the author's first name. Year of publication. Name of the thesis. The type of the thesis, the university where it was given, the total number of pages, its province and the word "unpublished" are written in parentheses.

**For example:**

Akıllı, H. 2019. Polatlı-Haymana (Ankara) civarı sıcak sularının izotop jeokimyası ( $\delta^{18}O$ ,  $\delta D$ ,  $3H$ ,  $\delta^{13}C$ ,  $\delta^{34}S$ ,  $87Sr/86Sr$ ) ve ana iz element bileşimleri ile incelenmesi. PhD Thesis, Ankara University, 255, Ankara (unpublished).

Argun Aktan, Ö. 2019. Marmara Denizi Batı Kıta Sahaneliği Yüzeysel Çökellerinde Jeojenik ve Antropojenik Ağır Metal Zenginleşmesine Yönelik Araştırmalar (Şarköy Kanyonu, KB Türkiye). MSc Thesis, Ankara University, 179, Ankara.

- Anonymous works should be arranged according to the publishing institution.

**For example:**

MTA. 1964. 1/500.000 ölçekli Türkiye Jeoloji Haritası, İstanbul Paftası. Maden Tetkik ve Arama Genel Müdürlüğü, Ankara.

- For the documents that are in print, no date is put after the name of the author, the name of the article and the source to be published should be specified and the word “in print” and / or “in review” should be written at the end (in parentheses).

**For example:**

Ishihara, S. The granitoid and mineralization. Economic Geology 75<sup>th</sup> Anniversary (in press).

- Information downloaded from the Internet should be given in the form of the name of the institution, its web address, and the date on which the web address was accessed. Turkish references should be given directly in Turkish and should be written in Turkish characters.

**For example:**

ERD (Earthquake Research Department of Turkey). <http://www.afad.gov.tr>. 3 March 2013.

- While citing the source, the original language should be adhered to, and the title of the article should not be translated.

## 6. Illustrations

- All of the drawings, photographs, plates and tables used in the article are referred to as “illustrating”.
- Illustrations should be used when their use is unavoidable or when they make the subject easier to understand.
- In the selection and arrangement of the format and size of the illustrations, an attitude should be made to prevent loss of space as much as possible considering the page length and layout of the bulletin.
- The number of illustrations used should be proportional to the size of the text.
- All illustrations should be submitted in separate files regardless of the text.
- Abbreviations should not be used in illustration explanations in the text and should be numbered in the order of mention within the text.
- Photographs and plates must be submitted as a computer file in which all details can be seen for the examination of the article, with EPS, TIFF or JPEG extension and at least 300 dpi resolution.

## 6.1. Figures

- Drawings and photographs other than the plate to be included in the article are evaluated together as “Figure” and numbered in the order of mention in the text.
- The figures should be prepared in computer considering the dimensions of a single column width as 7.4 cm or double column width as 15.8 cm. The figure area with its caption should not exceed 15.8x21 cm.
- While preparing the figures, unnecessary details should not be included and care should be taken not to use more space than necessary for the transfer of information.
- In figure descriptions, a space should be left after the word “Figure” is written, and the number is given in the usual sequence number, followed by a hyphen (-) and a space again, and a description of the relevant figure should be written. If the figure legend exceeds the bottom lines, the following lines should to be written after the “Figure 1-” statement alignment. Figure descriptions should be created as follows, without exceeding the edges of the figure and justified on both sides.

**For example:**

Figure 1- The district of Sandıklı (Afyon); a) geological map of the southwest, b) the general vertical section of the study area (Seymen, 1981), c) Turkey’s most important neotectonic structures (modified from Koçyiğit, 1994).

- Drawings should be drawn in computer properly, clean and with care.
- The use of thin lines that may disappear when minimized in figures should be avoided.
- Symbols or letters used in all drawings should not be less than 2 mm (7 pt.) in Times New Roman.
- All standardized symbols used in the drawings should preferably be explained in the drawing, if they are too long then they should be explained in the figure below.
- Bar scale should be used in all drawings and the north direction should be indicated on all maps.
- The name of the author, description of the figure, figure number should not be included in the drawing.

- Photographs should reflect the aims of the subject and should be in adequate numbers.
- Figures should be framed.

## 6.2. Plates

- Plates should be used in cases where multiple photographs are required to be printed together on a special paper.
- Plate dimensions must be equal to the size of the bulletin's usable area of the page.
- Figure numbers should be written under each of the figures on the plate and bar scale should be used.
- Original plates must be attached to the final copy to be submitted in the case of acceptance of the manuscript.
- Figures and plates should be numbered among themselves and independently. Figures should be numbered with Latin numerals and plates with Roman numerals (eg Figure 1, Plate I).
- There should be no explanation text on the figures inside the plate.

## 6.3. Tables

- All tables should be arranged in word format and should be prepared in Times New Roman.
- Tables should not exceed the size of 15x8 cm together with the table caption.
- Table explanations should be created without exceeding the edges of the figure and justified as in the example below.

### *For example:*

Table 1- Hydrogeochemical analysis results of geothermal waters in the study area.

## 7. Nomenclature and Abbreviation

- Abbreviations must be in the accepted international or national form. Unusual nomenclature and abbreviations that are not standardized in the article should be avoided. In cases where it is deemed necessary to use such nomenclature and abbreviations, the way and method followed should be explained.
- There should not be a dot between the words initials used in standard abbreviations (such as MTA, DSİ).
- Abbreviations of geography aspects should be made in English (N, S, E, W, NE and etc.).

The word group to be abbreviated should be written clearly where it is mentioned first time and the abbreviation should be given in parentheses, then only the abbreviated form should be written throughout the article.

- Systems with international validity (m, inch, etc.) should be used as the unit of measure. Decimals should be separated with commas in Turkish articles and with a period in English articles.
- The names of figures, plates and tables in the article should not be abbreviated. For example, "As seen in the generalized stratigraphic section of the region (Figure 1) ....."

## 7.1. Chronostatigraphic and Geochronologic Nomenclature

- "International Chronostratigraphic Chart" (<https://stratigraphy.org/chart>), which is updated annually by the International Stratigraphic Committee, should be taken into consideration in chronostratigraphic and geochronological nomenclature.
- Position within a chronostratigraphic unit can be expressed in adjectives indicating the position, for example: lower, middle, upper and etc. When using these adjectives, it should be decided whether the lower, middle and upper distinction is formal / informal in the International Chronostratigraphic Chart.

### *For example:*

lower Miocene, Upper Holocene and etc.

- When stating the time where a geochronological unit is, temporal adjectives such as; early, middle, late and etc. are used. When using these adjectives, the International Chronostratigraphic Chart should be taken into consideration to decide whether the adjectives begin with capital or lowercase letters.

### *For example:*

early Miocene, Late Holocene etc.

## 7.2. Paleontological Nomenclature and Spelling of Fossil Names

- Original names of fossils should be used.

### *For example:*

*Nummulites* with limestone

- Fossil genus and species names are written in italics, cf., aff. and gr. etc. expressions are written as normal (perpendicular). When writing fossil names for the first time, the surnames of the people who identify them and the year in which they were first defined should be written. In later uses, the surnames and the year in which they are defined may not be written. The surnames and dates of identifiers coming at the end of the fossil names are not references, they should not be included in the mentioned documents.

**For example:**

*Alveolina aragonensis* Hottinger, 1960 not a reference.

*Alveolina* cf. *aragonensis* Hottinger, 1960 not a reference.

*Alveolina* aff. *aragonensis* Hottinger, 1960 not a reference.

*Alveolina* gr. *aragonensis* Hottinger, 1960 not a reference.

- After the first use of the same genus in the text is written clearly, it can be abbreviated as in the example so that it will not be confused with another genus in later use.

**For example:**

*Alveolina aragonensis*, *A. polathensis*, *A. ellipsoidalis* etc.

- If the date is in parentheses after the person describing it after the name of the fossil in the text, this is a reference and should be included in the mentioned documents.

**For example:**

*Alveolina aragonensis* Hottinger (1960) is a reference.

- The following rules should be taken into account when writing the systematic paleontologic section.
  - a. First of all, genus, species and subspecies to be identified should be written in hierarchical order like the order, upper family, family type species and so on. Later, the species to be described should be written together with the surnames and date of the people who defined the subspecies name. If there is a photograph of the described fossil, the plate or figure with the photograph should be added under the fossil name. The names of the authors listed here are not references, so they are not included in the reference.

**For example:**

Order: Foraminiferida Eichwald, 1830

Superfamily: Alveolinacea Ehrenberg, 1839

Family: Alveolinidae Ehrenberg, 1839

Type Genus: *Borelis* de Montfort, 1808

Type Species: *Borelis melenoides* de Montfort, 1808  
= *Nautilus melo* Fichtel and Moll, 1798

*Borelis vonderschmitti* (Schweighauser, 1951)

(Plate II, Figure 3-5 or Figure 3A-H).

- b. Similar or synonyms (synonym) list should be left-aligned in chronological order. The page and figure number of the synonymous fossil in the relevant study should be included in the synonymous list. Authors in the synonymous list are references and must be included in the references.

**For example:**

**1951** *Neoalveolina vonderschmitti* **Schweighauser**, page 468, Figures 1-4.

**1974** *Borelis vonderschmitti* (Schweighauser), **Hottinger**, page 67, plate 98, Figures 1-7.

- c. After the synonymous list is given, the definition, explanations (similarities and differences), dimensions, material, stratigraphic distribution (according to the characteristics of the fossil) should be written.
- d. If the fossil is defined for the first time (new species) in the systematic paleontology section, the origin of the name, holotype, type locality, material, description, explanation (similarity and differences), age and geographical distribution, dimensions (according to the features that define the fossil) should be written. Photographs of the fossil identified for the first time by the authors must necessarily be placed in plates or figures.
- e. Bar scale indicating the size of fossils must be used definitely in plates / figures.

## 8. References

- In the references to be made in the Main Text, only the surnames of the authors and the publication year of the mentioned article should be specified. Referencing should be arranged according to one of the following examples:
- Referring to a publication with a single author (in chronological order):

-Altınlı (1972, 1976) defined the Bilecik sandstone in detail.

It is known that the fold axes of the Devonian and Carboniferous units around İstanbul are N-S trending (Ketin, 1953, 1956; Altınlı, 1999).

- Referring to a publication with two authors:
  - The upper parts of the unit include Ilerdian fossils (Sirel and Gündüz, 1976; Keskin and Turhan, 1987, 1989).
- Referring to a publication with more than two authors:
  - According to Caner et al. (1975), the Alıcı formation reflects the conditions of fluvial environment.
  - Unit disappears by wedging towards E (Tokay et al., 1984).
- Referring to a reference in another publication:

It is known that Lebling mentioned about the existence of Liassic around Çakraz (Lebling, 1932; Charles, 1933).

- When referring to the works of the authors with the same surname in the same year, referring the authors' first names by writing their initials:
  - Many studies have been done in the field of structural geology in the study area (Gutnic et al., 1979; Yılmaz A., 1983; Yılmaz, İ., 1983; Poisson et al., 1984 etc.).

## **9. Prints Sent to Authors**

Two copies of the relevant issue published in the Bulletin of the Mineral Research and Exploration are sent to the authors.

## **10. Terms of Publication and Copyrights**

- Some or all of the articles to be published in the Bulletin of the Mineral Research and Exploration should not have been published before.
- Authors who submit a publication to the Bulletin of the Mineral Research and Exploration are deemed to have accepted the bulletin's publication rules in advance.
- The copyright of the manuscripts accepted for publication and converted into publications belongs to the General Directorate of Mineral Research and Exploration (MTA).

The authors of the study sign the relevant forms within the scope of the provisions specified in the Regulation of the Editorial Board regarding the transfer of copyright and submit them to the Editorial Board. After the publication of the article, MTA may pay royalty fees to the authors of the article for their declarations within the scope of the "Regulation on the Editorial and Processing Fees to be paid by the Public Organizations and Institutions".

NOTE: Information and forms about Bulletin of the Mineral Research and Exploration can be accessed from the website: <http://dergi.mta.gov.tr/index.php>.